Mean field theories for the aging and yielding of athermal amorphous solids

DISSERTATION

for the award of the degree
"Doctor Rerum Naturalium" (Dr.rer.nat.)
of the Georg-August Universität Göttingen

within the doctoral program
Physics
of the Georg-August University School of Science (GAUSS)

submitted by

Jack Thomas Parley
from Tokyo, Japan

Göttingen, 2022

Thesis committee

Prof. Dr. Peter Sollich
Institut für Theoretische Physik,
Georg-August Universität Göttingen

Prof. Dr. Matthias Krüger
Institut für Theoretische Physik,
Georg-August Universität Göttingen

Prof. Dr. Annette Zippelius
Institut für Theoretische Physik,
Georg-August Universität Göttingen

Members of the examination board

Prof. Dr. Peter Sollich
Institut für Theoretische Physik,
Georg-August Universität Göttingen

Prof. Dr. Matthias Krüger
Institut für Theoretische Physik,
Georg-August Universität Göttingen

Further members of the examination board

Prof. Dr. Annette Zippelius
Institut für Theoretische Physik,
Georg-August Universität Göttingen

Prof. Dr. Marcus Müller
Institut für Theoretische Physik,
Georg-August Universität Göttingen

Prof. Dr. Ramin Golestanian
Department of Living Matter Physics,
Max Planck Institute for Dynamics and Self-Organization

Prof. Dr. Stefan Klumpp
Institut für Dynamik komplexer Systeme,
Georg-August Universität Göttingen

Date of the oral examination: May 11, 2022

Declaration of Authorship

I herewith formally declare that:

- I have written the submitted thesis independently.
- I clearly marked and separately listed all the literature and all other sources which I employed while producing this academic work, either literally or in content.
- The thesis was not used in the same or in a similar version to achieve an academic grading or is being published elsewhere.
- The digital version of the thesis is identical to the attached bound copies.
- Results presented in Chapter 2 have been published in [1] and those of Chapter 3 submitted for publication in the preprint [2], while most results of Chapter 4 have been published in [3].

Göttingen, March 31, 2022
Jack Thomas Parley

Abstract

In this thesis we study mean field elastoplastic models to understand athermal amorphous solids, which show complex slow relaxation (aging) phenomena and intricate mechanical responses under deformation. These models consider the dynamics of mesoscopic blocks of material, which alternate between elastic and plastic deformation. In mean field, the interactions mediated by the elastic stress propagator are treated as a mechanical noise. Our main contribution in this thesis is to extend these models in two important directions, concerning the nature of the mechanical noise, in the first part, and the disordered local energy landscape, in the second. Although the groundwork for such extensions was already laid out in the literature, these previous studies were limited to the case of steady shear.

In the first part, we construct a novel time-dependent mean field elastoplastic model, incorporating the power-law mechanical noise spectrum arising from localized plastic events. Local stresses are driven by power-law distributed mechanical noise from yield events throughout the material, in contrast to the well-studied Hébraud-Lequeux model where the noise is Gaussian. This model allows the exploration of general time-dependencies, including aging and arbitrary rheological protocols. We first use a mapping to a mean first passage time problem to study the phase diagram in the absence of shear, which shows a transition between an arrested and a fluid state. We then introduce a boundary layer scaling technique for low yield rate regimes, which we first apply to study the scaling of the steady state yield rate on approaching the arrest transition. These scalings are further developed to study the *aging* behaviour in the "jammed" regime, for different values of the exponent μ characterizing the mechanical noise spectrum. We find that the yield rate decays as a power-law for $1 < \mu < 2$, a stretched exponential for $\mu = 1$ and an exponential for $\mu < 1$, reflecting the relative importance of far-field and near-field events as the range of the stress propagator is varied. Comparison of the mean-field predictions with aging simulations of a lattice elastoplastic model shows excellent quantitative agreement, up to a simple rescaling of time.

We then study the linear response to strain in the model, which allows for direct comparison to stress measurements in particle simulations or experiments. In the "jammed" regime of the model where there is aging, we find that the stress relaxes incompletely to an age-dependent plateau, on a timescale which grows with material age. We determine the scaling behaviour of this aging linear response analytically, finding that key scaling exponents are universal and independent of the noise exponent μ. For $\mu > 1$, we find simple aging, where the stress relaxation timescale scales linearly with the age t_w of the material. At $\mu = 1$, which corresponds to interactions mediated by the physical elastic propagator, we find instead a $t_w^{1/2}$ scaling arising from the stretched exponential decay of the plastic activity. We compare these predictions with measurements of the linear response in computer simulations of a model jammed system of repulsive soft athermal particles, during its slow dissipative relaxation towards mechanical equilibrium, and find good agreement with the theory.

In the second part, we include the disordered local energy landscape by considering a distribution of yield barriers within the model. We first focus on the behaviour of athermal amorphous solids subject to oscillatory shear. We show that under oscillatory shear the model presents a genuine dynamical transition between

an elastic and a yielded state, and determine analytically the threshold energy distinguishing two qualitatively distinct classes of initial conditions. The mean field model reproduces the behaviour found in particle simulations: samples prepared above the threshold mechanically anneal towards the threshold state as the common yield point is approached, where the relaxation time diverges. Samples prepared below the threshold remain insensitive to shear up to a yield strain amplitude beyond the common yield point. Beyond this point, they display a non-trivial, non-monotonic approach to the yielded state. We identify this with the fatigue limit, and find that the number of cycles to yield diverges as the strain amplitude is decreased towards this limit from above. The model also sheds light on the important differences between yielding under oscillatory shear and uniform shear, and the relative role played by shear banding. We also study the implications of disorder for the study of shear startup and creep flow within mean field elastoplastic models. We argue that the inclusion of disorder allows for a more realistic way of modelling different degrees of initial annealing, and plays an important role in a range of rheological protocols.

Acknowledgements

I thank first and foremost my "Doktorvater" Peter Sollich. I consider myself fortunate to have been his student, and am grateful to him for sharing with me part of his scientific rigour and expertise. I thank him for granting me this opportunity in the first place, for his enduring patience especially in the initial stages, and for always taking the time and energy to make sure I found the right path.

I also thank other members of the Sollich group, in particular my post-doc colleagues Diego Tapias and Rituparno Mandal, for their friendship and support during this thesis. I further thank our two external collaborators, Profs. Suzanne Fielding (Durham, UK) and Srikanth Sastry (Bangalore, India) for their useful feedback and valuable contribution to the quality of the respective publications. I finally thank the members of the thesis advisory committee, Profs. Matthias Krüger and Annette Zippelius, and all the other members of the examination board.

This thesis is dedicated to my parents and brother, and to my partner for their love and support during this period.

Contents

Chapter 1

Introduction

Amorphous solids are all around us, ranging from window glass to toothpaste, foams and emulsions. Understanding the physical mechanisms by which a disordered assembly of repulsive particles can give rise to a rigid solid is a very non-trivial, fundamental question in itself [4]. Two main paradigms have emerged [5]: the jamming transition [6], relevant for e.g. granular matter and foams, and the glass transition [7], as occurring e.g. in colloidal suspensions. The astounding complexity of the problem is reflected in the plethora of physical theories which have been proposed for the glass transition, ranging from exact infinite-dimensional approaches [8] to kinetically constrained models [9] or mode-coupling theory [10, 11], to name a few.

Although these materials show solid behaviour, under a large enough shear deformation they eventually (if material failure is avoided) begin to flow [12], one may think of e.g. toothpaste. This phenomenon is generally referred to as *yielding*, and is of both fundamental and practical importance [13]. Recent years have seen many attempts from the statistical physics community (see introduction to Chapter 4) to understand this transition from an elastically deforming to a plastically flowing state.

We present briefly the terms elastic/plastic, which denote two distinct modes of deformation, and will form the basis of the elastoplastic modelling approach discussed below. For an elastic material (or block of material), the deformation away from a fixed microscopic reference state is reversible [14], i.e. the same reference state can be recovered upon reversal of the strain. On the other hand, plastic deformation [13] refers to generally irreversible changes (with associated energy dissipation) in the microscopic topological structure, e.g. changes in the local neighbourhood of some particles. Because of this it is useful to decompose the deformation into an elastic strain, describing the deformation with respect to a reference state, and the plastic strain, which accounts for the changing reference [13].

Unlike dislocations [15] in crystals, it is a priori unclear what the elementary mechanisms of plasticity should be in an amorphous solid. However, starting from the pioneering work of Argon and Kuo with bubble rafts as an analog for metallic glass [16], a large body of numerical and experimental works have led to the notion of localised rearrangements [17] (also called shear transformations) which govern the plastic activity. Local yield events have been identified in experiments in e.g. colloidal systems [18] and concentrated emulsions [19], as well as in many atomistic simulations of low-temperature shear [13, 20–23]. In the *athermal* regime, which may be achieved at low temperature or due to the size of the constituents, and on which we will focus in this thesis, they are believed to be the elementary constituents of plastic deformation in amorphous solids [24].

Such a localised rearrangement, involving of the order of dozens of particles, of course has also an important impact on the rest of the material, and may affect the appearance or not of other rearrangements elsewhere. This is especially visible in

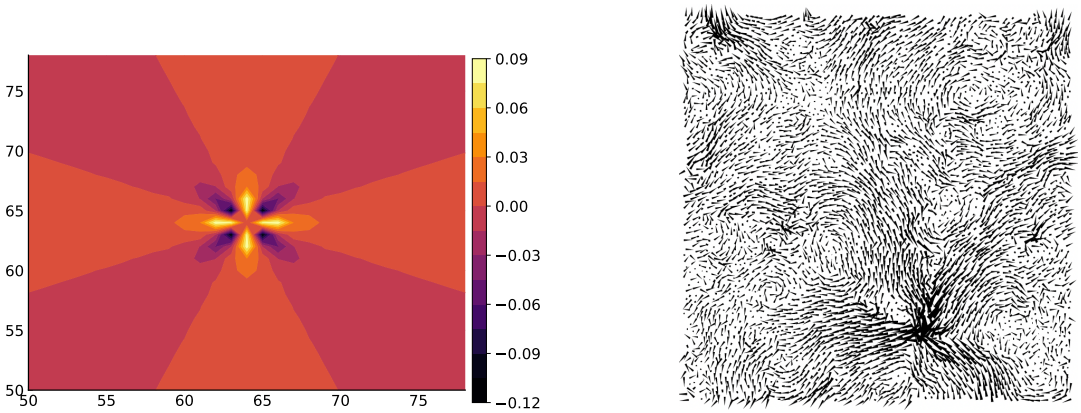

(A) (B)

FIGURE 1.1: Consequences of a plastic rearrangement in 2D. (A): colour map of the stress propagator elements after a unit stress drop at the center of a 128×128 square lattice (see Sec. 2.7 for details; for the purpose of the colour map we have set the central stress propagator element to zero). Data generated by Prof. Suzanne Fielding. (B): non-affine elastic displacement field (related to the stress through the gradient) just before a plastic event (occurring in bottom right of the figure) in a computer glass under athermal quasistatic shear. Note in both cases the common quadrupolar structure. (B) reprinted with permission from [Maloney and Lemaître, Phys. Rev. Lett., 93, 195501 (2014)]. Copyright (2014) by the American Physical Society.

the avalanche behaviour shown by amorphous solids under quasistatic shear [21]. In fact, a localised rearrangement embedded within a homogeneous elastic medium can be idealised as two force dipoles [25]. From the continuum equations of elasticity [14], one may derive the shear stress increment field caused by this event, which is determined by the elastic propagator $\mathcal{G}$. This corresponds in fact to a classical problem solved in the 50s by Eshelby [26] in 3D, namely that of an inclusion of arbitrary shape in an elastic medium. Two important properties of this propagator [25], which will be key features of our modelling approach, are that it is long-range (decaying as r^{-d} in the radial distance, with d the dimension), and has a varying sign (e.g. shows a quadrupolar structure in 2D, see Fig. 1.1).

The notion of localised mesoscopic blocks of material alternating between elastic loading and plastic rearrangements, while interacting with rearrangements happening elsewhere through the stress propagator, forms the basis of so-called elastoplastic models [13]. Keeping only key ingredients of the deformation dynamics these models can apply to a wide range of materials, which may be on completely different stress or energy scales, but share the same elementary elastoplastic dynamics. Elastoplastic models have been particularly successful for understanding the yielding transition under shear deformation [27–34]. This includes mean field elastoplastic approaches allowing for analytical calculations: noted examples are the shear-transformation-zone (STZ) theory [35], the soft glassy rheology (SGR) model [36], and the Hébraud-Lequeux (HL) model [37]. These differ in the details of the dynamical rules prescribed for the rearranging elements and in the way the interactions are treated. In the case of the HL model, spatial interactions are treated as mechanical noise that is self-consistently coupled to the average level of plastic activity in the material, as one expects for a purely athermal system. Here, we will greatly expand the scope of this mean field approach. Before we give an outline of these extensions,

however, we present briefly two important phenomena in amorphous solids, which will draw the focus of interest in this thesis: slow relaxation in athermal systems, and yielding under oscillatory shear.

As a paradigmatic model for slow athermal relaxation, we may consider the suspension of soft harmonic spheres of [38]. This particle model has been extensively studied [39], and has served as a useful model to disentangle the effect of the glass and jamming transitions [40]. Considering overdamped Langevin dynamics in the absence of shear and at zero temperature, the behaviour is simply set by the damping coefficient ξ against the solvent, the energy scale ϵ of the pairwise harmonic interaction, and the typical particle size a. Together, they yield a dissipation timescale $\xi a^2/\epsilon$ which controls the relaxation dynamics. Starting from a purely random high energy configuration, although one may a priori expect that such a system would relax exponentially quickly, it instead shows slow relaxation, typical of *aging* systems [38]. Aging phenomena have been extensively studied, e.g. in spin glasses [41] or colloidal glasses [7, 42], but in these cases the aging is generally driven by thermal effects, in contrast to the purely athermal dynamics considered here. Moreover, the athermal system of [38] shows highly heterogeneous dynamics, with localised hotspots of non-affine rearrangement similar to the plastic rearrangements under shear. This suggests the relevance of studying such a system from an elastoplastic perspective.

One is also intrested in the rheology of such a system. The term rheology refers to mechanical response under deformation; this may be probed in many different ways. Although the simplest scenario is that of steady shear, others include linear/non-linear response to step strain, shear startup, and creep dynamics under an imposed stress. The main goal in theoretical studies of rheology is to obtain a constitutive equation, relating the (generally tensorial) stress at a given time to the history of applied shear [43]. In thermal (e.g. colloidal hard sphere) glasses, results are obtainable from first principles through mode-coupling theory [11, 43]. In the aging regime, a fundamental issue to understand is the difference between (entropy-dominated) thermal glasses and an athermally aging system as described above. A particularly insightful and useful way of shedding light on this is by studying the *aging rheology*. Aging rheological behaviour has been studied in detail theoretically in the soft glassy rheology model [44], and experimentally in microgel pastes [45] or in a class of thermosensitive suspensions [46–48].

The second phenomenon we focus on is the yielding of amorphous solids or glasses under oscillatory shear deformation. This is currently a very active topic with many unanswered questions, in particular following a series of particle simulation studies [49–51] which investigated the dependence on the initial annealing of the glass. Glasses present a spectacularly complex potential energy landscape [52, 53] due to their structural disorder. Better annealed initial conditions, quantified by a lower potential energy, are generally obtained by a slow process of thermal annealing, whereby the system can reach deeper regions of the landscape through thermal activation over barriers [7]. In [49] and [50], single computer glass-forming models possessing such a complex landscape were prepared with different levels of thermal annealing, and shown to reproduce behaviours ranging from smooth, ductile yielding (for poorly annealed samples) to abrupt brittle yielding (well annealed samples). Examples of real materials displaying the first class of yielding are colloidal glasses [18], foams [54] and emulsions [55], while brittle yielding has been studied in depth in metallic glasses [56, 57]. A fascinating finding of the particle simulations [49, 50] is the appearance of a threshold energy, to which all poorly annealed glasses converge. Yielding under oscillatory shear, although until recently

less studied than uniform shear [34, 58–63], is in addition more informative of the structure of the material. It allows to probe steady state properties after many cycles and presents a sharp yield point, both in contrast to the uniform case (see Chapter 4).

Both of these phenomena raise many open questions: we now outline the answers provided in this thesis.

Broadly speaking, our work extends existing mean field approaches in two important directions. The first direction, relevant for Chapters 2 and 3, concerns the nature of the mean field mechanical noise considered. The well-studied Hébraud-Lequeux (HL) model [37], despite its many successes [64–69], relies on a simplified Gaussian mechanical noise. Deriving the noise term from the Eshelby stress propagator, however, in fact leads to a power-law mechanical noise [28, 70]. In Chapter 2, we firstly derive an HL-like time dependent model, with the "proper" mean field power-law noise statistics. We then show that this has a profound impact on the aging behaviour of the plastic activity, studied previously in [71] for the HL model. We finally compare the mean field predictions for the slow relaxation of the plastic activity against simulations (carried out by Prof. Suzanne Fielding, Durham UK) of a two-dimensional lattice elastoplastic model, finding excellent agreement.

The plastic activity, however, is difficult to measure directly in particle simulations or experiments. In Chapter 3, we therefore study in depth the linear response to strain of the proposed model. We characterise in particular the scaling behaviour of the aging linear response: unlike the plastic activity, this can be compared directly to stress measurements in experiments or particle simulations. We further perform such a comparison, taking as reference molecular dynamics simulations (performed by Dr. Rituparno Mandal) of the model athermal system of [38], and find good agreement with the theory.

The second direction, pursued in detail in Chapter 4 to understand yielding under oscillatory shear, is the inclusion of disorder within the model through a distribution of local yield barriers. Here it is the inclusion of this local disordered energy landscape, capturing in a simplified manner the complex global energy landscape of glasses, which will be key to reproducing the main features found in particle simulations. Although a disordered version of the HL model was introduced previously in [66], only steady shear was considered and the model was not developed further. In Chapter 4 we show that under oscillatory shear, the disordered HL model is capable of describing a genuine dynamical yielding transition, reproduces qualitatively the initial annealing dependence and contributes to the understanding of fatigue failure in well-annealed glasses. The mean field model also sheds light on the differences with respect to yielding under uniform shear, and the relative role played by shear banding. We further argue that the inclusion of local disorder in the model allows for a more realistic modelling of initial annealing compared to previous approaches, and also plays an important role in various other rheological protocols such as shear startup and creep flow under an imposed stress (treated in Chapter 5).

In Chapter 5, we conclude this thesis with a summary of the main results and an outlook towards future research. We also include some preliminary results addressing open questions.

Chapter 2

Aging in a mean field elastoplastic model of amorphous solids

Most of the following chapter, except parts of Sections 2.1 and 2.8, has been reproduced from the published paper [1].

2.1 Introduction

In the first section of this chapter (Sec. 2.2), we will begin by deriving a novel mean-field time-dependent elastoplastic model. We will do so by imposing a set of minimal local elastoplastic update rules, which will be followed by N mesoscopic blocks. These may be considered to occupy sites on a (e.g. regular) spatial lattice, as in previous approaches [13]. We will then reduce the full N-body problem, via a mean field factorization, to a 1-body master equation for the distribution of local stress.

As already pointed out in the introductory Chapter 1, the novel, improved feature with respect to the well-studied Hébraud-Lequeux (HL) model [37] will be the presence of power-law distributed mechanical noise. In HL, the noise term is taken to be diffusive, corresponding to Gaussian white noise. Despite its simplicity, HL manages to predict a transition between a fluid and an arrested state, reproducing in the latter regime the Herschel-Bulkley law [72], which fits well the stationary flow behaviour of many yield stress materials [12]. This includes examples [12] such as toothpastes, paints, and even blood flow in an artery.

As argued in [28] (see also the earlier work [70]), however, and as discussed more in detail below, deriving the mean field mechanical noise from the elastic propagator actually leads to a power-law distributed noise. Although introduced there, the analysis of [28] was limited to quasistatic shear, i.e. in the limit $\dot{\gamma} \to 0$, where $\dot{\gamma}$ is the applied shear rate. This followed previous work, aimed at developing a scaling description of the yielding transition at zero temperature using lattice elastoplastic models [27]. This scaling description was shown to be controlled by the statistics of "weakest" blocks. Denoting by x_i the "stability" of a block i, defined as the deviation of the local stress with respect to the local yield threshold, the distribution of local stabilities across the system was shown to follow $P(x) \sim x^\theta$ with $0 < \theta < 1$, referred to as a *pseudogap* [27]. Molecular dynamics (MD) studies confirm this scenario [73, 74]. In [28] it was shown that, among other things, the introduction of power-law mechanical noise into the mean field description successfully captures the finite-dimensional value of the exponent θ quantitatively in $d = 4$, and very well in $d = 3$. This suggests that this is the "true" mean field description in the sense that it applies in large dimensions [28]. Here, we extend this approach beyond the quasistatic limit, in order to study general time-dependent aging and rheological phenomena.

After deriving the model, in Sec. 2.3 we determine its phase diagram, separating the arrested (i.e. "jammed" or "glassy") and flowing (liquid) states. In Sec. 2.5, we introduce a boundary layer scaling technique for the regime of low yield rate (plastic events per unit time). This section builds on the analysis carried out in [71] on the HL model. Important differences arise, however, in the case of power-law noise, e.g. due to the presence of non-local boundary conditions. This will greatly affect the boundary layer structure.

In Sec. 2.4, the boundary layer technique is first applied to find the scaling of the yield rate above the arrested-flowing transition. Then, we deploy the method to study the aging behaviour in Sec. 2.6. This will constitute the basis of Chapter 3, where we will study rheological protocols in which a perturbation is applied only after a given waiting time, allowing for direct comparison to particle simulations or experiments. In Sec. 2.7, as a first check we compare the mean-field predictions for the aging behaviour of the yield rate against simulations (carried out by Prof. Suzanne Fielding, Durham UK) of a two-dimensional lattice elastoplastic model. We provide a summary of the chapter in Sec. 2.8.

2.2 Model derivation

Following the general philosophy of elastoplastic models [13], we regard our system of interest as divided into N mesoscopic blocks centred on the sites of a regular (e.g. square) lattice; to each block we assign a local shear stress. We begin with a description of the stochastic rules governing the local stress dynamics. Considering initially dynamics in discrete time, we introduce the following update rules. Take the time step Δt small enough so that there is at most one yield event per time interval, and label the site where this event takes place by l. The yielding rule is given by

$$\sigma_l(t+\Delta t) = 0 \quad \text{with probability } \frac{\Delta t}{\tau_{\rm pl}} \quad \text{if } |\sigma_l(t)| > \sigma_c \tag{2.1}$$

This means that a yield event, where particles rearrange plastically, resets the local stress to zero [1]. Such a plastic rearrangement takes place at a fixed rate $\tau_{\rm pl}^{-1}$ once the local stress exceeds the local yield threshold σ_c.

The stresses at all other sites $\{\sigma_i\}$, $i \neq l$, evolve as

$$\sigma_i(t+\Delta t) = G_0\dot{\gamma}\Delta t + \sigma_i(t) + \delta\sigma_i \tag{2.2}$$

This incorporates a drift term due to the external shear rate $\dot{\gamma}$, multiplied by the local shear modulus G_0, and a stress "kick" $\delta\sigma_i$ that models the Eshelby stress propagation from the yield event at site l; $\delta\sigma_i$ of course depends on l but we do not write this explicitly. From the beginning we consider here a mean-field description of this mechanical noise, which can be derived from the full spatial Eshelby stress propagator [25, 26] by treating the site of the yield event as randomly chosen across the system. It is then straightforward to show [28] that for a stress propagator decaying as $\sim r^{-\beta}$ in dimension d, the noise kicks will be distributed as $\rho(\delta\sigma) \sim |\delta\sigma|^{-\mu-1}$ with an exponent

$$\mu = \frac{d}{\beta} \tag{2.3}$$

[1] We consider here a full local stress relaxation. The post-yield local stress may however also be modelled as drawn from a distribution of residual stress other than a Dirac function at zero. Previous studies have shown this not to change the behaviour qualitatively [64].

For the physical propagator with $\beta = d$ (Ref. [25]) this leads to $\mu = 1$. We note though that recent works [30, 31] suggest that exponent values in the range $1 < \mu < 2$ may also have physical relevance, once the description is coarse-grained further to study the aggregate effect of avalanches of yield events that can potentially span a large number of sites. Studying this range is also important in itself due to the marginal character of $\mu = 1$, which will need to be approached as a limiting case. Varying μ can be thought of as varying the range of the stress propagation: larger μ corresponds to smaller β and hence longer range propagation. In fact for $\mu \to 2$ we will find that our model reduces to the HL model with its effectively infinite interaction range. Conversely, for $\mu < 1$ stress propagation is essentially local.

Besides the exponent μ, the second key parameter of the model is the coupling A, related to the prefactor of the aforementioned power-law behaviour of $\rho(\delta\sigma)$. We can distinguish here two different approaches.

The first approach is based on [70, 75]. There, a two-dimensional glassy system was studied under quasistatic shear, and a phenomenology was presented in terms of "active" zones corresponding to shear transformation zones, which are distributed randomly throughout the system and can "flip" leading to a plastic event. With this picture in mind, the coupling A is proportional to the area fraction (in $d = 2$) of the system occupied by the active zones. We derive this explicitly for a 2D circular geometry in App. 2.D, where we find $A \propto \varphi = N r_0^2 / R^2$. φ is a dimensionless packing density, where r_0 is the radius of the rearranging clusters and R that of the total system. The proportionality constant (see App. 2.D) involves the strength of the elastic interactions. Therefore the coupling A may be thought of as being related to structural details of the system, setting the effective coupling between mesoscopic elements in a way that is reminiscent of the effective mechanical temperature that appears in the shear-transformation-zone (STZ) [35] or soft glassy rheology (SGR) [36] theories.

In a second approach (Sec. 2.7), where we consider instead the case of sites fixed to positions on a lattice, we will derive the value of A by fitting directly the histogram of stress increments $\{\delta\sigma\}$, this value of A being fixed by geometry (e.g. $A \approx 0.32$ for a 2D square lattice, see below). To include both cases, we treat A as a variable parameter in the following.

The power law behaviour $\rho(\delta\sigma) \sim |\delta\sigma|^{-\mu-1}$ derived above is exact for small $\delta\sigma$, corresponding to the small effects of far away yield events, but must eventually be cut off at the largest $|\delta\sigma|$ resulting from yield events at neighbouring sites. The explicit calculation in $d = 2$ (Appendix 2.D) that accounts for the full angular dependence of the stress propagator gives a soft upper cutoff, where $\rho(\delta\sigma)$ goes to zero continuously.

For simplicity [2] we nonetheless use for the calculations a hard upper cutoff $\delta\sigma_u$ as proposed in Ref. [28], and a lower cutoff chosen as $\delta\sigma_u N^{-1/\mu}$ that goes to zero for $N \gg 1$. This resulting simplified mechanical noise distribution takes the form

$$\rho(\delta\sigma) = \frac{A}{N}|\delta\sigma|^{-\mu-1}, \quad \delta\sigma_u N^{-1/\mu} < |\delta\sigma| < \delta\sigma_u \tag{2.4}$$

By normalization, $\delta\sigma_u$ is then related to the prefactor (coupling) A by

$$\delta\sigma_u = \left(\frac{2A}{\mu}\right)^{1/\mu} \tag{2.5}$$

[2] This will change quantitative aspects such as the location of the phase diagram; however, the scaling forms below are determined by the asymptotic power-law regime for small $|\delta\sigma|$, making the precise form of the upper cutoff irrelevant.

It is important to note that the form (2.5) relies on a specific choice of the ratio between upper and lower cutoff. This was taken as $N^{1/\mu}$ in Ref. [28], but in general involves a geometrical factor that will depend on the system. This means that (even within the assumption of a hard upper cutoff), the value of $\delta\sigma_{\rm u}$ is not unambiguously fixed by A, a fact that we will return to in Sec. 2.7.

From the noise distribution (2.4) we extract, after a yield event at site l, independently and identically distributed (i.i.d.) stress increments $\delta\sigma_i$ for all other sites ($i \neq l$). We add to each $\delta\sigma_i$ in (2.2) the term $-\sum_{k\neq l}\delta\sigma_k/(N-1)$. This counterterm is formally necessary to ensure that stress propagation has a net zero effect on the total stress $\sum_{i\neq l}\sigma_i$ outside the block that yields. For large N we will see that the counterterm has a negligible effect because due to the symmetry of $\rho(\delta\sigma)$, $\sum_{k\neq l}\delta\sigma_k/(N-1)$ is of order $N^{1/2}/N = N^{-1/2}$.

We next transform the above dynamical rules into a master equation for the joint time evolution of the stresses $\boldsymbol{\sigma} = (\sigma_1,\ldots,\sigma_N)$ at all N sites. Given the above assumptions, the transition rate from configuration $\boldsymbol{\sigma}'$ to $\boldsymbol{\sigma}$ associated to a yield event at site l is

$$K_l(\boldsymbol{\sigma}|\boldsymbol{\sigma}') = \frac{1}{\tau_{\rm pl}}\theta(|\sigma_l'|-\sigma_c)\delta(\sigma_l)\left\langle\prod_{j\neq l}\delta\left(\sigma_j-\left(\sigma_j'+\delta\sigma_j-\frac{1}{N-1}\sum_{k\neq l}\delta\sigma_k\right)\right)\right\rangle \tag{2.6}$$

where one may identify the factors stemming from the local yielding rule (2.1) and the stress update at all other sites (2.2). The brackets denote an average over the distribution of stress kicks $\delta\sigma_i$, which we recall are sampled independently from the same distribution $\rho(\delta\sigma)$. Bearing in mind that a yield event can occur at any site l and incorporating the loading by external shear in (2.2) gives then the master equation

$$\partial_t P(\boldsymbol{\sigma}) = -G_0\dot\gamma\sum_i\partial_{\sigma_i}P(\boldsymbol{\sigma}) + \sum_l\int\left(K_l(\boldsymbol{\sigma}|\boldsymbol{\sigma}')P(\boldsymbol{\sigma}') - K_l(\boldsymbol{\sigma}'|\boldsymbol{\sigma})P(\boldsymbol{\sigma})\right)\mathrm{d}\boldsymbol{\sigma}' \tag{2.7}$$

We can now reduce this description to one for the distribution of *local* stresses, proceeding in a similar fashion to Ref. [76]. We assume a mean-field factorization $P(\boldsymbol{\sigma}) = \prod_i P_i(\sigma_i)$, which we expect to become exact for $N\to\infty$ as each local stress couples to the others only via the total number of yield events. From equation (2.7) one can then obtain the time evolution of $P_i(\sigma_i)$ by integrating out the remaining $N-1$ stresses (see Appendix 2.A), which will include the effect of stress kicks from yield events at other sites. The final form of the master equation for the local stress distribution $P(\sigma) = (1/N)\sum_i\langle\delta(\sigma-\sigma_i)\rangle = (1/N)\sum_i P_i(\sigma)$ reads

$$\begin{aligned}\partial_t P(\sigma,t) &= -G_0\dot\gamma\partial_\sigma P(\sigma,t)\\ &\quad + A\Gamma(t)\int_{\sigma-\delta\sigma_{\rm u}}^{\sigma+\delta\sigma_{\rm u}}\frac{P(\sigma',t)-P(\sigma,t)}{|\sigma-\sigma'|^{\mu+1}}\mathrm{d}\sigma' - \frac{\theta(|\sigma|-\sigma_c)}{\tau_{\rm pl}}P(\sigma,t) + \Gamma(t)\delta(\sigma)\end{aligned} \tag{2.8}$$

where we have defined the yield rate

$$\Gamma(t) = \frac{1}{\tau_{\rm pl}}\int_{-\infty}^{\infty}\theta(|\sigma|-\sigma_c)P(\sigma,t)\mathrm{d}\sigma \tag{2.9}$$

In the following we will generally consider the dimensionless form of (2.8), setting the threshold stress $\sigma_c = 1$ and the plastic timescale $\tau_{\rm pl} = 1$.

Equation (2.8) is our desired time-dependent mean-field model for the elasto-plastic dynamics of amorphous solids. It generalizes the model originally proposed by Lin and Wyart [28], which was restricted to steady state scenarios. This model was described in terms of an accumulated plastic strain $\gamma^{\rm pl}$. It can be recovered from the general formulation (2.8) by considering constant global stress $\langle\sigma\rangle$, i.e. a stress-controlled protocol. From (2.8) we have then $0 = \partial_t\langle\sigma\rangle = G_0\dot{\gamma} - v\Gamma$ where the "velocity" v relating shear rate and yield rate is the average stress of yielding sites, i.e. the average over the distribution $\theta(|\sigma|-1)P(\sigma,t)/\Gamma(t)$. Using then that the plastic strain increments with each yield event so that $\dot{\gamma}^{\rm pl} = \Gamma$ one obtains equation (8) in Ref. [28] for $P(x,\gamma^{\rm pl})$, where $x = 1-\sigma$.

The well-studied HL model [37] may also be derived as a limiting case of (2.8): it corresponds to the limit $\mu \to 2$, taken from below. To see this one can use a Kramers-Moyal expansion to express the convolution with a power law kernel in the second line of (2.8) as an infinite series of even-order derivatives $(\partial/\partial\sigma)^{2n}P$. The prefactor of the diffusive term ($n=1$) then works out as $\alpha_{\rm eff}\Gamma$ with

$$\alpha_{\rm eff} = \frac{A}{2-\mu}\delta\sigma_{\rm u}^{2-\mu} = \frac{A}{2-\mu}\left(\frac{2A}{\mu}\right)^{2/\mu-1} \tag{2.10}$$

Keeping now $\alpha_{\rm eff}$ fixed while taking $\mu \to 2^-$, one finds that $A \sim 2-\mu$ to leading order, with the consequence that all terms involving higher-order derivatives of P ($(\partial/\partial\sigma)^4P$ etc) become negligible (see Appendix 2.A for details). The master equation then becomes that of the HL model [37]

$$\frac{\partial P(\sigma,t)}{\partial t} = -G_0\dot{\gamma}\frac{\partial P}{\partial\sigma} + \alpha\Gamma(t)\frac{\partial^2 P}{\partial\sigma^2} - \theta(|\sigma|-1)P + \Gamma(t)\delta(\sigma) \tag{2.11}$$

where $\Gamma(t)$ is the yield rate as defined above while the stress propagation now takes the form of Brownian motion with diffusion constant $D(t) = \alpha\Gamma(t)$. Note that for $\mu < 2$ the relation (2.10) can be used to approximate our model (2.8) by an effective HL model, which as we will see below gives a reasonable qualitative account of the phase diagram.

2.3 Phase diagram

The HL model [37] was shown, despite its simplicity, to display a *dynamical arrest transition* as the coupling α is varied. In particular, for $\alpha > \alpha_c = 1/2$ (in dimensionless form) there exists a steady state distribution $P^{\rm ss}(\sigma)$ with nonzero yield rate Γ even in the absence of external shear, and the low shear rate rheology is that of a Newtonian liquid. In contrast, below the critical value α_c only frozen steady states with $\Gamma = 0$ exist and the system exhibits a finite yield stress, hence the description of it as being *arrested*.

In the present model we expect a similar transition at a critical coupling A_c, and working out the corresponding phase diagram will be necessary to identify the correct parameter regime for studying the aging behaviour. In order to identify the critical value $A_c(\mu)$, which will also depend on the exponent μ, it will be useful to consider the steady state version of (2.8) divided by Γ:

$$A\int_{\sigma-\delta\sigma_{\rm u}}^{\sigma+\delta\sigma_{\rm u}} \frac{P^{\rm ss}(\sigma') - P^{\rm ss}(\sigma)}{|\sigma-\sigma'|^{\mu+1}}{\rm d}\sigma' + \delta(\sigma) - \frac{\theta(|\sigma|-1)}{\Gamma}P^{\rm ss} = 0 \tag{2.12}$$

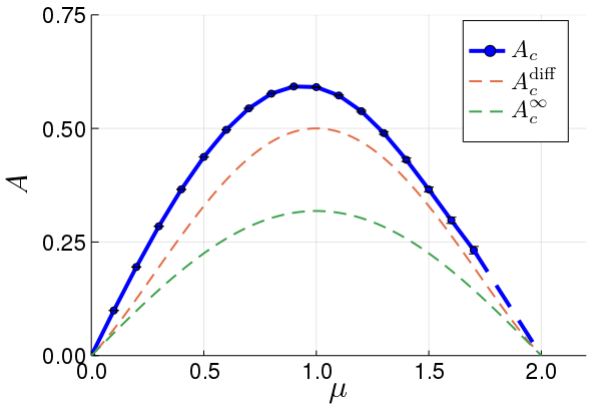

FIGURE 2.1: Phase diagram in the $A - \mu$ plane. The numerically exact $A_c(\mu)$ in blue separates the liquid regime (above) from the amorphous solid (below). Due to the increase in numerical error as $\mu \to 2$ (see Appendix 2.E.2), we show the last segment as an interpolation (blue dashed line). In addition, we show for comparison the diffusive (orange) and infinite cut-off (green) approximations to $A_c(\mu)$.

In the limit where $A \to A_c$ and correspondingly $\Gamma \to 0$, the final yielding term may be replaced by an absorbing boundary condition enforcing $P^{\mathrm{ss}}(\sigma) = 0$ for $|\sigma| > 1$. The critical boundary may then be computed numerically (for details see Appendix 2.E.2) giving the phase diagram shown in Figure 2.1. The resulting curve $A_c(\mu)$ is bell-shaped, with a peak at $\mu \simeq 1$.

Also shown is a "diffusive approximation" A_c^{diff}, which approximates the power-law noise for $\mu < 2$ with Gaussian noise of the same variance. This is obtained by equating the α_{eff} defined earlier in (2.10) to $\alpha_c = 1/2$. This approach reproduces the general features of the curve $A_c(\mu)$. It becomes exact as expected in the limit $\mu \to 2$, where our model approaches the HL model. Conversely the approximation becomes worse (as can be seen by plotting e.g. the ratio A_c/A_c^{diff}) as μ is decreased, especially in the region $\mu < 1$ where the dynamics is increasingly dominated by large stress kicks. Interestingly, the approximation A_c^{diff} lies consistently below the true $A_c(\mu)$, indicating that the power-law noise is actually less efficient in "liquifying" the system than Gaussian stress kicks with the same variance. Intuitively this can be rationalized from the large heterogeneity of power-law mechanical noise, where the variance is dominated by the large stress kicks while most kicks are in fact negligibly small. In studying the aging dynamics below we will find a similar effect, with the system aging towards an arrested state faster as μ is decreased.

We can develop a second approximation for $A_c(\mu)$ by exploiting a reinterpretation of (2.12) as the steady state condition for what is known as a Lévy flight [77] with absorbing boundaries. Indeed, if we think of the local stress σ as the position coordinate of an effective particle then this particle "diffuses" in power-law distributed steps, i.e. subject to Lévy noise. This is the defining property of a Lévy flight. The reinjection term $\delta(\sigma)$ effectively sets the initial condition $\sigma = 0$ of the particle, from which it executes its Lévy flight until it hits the absorbing region $|\sigma| > 1$. Calling the resulting time-decaying distribution $g(\sigma, t)$, the problem may be solved by separation of variables, writing

$$g(\sigma, t) = \sum_k \psi_k(\sigma) e^{-t/\tau_k} \int_{-1}^{1} \psi_k(y) g(y, 0) \mathrm{d}y \tag{2.13}$$

in terms of the eigenmodes $\psi_k(\sigma)$ and their decay times τ_k. These are related by the eigenvalue equation $A\mathcal{L}\psi_k(\sigma) = -\frac{1}{\tau_k}\psi_k(\sigma)$, where $\mathcal{L}$ denotes the propagator

$$\mathcal{L}\psi(\sigma) = \int_{\sigma-\delta\sigma_u}^{\sigma+\delta\sigma_u} \frac{\psi(\sigma') - \psi(\sigma)}{|\sigma - \sigma'|^{\mu+1}} \mathrm{d}\sigma' \tag{2.14}$$

The eigenfunctions $\psi_k(\sigma)$ scale near the boundaries as [78] $\psi_k(\sigma) \sim (1 - |\sigma|)^{\mu/2}$. This singular behaviour will be picked up by the *critical distribution*, defined as the limit of the steady state $P_c(\sigma) = \lim_{A\to A_c} P^{\mathrm{ss}}(\sigma)$ as the critical coupling is approached (see Section 2.5).[3]

Continuing with the Lévy flight argument above, the survival probability of the effective particle at time t may be written as $S(t) = \int_{-1}^{1} g(\sigma, t)\mathrm{d}\sigma$, and from this in turn we may derive the mean first passage time $\tau_{\mathrm{FP}} = \int_0^\infty S(t')\mathrm{d}t'$ until the particle is absorbed. To obtain a normalized steady state distribution $P_c(\sigma)$ at $A = A_c$, this mean lifetime needs to balance the reinjection which occurs at rate 1, so that

$$\tau_{\mathrm{FP}} = 1 \tag{2.15}$$

This condition then implicitly determines the value of A_c. In the HL model, one can follow the same argument and write the equivalent of equation (2.12). Applying the well-known result for a particle diffusing with unit variance Brownian noise in a box, one finds $\tau_{\mathrm{FP}}(\alpha) = 1/(2\alpha)$. With the condition (2.15) this then directly gives the critical coupling $\alpha_c = 1/2$.

In our model with cut-off Lévy noise the mean lifetime cannot be obtained analytically, and $A_c(\mu)$ must be determined by finding τ_{FP} numerically for a range of A and solving for the value of A – the "Lévy flight intensity" – where (2.15) is satisfied. In the absence of a cutoff, however, there is an analytical expression for the mean first passage time [79], which applied to our model gives

$$A_c^\infty(\mu) = \frac{1}{\pi} \sin\left(\frac{\mu\pi}{2}\right) \tag{2.16}$$

This is also included in Figure 2.1 for comparison. It shows again the same bell-shaped form; however, as one would expect it lies significantly below the true $A_c(\mu)$: without a cutoff the overall noise intensity is higher so the system stays liquid down to lower A.

2.4 Boundary layer equation

To understand the scaling of the activity in steady state above the dynamical arrest transition, as well as for our later analysis of the aging behaviour, we introduce here a boundary layer framework. This is inspired by Ref. [71], where the HL model is studied in the same spirit.

It will be useful to write the local stress distribution $P(\sigma, t)$ in terms of the yield rate as $P(\sigma, \Gamma)$. In the steady state the yield rate Γ will be constant, whereas during the aging we expect it to decay in time. In either case we will consider an expansion of the master equation (2.8) for $\Gamma \ll 1$.

[3] The exponent $\mu/2$ corresponds to the *pseudogap* exponent in [28]

To motivate the approach below, consider the aging behaviour of $P(\sigma, t)$. Without shear to load local sites elastically, one expects that at long times the stress dynamics (2.8) will be dominated by local stress with values around the yield threshold $\sigma = \pm 1$, which we refer to as the boundary layer. To estimate the thickness of this layer we note that once the local stress at a site crosses the threshold it takes a typical time $\tau_{\rm pl}$ to be reset to zero by a yield event. In this time it receives a number of kicks of order $\Gamma\tau_{\rm pl}$, which in dimensionless units is just Γ. The typical stress changes occurring during this time are given by the Hurst exponent [77] $H = 1/\mu$, so that we expect the width of the boundary layer to scale as $\sigma \mp 1 \sim \Gamma^H = \Gamma^{1/\mu}$. (The two signs relate to yielding at $+\sigma_c = +1$ and $-\sigma_c = -1$, respectively.)

To incorporate the presence of the boundary layer into our analysis we need to consider the behaviour of $P(\sigma, \Gamma)$ separately in the interior (sub-threshold) region $|\sigma| < 1$, the exterior region $|\sigma| > 1$ and the boundary layer. We consider symmetric distributions, $P(\sigma, \Gamma) = P(-\sigma, \Gamma)$, which in an unsheared steady state is automatic while for the aging dynamics it only requires a symmetric initial stress distribution. To connect the interior or exterior part of the distribution with the boundary layer we introduce a parameter ϵ such that $\Gamma^{1/\mu} \ll \epsilon \ll 1$. This then allows us to split the ansatz for $P(\sigma, \Gamma)$ into three different regions as sketched in Figure 2.2 and verified from numerical simulation data in Figures 2.3, 2.4 and 2.5:

- In the interior region $|\sigma| < 1 - \epsilon$ (region III in Fig. 2.2) we write $P(\sigma, \Gamma) = Q_0(\sigma) + \Gamma^a Q_1(\sigma)$, where $Q_0(\sigma) = \lim_{\Gamma \to 0} Q(\sigma, \Gamma)$ and Q_1 is the leading order correction for small Γ. We will refer to $Q_0(\sigma)$ as the *frozen-in* distribution, and it will present the $(1 - |\sigma|)^{\mu/2}$ singularity discussed in Section 2.3. In the scaling analysis for the steady state it will correspond to the critical distribution $P_c(\sigma)$.

- The exterior tail for $\sigma > 1 + \epsilon$ (region II in Fig. 2.2), which is symmetrically related to the left tail at $\sigma < -1 - \epsilon$. In the exterior region we write the distribution as $P(\sigma, \Gamma) = \Gamma^b T_1(\sigma)$, where b is the exponent of the leading order term.

- In the boundary layer region (region I in Fig. 2.2), for $1 - \epsilon < \sigma < 1 + \epsilon$ (and similarly $-1 - \epsilon < \sigma < -1 + \epsilon$), we write the scaling function in terms of a rescaled stress variable $z = \Gamma^{-1/\mu}(\sigma - 1)$ that from our argument above should be of order unity. In the boundary layer we therefore write $P(\sigma, \Gamma) \equiv \tilde{P}(z, \Gamma)$ with the form of $\tilde{P}(z, \Gamma)$ to be determined below.

The task is now to substitute the above ansatz into the master equation (2.8), separately for σ in the three different regions: interior, boundary layer and exterior. We limit the discussion here to the boundary layer, which will be the most important for the physics, and leave further details for Appendix 2.C.

In the boundary layer there will be a contribution from the frozen-in distribution. On the scale of the boundary layer this will be given by the singular behaviour $Q_0(\sigma) \simeq q_0(1 - \sigma)^{\mu/2}$, which written in terms of z is $\Gamma^{1/2} q_0(-z)^{\mu/2}$ with $z < 0$. We deduce that $\tilde{P}(z, \Gamma)$ may be split into a frozen part and a correction, which again we write at leading order:

$$\tilde{P}(z, \Gamma) = \Gamma^{1/2} q_0(-z)^{\mu/2} \theta(-z) + \Gamma^c R_1(z) \tag{2.17}$$

The exponent c can be determined by matching the boundary layer function to $P(\sigma, \Gamma)$ in the exterior region, which decays as $(\sigma - 1)^{-\mu/2}$ (see Appendix 2.C.1), with the result $c = 1/2$ so that the two exponents in (2.17) are equal and we can

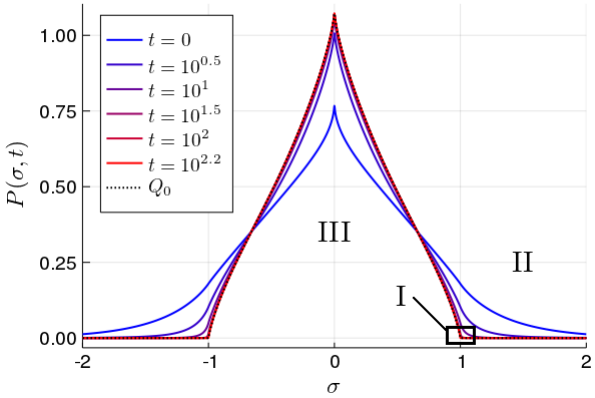

FIGURE 2.2: Distribution $P(\sigma,t)$ at increasing (from blue to red) times t during aging, obtained by numerical solution of (2.8), using as parameters $\mu = 1.7$, $A = 0.15$ starting from the reference steady state (see Sec. 2.6). Also shown is the frozen-in distribution $Q_0(\sigma)$ (dotted line lying almost on top of distribution for $t = 10^{2.2}$).

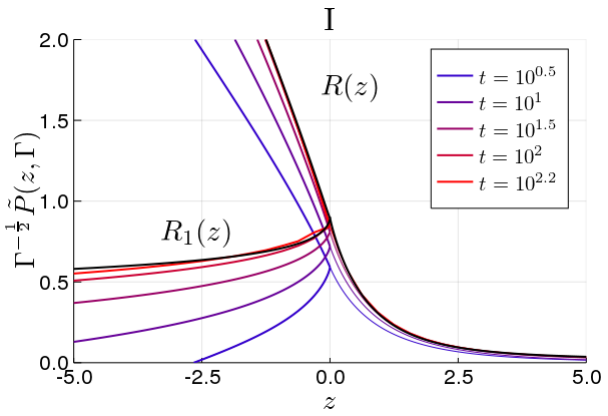

FIGURE 2.3: Boundary layer (zoom on region I of Fig. 2.2). In the upper curves we show $\Gamma^{-1/2}\tilde{P}(z,\Gamma)$, while in the lower curves we show $\Gamma^{-1/2}\tilde{P}(z,\Gamma) - q_0(-z)^{\mu/2}\theta(-z)$, with q_0 fitted from the frozen-in distribution $Q_0(\sigma)$; recall that $z = \Gamma^{-1/\mu}(\sigma - 1)$. As t increases and $\Gamma \to 0$, the lower curves approach $R_1(z)$, which is obtained by solving (2.21) numerically (see App. 2.E.3), while the upper curves collapse onto $R(z)$ from (2.19).

write (as before to leading order in Γ)

$$\tilde{P}(z,\Gamma) = \Gamma^{1/2} R(z) \tag{2.18}$$

$$R(z) = q_0(-z)^{\mu/2}\theta(-z) + R_1(z) \tag{2.19}$$

From the master equation in the boundary layer region we can obtain an equation for the unknown scaling function $R_1(z)$, which we refer to as the *boundary layer equation*. Without delving into details, three aspects are worth pointing out.

Firstly, in the boundary layer, cut-off effects disappear and we are left with pure power law behaviours. This is due to the rescaling introduced. Considering for

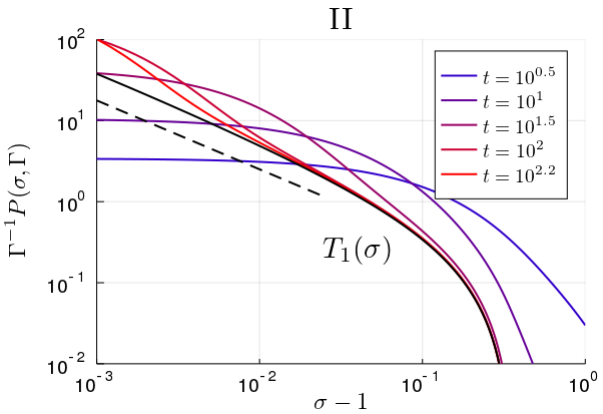

FIGURE 2.4: External region (II) from Fig. 2.2. We show $\Gamma^{-1}P(\sigma,\Gamma)$, which for long times collapses onto $T_1(\sigma)$ (Eq. 2.76). Also shown (dashed line) is the expected power-law behaviour $(\sigma-1)^{-\mu/2}$ for $\sigma - 1 \ll 1$ (2.77).

example the Lévy propagation on $R_1(z)$, we have that

$$\Gamma^{1/2}\int_{1-\epsilon}^{1+\epsilon}\frac{R_1(\Gamma^{-\frac{1}{\mu}}(\sigma'-1))-R_1(\Gamma^{-\frac{1}{\mu}}(\sigma-1))}{|\sigma-\sigma'|^{\mu+1}}\mathrm{d}\sigma' = \Gamma^{-1/2}\int_{-\epsilon\Gamma^{-\frac{1}{\mu}}}^{\epsilon\Gamma^{-\frac{1}{\mu}}}\frac{R_1(z')-R_1(z)}{|z-z'|^{\mu+1}}\mathrm{d}z' \tag{2.20}$$

We can then take the limits $\pm\epsilon\Gamma^{-1/\mu}$ of the integral to infinity because of the way we have defined the boundary layer, with $\Gamma^{1/\mu} \ll \epsilon$ and therefore $\epsilon\Gamma^{-1/\mu} \gg 1$.

A second important aspect of the boundary layer equation is that the interior and exterior scaling functions do not make any leading order contributions within the boundary layer; they only appear indirectly through the condition that the tails of $R_1(z)$ must match the behaviour of $T_1(\sigma)$ and $Q_1(\sigma)$ respectively as $\sigma \to 1$, as required for continuity of $P(\sigma,\Gamma)$.

Finally, the terms arising from the time derivative ∂_t, which are from the beginning absent in the steady state case, will also be irrelevant in the aging because $\Gamma(t)$ will vary sufficiently slowly (see Appendix 2.C.2).

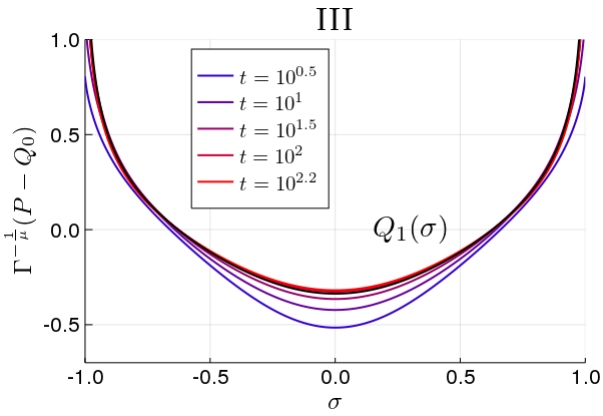

FIGURE 2.5: Interior region (III) from Fig. 2.2. We show $\Gamma^{-1/\mu}(P - Q_0)$, which at later times collapses onto the analytical prediction for the leading order interior function $Q_1(\sigma)$ from (2.81).

Overall, the *boundary layer equation* takes the form

$$A\int_{-\infty}^{\infty}\frac{R_1(z')-R_1(z)}{|z-z'|^{\mu+1}}\mathrm{d}z'+AS(z)-\theta(z)R_1(z)=0 \tag{2.21}$$

The second term is a source $S(z)$, which arises from applying the Lévy propagator to the frozen part of the stress distribution. Explicitly it reads

$$S(z)=q_0\,\mathrm{B}\Big(\frac{\mu}{2},1+\frac{\mu}{2}\Big)\,z^{-\mu/2},\quad z>0 \tag{2.22}$$

where B denotes the Beta function. Physically, then, the boundary layer equation describes how sites can have their local stress increased into the unstable region ($z>0$) by yield events elsewhere; this is the source term $AS(z)$. These sites can then yield as indicated by the last term in (2.21), or their stress may change due to further stress kicks (first term). The equation then simply states that these effects must balance in a stationary or slowly aging system.

The boundary layer equation (2.21) admits different asymptotic solutions in the regimes $1<\mu<2$, $\mu=1$ and $\mu<1$. This will be the key to the distinct scaling and aging behaviours in the different regimes. We defer a detailed analysis (in particular for the case $\mu=1$) to Appendix 2.C.4 and only outline the main properties here.

Splitting $R_1(z)$ into $R_1^{\mathrm{ext}}(z)$ for $z>0$ and $R_1^{\mathrm{int}}(z)$ for $z<0$, we focus on the asymptotic forms of these functions for $|z|\gg 1$. As indicated by the superscripts, $R_1^{\mathrm{ext}}(z)$ will have to match up with $P(\sigma,\Gamma)$ in the exterior region, while $R_1^{\mathrm{int}}(z)$ will need to do so with the interior function.

It is straightforward to deduce from equation (2.21) that the exterior asymptote must balance the form of the source, so that

$$R_1^{\mathrm{ext}}(z)=C_{\mathrm{ext}}z^{-\mu/2}\quad\text{for}\quad z\gg 1 \tag{2.23}$$

For the interior asymptotic behaviour we assume a power law form $R_1^{\mathrm{int}}(z)=C_{\mathrm{int}}|z|^{-\phi}$ and find by appropriate rescaling of the integration variable that the boundary layer equation (2.21) in the regime $|z|\gg 1$, $z<0$ becomes

$$\left(\int_0^{\infty}\frac{x^{-\phi}-1}{|x-1|^{\mu+1}}\mathrm{d}x-\frac{1}{\mu}\right)C_{\mathrm{int}}|z|^{-\phi-\mu}+\int_0^{\infty}\frac{R_1^{\mathrm{ext}}(z')}{|z-z'|^{\mu+1}}\,\mathrm{d}z'=0 \tag{2.24}$$

There are then two possible solutions for the exponent ϕ. In the regime $1<\mu<2$, one can show that the final integral term may be neglected, and equation (2.24) can then be solved by using the property

$$\int_0^{\infty}\frac{x^{-\phi}-1}{|x-1|^{\mu+1}}\mathrm{d}x=\frac{1}{\mu}\quad\text{for}\quad\phi=-\frac{\mu}{2}\text{ or }1-\frac{\mu}{2} \tag{2.25}$$

We choose the second value $\phi=1-\mu/2$ as we expect a decaying power law for $R_1^{\mathrm{int}}(z)$. This solution we refer to as the *homogeneous* solution, given that it is obtained by neglecting the integral term, which represents a source arising from jumps from the unstable region $z'>0$. If this integral term were absent, the power law solution for $R_1^{\mathrm{int}}(z)$ would hold for $\forall z<0$, not just asymptotically; it would then correspond to one of the two alternative power law behaviours (whose exponents are the two values of ϕ in (2.25)) of a Lévy flight in front of an absorbing boundary.

In the regime $\mu<1$ we find that we require an *inhomogeneous* solution of (2.24),

where all terms are kept. Here we take instead $\phi = \mu/2$, which with an appropriate choice of $C_{\rm int}$ allows us to cancel the source term from $z' > 0$. Finally, in the marginal case $\mu = 1$, where the exponent crosses over from $\phi = 1 - \mu/2$ to $\phi = \mu/2$, one can show (Appendix 2.C.4) that a superposition of both solutions gives the form $R_1^{\rm int}(z) = C_{\rm int} z^{-1/2} \ln(|z|)$, involving a log-correction to the power law. Summarizing, the boundary layer function R_1 on the interior side has the asymptotic behaviour

$$R_1^{\rm int}(z) \overset{|z|\gg 1}{\sim} \begin{cases} |z|^{-(1-\mu/2)}, & \text{for} \quad 1 < \mu < 2 \\ |z|^{-1/2} \ln(|z|), & \text{for} \quad \mu = 1 \\ |z|^{-\mu/2}, & \text{for} \quad \mu < 1 \end{cases} \tag{2.26}$$

The physical implications of these solutions will be discussed further below. In brief, these will arise because as explained above, the interior tail of the boundary layer function $R_1^{\rm int}(z)$ has to match the $\sigma \to 1^-$ behaviour of $Q_1(\sigma)$, and will therefore determine the scaling of the interior correction with Γ, given by the exponent a defined above. Explicitly, for the case $1 < \mu < 2$ in the asymptotic $|z| \gg 1$ tail one has $\Gamma^{1/2} R_1^{\rm int}(z) \sim \Gamma^{1/2} z^{-(1-\mu/2)}$, which has to match with $Q_1(\sigma) \sim \Gamma^a (1-\sigma)^{-(1-\mu/2)}$, so that $a = 1/\mu$. Arguing similarly for $\mu < 1$, one finds $a = 1$. For the case $\mu = 1$, if we expand the asymptotic behaviour of $R_1^{\rm int}(z)$ in terms of σ we find

$$\Gamma^{1/2} R_1^{\rm int}(z) \sim \Gamma (1-\sigma)^{-1/2} \left[|\ln(\Gamma)| + \ln(1-\sigma) \right] \tag{2.27}$$

The matching must take place for $1 - \sigma \gtrsim \epsilon$, where ϵ was defined as $1 \gg \epsilon \gg \Gamma^{1/\mu}$, so that the second term in the brackets may be neglected. Overall we then have that for $\sigma \to 1^-$ the interior function has to behave as $Q_1(\sigma) \sim \Gamma |\ln(\Gamma)| (1-\sigma)^{-1/2}$, so that $a = 1$ with a logarithmic correction.

2.5 Steady state scaling

We now apply the approach above to deduce the critical scaling of the plastic rate above the transition. In the HL model (Eq. 2.11), the steady state distribution $P^{\rm ss}(\sigma)$ can be found analytically for any [66, 80] $\alpha > \alpha_c$. In Figure 2.6 we show the result for $\alpha = 1$, together with the steady state in the $\mu = 1$ model, with the same yield rate Γ. Although this value is well within the liquid regime, one may already note the differences between the two models: namely the straight line segments and exponential tails of the HL model become forms with no simple analytical expression.

For the HL model one can find an exact relation between α and Γ, which comes out of the normalisation condition on $P^{\rm ss}(\sigma)$. Writing α in terms of a rescaled distance to the transition $\tilde{\alpha}$, this relation reads:

$$\tilde{\alpha} \equiv \frac{\alpha - \alpha_c}{\alpha_c} = 2\left(\sqrt{\alpha\Gamma} + \alpha\Gamma\right) \tag{2.28}$$

so that

$$\tilde{\alpha} = \mathcal{O}(\Gamma^{1/2}) \tag{2.29}$$

for $\Gamma \ll 1$.

For the present model, on the other hand, we lack an analytical expression of the steady state stress distribution and its norm in terms of (A,Γ), and have to calculate the latter numerically in general. To find the critical scaling of Γ above the transition analytically, we then proceed by considering a perturbation of the critical distribution $P_c(\sigma)$ defined in Section 2.3. We defer the details to App. 2.B, where considering

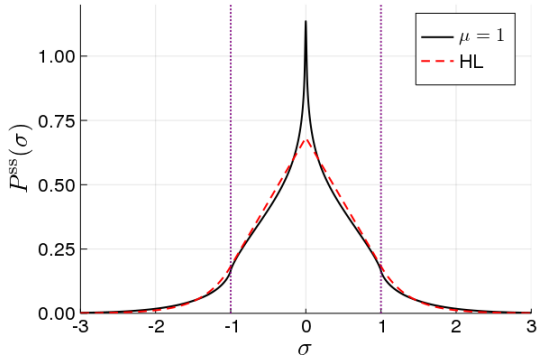

FIGURE 2.6: Steady state stress distribution in the liquid regime for $\mu = 1$ and the HL model ($\mu \to 2$), for fixed yield rate $\Gamma = 0.134$. Dotted lines mark the local yield thresholds $\sigma_c = \pm 1$. Whereas in the HL limit the form is a combination of exponentials and linear segments, for $\mu < 2$ there is no simple analytical expression.

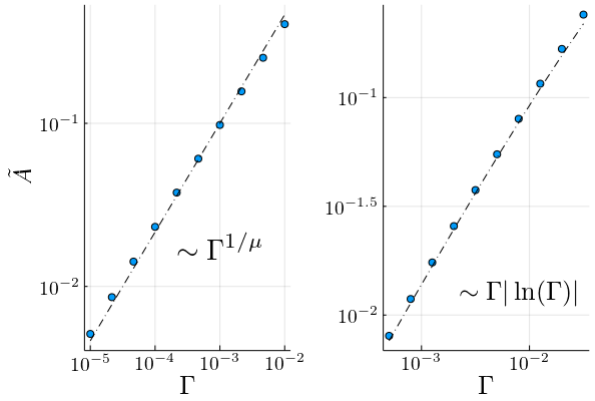

FIGURE 2.7: Critical scaling of plastic activity, obtained numerically for $\mu = 1.5$ (left) and $\mu = 1$ (right). The dashed lines show the theoretical prediction according to (2.30).

the steady state condition (2.12), we show that one can again express the problem in terms of the boundary layer equation (2.21). This leads to the following scalings

$$\tilde{A} \equiv \frac{A - A_c}{A_c} = \begin{cases} \mathcal{O}(\Gamma^{1/\mu}), & \text{for} \quad 1 < \mu < 2 \\ \mathcal{O}(\Gamma\,|\ln(\Gamma)|), & \text{for} \quad \mu = 1 \\ \mathcal{O}(\Gamma), & \text{for} \quad \mu < 1 \end{cases} \tag{2.30}$$

In Figure 2.7 we show our numerical results (see Appendix 2.E.2 for details) for the asymptotic scaling of $\tilde{A}$ with Γ. The results are in excellent agreement with the analytical prediction above (2.30), both for $\mu = 1.5$ and $\mu = 1$. Note also that for $\mu \to 2$, our prediction recovers the scaling in the known HL case (2.29).

The analysis of the steady state regime also provides intuition for the more complicated aging behaviour that we study next. Following the interpretation of the dynamics as that of an effective particle diffusing from the origin, we show in App. 2.B that $\tilde{A} \sim \Delta\tau^{\rm ext}$, where $\Delta\tau^{\rm ext}$ is the extra time that a particle lives before yielding when $\Gamma > 0$. This extra time arises because yielding is no longer effectively instantaneous for nonzero Γ, and from (2.30) it scales as $\Delta\tau^{\rm ext} \sim \tilde{A} \sim \Gamma^{1/\mu}$. Now during the aging the effective diffusion process will take place at ever decreasing Γ. For $\Gamma \ll 1$ we then see that $\Delta\tau^{\rm ext} \sim \Gamma^{1/\mu} \ll \Gamma^{1/2}$ for $\mu < 2$. The extra time the particle lives

before yielding $\Delta\tau^{\text{ext}}$ thus drops to zero faster for $\mu < 2$, so that the system will not be able to sustain so many yield events and will age towards an arrested state faster than in the HL case. We will see this intuition confirmed in the analysis below.

2.6 Aging in the glassy regime

In Section 2.3 the phase diagram of the model was presented, and we distinguished between a liquid and a glassy phase depending on the strength of the coupling A. In the liquid region $A > A_c$ there is a steady state distribution $P^{\text{ss}}(\sigma)$ with a constant plastic activity $\Gamma > 0$. As a representative for the liquid regime and a reference distribution for the following, we may take the $P^{\text{ss}}(\sigma)$ with the yield rate corresponding to that of the HL model with $\alpha = 1$ ($\Gamma = 0.134$). This distribution (for $\mu = 1$) is shown in Figure 2.6, along with its HL analogue.

We are interested in the aging behaviour in the glassy regime $A < A_c$, where due to the absence of a steady state distribution with $\Gamma > 0$ the plastic activity will decay as the system approaches some, potentially initial condition dependent, frozen-in stress distribution $Q_0(\sigma)$. For the purposes of studying the slow decay of $\Gamma(t)$, we assume that the system starts in a configuration with unstable sites, which may be the result of an initial preparation such as stirring, and the system is then left to evolve at a value of the coupling $A < A_c$. To simplify the analytical study we focus here on symmetric initial distributions. We have considered as initial configuration with unstable sites mainly the above $P^{\text{ss}}(\sigma)$, but also top hat and Gaussian distributions, with qualitatively identical results (data not shown). Asymmetric initial distributions could arise e.g. by pre-shear. Regardless of how the initial state is prepared, we study here the form of the asymptotic decay of $\Gamma(t)$, which we expect to be qualitatively unaffected by the details of the initial distribution [4].

The aging behaviour considered here can be thought of as modelling the dissipative decay in activity in an athermal system, which is left to evolve in quiescent conditions after, for example, shear melting [81] or a sudden increase in density in thermosensitive core-shell microgel particles, whose size can be controlled by varying temperature [48]. In the ensuing dynamics, given the athermal nature of the system rearrangements may only be triggered by events taking place elsewhere in the material. In a recent study of such relaxation in an athermal system [38], rearrangements are found to be reminiscent of the Eshelby events considered here.

2.6.1 Aging for $1 < \mu < 2$

To study the aging behaviour, we turn again to the expansion in $\Gamma \ll 1$ presented in Section 2.4. In contrast to the analysis of the steady state scaling, however, we will now have a rate of rearrangements that decreases in time. Nevertheless one may still consider the same boundary layer ansatz, now with $\Gamma(t)$.

We defer the detailed analysis to Appendix 2.C. The most important step is establishing the equation of motion in the interior region. Following the general ansatz presented in Section 2.4, the distribution is to leading order $P(\sigma, \Gamma) = Q_0(\sigma) + \Gamma^{1/\mu} Q_1(\sigma)$. The equation of motion in this region can then be written as

$$\partial_t P = \frac{1}{\mu}\Gamma^{1/\mu-1}\dot{\Gamma} Q_1 = A\Gamma\mathcal{L}\left(\Gamma^{1/\mu} Q_1 + Q_0\right) + \Gamma\delta(\sigma) \tag{2.31}$$

[4] Although we have not studied in detail the aging of asymmetric distributions in the current model, for the HL model [71] the same asymptotic decay and scalings are shown to hold also for the asymmetric case, under generic assumptions.

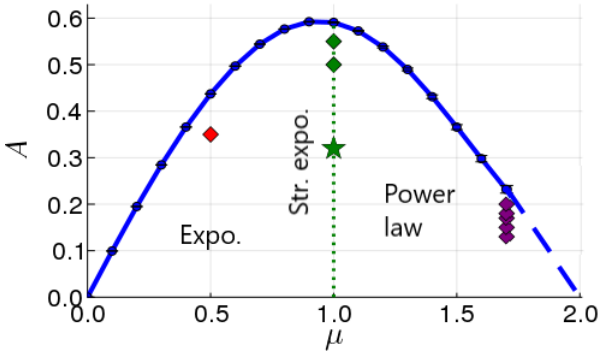

FIGURE 2.8: Location in the phase diagram of the points where numerical results on the aging behaviour are shown: power law region ($\mu = 1.7, A = 0.2$, 0.18, 0.17, 0.15 and 0.13, purple, see Figs. 2.9, 2.10), stretched exponential line ($\mu = 1, A = 0.55$ and 0.5, green, see Figs. 2.11, 2.12), exponential decay ($\mu = 0.5, A = 0.35$, red, see Fig. 2.13). The green star indicates the parameters of the lattice model ($\mu = 1, A = 0.32$, see Sec. 2.7). This last position should be taken as a qualitative indication only, given that the stress kick distribution in the lattice model is not exactly of the upper cutoff form (2.5); this form affects the precise location of the phase boundary.

up to terms of higher order in Γ that we omit. We may now distinguish between two cases. Firstly, in the critical case $A = A_c$ (critical aging) the combination $A\mathcal{L}Q_0 + \delta(\sigma)$ vanishes because of the limiting (for $\Gamma \to 0$) steady state condition, so that the prefactors of the remaining terms in (2.31) involving Q_1 must be the same. This gives $\dot{\Gamma} \sim \Gamma^2$ and hence $\Gamma(t) \sim 1/t$. This is independent of μ and so one would expect the same critical behaviour to hold also for $\mu \to 2$, i.e. for the HL model. This can indeed be shown, by extending the analysis in Ref. [71]; we omit the details.

In the generic case $A < A_c$ the sum $A\mathcal{L}Q_0 + \delta(\sigma)$ in (2.31) no longer vanishes. As this sum appears in (2.31) with prefactor Γ, in order to balance it and obtain a time-independent Q_1, we also need the left hand side to be of order Γ. This leads to the conclusion that $\dot{\Gamma} \sim \Gamma^{2-1/\mu}$, from which one deduces that $\Gamma(t)$ decays in time in a power-law fashion as

$$\Gamma(t) = Bt^{-\mu/(\mu-1)} \tag{2.32}$$

Here the prefactor B is related to the frozen-in distribution $Q_0(\sigma)$, and like the latter is therefore expected to be dependent on initial conditions. In the limit $\mu \to 2^-$, this prediction is consistent with the aging behaviour $\Gamma \sim t^{-2}$ that was found independently for the HL model [71].

To test the decay (2.32) numerically, we perform numerical tests by using a pseudospectral method on a discrete grid of σ-values (see Appendix 2.E.1) to solve the equation of motion (2.8) for $P(\sigma, t)$. We choose as initial condition the liquid steady state with $\Gamma = 0.134$ (see above), and set A to a value below the dynamical arrest transition.

The results are displayed in Figures 2.9 and 2.10, where we choose $\mu = 1.7$ throughout; Fig. 2.8 gives an overview of where the (μ, A)-pairs are located in the phase diagram. In the first plot (Fig. 2.9) we show the behaviour of $\Gamma(t)$ in log-log scale, for several values of A below the transition, along with the corresponding predicted power law. We see a good agreement, although reaching the asymptotic behaviour is challenging. Numerically, this is due to the fact that one can no

longer obtain reliable numerical data when the scale of the boundary layer $\Gamma^{1/\mu}$ becomes of the order of the discretization interval $d\sigma$. This problem is accentuated as μ is decreased, due to the scaling $\Gamma^{1/\mu}$ which implies a narrower boundary layer. Also, lower values of A are more challenging, given that the yield rate decays more quickly and the above numerical limit is reached sooner. The limit can be seen in Fig. 2.10 as the point where results for different σ-discretizations start to differ (thin lines).

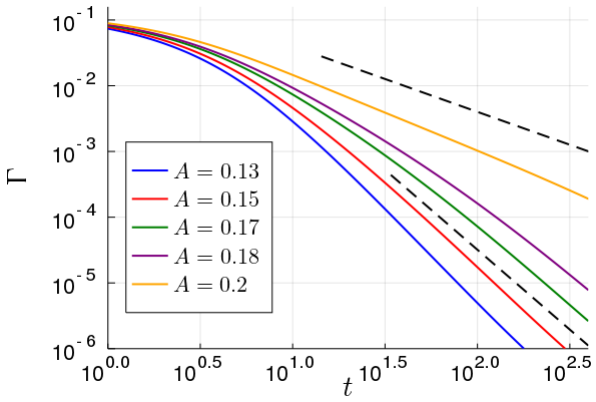

FIGURE 2.9: Decay of $\Gamma(t)$ for $\mu = 1.7$, at five different values of A below the dynamical arrest transition, starting from the liquid steady state with $\Gamma = 0.134$. The lower dashed line shows the predicted power law asymptote $\Gamma \sim t^{-\mu/(\mu-1)}$, with $\mu/(\mu-1) \simeq 2.428$. The upper dashed line shows the asymptotic power law at $A = A_c$, $\Gamma \sim t^{-1}$.

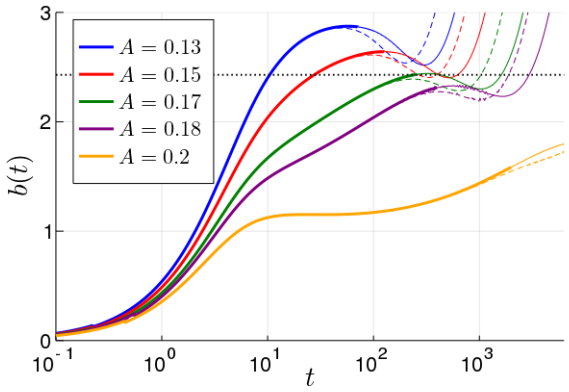

FIGURE 2.10: Evolution of the log derivative $b(t)$ of the yield rate, defined in the text, for the same runs as in Figure 2.9. The four upper curves ($A = 0.13, 0.15, 0.17, 0.18$) converge towards the predicted exponent value $\mu/(\mu-1) \simeq 2.428$ (dotted line). The highest value of $A = 0.2$ is affected by the critical behaviour $\Gamma \sim t^{-1}$ at $A = A_c$. Dashed curves indicate runs on a coarser (by a factor of 2) σ-grid; the limit of reliability of the numerical results is reached where these start to deviate (thinner lines).

Physically, the covergence to the power-law asymptote is affected by two crossover behaviours. To illustrate this, in the second plot (Fig. 2.10) we show the log-derivative

$$b(t) = -\frac{\mathrm{d}\ln(\Gamma)}{\mathrm{d}\ln(t)} \tag{2.33}$$

This is an effective power law exponent that at long times should converge to the value $\mu/(\mu-1)$. On the one hand, for larger A (see $A = 0.2$ in Fig. 2.10) closer to $A = A_c$ the convergence is affected by a transient where the system behaves as in the critical case, with the yield rate decaying as $\Gamma \sim t^{-1}$. For smaller A (see $A = 0.13$), on the other hand, $b(t)$ increases very rapidly in the transient. This is because here we approach the limiting behaviour for $A \to 0$, where there is no stress redistribution and $\Gamma(t)$ decays as a pure exponential. This rapid increase in $b(t)$ at low A is the reason why for $A = 0.13$ and 0.15 in Fig. 2.10 the effective exponent converges to its limit from above, while for the higher values $A = 0.17$ and 0.18 it does so from below.

2.6.2 Aging for $\mu = 1$

We next turn to the aging behaviour in the marginal case $\mu = 1$. As outlined in Sec. 2.4, in this case the *homogeneous* and the *inhomogeneous* solutions of the boundary layer equation merge, resulting in a log-correction to the asymptotic power law on the interior side of the boundary layer function $R_1^{\text{int}}(z) \sim |z|^{-1/2}\ln(|z|)$. This now determines the form of the interior distribution, whose non-frozen part has to match $\Gamma^{1/2}R_1(z)$ for $\sigma \to 1$. As described in Section 2.4, using that $z = (\sigma-1)/\Gamma$ for $\mu = 1$ one has $\Gamma^{1/2}|z|^{-1/2}\ln(|z|) \simeq |\sigma-1|^{-1/2}\Gamma|\ln(\Gamma)|$ to leading order so that the distribution in the interior must take the form $P(\sigma,\Gamma) = Q_0(\sigma) + \Gamma|\ln(\Gamma)|Q_1(\sigma)$. Proceeding as in the case $\mu > 1$, the time dependence of Γ may now be derived from the equation of motion in the interior, where the time decay of the bulk of the probability distribution has to balance the jumps out to the unstable region, leading to

$$\partial_t\left(-\Gamma\ln(\Gamma)\right) = -C_1\Gamma \tag{2.34}$$

where $C_1 > 0$ is a constant. Solving this differential equation for $\Gamma(t)$ leads to

$$\Gamma(t) \sim e^{-\sqrt{2C_1 t}} \tag{2.35}$$

In the long time regime, therefore, we obtain a *stretched exponential* behaviour. The prefactor of the power law (C_1) is initial condition dependent as it is again related to the frozen-in distribution $Q_0(\sigma)$.

In the following we show the result of numerical simulations, where starting from our reference steady state we study the evolution at two values of A below the transition, $A = 0.55$ and $A = 0.5$ (see Fig. 2.8). We choose these higher values of A for $\mu = 1$ because for smaller values the yield rate becomes small very rapidly and the stretching regime is then difficult to resolve clearly. In the first plot (Fig. 2.11), we graph the yield rate in logarithmic scale against $\sqrt{t}$ and obtain a good agreement with the predicted straight line. In the second plot (Fig. 2.12) we show instead $(\ln(\Gamma(t)))^2$, which makes it easier to discern the asymptotic region with its linear increase in time.

2.6.3 Exponential decay for $\mu < 1$

In this regime we have not carried out a full boundary layer analysis. From a physical perspective, we expect it to be less relevant: in contrast to $\mu = 1$ (which is obtained directly from the elastoplastic decay of the propagator) and $1 < \mu < 2$ (for which there are coarse-graining arguments as in Refs. [30, 31]), there seems to be little evidence for this kind of noise distribution in real systems. We therefore show here only the results of a numerical evaluation. These are consistent with a purely

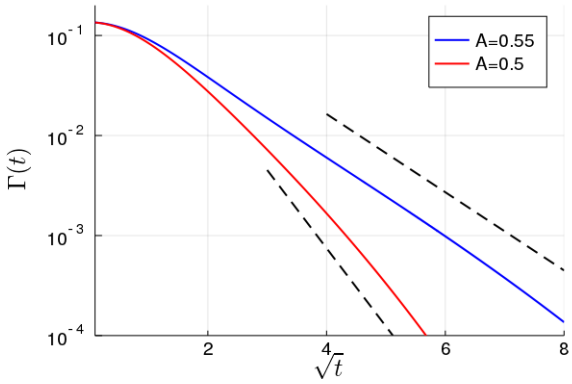

FIGURE 2.11: Decay of $\Gamma(t)$ against $\sqrt{t}$, at $A = 0.55$ and $A = 0.5$ starting at the steady state with $\Gamma = 0.134$ for $\mu = 1$. Dashed lines show the predicted exponential decay with $\sqrt{t}$.

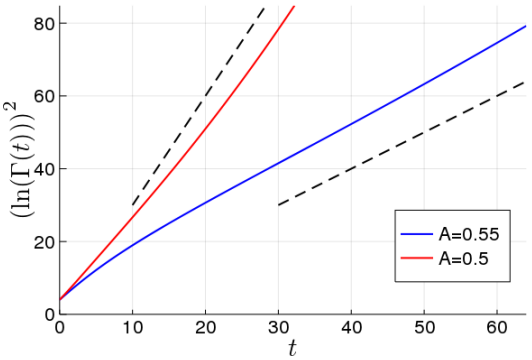

FIGURE 2.12: Same data as in Figure 2.11, with the same x and y ranges but now plotting $(\ln(\Gamma(t)))^2$ against t. This shows more clearly the linear growth (dashed lines) as predicted by equation (2.35).

exponential decay, as can be seen in Fig. 2.13 for $\mu = 0.5$, where the system evolves at $A = 0.35$ starting from the reference steady state (see Fig. 2.8).

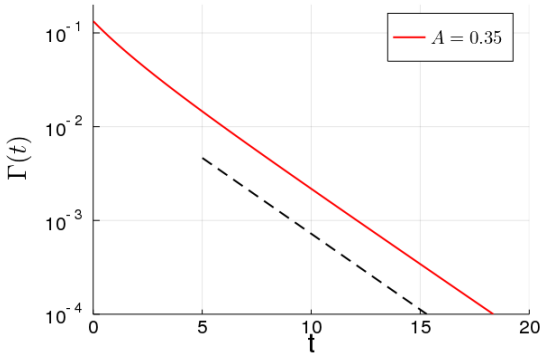

FIGURE 2.13: Yield rate decay at $A = 0.35$, starting from a liquid-like steady state, for $\mu = 0.5$. The dashed curve shows the exponential decay of $\Gamma(t)$.

2.7 Aging in a lattice elastoplastic model

In this final section we compare our mean field results to the aging behaviour found in a lattice elastoplastic model. This is important in order to test how well the mean field approximation, which discards spatial correlations, can approximate the full spatial dynamics. The simulations of the lattice elastoplastic model were carried out by Prof. Suzanne Fielding (Durham University, UK).

The implementation of the elastoplastic model combines elastic loading and stochastic relaxation of a single element on each lattice site, with a spatially discretised fluid/continuum mechanical approach to enforcing Eshelby stress propagation after each stress drop, via the Stokes equation coupled to an additional elastic stress. On a timescale that scales with η/G_0, where η is the viscosity and G_0 the elastic modulus of the local mesoscopic blocks, the Eshelby quadrupole in 2D is recovered, of course here in the form appropriate to a discrete square lattice with periodic boundary conditions. To compare with our model we therefore take a value of the viscosity $\eta/G_0 \ll 1$, as we had assumed – in common with most elastoplastic models [13] – that stress propagation after yielding takes place effectively instantaneously.

In order to connect our modelling approach with the lattice model, we first extract the corresponding value of A. To do so, we look at the list of L^2 stress propagator elements $\{\delta\sigma_i\}$ after a unit stress drop at the origin in a square lattice of size $L \times L$. Taking the positive elements, we sort them from largest to smallest and plot the ranking in the sorted list against the value of the element. This is shown in Figure 2.14, and corresponds to a cumulative count of how many propagator elements are larger than a given $\delta\sigma$. For small $\delta\sigma$, where the power law behaviour (2.4) holds (see more below on the distribution at large $\delta\sigma$), this unnormalized cumulative distribution behaves as $P(x < \delta\sigma) \simeq A/\delta\sigma$. Therefore we can extract A as the prefactor of the power law for small $\delta\sigma$ in Figure 2.14, giving $A \approx 0.32$.

We can now run our mean field dynamics for $P(\sigma, t)$ with the appropriate $A = 0.32$, starting from the same initial stress distribution as in the lattice model (Figure 2.15). The lattice data (green) is from a 4096×4096 system, where we can reliably measure yield rates down to around $\Gamma = 5 \times 10^{-6}$; at this point only $\mathcal{O}(10^2)$ unstable sites remain and finite size fluctuations become noticeable. In a first approach (red

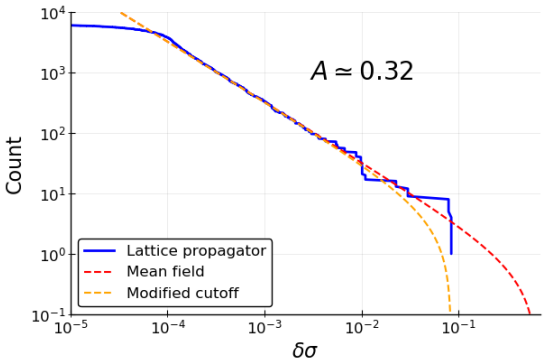

FIGURE 2.14: Cumulative count of the number of propagator elements larger than a given $\delta\sigma$, which drops to zero at the maximum stress kick. The lattice elements (blue) are compared to the model defined here (red) and to a power-law model with a modified cutoff (orange).

line), we compare this to the mean field model with $A = 0.32$ with the definition of the upper cutoff in Section 2.2. However, as can be seen already in Figure 2.14, the large near-field lattice propagator elements are actually cut off at a smaller value on the lattice. In the lattice data fewer yield events are therefore triggered and the plastic activity $\Gamma(t)$ is lower, with a faster decay.

In a second approach, therefore, we consider the mean field model with a modified cutoff chosen as the largest propagator element on the lattice. This results in predictions (yellow line in Figure 2.15) that are rather closer to the simulation results, but it obviously still neglects some details of the distribution of near-field propagator elements. This includes the fact that the lattice propagator list is not in fact entirely symmetric, e.g. because of the fact that the largest positive propagator elements occur for nearest neighbours while the largest negative ones (in the $\pm 45^\circ$ directions on the lattice) arise from next nearest neighbours. We therefore finally run (blue line in Figure 2.15) the mean field theory using as our stress kick distribution the actual list of lattice propagator elements. This is implemented using a Gillespie algorithm that draws stress kicks randomly from this list [5]. Such an approach still gives a somewhat slower decay of the yield rate than the full lattice run, in fact more so than the power law stress kick distribution with the modified cutoff (yellow line in Figure 2.15).

More remarkable than the quantitative differences between the three implementations of the mean field description, however, is the very good qualitative agreement with the simulation data. In fact, with a simple rescaling of time for each mean field prediction we can achieve a near-perfect overlap with the simulation data, as shown in the inset of Figure 2.15. The rescaling factors are modest ($c = 1.7, 1.29, 1.12$, respectively for the three mean field approaches) but greater than unity, showing that the mean field "reshuffling" of stress propagation tends to trigger more yield events across the system than in the underlying lattice model.

In the inset of Fig. 2.15 we plot the rescaled data in the same form as in Fig. 2.12 to demonstrate that, importantly, the simulation data conform to the predicted stretched exponential asymptote. Surprisingly, though, even the pre-asymptotic yield rate decay is very well captured by the mean field theory. These results support the idea that the propagator, which decays as r^{-2} in $d = 2$, is long range enough (see e.g.

[5] For lattices of different sizes, the large $\delta\sigma$ details of the list of propagator elements are identical. In order to run Gillespie simulations with an arbitrary number of sites, we proceed by extrapolating the small $\delta\sigma$ power law in order to obtain the desired number of propagator elements.

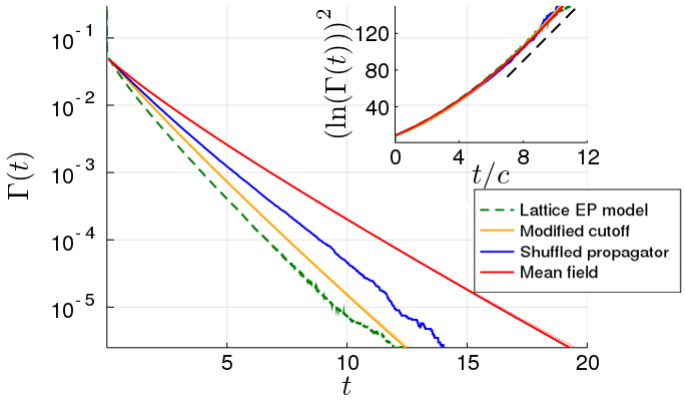

FIGURE 2.15: Yield rate decay for $A = 0.32$ starting from the same initial distribution, for the full lattice model and the three mean field approaches described in the text. In the inset, the data are collapsed by rescaling time for each mean field prediction, and then fitted to a stretched exponential decay.

the discussion in Ref. [30]) for our mean field predictions for the aging behaviour to apply almost quantitatively.

2.8 Summary

We have constructed in this chapter a time-dependent mean-field elastoplastic model of amorphous solids, incorporating the power-law mechanical noise spectrum arising from localized plastic events [28, 70, 75]. This model allows the exploration of general time-dependencies, including aging and arbitrary rheological protocols. We have shown firstly the phase diagram of the model (in the absence of external shear), which separates the arrested (i.e. glassy) from the flowing (liquid) states. We then developed a boundary layer scaling approach, with the aim of studying the behaviour of the model at very low yield rates, as they appear e.g. during aging. As a first application, this allowed us to find the various scalings of the plastic rate in the (stationary) liquid regime just above the dynamical arrest transition.

Our main findings concern the long time aging regime, the mean-field predictions for which we summarize here. We obtained three different regimes as the exponent $\mu = d/\beta$ characterizing the noise spectrum was varied. We recall that β is a general decay exponent of the propagator $r^{-\beta}$, so that varying μ can be thought of as tuning the interaction range. We found that for $1 < \mu < 2$ the plastic activity $\Gamma(t)$ decays in a power-law fashion as $\sim t^{-\mu/(\mu-1)}$, reflecting the dominance of far-field events in determining the long-time dynamics. For $\mu < 1$, on the other hand, near field events are dominant, and the relaxation becomes exponential. This is encoded in the boundary layer equation, where the crossing of the boundary is dominated by “small" jumps in the first case and “large" jumps in the second, giving rise to the *homogeneous* and *inhomogeneous* solutions respectively as described in Section 2.4. In the marginal case $\mu = 1$, where both near and far-field events are relevant, we found a stretched exponential decay of $\Gamma(t)$ that arises mathematically from the superposition of the two types of boundary layer solution. We compared this last case to simulations on a lattice elastoplastic model, and found a decay consistent with the predicted stretched exponential. In fact even the pre-asymptotic decay of the plastic activity is extremely well captured by the mean field predictions, up to a modest

rescaling of time. This lends strong support to our mean field approach to the dynamics of amorphous solids.

Ideally, one wants to go beyond a comparison to a lattice elastoplastic model, and consider instead particle-based simulations or even experiments. As mentioned in Chapter 1, a direct comparison of the behaviour of the yield rate is challenging. This would require a method for extracting the rate of plastic rearrangements $\Gamma(t)$ from particle-based simulation data. This method would, in particular, have to be able to separate events that occur together in avalanches, which is a significant challenge (see e.g. the methods employed in Ref. [82]). We will discuss this comparison further in Chapter 5. In the next chapter we will instead study the predictions of the model for the aging linear response to strain, which unlike the yield rate can be compared directly to stress measurements in particle-based simulations or experiments.

2.A Derivation of time-dependent model

2.A.1 Reduction to stress distribution dynamics

We show here the details of the derivation of the dynamics (2.8) for the local stress distribution from the full N-body master equation (2.7). In this master equation the spatial structure of the stress propagation has already been removed and replaced by i.i.d. stress kicks. Correlations do remain in the transition kernel (2.6) for finite N but will disappear as $N \to \infty$. We thus assume directly the factorization

$$P(\boldsymbol{\sigma}) = \prod_i P_i(\sigma_i) \tag{2.36}$$

We are then interested in finding the dynamics of the stress distribution

$$P(\sigma) = \frac{1}{N}\sum_i \langle \delta(\sigma - \sigma_i)\rangle = \frac{1}{N}\sum_i P_i(\sigma) \tag{2.37}$$

Each local $P_i(\sigma_i)$ can be obtained by marginalising out the remaining variables,

$$P_i(\sigma_i) = \int \{\prod_{j\neq i} \mathrm{d}\sigma_j\} P(\boldsymbol{\sigma}) \tag{2.38}$$

This is trivial to do with the drift term of the master equation (2.7). From the transition rates K_l, on the other hand, we will obtain two terms, which we call I_1 and I_2. These correspond respectively to the case when $l = i$ (so that the site that is yielding is the site for which we are finding the marginal distribution) and when $l \neq i$. We thus have

$$\partial_t P_i(\sigma_i) = \int \{\prod_{j\neq i} \mathrm{d}\sigma_j\} \partial_t P(\boldsymbol{\sigma}) = -\dot{\gamma}\partial_{\sigma_i} P_i(\sigma_i) + I_1 + I_2 \tag{2.39}$$

To simplify matters, we will at first carry out the calculations without the counterterm enforcing zero net stress change. We will justify this explicitly at the end, but intuitively one may already expect that this term gives sub-leading corrections for large N. Indeed the sum over random positive and negative increments will scale as $\sum_{k\neq l} \delta\sigma_k \sim \sqrt{N-1}\sqrt{\langle \delta\sigma^2\rangle}$, so that we are considering in the end a term of order $\sqrt{\langle \delta\sigma^2\rangle}/\sqrt{N-1}$, which is negligible compared to a typical stress kick $\delta\sigma$ for $N \gg 1$. Leaving out the counterterm and exploiting that the stress kicks are i.i.d.

random variables, we can generically simplify the delta term in the rates (2.6) to

$$\left\langle \prod_{j\neq l} \delta\left(\sigma_j - \left(\sigma'_j + \delta\sigma_j\right)\right)\right\rangle = \prod_{j\neq l}\rho(\sigma_j - \sigma'_j) \tag{2.40}$$

We begin now with the term I_1, corresponding to the case $l = i$. This is given by

$$I_1 = \int \{\prod_{j\neq i} \mathrm{d}\sigma_j\}\mathrm{d}\boldsymbol{\sigma}' \left[K_i(\boldsymbol{\sigma}|\boldsymbol{\sigma}')P(\boldsymbol{\sigma}') - K_i(\boldsymbol{\sigma}'|\boldsymbol{\sigma})P(\boldsymbol{\sigma})\right] \tag{2.41}$$

where the rate is simply

$$K_i(\boldsymbol{\sigma}|\boldsymbol{\sigma}') = \theta(|\sigma'_i| - 1)\delta(\sigma_i)\prod_{j\neq i}\rho(\sigma_j - \sigma'_j) \tag{2.42}$$

Carrying out the marginalisation (2.41), one obtains that

$$I_1 = \left(\int \mathrm{d}\sigma'_i\theta(|\sigma'_i| - 1)P_i(\sigma'_i)\right)\delta(\sigma_i) - \theta(|\sigma_i| - 1)P_i(\sigma_i) \tag{2.43}$$

Therefore, when the yielding takes place at the site i itself we obtain the yielding and the reinjection terms in the master equation, as one would expect.

The other term, I_2, which corresponds to yield events at sites $l \neq i$, must then give rise to the propagator in the master equation. We need to compute

$$I_2 = \sum_{l\neq i}\int \{\prod_{j\neq i} \mathrm{d}\sigma_j\}\mathrm{d}\boldsymbol{\sigma}' \left[K_l(\boldsymbol{\sigma}|\boldsymbol{\sigma}')P(\boldsymbol{\sigma}') - K_l(\boldsymbol{\sigma}'|\boldsymbol{\sigma})P(\boldsymbol{\sigma})\right] \tag{2.44}$$

In both terms the integrals over $\mathrm{d}\sigma_k\mathrm{d}\sigma'_k$ for $k \notin \{i, l\}$ just give factors of unity while the integration over $\mathrm{d}\sigma_l\mathrm{d}\sigma'_l$ results in a factor $\int \mathrm{d}\sigma_l\theta(|\sigma_l| - 1)P_l(\sigma_l)$. This leaves

$$I_2 = \sum_{l\neq i}\left(\int \mathrm{d}\sigma_l\theta(|\sigma_l| - 1)P_l(\sigma_l)\right) \times \int \mathrm{d}\sigma'_i\rho(\sigma_i - \sigma'_i)[P_i(\sigma'_i) - P_i(\sigma_i)] \tag{2.45}$$

We divide and multiply this expression by N and add the $l = i$ term to the sum as it will only give a negligible $\mathcal{O}(1/N)$ correction:

$$I_2 = \frac{1}{N}\sum_{l}\left(\int \mathrm{d}\sigma_l\theta(|\sigma_l| - 1)P_l(\sigma_l)\right) \times \int \mathrm{d}\sigma'_i N\rho(\sigma_i - \sigma'_i)[P_i(\sigma'_i) - P_i(\sigma_i)] \tag{2.46}$$

where

$$N\rho(\sigma_i - \sigma'_i) = N\frac{A}{N}|\sigma_i - \sigma'_i|^{-1-\mu} = A|\sigma_i - \sigma'_i|^{-1-\mu} \tag{2.47}$$

This is the propagator in the master equation; the lower cutoff $\sim N^{-1/\mu}$ of $\rho(\delta\sigma)$ is immaterial here as it becomes negligible for $N \gg 1$. Defining then the yield rate as the average

$$\Gamma = \frac{1}{N}\sum_{l}\int \mathrm{d}\sigma_l\theta(|\sigma_l| - 1)P_l(\sigma_l) = \int \mathrm{d}\sigma\ \theta(|\sigma| - 1)P(\sigma) \tag{2.48}$$

and inserting the results for I_1 and I_2, equation (2.39) becomes

$$\partial_t P_i(\sigma_i) = -\dot{\gamma}\partial_{\sigma_i} P_i(\sigma_i) + A\Gamma \int_{\sigma_i-\delta\sigma_u}^{\sigma_i+\delta\sigma_u} \frac{P_i(\sigma_i') - P_i(\sigma_i,t)}{|\sigma_i - \sigma_i'|^{\mu+1}} \mathrm{d}\sigma_i' - \theta(|\sigma_i|-1)P_i(\sigma_i) + \Gamma\delta(\sigma_i) \quad (2.49)$$

Summing over i and dividing by N then gives the master equation (2.8) in the main text.

We finally have to show that the term enforcing a zero net stress change after the yield event is indeed negligible for $N \gg 1$. Instead of the simplified form (2.40) we take into account now the full form of the rates (2.6) including this enforcing term, and look for the corresponding contribution to I_1 (2.41) and I_2 (2.44). Carrying out firstly the integrals over $\mathrm{d}\sigma_j \mathrm{d}\sigma_j'$ for $j \neq i$, the delta terms over $j \neq i$ all give factors of 1 as was the case previously. We are then left only to deal with the term concerning site i. Introducing Fourier transforms, we can rewrite the delta function defining this term in the following manner:

$$\delta\left(\sigma_i - \left(\sigma_i' + \delta\sigma_i - \frac{1}{N-1}\sum_{k\neq l}\delta\sigma_k\right)\right) = \int \frac{\mathrm{d}\lambda}{2\pi} \prod_{k\neq l,i} e^{i\lambda\delta\sigma_k/(N-1)} e^{i\lambda\left(\sigma_i - \sigma_i' - \delta\sigma_i(1-1/(N-1))\right)} \quad (2.50)$$

This term now needs to be averaged over the i.i.d. stress increment distributions. Doing so we find that

$$\left\langle \delta\left(\sigma_i - \left(\sigma_i' + \delta\sigma_i - \frac{1}{N-1}\sum_{k\neq l}\delta\sigma_k\right)\right)\right\rangle = \int \frac{\mathrm{d}\lambda}{2\pi} \hat{\rho}\left(\frac{\lambda}{N-1}\right)^{N-2} e^{i\lambda(\sigma_i-\sigma_i')} \hat{\rho}\left(-\lambda\left(\frac{N-2}{N-1}\right)\right) \quad (2.51)$$

in terms of the characteristic function

$$\hat{\rho}(s) = \int \mathrm{d}(\delta\sigma)\rho(\delta\sigma)e^{i\delta\sigma s} \quad (2.52)$$

Expanding this characteristic function for small argument, one can write

$$\hat{\rho}(s) = 1 - \frac{1}{2}\langle\delta\sigma^2\rangle s^2 + \mathcal{O}(s^4) \quad (2.53)$$

where the variance $\langle\delta\sigma^2\rangle$ of the microscopic stress kick distribution is given by

$$\langle\delta\sigma^2\rangle = 2\int_{\delta\sigma_u N^{-1/\mu}}^{\delta\sigma_u} \mathrm{d}(\delta\sigma)\rho(\sigma)\delta\sigma^2 = \frac{2A}{N(2-\mu)}\delta\sigma_u^{2-\mu} + \mathcal{O}(N^{-2/\mu}) \equiv \frac{B}{N} + \mathcal{O}(N^{-2/\mu}) \quad (2.54)$$

The first term involving $\hat{\rho}$ in (2.51) can now be shown to scale as

$$\hat{\rho}\left(\frac{\lambda}{N-1}\right)^{N-2} \sim 1 + \mathcal{O}\left(\frac{B\lambda^2}{N^2}\right) \quad (2.55)$$

The final factor in (2.51) can be expanded in a similar fashion

$$\hat{\rho}\left(-\lambda\left(1-\frac{1}{N-1}\right)\right)=\hat{\rho}(-\lambda)+\frac{\lambda}{N-1}\hat{\rho}'(-\lambda)+\mathcal{O}\left(\frac{1}{N^2}\right) \tag{2.56}$$

For large N the correction terms can be neglected and (2.51) becomes simply

$$\int\frac{\mathrm{d}\lambda}{2\pi}\hat{\rho}(-\lambda)e^{i\lambda(\sigma_i-\sigma_i')}=\rho(\sigma_i-\sigma_i') \tag{2.57}$$

as it would be if we had neglected the enforcing term from the beginning. The above analysis shows that the leading corrections to this result are $\mathcal{O}\left(1/N\right)$.

2.A.2 The Hébraud-Lequeux limit

We here show in detail how the HL diffusive model is obtained in the limit $\mu\to 2^-$ of equation (2.8) in the main text. This means specifically that the stress propagation term in the second line must reduce to the diffusive form $\alpha\Gamma(t)\partial_\sigma^2 P$ in (2.11). To demonstrate this, we apply to this term the Kramers-Moyal expansion of a master equation, which has the form

$$\frac{\partial P(\sigma,t)}{\partial t}=\sum_{n=1}^{\infty}\frac{(-1)^n}{n!}\frac{\partial^n}{\partial\sigma^n}\left(a_n(\sigma)P(\sigma,t)\right) \tag{2.58}$$

The coefficients $a_n(\sigma)$, which in general may depend on σ, are the jump moments, i.e. the moments of the change in σ weighted by the corresponding transition rate. In our case these are independent of the original stress and given by

$$a_n=\int(\delta\sigma)^n\Gamma\rho(\delta\sigma)\mathrm{d}(\delta\sigma) \tag{2.59}$$

(We have dropped the time-dependence of Γ here, for simplicity of notation.) In other words, the a_n are obtained as the moments of the Lé kernel in (2.8), which explicitly reads

$$\Gamma\rho(\delta\sigma)=\frac{A\Gamma}{|\delta\sigma|^{1+\mu}} \tag{2.60}$$

Bearing in mind the upper cutoff $\delta\sigma_\mathrm{u}$ on $|\delta\sigma|$, the coefficients a_n then take the following form for even $n=2,4,6,\ldots$ (for odd n they are zero as the kernel is an even function):

$$a_n=2A\Gamma\int_0^{\delta\sigma_\mathrm{u}}\delta\sigma^{n-1-\mu}\mathrm{d}(\delta\sigma)\quad=\quad\frac{2A\Gamma}{n-\mu}\left(\frac{2A}{\mu}\right)^{n/\mu-1} \tag{2.61}$$

We will fix the second jump moment to a constant by setting $a_2=2\alpha\Gamma$, where α is equal to the α_eff introduced in the main text

$$\alpha=\frac{A}{2-\mu}\left(\frac{2A}{\mu}\right)^{2/\mu-1} \tag{2.62}$$

Inverting this relation, one finds that for the second jump moment to stay fixed the prefactor A must vary with μ as

$$A(\mu)=\frac{\mu}{2}\left(2\alpha\frac{2-\mu}{\mu}\right)^{\mu/2} \tag{2.63}$$

Inserting this into equation (2.61) we find that the coefficients of the Kramers-Moyal expansion take the form

$$a_n = \Gamma \frac{\mu}{n-\mu} \left(2\alpha \frac{2-\mu}{\mu} \right)^{n/2} \tag{2.64}$$

We can now take the limit $\mu \to 2^-$ at fixed α. One sees from the previous expression that in this limit

$$a_n \simeq \frac{2\Gamma}{n-2} \alpha^{n/2} (2-\mu)^{n/2} \to 0 \quad \forall n \geq 4 \tag{2.65}$$

We have therefore shown that all coefficients of the Kramers-Moyal expansion except the second one vanish for $\mu \to 2$. The remaining $n = 2$ term then gives exactly the diffusive contribution $(1/2)\partial_\sigma^2(a_2 P) = \alpha\Gamma\partial_\sigma^2 P$ that is used in the HL model to represent stress propagation.

2.B Derivation of steady state scaling

Considering again the steady state condition (2.12), we view the stress distribution as a perturbed version of the critical distribution $P_c(\sigma)$ defined in Section 2.3, which to connect with the boundary layer ansatz we write as $Q_0(\sigma)$, so that $P(\sigma, \Gamma) = Q_0(\sigma) + \delta P(\sigma, \Gamma)$. Inserting this into (2.12) and using the steady state condition for $Q_0(\sigma)$ at $A = A_c$, one finds for $\delta P(\sigma)$:

$$A\mathcal{L}\delta P(\sigma) - \frac{\theta(|\sigma|-1)}{\Gamma}\delta P(\sigma) - \tilde{A}\delta(\sigma) + AS_0(\sigma) = 0 \tag{2.66}$$

where we have defined

$$\tilde{A} \equiv \frac{A - A_c}{A_c} \tag{2.67}$$

and $S_0(\sigma)$ is given by

$$S_0(\sigma) = \theta(|\sigma|-1) \int_{-1}^{1} \frac{Q_0(\sigma')}{|\sigma - \sigma'|^{1+\mu}} \mathrm{d}\sigma' \tag{2.68}$$

To find the critical scaling, we consider as in the HL model the normalization condition. Due to the linearity of equation (2.66), we can split δP into a negative part $-\Delta^{\text{orig}}(\sigma, \Gamma)$ from the (negative) source $-\tilde{A}\delta(\sigma)$ at the origin, and a positive part $\Delta^{\text{ext}}(\sigma, \Gamma)$ from $AS_0(\sigma)$. One can then write the normalization condition as a condition on the integrals of these functions:

$$\int \delta P(\sigma, \Gamma) \mathrm{d}\sigma \stackrel{!}{=} 0 = -\int \Delta^{\text{orig}} \mathrm{d}\sigma + \int \Delta^{\text{ext}} \mathrm{d}\sigma \tag{2.69}$$

To obtain the first of these integrals we note that $\Delta^{\text{orig}}(\sigma)$ solves exactly the standard steady state condition (2.12), except that the source term is smaller by a factor $\tilde{A}$. Thus $\int \Delta^{\text{orig}}(\sigma) \mathrm{d}\sigma$ is given by $\tilde{A}$ times the mean lifetime $\tau_{\text{FP}}(A, \Gamma)$ of an effective particle diffusing from the origin. The lifetime $\tau_{\text{FP}}(A, \Gamma)$ may be approximated by the value $\tau_{\text{FP}}(A_c, \Gamma \to 0) = 1$ up to higher order corrections in the small quantities Γ and $\tilde{A}$. These can be neglected for the purpose of finding the leading scaling relations, thus simplifying the normalization condition to

$$\int \Delta^{\text{orig}}(\sigma, \Gamma) \mathrm{d}\sigma \simeq \tilde{A} = \int \Delta^{\text{ext}}(\sigma, \Gamma) \mathrm{d}\sigma \tag{2.70}$$

We may now find the critical scaling by considering only the term $\Delta^{\rm ext}(\sigma,\Gamma)$, which follows equation (2.66) without the term at the origin. Coming back to the interpretation in terms of first passage times, one may think of the integral over $\Delta^{\rm ext}$ as a $\Delta\tau^{\rm ext}$. This is the extra time that a particle lives before yielding when $\Gamma > 0$, where yielding is no longer instantaneous but happens (in the rescaled equation) at a finite but large rate $\mathcal{O}(1/\Gamma) \gg 1$.

We can now follow the ansatz introduced in Sec. 2.4 (without the frozen-in term $Q_0(\sigma)$) to write $\Delta^{\rm ext}(\sigma,\Gamma)$ piecewise in the interior, boundary layer and exterior regions. Firstly, for the exterior region, where we write $\Delta^{\rm ext} = \Gamma T_1(\sigma)$, we find from (2.66) to leading order that $T_1(\sigma) = AS_0(\sigma)$ (the first term is smaller by an order of Γ).

Proceeding to the boundary layer region, where $\Delta^{\rm ext}(\sigma,\Gamma) = \Gamma^c R_1(z)$ (without the frozen part), we need to incorporate the source $S_0(\sigma)$, in its limiting form that applies within the boundary layer. To deduce this form we introduce the scaling variable $y = (1-\sigma')/(\sigma-1)$ and use that for $\sigma - 1 \ll 1$ the integral (2.68) will be dominated by the singular behaviour $Q_0(\sigma') \simeq q_0(1-\sigma')^{\mu/2}$ near the boundary:

$$
\begin{aligned}
S_0(\sigma) &= q_0(\sigma-1)^{-\mu/2}\int_0^{2/(\sigma-1)} \frac{y^{\mu/2}}{(1+y)^{\mu/2}}\,\mathrm{d}y && (2.71)\\
&\simeq q_0\,\mathrm{B}\Big(\frac{\mu}{2},1+\frac{\mu}{2}\Big)\,(\sigma-1)^{-\mu/2} && (2.72)\\
&= \Gamma^{-1/2} q_0\,\mathrm{B}\Big(\frac{\mu}{2},1+\frac{\mu}{2}\Big)\,z^{-\mu/2} && (2.73)
\end{aligned}
$$

Comparing with (2.22) we see that this is precisely $\Gamma^{-1/2}S(z)$. On the other hand, because of the matching between $\Gamma^c R_1(z)$ and $T_1(\sigma)$ for $z \gg 1$ and $\sigma - 1 \ll 1$ we find that $c = 1/2$, as in Sec. 2.4. Writing the propagation in terms of rescaled variables as in (2.20), and together with the yielding term, we obtain finally that $R_1(z)$ as defined above for the boundary layer behaviour of $\Delta^{\rm ext}(\sigma)$ follows precisely the original boundary layer equation (2.21).

Considering the solution of the boundary layer equation on the interior as described in Sec. 2.4, one can now deduce the scaling with Γ of $\Delta^{\rm ext}(\sigma)$ in the interior region. The integral $\int \Delta^{\rm ext}(\sigma,\Gamma)\mathrm{d}\sigma$ is dominated by this interior region, so that via equation (2.70) we are eventually led to the critical scaling of the plastic activity (2.30).

2.C Scaling of $P(\sigma,\Gamma)$

In this appendix we give further details on the expansion for $\Gamma \ll 1$ of the distribution $P(\sigma,\Gamma)$. As outlined in the main text, the basis of the analysis is the boundary layer ansatz, whereby $P(\sigma,\Gamma)$ is expressed in a piecewise manner in the different regions (see also below). This ansatz must then be inserted into the master equation in order to obtain equations for the scaling functions. Restricting ourselves to the 1st order in the expansion, these are $R_1(z)$, $T_1(\sigma)$ and $Q_1(\sigma)$, for the boundary layer (from now on BL), exterior and interior regions respectively. The frozen-in distribution $Q_0(\sigma)$ corresponds to the critical distribution $P_c(\sigma)$ in the steady state scaling analysis (Sec. 2.5), whereas in the aging it is fixed indirectly by the initial condition. We further restrict the analysis to the symmetric case. In the aging setting, parity is conserved by the time evolution, so the stress distribution will be symmetric if the same is true of the initial distribution, i.e. $P_0(-\sigma) = P_0(\sigma)$. We can then just focus on

the bulk ($-1+\epsilon \leq \sigma \leq 1-\epsilon$) and the right hand side BL ($1-\epsilon < \sigma < 1+\epsilon$) and tail ($\sigma \geq 1+\epsilon$).

We will concentrate on the regime $1 < \mu < 2$, from which the marginal case $\mu = 1$ may be obtained as a limiting case. The BL ansatz for $P(\sigma, \Gamma)$ is

$$P(\sigma,\Gamma) = \left\{ \begin{array}{ll} Q_0(\sigma) + \Gamma^{1/\mu} Q_1(\sigma), & \text{for} \quad -1+\epsilon \leq \sigma \leq 1-\epsilon \\ \Gamma^{1/2} R(z), & \text{for} \quad 1-\epsilon < \sigma < 1+\epsilon \\ \Gamma T_1(\sigma), & \text{for} \quad \sigma \geq 1+\epsilon \end{array} \right\} \tag{2.74}$$

where the scaling function in the BL is written in terms of the re-scaled stress variable $z = \Gamma^{-1/\mu}(\sigma - 1)$.

There are some comments to be made on the ansatz above. In particular we have already inserted the final values $a = 1/\mu$, $b = 1$ and $c = 1/2$ of the exponents introduced in the main text:

- The $b = 1$ exponent for the external tail is clear from the analysis below of the external equation (in 2.C.1), where the external part of $P(\sigma, \Gamma)$ will be shown to be given by Q_0 convolved with the Lévy kernel, and thus proportional to the intensity $A\Gamma$ of this Lévy propagator.

- The exponent $c = 1/2$ comes from matching the asymptotic power law of the BL function on the exterior, $R_1^{\text{ext}}(z)$ for $z \gg 1$, with the exterior tail $T_1(\sigma)$ for $\sigma - 1 \ll 1$. In this regime $\Gamma T_1(\sigma) \sim \Gamma(\sigma-1)^{-\mu/2}$, which has to match with $\Gamma^c R(z) \sim \Gamma^c z^{-\mu/2}$ thus entailing $c = 1/2$.

- As already pointed out in Section 2.4 of the main text, the exponent $a = 1/\mu$ similarly stems from the match-up of the asymptotic power law of the BL function on the interior, $R_1^{\text{int}}(z)$ for $|z| \gg 1$, with the interior function $Q_1(\sigma)$ for $1 - \sigma \ll 1$.

As already explained in the main text, the BL function $R(z)$ can be split further into a frozen contribution from $Q_0(\sigma)$ and a nontrivial piece we denote by $R_1(z)$. We recall equation (2.19): $R(z) = q_0(-z)^{\mu/2}\theta(-z) + R_1(z)$.

We can now proceed by writing the full equation of motion, separately for the three different regions in σ.

2.C.1 External tail

The equation of motion (2.8) in the (positive) external region for $T_1(\sigma)$, which for convenience we divide once by Γ, reads (from now on we do not write the upper cut-off on the stress changes and leave this implicit in the power law kernel):

$$\begin{aligned} \frac{1}{\Gamma}\partial_t P(\sigma,\Gamma) = \frac{\dot{\Gamma}}{\Gamma} T_1(\sigma) = A\Bigg(& \int_{-1+\epsilon}^{1-\epsilon} \frac{\Gamma^{1/\mu} Q_1(\sigma') + Q_0(\sigma')}{|\sigma-\sigma'|^{\mu+1}} \mathrm{d}\sigma' \\ & + \int_{1-\epsilon}^{1+\epsilon} \frac{\Gamma^{1/2} R_1(\Gamma^{-1/\mu}(\sigma'-1))}{|\sigma-\sigma'|^{\mu+1}} \mathrm{d}\sigma' + \Gamma^{1/2} \int_{1-\epsilon}^{1} \frac{q_0(-z')^{\mu/2}}{|\sigma-\sigma'|^{\mu+1}} \mathrm{d}\sigma' \\ & + \int_{1+\epsilon}^{\infty} \frac{\Gamma(T_1(\sigma') - T_1(\sigma))}{|\sigma-\sigma'|^{\mu+1}} \mathrm{d}\sigma' - \Gamma T_1(\sigma) \int_{-\infty}^{1+\epsilon} \frac{1}{|\sigma-\sigma'|^{\mu+1}} \mathrm{d}\sigma' \Bigg) - T_1(\sigma) \end{aligned} \tag{2.75}$$

The leading order terms in this equation are $O(1)$, and accordingly we have omitted incoming terms from the other side of the domain, i.e. $\sigma' < -1+\epsilon$, which vanish as $\Gamma \to 0$. The term from the time derivative $\dot{\Gamma}/\Gamma$ is also of lower order for any $\Gamma(t)$

decaying slower than an exponential (this is true both for the power-law decay for $1<\mu<2$ and the stretched exponential at $\mu=1$).

Taking into account the asymptotic power-law forms of the interior $R_1^{\text{int}}(z)$ and exterior $R_1^{\text{ext}}(z)$ boundary layer function, one sees that the integral involving $R_1(z)$ is dominated by the upper and lower end. The dominance of the integral by its power-law asymptotes means that the shape of $R_1(z)$ inside the boundary layer is irrelevant here, thus we can simply extrapolate T_1 from the outside and Q_1 from the inside into the boundary layer (i.e. consider $\epsilon\to 0$). Likewise, the contribution from the $\mu/2$ power-law term can be seen as just being the extension of the integral over the frozen-in distribution $Q_0(\sigma)$ all the way up to the boundary.

Collecting the leading order terms one therefore has

$$T_1(\sigma)=A\int_{-1}^{1}\frac{Q_0(\sigma')}{(\sigma-\sigma')^{\mu+1}}\mathrm{d}\sigma' \tag{2.76}$$

So the external function is simply given by the convolution of the frozen-in distribution $Q_0(\sigma)$ with the Lévy kernel. Physically, this means that local stresses above the yield threshold typically arise when sub-threshold elements, with stresses following the frozen-in distribution $Q_0(\sigma)$, are perturbed by a single stress kick. We can evaluate the convolution explicitly in the limit where $\sigma-1\ll 1$, which will have to match up with the BL function $R_1(z)$ for $z\gg 1$. Changing variable to $y=(1-\sigma')/(\sigma-1)$, and using that $Q_0(\sigma')\sim q_0(1-\sigma')^{\mu/2}$, we can rewrite (2.76) as

$$T_1(\sigma)=Aq_0(\sigma-1)^{-\mu/2}\int_0^{\frac{2}{\sigma-1}}\frac{y^{\mu/2}}{(1+y)^{\mu+1}}\mathrm{d}y\simeq Aq_0\,\mathrm{B}\Big(\frac{\mu}{2},1+\frac{\mu}{2}\Big)(\sigma-1)^{-\mu/2} \tag{2.77}$$

which decays in the $\sim(\sigma-1)^{-\mu/2}$ fashion stated in the main text.

2.C.2 Contributions to the boundary layer

The equation of motion (2.8) (again divided once by Γ) in the boundary layer region reads:

$$\begin{aligned}\frac{1}{\Gamma}\partial_t\tilde{P}(z,\Gamma)=\frac{1}{2}\Gamma^{-1/2}\frac{\dot{\Gamma}}{\Gamma}R_1(z)-\Gamma^{-1/2}\frac{\dot{\Gamma}}{\Gamma}R_1'(z)\frac{z}{\mu}=A\Bigg(&\int_{-1+\epsilon}^{1-\epsilon}\frac{\Gamma^{1/\mu}Q_1(\sigma')+Q_0(\sigma')}{|\Gamma^{1/\mu}z-(\sigma'-1)|^{\mu+1}}\mathrm{d}\sigma'\\&+\int_{1+\epsilon}^{\infty}\frac{\Gamma T_1(\sigma')}{|\Gamma^{1/\mu}z-(\sigma'-1)|^{\mu+1}}\mathrm{d}\sigma'+\Gamma^{-1/2}\int_{-\epsilon\Gamma^{-1/\mu}}^{\epsilon\Gamma^{-1/\mu}}\frac{R_1(z')-R_1(z)}{|z-z'|^{\mu+1}}\mathrm{d}z'\\&+\Gamma^{-1/2}q_0\int_{-\epsilon\Gamma^{-1/\mu}}^{\epsilon\Gamma^{-1/\mu}}\frac{(-z')^{\mu/2}\theta(-z')-(-z)^{\mu/2}\theta(-z)}{|z-z'|^{\mu+1}}\mathrm{d}z'\\&-\Gamma^{1/2}R_1(z)\int_{\text{out}}\frac{1}{|\Gamma^{1/\mu}z-(\sigma'-1)|^{\mu+1}}\mathrm{d}\sigma'\Bigg)-\theta(z)\Gamma^{-1/2}R_1(z)\end{aligned} \tag{2.78}$$

where we have already rewritten the integrals inside the BL in terms of the scaling variable $z'=\Gamma^{-1/\mu}(\sigma'-1)$, and correspondingly expressed σ in terms of z as $\sigma=z\Gamma^{1/\mu}+1$. As in Appendix 2.C.1, we again omit the lower order incoming terms from $\sigma'<-1+\epsilon$. We have also introduced the notation $\int_{\text{out}}$, to denote the integration over the region $(-\infty,1-\epsilon)\cup(1+\epsilon,+\infty)$.

The BL equation (2.21) for $R_1(z)$ stated in the main text now follows from (2.78) using two arguments:

- Firstly, the left hand side terms stemming from the time derivative are of lower order than the leading order terms $\mathcal{O}(\Gamma^{-1/2})$ in the equation. For the case $1 < \mu < 2$, where we will find that $\Gamma(t)$ decays in a power-law fashion as $\Gamma(t) \sim t^{-\mu/(\mu-1)}$, one has $\dot{\Gamma}/\Gamma = -\frac{\mu}{\mu-1}\Gamma^{(\mu-1)/\mu}$ and the time derivative terms are smaller by this factor than the leading $\Gamma^{-1/2}$ terms. In the case $\mu = 1$, where we will find a stretched exponential, we also have that $\dot{\Gamma}\Gamma^{-3/2} \ll \Gamma^{-1/2}$ and so the time-derivative part is again of lower order and can be discarded in the final leading order equation for $R_1(z)$.

- Due to the way the boundary layer is defined, namely the fact that $\epsilon\Gamma^{-1/\mu} \gg 1$, it is simple to show that the terms propagating the bulk and exterior functions Q_0, Q_1 and T_1 into the boundary layer ($z = \mathcal{O}(1)$) are negligible. The bulk and exterior functions therefore only appear as matching conditions for the asymptotic power laws of $R_1(z)$.

Overall, the left hand side of (2.78) can be discarded to leading order, as can the first and second terms on the right; in the third and fourth term the integration limits become $(-\infty, +\infty)$ and the fifth term is again subleading. Evaluating the R_1-independent fourth term explicitly then gives exactly (2.21) in the main text.

2.C.3 Equation in the interior

The equation of motion (2.8) (divided once by Γ) in the interior region, where we write to leading order $P(\sigma, \Gamma) = Q_0(\sigma) + \Gamma^{1/\mu}Q_1(\sigma)$, reads

$$\begin{aligned}\partial_t P = \frac{1}{\mu}\Gamma^{\frac{1}{\mu}-1}\frac{\dot{\Gamma}}{\Gamma}Q_1(\sigma) = A\Bigg(&\int_{1+\epsilon}^{\infty}\frac{\Gamma T_1(\sigma')}{|\sigma-\sigma'|^{\mu+1}}\mathrm{d}\sigma' + \int_{-\infty}^{-1-\epsilon}\frac{\Gamma T_1(-\sigma')}{|\sigma-\sigma'|^{\mu+1}}\mathrm{d}\sigma' \\ &+ \int_{1-\epsilon}^{1+\epsilon}\frac{\Gamma^{\frac{1}{2}}R_1(\Gamma^{-\frac{1}{\mu}}(\sigma'-1))}{|\sigma-\sigma'|^{\mu+1}}\mathrm{d}\sigma' + \int_{-1-\epsilon}^{-1+\epsilon}\frac{\Gamma^{\frac{1}{2}}R_1(\Gamma^{-\frac{1}{\mu}}(-1-\sigma'))}{|\sigma-\sigma'|^{\mu+1}}\mathrm{d}\sigma' \\ &+ \Gamma^{\frac{1}{\mu}}\int_{-1+\epsilon}^{1-\epsilon}\frac{Q_1(\sigma')-Q_1(\sigma)}{|\sigma-\sigma'|^{\mu+1}}\mathrm{d}\sigma' + \int_{-1}^{1}\frac{Q_0(\sigma')-Q_0(\sigma)}{|\sigma-\sigma'|^{\mu+1}}\mathrm{d}\sigma' \\ &- (\Gamma^{\frac{1}{\mu}}Q_1(\sigma)+Q_0(\sigma))\int_{\text{out}}\frac{1}{|\sigma-\sigma'|^{\mu+1}}\mathrm{d}\sigma'\Bigg) + \delta(\sigma) \end{aligned} \tag{2.79}$$

where we again use the notation $\int_{\text{out}}$, this time to denote the integration over the region $(-\infty, -1+\epsilon) \cup (1-\epsilon, +\infty)$. It is clear to see in (2.79) that the leading order terms on the right hand side are $O(1)$, and are given by

$$A\left(\int_{-1}^{1}\frac{Q_0(\sigma')-Q_0(\sigma)}{|\sigma-\sigma'|^{\mu+1}}\mathrm{d}\sigma' - Q_0(\sigma)\int_{\text{out}}\frac{1}{|\sigma-\sigma'|^{\mu+1}}\mathrm{d}\sigma'\right) + \delta(\sigma) \tag{2.80}$$

This term is nonzero for any $A < A_c$. To balance it and obtain a time-independent Q_1 we need the left hand side of (2.79) to be also of order $O(1)$, thus leading to the conclusion that $\dot{\Gamma}/\Gamma = O(\Gamma^{(\mu-1)/\mu})$. This implies that $\Gamma(t)$ decays in time in a power-law fashion as $\Gamma(t) = Bt^{-b}$, with $b = \frac{\mu}{\mu-1}$, as stated in the main text. In particular one has $\dot{\Gamma}/\Gamma = -bt^{-1} = -b\Gamma^{1/b}B^{-1/b}$, where B represents the prefactor of the power-law decay and can be extracted from the numerical solution of the dynamics. We

therefore obtain an equation for $Q_1(\sigma)$

$$Q_1(\sigma) = -(\mu-1)B^{(\mu-1)/\mu}\left(A\left(\int_{-1}^{1}\frac{Q_0(\sigma')-Q_0(\sigma)}{|\sigma-\sigma'|^{\mu+1}}\mathrm{d}\sigma' - Q_0(\sigma)\int_{\text{out}}\frac{1}{|\sigma-\sigma'|^{\mu+1}}\mathrm{d}\sigma'\right)+\delta(\sigma)\right) \tag{2.81}$$

An example for this function is shown in Figure 2.5 in the main text.

2.C.4 $R_1^{\text{int}}(z)$ for $\mu = 1$

For the $\mu = 1$ case, we will take the limit $\mu \to 1^+$ of equation (2.78), and perform an analysis similar to the one carried out in Ref. [83]. As mentioned above, the time derivative part on the left will be neglected, which will turn out be consistent at the end given the decay of $\Gamma(t)$.

We therefore have again the equation:

$$A\int_{-\infty}^{\infty}\frac{R_1(z')-R_1(z)}{|z-z'|^{\mu+1}}\mathrm{d}z' + S(z) - \theta(z)R_1(z) = 0 \tag{2.82}$$

and write the source $S(z)$ as

$$S(z) = C_S z^{-\mu/2}, \quad C_S = q_0\,\mathrm{B}\left(\frac{\mu}{2}, 1+\frac{\mu}{2}\right) \tag{2.83}$$

For large positive z, the first (propagator) term is always subleading compared to R_1 itself so asymptotically R_1 has to exactly balance the source term:

$$R_1^{\text{ext}}(z) = C_{\text{ext}} z^{-\mu/2} \tag{2.84}$$

with $C_{\text{ext}} = C_S$. Next we consider the BL equation (2.82) for large negative z ($z < 0$, $|z| \gg 1$). We split the propagator term in (2.82) into three parts, which correspond respectively to jumps within the stable $z < 0$ region, jumps out to the unstable $z > 0$ region and incoming jumps from the unstable region (this term was negligible for large negative z in the $\mu > 1$ case):

$$\int_{-\infty}^{\infty}\frac{R_1(z')-R_1(z)}{|z-z'|^{\mu+1}}\mathrm{d}z' = \int_{-\infty}^{0}\frac{R_1^{\text{int}}(z')-R_1^{\text{int}}(z)}{|z-z'|^{\mu+1}}\mathrm{d}z' - R_1^{\text{int}}(z)\int_0^{\infty}\frac{1}{|z-z'|^{\mu+1}}\mathrm{d}z' + \int_0^{\infty}\frac{R_1^{\text{ext}}(z')}{|z-z'|^{\mu+1}}\mathrm{d}z' \tag{2.85}$$

Using the asymptotic behaviour of $R_1^{\text{ext}}(z')$ for large positive z', the last term with the jumps from the exterior part of the BL can be evaluated for large negative z as

$$C_{\text{ext}}\mathrm{B}(1-\mu/2, 3\mu/2)|z|^{-3\mu/2} \equiv C_+|z|^{-3\mu/2} \tag{2.86}$$

Given that we want to balance this term, and the convolutions with the power law kernel always reduce the power law exponent by μ, we write an ansatz for the interior BL behaviour as

$$R_1^{\text{int}}(z) = C_{\text{int}}|z|^{-\mu/2} \tag{2.87}$$

With this, all terms in equation (2.82) scale as $|z|^{-3\mu/2}$ for large negative z. After appropriate rescalings, this equation then becomes

$$\left(C_{\rm int} \int_0^\infty \frac{x^{-\mu/2}-1}{|1-x|^{\mu+1}} {\rm d}x - \frac{1}{\mu} C_{\rm int} + C_+ \right) |z|^{-3\mu/2} = 0 \tag{2.88}$$

From here we can find $C_{\rm int}$, which will be given by:

$$C_{\rm int} = \frac{C_+}{\frac{1}{\mu} - \int_0^\infty \frac{x^{-\mu/2}-1}{|1-x|^{\mu+1}} {\rm d}x} \tag{2.89}$$

Given that this is the solution to the BL equation taking into account the source generated by jumps from the $z > 0$ region (2.86), we call it the *inhomogeneous* solution and write it as

$$R_1^{\rm inti}(z) = C_{\rm int}^{\rm i} |z|^{-\mu/2} \tag{2.90}$$

where $C_{\rm int}^{\rm i}$ is given by equation (2.89).

In Section 2.4 of the main text the exponent of the *homogeneous* solution was worked out (the second exponent in Eq. (2.25)). The full solution (always in the regime of large negative z) may then be written as a superposition

$$R_1^{\rm int}(z) = R_1^{\rm inth}(z) + R_1^{\rm inti}(z) = C_{\rm int}^{\rm h} |z|^{-(1-\mu/2)} + C_{\rm int}^{\rm i} |z|^{-\mu/2} \tag{2.91}$$

For the purposes of taking the limit $\mu \to 1^+$ we introduce $\delta = \mu - 1$, so that the limit becomes $\delta \to 0^+$. In this limit, the (negative) denominator of (2.89) goes to zero linearly in δ (the exact prefactor from numerics is consistent with $\pi^2/2$; we absorb this into a rescaled version $\hat{C}_+$ of C_+). We can therefore write the solution when $\delta \ll 1$ in the following form:

$$R_1^{\rm int}(z) = C_{\rm int}^{\rm h}(\delta) |z|^{-(1-\delta)/2} - \frac{\hat{C}_+}{\delta} |z|^{-(1+\delta)/2} \tag{2.92}$$

In order for this to stay finite as $\delta \to 0$, the diverging last term has to be cancelled to leading order. This entails, from equation (2.92), that

$$C_{\rm int}^{\rm h} = C_{\rm BL} + \frac{\hat{C}_+}{\delta} \tag{2.93}$$

and so the prefactor of the homogeneous solution picks up a positive divergence in order to balance the negative divergence in the inhomogeneous one.

We now take the limit $\delta \to 0^+$ in equation (2.92), and work out the form of the boundary layer function $R_1(z)$ in the limit $z \to -\infty$. Inserting the form of $C_{\rm int}^{\rm h}$ we have just derived, this becomes

$$R_1^{\rm int}(z) = |z|^{-1/2} \left((C_{\rm BL} + \frac{\hat{C}_+}{\delta}) |z|^{\delta/2} - \frac{\hat{C}_+}{\delta} |z|^{-\delta/2} \right) \tag{2.94}$$

We now expand in the exponent:

$$|z|^{\delta/2} = e^{\delta/2 \ln(|z|)} = 1 + \frac{\delta}{2} \ln(|z|) + \mathcal{O}(\delta^2) \tag{2.95}$$

and plug this expansion back into equation (2.94) to obtain

$$\lim_{\delta\to 0} R_1^{\text{int}}(z) = |z|^{-1/2}\left(C_{\text{BL}} + \hat{C}_+ \ln(|z|)\right) \overset{|z|\gg 1}{\approx} \hat{C}_+ |z|^{-1/2}\ln(|z|) \tag{2.96}$$

We therefore see that the interior tail of the boundary layer function acquires a logarithmic correction at $\mu = 1$.

2.D Derivation of $\rho(\delta\sigma)$ for a circular geometry

In this appendix we perform the explicit derivation of the mechanical noise spectrum $\rho(\delta\sigma)$ in the 2D case considering a circular geometry. In 2D, the stress field caused by a local plastic event at the origin reads in polar coordinates

$$\delta\sigma(r,\theta) = G_0 a^2 \frac{\cos(4\theta)}{r^2} \tag{2.97}$$

We then consider a circular geometry, so that the cluster of rearranging particles at the origin occupies a radius r_0, while the rest of the mesoscopic elements lie uniformly within the ring around this, i.e. at a distance $r_0 < r < R$, R being the radius of the total system. The distribution over site *positions* then reads

$$\rho(r,\theta) = \frac{r}{\pi(R^2 - r_0^2)} \mathrm{d}r\mathrm{d}\theta \tag{2.98}$$

In order to obtain the distribution over stress increments $\rho(\delta\sigma)$, we need to perform the transformation $(r,\theta) \to \delta\sigma$ on the distribution (2.98), using the relation (2.97):

$$\rho(\delta\sigma) = \frac{1}{\pi(R^2 - r_0^2)} \int_{r_0}^{R} \mathrm{d}r \int_0^{2\pi} \mathrm{d}\theta\, r\, \delta\left(\delta\sigma - G_0 a^2 \frac{\cos(4\theta)}{r^2}\right) \tag{2.99}$$

We set $\theta' = 4\theta$ so that the angular integration becomes $(1/4)\int_0^{8\pi}\mathrm{d}\theta'$; because of the periodicity of $\cos(\theta')$ we can then equivalently restrict the integration to $2\int_0^{\pi}\mathrm{d}\theta'$. We now focus first on the positive half of the distribution ($\delta\sigma > 0$), which corresponds to $\theta' < \pi/2$; the negative half may be obtained by symmetry. Performing then the variable change $x = \cos(\theta')$, we have for $\delta\sigma > 0$

$$\rho(\delta\sigma) = \frac{2}{\pi(R^2 - r_0^2)} \int_{r_0}^{R} \mathrm{d}r \int_0^1 \mathrm{d}x \frac{r}{\sqrt{1-x^2}} \delta\left(\delta\sigma - G_0 a^2 \frac{x}{r^2}\right) \tag{2.100}$$

Using the properties of the delta function, we can then rewrite

$$\delta\left(\delta\sigma - G_0 a^2 \frac{x}{r^2}\right) = \frac{r^3}{2G_0 a^2 x} \delta\left(r - \sqrt{\frac{G_0 a^2 x}{\delta\sigma}}\right) \tag{2.101}$$

We can now perform the integral over r in (2.100):

$$\int_{r_0}^{R} r^4 \delta\left(r - \sqrt{\frac{G_0 a^2 x}{\delta\sigma}}\right) \mathrm{d}r \quad = \quad \left(\frac{G_0 a^2 x}{\delta\sigma}\right)^2 \tag{2.102}$$

provided that

$$\frac{\delta\sigma r_0^2}{G_0 a^2} < x < \min\left(1, \frac{\delta\sigma R^2}{G_0 a^2}\right) ; \tag{2.103}$$

otherwise the integral vanishes. Therefore the full integral (2.100) becomes

$$\rho^{+}(\delta\sigma) = \frac{G_0 a^2}{\pi(R^2 - r_0^2)} \delta\sigma^{-2} \int_{\frac{\delta\sigma r_0^2}{G_0 a^2}}^{\min\left(1, \frac{\delta\sigma R^2}{G_0 a^2}\right)} \frac{x}{\sqrt{1-x^2}} \mathrm{d}x \tag{2.104}$$

Performing the last integral and making use of the symmetry $\rho(-\delta\sigma) = \rho(\delta\sigma)$, the final expression for the stress kick distribution reads

$$\rho(\delta\sigma) = \frac{G_0 a^2}{\pi(R^2 - r_0^2)} \delta\sigma^{-2} \times \left(\sqrt{1 - \left(\frac{\delta\sigma r_0^2}{G_0 a^2}\right)^2} - \sqrt{1 - \left(\min\left(1, \frac{|\delta\sigma| R^2}{G_0 a^2}\right)\right)^2} \right) \tag{2.105}$$

This distribution has two main features with respect to the pure power law distribution used in the main text. Firstly, it goes to zero continuously as $\delta\sigma$ approaches the highest possible stress kick in the system $G_0 a^2 / r_0^2$, instead of presenting a hard cutoff (see Figure 2.16). Secondly, the system size-dependent lower cutoff is also no longer sharp; instead $\rho(\delta\sigma)$ drops smoothly to a nonzero value as $|\delta\sigma|$ decreases below $G_0 a^2 / R^2$. In the limit $R \to \infty$ and for $\delta\sigma$ below the upper cutoff one recovers the expected $\delta\sigma^{-2}$ power law decay.

Finally, we discuss the result (2.105) in connection to the form of $\rho(\delta\sigma)$ used in the main text, defined by (2.4) and (2.5). To explore this, we replace the physical r^{-2} propagator decay (2.97) by $G_0 a^\beta \cos(4\theta)/r^\beta$, with a general decay exponent β. If we then carry out the same steps as described above, we obtain in the power-law region

$$\rho(\delta\sigma) = \frac{c_\mu \mu (G_0 a^\beta)^\mu}{\pi(R^2 - r_0^2)} |\delta\sigma|^{-1-\mu} \tag{2.106}$$

where we have defined $\mu = d/\beta = 2/\beta$ as in the main text. The constant c_μ arises from the angular integration and is equal to

$$c_\mu = \int_0^1 \frac{x^\mu}{\sqrt{1-x^2}} \mathrm{d}x = \frac{\sqrt{\pi}\,\Gamma\left(\frac{\mu+1}{2}\right)}{2\Gamma\left(\frac{\mu}{2}+1\right)} \tag{2.107}$$

so that c_1=1, while in the limit case $\mu = 2$ one has $c_2 = \pi/4$.

We now need to relate the area of the system to the number of mesoscopic elements or zones N. To do so we introduce a dimensionless *packing density*

$$\varphi = \frac{N r_0^2}{R^2} \tag{2.108}$$

so that the distribution (2.106) may be written as

$$\rho(\delta\sigma) = \frac{A}{N} |\delta\sigma|^{-\mu-1} \quad \text{with} \quad A = \frac{c_\mu \varphi \mu}{\pi} \left(\frac{G_0 a^\beta}{r_0^\beta}\right)^\mu \tag{2.109}$$

The maximum stress change in the system $\delta\sigma_\mathrm{u}$ can also be written in terms of the coupling A, as

$$\delta\sigma_\mathrm{u} = \frac{G_0 a^\beta}{r_0^\beta} = \left(\frac{A\pi}{c_\mu \varphi \mu}\right)^{1/\mu} \tag{2.110}$$

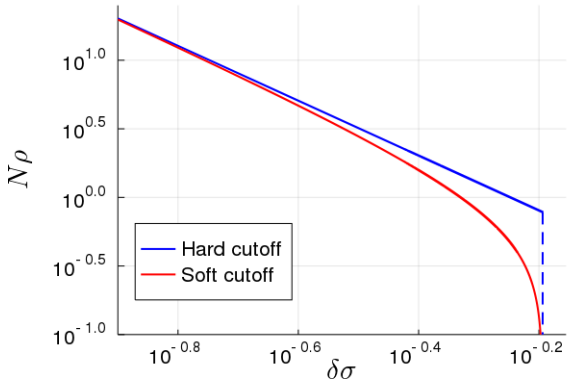

FIGURE 2.16: Comparison of the hard cutoff expression (2.4) with the soft cutoff form (2.105). $A = 0.32$ in the hard cutoff form; parameters in the soft cutoff version were chosen to have the same upper cutoff and power-law prefactor.

We see from (2.109) that the strength of the coupling constant A depends crucially on the packing density φ. On a lattice, the coupling A will be fixed once and for all by the geometry of the underlying grid. However, if one takes the view in Ref. [70] of a variable density of "active" zones, which may be related to an effective mechanical temperature regulating the activity in the system, it becomes meaningful to think of a tunable coupling constant A depending on the state of the system.

2.E Numerical methods

2.E.1 Pseudospectral method

In integrating the master equation (2.8) numerically, the main challenge is the treatment of the stress propagation term. This Lévy propagator takes a simpler form in Fourier space:

$$\int_{\sigma-\delta\sigma_u}^{\sigma+\delta\sigma_u} \frac{P(\sigma')-P(\sigma)}{|\sigma-\sigma'|^{\mu+1}}\mathrm{d}\sigma' \xrightarrow{\mathcal{F}} -|k|^{\mu}H_{\mu}(k\,\delta\sigma_u)\hat{P}(k) \tag{2.111}$$

with

$$H_{\mu}(y) = \int_0^y \frac{1-\cos t}{t^{\mu+1}}\mathrm{d}t \tag{2.112}$$

For a Lévy flight without cutoff, i.e. $\delta\sigma_u \to \infty$, $H_{\mu}(k\,\delta\sigma_u)$ converges to $I_{\mu} = -\cos(\mu\pi/2)\Gamma(-\mu)$ for $\mu \neq 1$, and $\frac{\pi}{2}$ for $\mu = 1$. On the other hand, $\hat{P}(k)$ is just the Fourier transform of the stress distribution

$$\hat{P}(k) = \int_{-\infty}^{\infty} e^{-ik\sigma}P(\sigma)\mathrm{d}\sigma \tag{2.113}$$

To evolve the master equation (2.8) numerically we can therefore proceed in the following manner. Firstly we set up a stress grid $\{\sigma_i\}$ $(i = 1,\ldots,M)$ of M points in a domain $(-l,l)$, along with the corresponding M points $\{k_i\}$ in Fourier space. The domain width $2l$ has to be wide enough to avoid the effect of periodic images; for the aging simulations $l = 4$ was used. To set up the discrete Fourier components of the propagator we evaluate the integral (2.112) numerically at each k_i, using an adaptive quadrature to account for the diverging power law in the integrand.

We can then employ a pseudospectral method, where we evolve alternately in stress and in Fourier space, using the FFT algorithm to switch between the two. Namely the Lévy propagator is applied in Fourier space, while all the other updates are realised in stress space. Finally we note that in the aging simulations, where the dynamics slows down at long times, we use an adaptive time step, which is fixed so that the maximum relative change in the system $\max_i \Delta P(\sigma_i)/P(\sigma_i)$ stays within the range $(5\times10^{-4}, 1\times10^{-3})$. In this way the timestep grows as the dynamics becomes progressively slower.

2.E.2 Discrete matrix

For calculating e.g. the mean first passage time that we employ to determine the phase diagram, we used an alternative numerical approach that allows us to implement absorbing boundary conditions.

For this we follow Ref. [79] and write down a discretized transition matrix of the propagator

$$A\int_{-l}^{l}\frac{P(\sigma')-P(\sigma)}{|\sigma-\sigma'|^{1+\mu}}\mathrm{d}\sigma' \tag{2.114}$$

We will start by considering the off-diagonal formally divergent integral; the second term, which corresponds to the diagonal, will be incorporated later by imposing probability conservation.

We define again a stress grid $\{\sigma_i\}$ $(i=1,\dots,M+1)$ of $M+1$ points in a domain $(-l,l)$ (including now both boundaries), with a corresponding stress discretization $\Delta\sigma = 2l/M$. For the off-diagonal term, it will be useful to represent the kernel as a discrete derivative:

$$|\sigma-\sigma'|^{-\mu-1} \simeq K(\sigma,\sigma') \equiv \frac{1}{\mu\Delta\sigma}\left[|\sigma-\sigma'|^{-\mu}-|\sigma-\sigma'+\Delta\sigma|^{-\mu}\right] \tag{2.115}$$

We can then write the integral in discretized form as

$$A\Delta\sigma\sum_j P(\sigma_j)K(\sigma_i,\sigma_j) \tag{2.116}$$

To implement the cutoff, we set $K=0$ for $|\sigma_i-\sigma_j|>\delta\sigma_\mathrm{u}$. The diagonal term is then

$$K(\sigma_i,\sigma_i) = \frac{2}{\mu\Delta\sigma}\left[-(\Delta\sigma)^{-\mu}+(\delta\sigma_\mathrm{u}+\Delta\sigma)^{-\mu}\right] \tag{2.117}$$

This is the same discretization as used in Ref. [79], except for the modification in order to account for the presence of the upper cutoff in the propagator $\delta\sigma_\mathrm{u}$. Absorbing boundary conditions are implemented by considering the discrete matrix of size $(M+1)\times(M+1)$, which effectively sets to 0 all other elements outside so that whenever the stress at a site is "kicked" out of the region $(-l,l)$ it is removed [78].

In Section 2.3 we use $l=1$, so that we can implement the absorbing boundary conditions at $\sigma=\pm\sigma_c=\pm1$. To obtain the points in the phase diagram (Figure 2.1), for a fixed μ we compute $\tau_\mathrm{FP}(A)$ and bisect in A until we find $\tau_\mathrm{FP}(A_c)=1$. $\tau_\mathrm{FP}(A)$ is computed in the way detailed in Ref. [79], where the discretization above is introduced precisely to tackle the problem of the mean first passage time of a Lévy flight in a domain with absorbing boundaries. It is worth commenting on the discretization error. As we commented in Figure 2.1, this error becomes larger as $\mu\to2^-$. As worked out in Ref. [79], in the limit $M\to\infty$ the error decays as $M^{\mu-2}$ for $1<\mu<2$,

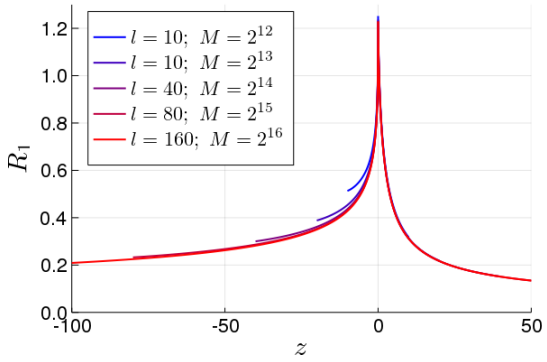

FIGURE 2.17: Convergence of the solution of the BL equation (2.21) with increasing size l of the computational domain; parameter values are $\mu = 1$, $A = 0.58$ and source prefactor $q_0 = 1$.

whereas for $\mu < 1$ this crosses over to M^{-1}. From the scaling with $M^{\mu-2}$ one sees that the method breaks down when $\mu \to 2^-$. Intuitively, this may be expected, as one would be attempting to approximate what is effectively a (local) second derivative by a power law.

To obtain the data in Figure 2.7 (Section 2.5), we solve for $\Delta^{\text{ext}}(\sigma)$ numerically, making use again of the above discrete matrix. In this case, however, where we are considering a small but finite $\Gamma \ll 1$, we use $l = 2 > 1$ in order to capture the external loss term in Eq. (2.66). We implement as above absorbing boundary conditions at $l = \pm 2$, but this does not affect the result, as $\Gamma \ll 1$ and we have checked that the distribution decays to zero well within the $\sigma \in (-2, 2)$ region.

2.E.3 Boundary layer equation

We discuss in this section the numerical solution of the BL equation (2.21) in the main text. This is required to obtain the full form of $R_1(z)$ for finite z, beyond the asymptotic power laws for large $|z|$ that we determine analytically in the main text.

The major difficulty in solving equation (2.21) is that one a priori needs to consider an infinite domain $z \in (-\infty, \infty)$. To overcome this we proceed in the following manner. We cut the infinite domain down to a finite interval $(-l, l)$, by exploiting the knowledge we have on the tails of $R_1(z)$. That is, we split the incoming term of the propagator as

$$\int_{-\infty}^{\infty} \frac{R_1(z')}{|z - z'|^{\mu+1}} \mathrm{d}z' = \int_{-l}^{l} \frac{R_1(z')}{|z - z'|^{\mu+1}} \mathrm{d}z' + \text{tail}_1(z) + \text{tail}_2(z) \tag{2.118}$$

where the two tails correspond respectively to the integrals over $\int_{-\infty}^{-l}$ and $\int_{l}^{\infty}$. In the two domains $z < -l$ and $z > l$, we assume the asymptotic forms of $R_1(z)$, which are power laws with prefactors proportional to $R_1(\pm l)$. Overall one can therefore include the two tail terms into the 1st and last column of the discrete transition matrix $K(\sigma_i, \sigma_j)$.

To check the convergence of the method, we can increase l and M (the number of grid points) while keeping the stress discretization $\Delta\sigma$ fixed. This is shown in Fig. 2.17 for $\mu = 1$, where we have assumed the asymptotic forms $|z|^{-1/2} \ln(|z|)$ on the left and $z^{-1/2}$ on the right. We can see that the method indeed converges as l and M are increased.

Chapter 3

Mean field description of aging linear response

Most of the following chapter, except parts of Sections 3.1 and 3.7, has been reproduced from the pre-print [2], which has been submitted for publication.

3.1 Introduction

As pointed out in the introductory Chapter 1, recent work [38, 84, 85] has shown that model athermal suspensions of soft particles can display non-trivial slow dynamics, typically referred to as aging. This *athermal* aging behaviour is to be contrasted with the aging of thermal colloidal glasses [42, 45] or spin glasses [41], which has been widely studied, using e.g. trap based models [86] built around thermal activation, or record dynamics [87]. The importance of "hotspots" of non-affine relaxation, reminiscent of local plastic (Eshelby) events, during the athermal aging process [38] leads us instead to propose an elastoplastic approach to the problem.

In Chapter 2 we introduced a mean field elastoplastic model and showed that it presents aging behaviour, characterised by a slow decay of the yield rate, i.e. the number of plastic events per unit time. Here we go beyond the analysis of Chapter 2 and study the aging of the linear shear response of the model, which unlike the yield rate can be directly compared to stress measurements in particle simulations or experiments. We also carry out such a comparison, taking as reference the aging soft athermal suspension mentioned above [38].

We recall that the time-dependent model we derived in Chapter 2 was defined by the following master equation

$$\begin{aligned}\partial_t P(\sigma,t) &= -G_0\dot\gamma\partial_\sigma P(\sigma,t)\\ &+ A\Gamma(t)\int_{\sigma-\delta\sigma_u}^{\sigma+\delta\sigma_u}\frac{P(\sigma',t)-P(\sigma,t)}{|\sigma-\sigma'|^{\mu+1}}\mathrm{d}\sigma' - \frac{\theta(|\sigma|-\sigma_c)}{\tau_{pl}}P(\sigma,t)+\Gamma(t)\delta(\sigma)\end{aligned} \tag{3.1}$$

with the yield rate

$$\Gamma(t) = \frac{1}{\tau_{pl}}\int_{-\infty}^{\infty}\theta(|\sigma|-\sigma_c)P(\sigma,t)\mathrm{d}\sigma \tag{3.2}$$

For clarity, we briefly recapitulate the phase diagram of the model in the (μ, A) plane, studied in Sec. 2.3, and reproduced in Fig. 3.1. For $A > A_c(\mu)$, the system is in a "liquid" phase behaving as a Newtonian fluid $\Sigma = \eta\dot\gamma$ under applied shear; here and throughout the macroscopic stress is taken as the average $\Sigma(t) = \int \mathrm{d}\sigma\, \sigma P(\sigma,t)$. Without shear, the system is able to sustain a steady state with finite yield rate $\Gamma^{ss} > 0$, behaving essentially as a Maxwell fluid with a finite relaxation time. The latter diverges as $A \to A_c^+$, with anomalous non-Maxwellian behaviour arising as

this critical point is approached (see below). The existence of such a steady state within the model has been argued to be unphysical [66], given that external driving should be necessary to maintain the dissipative plastic events. On the other hand, one may argue that Eshelby events can also be identified in unsheared liquids [88]. The steady state regime may also be relevant to the questions raised in [89], where elastoplasticity was shown to mediate dynamical heterogeneity in supercooled liquids. We will discuss this issue further in Chapter 5.

We will in any case focus mainly on the aging regime below. In this glassy phase for $A < A_c(\mu)$, there is no steady state with $\Gamma > 0$ in the absence of shear, and the yield rate decays as the system approaches an initial condition dependent frozen-in stress distribution $Q_0(\sigma) \equiv P_0(\sigma, t \to \infty)$ (recall e.g. Fig. 2.2). This distribution was shown to exhibit (in Chapter 2 and in [28]) pseudogap scaling near the yield threshold, $Q_0(\sigma) \sim (\sigma_c - |\sigma|)^{\mu/2}$. This behaviour is found also in the steady state stress distribution on the liquid side in the limit $\Gamma \to 0$, and is in agreement with the results of MD simulations [73, 74].

In Chapter 2, we studied the slow decay of $\Gamma(t)$ by evolving the unperturbed dynamics starting from an initial distribution with enough unstable sites. This was argued to represent the dynamics of the system after an initial preparation, such as stirring, shear melting or a sudden change in density. If the system is athermal, the ensuing dissipative dynamics is driven by rearrangements that can only be triggered by events taking place elsewhere in the system, as described here. The yield rate was found to decay as a power law $\Gamma(t) \sim t^{-\mu/(\mu-1)}$ for $1 < \mu < 2$, a stretched exponential $\Gamma(t) \sim e^{-B\sqrt{t}}$ for $\mu = 1$ and an exponential for $\mu < 1$, reflecting the relative importance of far-field and near-field events as the range of the stress propagator is varied. The different regimes are sketched in Fig. 3.1, where we indicate also the different parameter values for which we will study the linear shear response numerically in this chapter. We include among these two parameter values pertaining to the case of *critical aging*, i.e. relaxation at criticality $A = A_c(\mu)$, where the yield rate decays as $\Gamma(t) \sim t^{-1}$ for all μ (see Sec. 2.6).

The chapter is structured as follows. In Sec. 3.2 we provide theoretical background on how the linear response, and in particular the viscoelastic moduli, are defined in the aging regime. We also set out how they can be calculated within our model. Next, in Sec. 3.3 we give an intuitive scaling argument that motivates our analytical results. In Sec. 3.4 we then derive these results in the aging regime, both in the time and in the frequency domain. Finally, in Sections 3.5 and 3.6 we specialise to the model with $\mu = 1$, first checking our results within full non-linear simulations of the mean field model and then comparing the theory to stress measurements (performed by Dr. Rituparno Mandal) in an athermal particle system. We conclude with a summary of the chapter in Sec. 3.7.

3.2 Theoretical background

We consider in this section the linear shear rheology of an amorphous system relaxing after preparation at time $t = 0$. We assume that a small step strain $\gamma(t) = \gamma_0 \theta(t - t_w)$ (with $\gamma_0 \ll 1$) is applied at a certain switch-on time, which we denote as the waiting time t_w. The corresponding shear stress is given by the linear constitutive equation

$$\sigma(t) = \int_{-\infty}^{t} G(t, t') \dot{\gamma}(t') \mathrm{d}t' \tag{3.3}$$

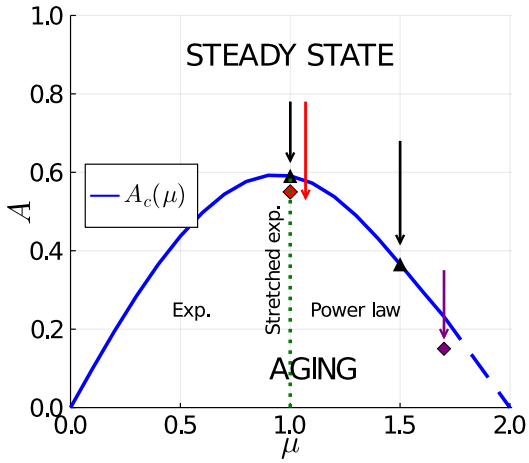

FIGURE 3.1: Phase diagram of the model in the (μ, A) plane (see Sec. 2.3), defined by the curve $A_c(\mu)$ (blue). The two black triangles ($\mu = 1.0, A = A_c(1.0)$ and $\mu = 1.5, A = A_c(1.5)$) and arrows indicate the numerical parameter values for which we study aging at criticality in Appendix 3.B. The purple ($\mu = 1.7, A = 0.15$) and red ($\mu = 1.0, A = 0.55$) diamonds and arrows show the cases studied for aging in the glass phase in Sec. 3.4.

where $G(t, t')$ is the so-called stress relaxation function. From this response to a step strain one may then derive the linear response to more complex perturbations such as oscillatory strain, as described below.

Within our mean field elastoplastic model, the shear perturbation manifests itself via its effect on the dynamics of the stress distribution $P(\sigma, t)$. In the generic aging case, both the unperturbed distribution $P_0(\sigma, t)$ and the unperturbed yield rate $\Gamma_0(t)$ will depend on time. We then expand the perturbed solution $P(\sigma, t)$ of the master equation (3.1) for $t > t_w$ as

$$P(\sigma, t) = P_0(\sigma, t) + \gamma_0 \, \delta P(\sigma, t) + \mathcal{O}(\gamma_0^2) \tag{3.4}$$

Likewise, for the yield rate we may write

$$\Gamma(t) = \Gamma_0(t) + \gamma_0 \, \delta\Gamma(t) + \mathcal{O}(\gamma_0^2) \tag{3.5}$$

To simplify the analysis we now assume as in [71] and in Chapter 2 that the system preparation leads to a symmetric initial stress distribution $P_0(\sigma, 0)$. The unperturbed dynamics preserves this symmetry, so that $P_0(\sigma, t) = P_0(-\sigma, t)\ \forall t$. With this assumption, one may show as in [71] that the first order correction to the yield rate $\delta\Gamma(t)$ vanishes. This simply follows from the invariance of the time evolution of the master equation (3.1) under joint sign reversal of σ and γ_0, which implies that $\delta P(\sigma, t)$ must be an odd function of σ, so that

$$\delta\Gamma(t) = \frac{1}{\tau_{\text{pl}}} \int_{-\infty}^{\infty} \mathrm{d}\sigma \, \theta(|\sigma| - \sigma_c) \delta P(\sigma, t) = 0 \tag{3.6}$$

If we now insert the perturbed form (3.4) of $P(\sigma, t)$ into the master equation (3.1), we find at $\mathcal{O}(\gamma_0)$ and for $t > t_w$ the following equation for the perturbation:

$$\partial_t \delta P(\sigma, t) = A\Gamma(t) \int_{\sigma - \delta\sigma_u}^{\sigma + \delta\sigma_u} \mathrm{d}\sigma' \, \frac{\delta P(\sigma', t) - \delta P(\sigma, t)}{|\sigma - \sigma'|^{\mu+1}} - \frac{\theta(|\sigma| - \sigma_c)}{\tau_{\text{pl}}} \delta P(\sigma, t) \tag{3.7}$$

The initial condition for this is found by integrating (3.1) in a small time interval around $t = t_w$, giving

$$\delta P(\sigma, t_w) = -\partial_\sigma P_0(\sigma, t_w) \tag{3.8}$$

Since we identify the macroscopic stress with the average over the local distribution, once we have found $\delta P(\sigma, t)$ the linear stress relaxation function can be computed as

$$G(t, t_w) = \int_{-\infty}^{\infty} d\sigma\, \sigma \delta P(\sigma, t) = 2 \int_0^{\infty} d\sigma\, \sigma \delta P(\sigma, t) \tag{3.9}$$

where the second equality follows from the anti-symmetry of δP. Using the initial condition (3.8) and bearing in mind that $P_0(\sigma, t_w)$ is normalised we have the initial value $G(t_w, t_w) = G_0$.

The steady state and aging stress relaxation are distinct in their dependence on the waiting time t_w. If the unperturbed system is already prepared in a steady state, $P_0(\sigma, t) = P^{ss}(\sigma)$ and $\Gamma_0(t) = \Gamma^{ss}$ are independent of time and we find as expected a time translation invariant (TTI) stress relaxation function $G(t, t_w) = G(t - t_w) \equiv G(\Delta t)$. In the aging regime, on the other hand, this invariance is lost and $G(t, t_w)$ in general depends on both time arguments.

A similar distinction may be made in the frequency response, for which we follow the generic discussion in [44]. For TTI systems, we may write the response to an oscillatory strain $\gamma(t) = \Re[\gamma_0 e^{i(\omega t + \phi)}]$ as $\sigma(t) = \Re[G^*(\omega)\gamma_0 e^{i(\omega t + \phi)}]$, where the viscoelastic spectrum $G^*(\omega) = G'(\omega) + iG''(\omega)$ is proportional to the Fourier transform of $G(\Delta t)$. In aging systems [44], the viscoelastic spectrum generically depends on three arguments: the oscillatory frequency ω, the time t when the stress is measured and the waiting time t_w. One finds

$$G^*(\omega, t, t_w) = G(t, t_w) e^{-i\omega(t - t_w)} + i\omega \int_{t_w}^{t} dt'\, G(t, t') e^{-i\omega(t - t')} \tag{3.10}$$

In the limit where $\omega(t - t_w) \gg 1$ (many oscillations before the stress measurement) and $\omega t_w \gg 1$ (large waiting time), equation (3.10) may approach the *forward spectrum* $G_f^*(\omega, t)$. This is calculated by assuming the strain is applied from the measurement time t *into the future*:

$$G_f^*(\omega, t) = i\omega \int_t^{\infty} dt'\, G(t', t) e^{-i\omega(t - t')} \tag{3.11}$$

We will show both numerically and analytically (in Appendix 3.D) that this limiting behaviour holds in our elastoplastic model. Note that generally we also require the condition $\omega \ll 1/\tau_{pl}$ to stay within the range of applicability of the model, which does not include e.g. dissipative effects from solvent viscosity that would become relevant at higher frequencies.

Finally, we propose an alternative approach for numerically calculating the aging frequency response $G^*(\omega, t, t_w)$, which helps to reduce oscillations that appear when using directly the original expression (3.10). This approach is inspired by experimental work [46–48] and is closer to how the frequency response is measured in reality, where one needs to measure the relative phase and amplitude across several periods. We take the stress signal $\sigma(t)$ and correlate it with the strain signal $\gamma(t)$ over a time window of m periods around an observation time t . We denote this averaged

response by $\bar{G}^*(\omega, t, t_w)$

$$\bar{G}^*(\omega, t, t_w) = \frac{\omega}{m\pi\gamma_0} \int_{t-\frac{m\pi}{\omega}}^{t+\frac{m\pi}{\omega}} \mathrm{d}t' \, \sigma(t') e^{-i(\omega t'+\phi)} \tag{3.12}$$

where as usual $\bar{G}^*$ can be separated into $\bar{G}^* = \bar{G}' + i\bar{G}''$. If we then express $\sigma(t)$ in terms of the *unaveraged* moduli $G^* = G' + iG''$, the above expression becomes:

$$\begin{aligned} &\bar{G}^*(\omega, t, t_w) \qquad (3.13)\\ = \; &\frac{\omega}{m\pi}\Bigg(\int_{t-\frac{m\pi}{\omega}}^{t+\frac{m\pi}{\omega}} \mathrm{d}t' \, \left(\cos(\omega t'+\phi)^2 G'(\omega, t', t_w) - \frac{1}{2}\sin(2(\omega t'+\phi)) G''(\omega, t', t_w) \right) \\ &+ i \int_{t-\frac{m\pi}{\omega}}^{t+\frac{m\pi}{\omega}} \mathrm{d}t' \, \left(\sin(\omega t'+\phi)^2 G''(\omega, t', t_w) - \frac{1}{2}\sin(2(\omega t'+\phi)) G'(\omega, t', t_w) \right) \Bigg) \end{aligned}$$

The oscillations in $G^*(\omega, t, t_w)$ are of frequency ω (see also Fig. 3.19 in Appendix 3.D). They are thus orthogonal to the constant and 2ω kernels in the averaging formula above, and therefore no longer present in the resulting averaged moduli.

To calculate $\bar{G}^*$ in practice, we express it directly in terms of the age-dependent relaxation function $G(t, t')$. In order to simplify this expression we make a particular choice for the phase of the strain signal $\gamma(t) = \Re[\gamma_0 e^{i(\omega t+\phi)}]$, fixing $\phi = -\omega t_w - \pi/2$. This ensures that $\gamma(t) = \gamma_0 \sin(\omega(t - t_w))$ and hence that the applied strain starts continuously from zero, leading to the simplified result [1]

$$\begin{aligned} \bar{G}^*(\omega, t, t_w) = \frac{\omega}{m\pi} \int_{t-\frac{m\pi}{\omega}}^{t+\frac{m\pi}{\omega}} \mathrm{d}t' \, \left[\sin\left(\omega(t'-t_w)\right) + i\cos\left(\omega(t'-t_w)\right) \right] \\ \times \int_{t_w}^{t'} \mathrm{d}t'' \, G(t', t'') \, \omega \cos\left(\omega(t''-t_w)\right) \end{aligned} \tag{3.14}$$

which we will use for the numerical results shown in Sec. 3.4. This form can also be obtained directly from (3.12) with the appropriate choice of the phase angle.

3.3 Overview of analytical results

Before we turn to analyse the aging linear response in detail, we give a brief overview of the analytical results, highlighting universal features that are independent of the noise exponent μ. Here and in the following, we set $\sigma_c = 1$ and $\tau_{\mathrm{pl}} = 1$, providing the stress and time units. In addition, without loss of generality we set $G_0 = 1$, so that $G(t_w, t_w) = 1$. This is not a choice of stress units (the unit of stress being set by the yield threshold); rather it represents a numerical constant that can simply be absorbed into the applied strain. Thanks to the normalisation of $\delta P(\sigma, t_w)$, we then have from Eq. (3.9) that

$$1 - G(t, t_w) = \int_{-\infty}^{\infty} \sigma \left(\delta P(\sigma, t_w) - \delta P(\sigma, t) \right) \mathrm{d}\sigma \tag{3.15}$$

which corresponds to the *amount of stress* that has been relaxed up to time t, due to plastic events. We will denote the total (asymptotic) amount of stress the system is

[1] We note for clarity that this special choice of phase is made solely to simplify the expression (3.14), and does not in itself contribute to reducing the oscillations in $G^*(\omega, t, t_w)$. The reduction of oscillations is accomplished by the averaging, and is independent of the choice of phase ϕ.

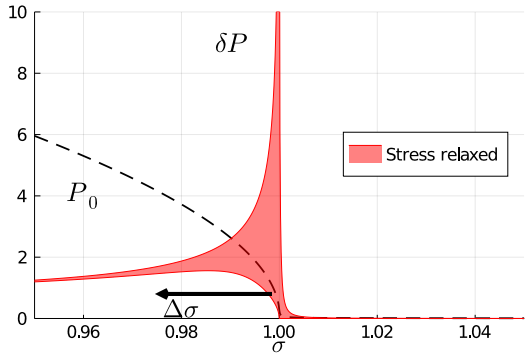

FIGURE 3.2: Sketch displaying the singular behaviours $P_0(\sigma, t_w) \sim (1-\sigma)^{\mu/2}$ and $\delta P(\sigma, t_w) \sim (1-\sigma)^{\mu/2-1}$ for $1-\sigma \ll 1$ (positive boundary layer), in this case for $\mu = 1$. δP decays significantly on the scale $\Delta\sigma$, so that the main contribution to the stress relaxation is the shaded area (the stress is actually the integral of $\sigma\delta P$, but $\sigma \approx 1$ in the relevant region). The negative boundary layer (at $\sigma = -1$, not shown) makes an equal contribution, with both terms in the integral (σ and δP) changing sign. P_0 has been amplified by a factor of 50 for visibility (dashed line).

able to relax as

$$1 - G_\infty(t_w) \equiv 1 - G(t \to \infty, t_w) \tag{3.16}$$

For a system which is able to relax fully, this quantity is thus unity.

The intuition behind our analytical results is given mainly by the following argument. Both in steady state and in aging, after the step strain is applied the relaxation is at first purely confined to two small symmetric regions around the boundaries $\sigma = \pm 1$. The two symmetric boundary layers make an equal contribution to the ensuing stress relaxation, so for the following discussion we focus on the positive boundary layer around $\sigma = 1$, corresponding to $1 - \sigma \ll 1$. In this region, blocks are close enough to instability so that their stress can diffuse across the boundary set by the yield threshold in the short time regime, and a significant decay in $\delta P(\sigma, t)$ takes place. More precisely, up to a time t we expect the diffusion due to mechanical noise to result in a stress scale

$$\Delta\sigma \sim \left(\int_{t_w}^{t} \Gamma(t') \mathrm{d}t' \right)^{H} \tag{3.17}$$

given by the Hurst exponent $H = 1/\mu$, and the corresponding form of the yield rate $\Gamma(t)$. From (3.15), this means that (assuming $\delta P(\sigma, t)$ has decayed enough, see also App. 3.C) the amount of stress relaxed up to time t is essentially given by the integral of the initial condition $\delta P(\sigma, t_w)$ over the range of stress $\Delta\sigma$ below the yield threshold (note that $\sigma \approx 1$ in this range).

We recall that this initial condition is given by the derivative of the unperturbed distribution (3.8). Now, both the unperturbed steady state close to the arrest transition, and the unperturbed aging distribution at long times ($\Gamma(t) \ll 1$), display a pseudogap behaviour $P_0(\sigma, t_w) \sim (1-\sigma)^{\mu/2}$ for $1-\sigma \ll 1$ (see Chapter 2). This means that the initial condition for the stress distribution perturbation has the scaling $\delta P(\sigma, t_w) \sim (1-\sigma)^{\mu/2-1}$ (see Fig. 3.2). To find the amount of stress relaxation, we need to integrate this over the scale $\Delta\sigma$, so that

$$1 - G(t, t_w) \sim \Delta\sigma^{\frac{\mu}{2}} \sim \left(\int_{t_w}^{t} \Gamma(t') \mathrm{d}t' \right)^{\frac{1}{2}} \quad \forall \mu \tag{3.18}$$

Remarkably, then, the exponent $1/2$ relating the amount of stress relaxation to the number of yield events is *universal* across all values of the exponent μ.

The detailed analytical results in the time domain – derived below – are displayed in Table 3.1 and can be related to the intuitive arguments above as follows. In the aging regime, the integral on the right hand side of (3.18) converges to a finite value. The relaxation is therefore confined to a range of stresses near the yield threshold and does not extend to the remainder or "bulk" of the stress distribution at long times. Thus the system is not able to relax the stress caused by the initial shear strain completely; instead the stress decays to a finite plateau.

For the steady state near the arrest transition, where $\Gamma(t) = \Gamma^{ss} \ll 1$, Eq. (3.18) implies an anomalous relaxation $1 - G(\Delta t) \sim \Delta t^{1/2}$ at short times. This eventually gives way to an exponential relaxation characteristic of a Maxwell fluid (see App. 3.A for details). In the case of critical aging, treated in App. 3.B, the relaxation does extend to the bulk at long times but is given by a power-law decay instead of an exponential. Turning to the frequency domain, results for which are displayed in Table 3.2, the ubiquity of the exponent $1/2$ is evident in the behaviour of the loss modulus; as explained below, this simply mirrors the short time behaviour in the time domain.

We saw above that the exponent $H\mu/2 = 1/2$ characterising the relaxation of stresses near the yield threshold is universal, i.e. independent of the exponent μ characterising the noise distribution. Interestingly, this universality can be traced back to a link between exponents of self-affine processes first proposed in [90]. The exponent $\mu/2$ (denoted ϕ in [90]) characterises the behaviour near an absorbing boundary, the yield threshold. This is related to the persistence exponent θ, which describes the algebraic decay $\sim t^{-\theta}$ of the probability of no return to an initial value, through $\theta = H\phi$. The persistence exponent θ, in turn, can be shown via the Sparre-Andersen theorem [91, 92] to take the universal value $\theta = 1/2$ for any random walk with a symmetric jump distribution. This corresponds to the $1/2$ exponent we will find throughout the present analysis, albeit without the interpretation in terms of persistence.

3.4 Aging regime

In the regime $A < A_c(\mu)$, where the system ages, one expects the decaying plastic activity to lead also to an aging linear response, given that there are fewer and fewer rearrangements available to relax the stress caused by the applied step strain. In the following we treat separately the cases $1 < \mu < 2$ and $\mu = 1$, where the yield rate decays respectively as a power law and as a stretched exponential (see also Fig. 3.1). In both cases we will find that because the integral of $\Gamma(t)$, which represents the total number of plastic events that will occur in the system, remains finite then the stress relaxation function decays incompletely from unity to a plateau. On the other hand, the scaling with age of both the plateau and the typical time taken to reach it, which are the main focus of interest of our study, will depend on the exponent μ.

3.4.1 $1 < \mu < 2$

Intuitive argument in time domain

In the regime $1 < \mu < 2$, it was shown in Chapter 2 that at long times the yield rate ages as a power law with exponent $\Gamma(t) \sim t^{-\mu/(\mu-1)}$. We now explore the consequences of this using the same intuitive argument as in Sec. 3.3, referring the reader

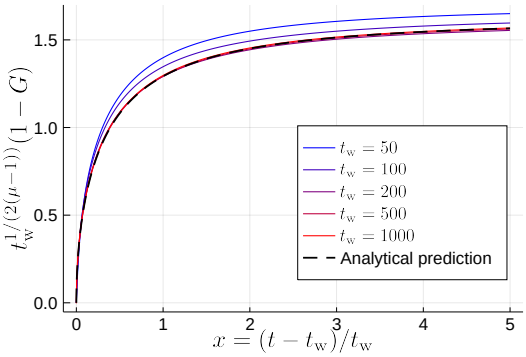

FIGURE 3.3: Stress relaxation obtained from numerically solving the linearised equation (3.7) for $\mu = 1.7$ and $A = 0.15$, starting from initial conditions extracted at different t_w from the unperturbed aging dynamics. The curves collapse following (3.20) and (3.19) for $t_w = 200$ and above.

to Appendix 3.C for a more detailed analysis of the full stress distribution perturbation $\delta P(\sigma, t)$. As already noted in Sec. 3.3, the whole relaxation is now confined to the initial regime around the boundary layers $|\sigma| \approx 1$. Taking into account that $\delta P(\sigma, t_w) \sim (1-\sigma)^{\mu/2-1}$ for large t_w (where $P_0(\sigma, t_w)$ is already close to $Q_0(\sigma)$), we have as before that $1 - G(t, t_w) \sim \Delta\sigma^{\mu/2}$ with $\Delta\sigma = \left(\int_{t_w}^{t} \Gamma(t')\mathrm{d}t'\right)^{1/\mu}$. For waiting times large enough for $\Gamma(t)$ to have entered the asymptotic regime we therefore have that

$$1 - G(t, t_w) \sim \left(\int_{t_w}^{t} \Gamma(t')\mathrm{d}t'\right)^{\frac{1}{2}} \approx c\, t_w^{-\frac{1}{2(\mu-1)}} \sqrt{1 - (1+x)^{-\frac{1}{\mu-1}}} \tag{3.19}$$

with c an initial condition-dependent constant. The dependence on the measurement time t can be expressed entirely via the rescaled time difference $x = (t - t_w)/t_w$, implying *simple aging* where relaxation timescales grow linearly with the age t_w. We also see from (3.19) that the amount of stress relaxation $1 - G$ saturates to a plateau, which we denote as

$$1 - G_\infty(t_w) = c t_w^{-\frac{1}{2(\mu-1)}} \tag{3.20}$$

To check these scaling predictions we compare them to direct numerical solutions of the time evolution (3.7), for the case $\mu = 1.7$, $A = 0.15$. We extract initial conditions $\delta P(\sigma, t_w)$ in Eq. (3.8) from numerics for the unperturbed system [2], at different waiting times t_w. For the shorter waiting times up to $t_w = 200$ we include pre-asymptotic effects by using the full form of $\Gamma(t)$ measured in the unperturbed dynamics before it enters the asymptotic power law (at around $t \simeq 400$), while for longer waiting times we use directly a fit of the asymptotic behaviour of $\Gamma(t)$ [3]. Plotting the resulting stress relaxation $1 - G$ vs $t - t_w$ and rescaling the time axis by t_w and the stress relaxation axis by the appropriate power of t_w from (3.20), we find very good agreement with the asymptotic expression (3.19) for $t_w = 200$ and above (see Fig. 3.3).

[2] Here and in what follows we use, as in Chapter 2, the steady state with $\Gamma = 0.134$ as initial distribution for the unperturbed aging dynamics.

[3] We note that, as discussed in Chapter 2, in the unperturbed numerics the power law asymptote of $\Gamma(t)$ is eventually cut off exponentially by the fact that the required discretization of the σ-axis can no longer resolve the boundary layer.

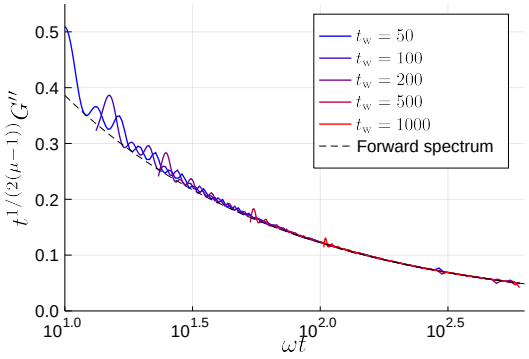

FIGURE 3.4: Loss modulus calculated using the averaged form (3.14) from the stress relaxation at different waiting times for $\mu = 1.7$, $A = 0.15$. We see a good agreement with the forward spectrum (3.21) for large t_w and after enough oscillations.

Frequency domain

As discussed in Sec. 3.3, in aging systems one may in general introduce an age-dependent frequency response $G^*(\omega, t, t_w)$ (3.10), with t the time of measurement. We show in Appendix 3.D that for our model $G^*(\omega, t, t_w)$ does approach the forward spectrum $G_f^*(\omega, t)$ (3.11) in the limits $\omega(t - t_w) \gg 1$, $\omega t \gg 1$ (with $\omega \ll 1$) discussed above in Sec. 3.2. The forward spectrum in turn is found to take the asymptotic form

$$\frac{G_f^*(\omega, t)}{1 - G_\infty(t)} \sim 1 - (1 - i)c \left(\frac{1}{\mu - 1}\right)^{\frac{1}{2}} \sqrt{\frac{\pi}{8}} w^{-\frac{1}{2}} \tag{3.21}$$

where we have defined a rescaled frequency $w \equiv \omega t$, and c is the same initial condition dependent constant as in (3.19).

The two main features of the aging moduli (3.21) directly reflect the behaviour (3.19) in the time domain. Firstly, we see that we need to rescale the magnitude of the moduli by $1 - G_\infty(t)$, which corresponds to the finite total amount of relaxation the system can undergo, and decays in time as the power law given in Eq. (3.20). On the other hand, we find that once the decaying total relaxation is taken into account, the frequency response becomes a function of $w \equiv \omega t$ only. This rescaling reflects the simple aging scaling of the typical relaxation time we found in the time domain.

As discussed in Sec. 3.2, for the purpose of numerically computing the aging frequency response we use the averaged form $\bar{G}^*(\omega, t, t_w)$ given in (3.14). Focussing on the same case $\mu = 1.7$, $A = 0.15$ we fix the frequency to $\omega = 0.1$ and calculate the integrals in (3.14) numerically, inserting directly the asymptotic form in the time domain (3.19) for a range of different waiting times (Fig. 3.4). We choose $m = 1$ (the results are very similar for $m = 2,4$), implying that we are averaging over one period around each observation time t, which we choose in the range from $t_w + \pi/\omega$ to $t_{max} = 6000$. In Fig. 3.4 we show the resulting loss modulus, which indeed approaches the asymptotic behaviour (3.21) for large enough t_w and after enough oscillations.

3.4.2 $\mu = 1$

Stress relaxation function

In the marginal case $\mu = 1$, it was found in Sec 2.6 that for a system relaxing in the glassy phase the yield rate decays at long times as a stretched exponential $\Gamma(t) \sim e^{-B\sqrt{t}}$, with a constant B that depends on the initial condition. Following again the scaling argument (3.18) for the relaxation within the boundary layer, we have in this case that

$$\begin{aligned} \frac{1-G(t,t_\mathrm{w})}{1-G_\infty(t_\mathrm{w})} &\equiv H(x,t_\mathrm{w}) \\ &= \left(1-e^{-B(\sqrt{t_\mathrm{w}+x\sqrt{t_\mathrm{w}}}-\sqrt{t_\mathrm{w}})}\frac{1+B\sqrt{t_\mathrm{w}+x\sqrt{t_\mathrm{w}}}}{1+B\sqrt{t_\mathrm{w}}}\right)^{1/2} \\ &\simeq \sqrt{1-e^{-Bx/2}} \quad \text{for} \quad t_\mathrm{w} \gg 1 \end{aligned} \tag{3.22}$$

where the rescaled time difference is now $x \equiv (t-t_\mathrm{w})/\sqrt{t_\mathrm{w}}$, and the value $1-G_\infty(t_\mathrm{w})$ at which the amount of stress relaxation saturates is

$$1-G_\infty(t_\mathrm{w}) = ce^{-\frac{B}{2}\sqrt{t_\mathrm{w}}}\left(B\sqrt{t_\mathrm{w}}+1\right)^{1/2} \tag{3.23}$$

with c again an initial condition dependent constant.

The case $\mu = 1$, therefore, no longer follows simple aging, and we find instead a square root scaling $x = (t-t_\mathrm{w})/\sqrt{t_\mathrm{w}}$ of the relaxation times with age. This scaling, as well as the large t_w expression for $1-G$ in the last line of Eq. (3.22), may be found alternatively by linearising the stretched exponential decay of $\Gamma(t)$ around t_w in the expression for the stress relaxation, i.e.

$$\begin{aligned} 1-G &\sim \left(\int_{t_\mathrm{w}}^{t} \mathrm{d}t'\, e^{-B\sqrt{t'}}\right)^{\frac{1}{2}} \simeq \left(\int_{t_\mathrm{w}}^{t} \mathrm{d}t'\, e^{-B\left(\sqrt{t_\mathrm{w}}+\frac{t'-t_\mathrm{w}}{2\sqrt{t_\mathrm{w}}}\right)}\right)^{\frac{1}{2}} \\ &\simeq (1-G_\infty(t_\mathrm{w}))\sqrt{1-e^{-Bx/2}} \end{aligned} \tag{3.24}$$

In Fig. 3.5 we compare again with numerical results from Eq. (3.7), for the case $\mu = 1$, $A = 0.55$. The value of B is fitted from the unperturbed dynamics, which in this case enters the asymptotic regime already for $t \gtrsim 20$ so that we do not see appreciable pre-asymptotic effects [4], and we study a range of waiting times from $t_\mathrm{w} = 20$ to 100. We find essentially perfect agreement with the finite-t_w form (3.22), which approaches the asymptotic expression (3.24) as t_w increases.

Frequency domain

To investigate the aging frequency response, we proceed as in the case $1 < \mu < 2$. The aging moduli again approach the forward spectrum, which is now given by (see Appendix 3.D),

$$\frac{G_f^*(\omega,t)}{1-G_\infty(t)} \sim 1-(1-i)c\sqrt{\frac{B}{2}}\sqrt{\frac{\pi}{8}}w^{-\frac{1}{2}} \tag{3.25}$$

with a rescaled frequency $w = \omega t^{1/2}$.

[4] As done above for $\mu = 1.7$, we extrapolate the asymptote of $\Gamma(t)$ to later times than we had access to in the unperturbed numerics, due to the same discretisation limit described there (the boundary layer becoming even harder to resolve for $\mu = 1$).

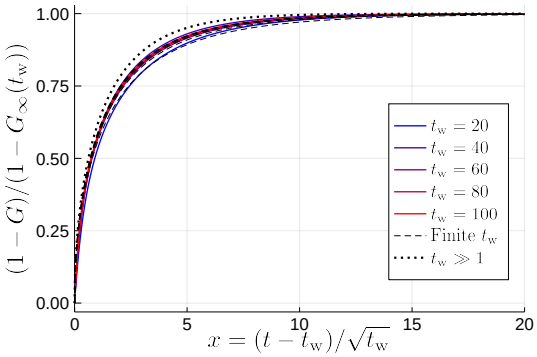

FIGURE 3.5: Stress relaxation obtained from numerically solving the linearised equation (3.7) for $\mu = 1$ and $A = 0.55$, starting from initial conditions extracted at different t_w from the unperturbed aging dynamics. With the appropriate rescalings, the curves are indistinguishable from the finite-t_w prediction $H(x, t_w)$ (3.22), which approaches the asymptotic expression (3.24) for $t_w \to \infty$ (dotted line).

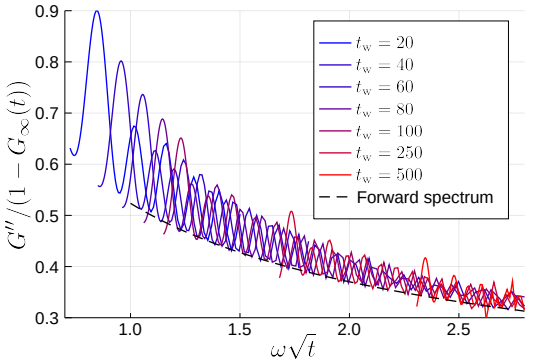

FIGURE 3.6: Loss modulus calculated using the averaged form (3.14) from the stress relaxation at different waiting times for $\mu = 1$, $A = 0.55$. The forward spectrum (3.25) is approached for large t_w and after enough oscillations.

Again, as for $\mu > 1$, the aging frequency-dependent moduli directly reflect the behaviour (3.22) in the time domain. It is important to note that although (3.25) and (3.21) look similar, the rescaled frequency w is different in the two cases. The shared $w^{-1/2}$ behaviour is a genuine commonality, on the other hand, stemming as it does from the universality discussed in Sec. 3.3.

Finally, we numerically compute the aging frequency response, using again the averaged form (3.14), for the case $\mu = 1$, $A = 0.55$ considered above. We choose $m = 1$, so that we average over one period around the observation time. In contrast to the case $1 < \mu < 2$, where results were independent of m (for $m = 2, 4$), here the averaging is sensitive to m due to the rapidly decaying magnitude $1 - G_\infty(t)$, which leads to a bias in the results for larger m. For $m = 1$, we see in Fig. 3.6 that the loss modulus does indeed approach the asymptotic form (3.25) after enough oscillations.

3.5 (Weakly) Non-linear behaviour ($\mu = 1$)

We next study numerically the non-linear response to step strain of the model. This will allow us to check that the linear theory developed so far does indeed hold for $\gamma_0 \ll 1$, and will also shed light on the extent of this linear regime. Furthermore, the

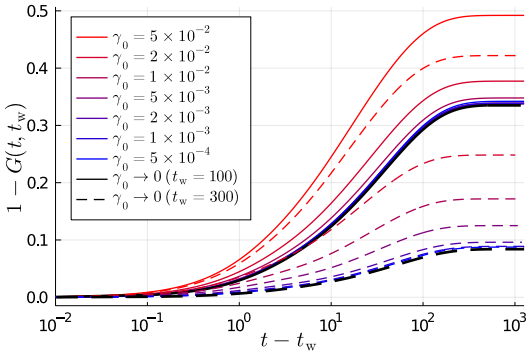

FIGURE 3.7: Stress relaxation following a step strain applied at $t_w = 100$ (full lines) and $t_w = 300$ (dashed lines), obtained from evolving the full master equation (3.1), for step strains γ_0 ranging from 5×10^{-2} (red) down to 5×10^{-4} (blue). This is compared with the relaxation obtained from the linearised equation (3.7). For $t_w = 100$ one finds agreement for $\gamma_0 \lessapprox 10^{-2}$; for $t_w = 300$, on the other hand, agreement with the linear theory holds only for $\gamma_0 \lessapprox 2 \times 10^{-3}$.

predictions we will obtain for the non-linear effects will in themselves be interesting for the comparison to the MD data in Sec. 3.6.

The non-linear, strain and age-dependent response function to a step strain $\gamma_0\,\theta(t - t_w)$ is written as

$$\sigma(t) = \gamma_0 G(t, t_w; \gamma_0) \tag{3.26}$$

which defines the nonlinear stress relaxation function $G(t, t_w; \gamma_0)$. In order for our discussion to be relevant also to the MD simulations presented in Sec. 3.6 we focus on $\mu = 1$, with a slightly higher value of the coupling ($A = 0.58$) than the one shown in Fig. 3.5. This provides us with a wider time range (up to around $t = 400$) in which to study aging properties before the yield rate becomes too small to resolve numerically.

We now consider a range of waiting times within this asymptotic regime, and study the non-linear response to a range of step strains. To do this, we now evolve the *full* master equation (3.1) after application of a step strain. In our discrete numerical setup, this amounts to shifting the initial distribution $P_0(\sigma, t_w)$ by a number of grid points $\gamma_0/\Delta\sigma$, where $\Delta\sigma$ is the stress discretisation. The smallest step amplitude we can reliably explore is then some small multiple of $\Delta\sigma$, in our case $\gamma_0 = 5 \times 10^{-4}$ (corresponding to $4\,\Delta\sigma$). Importantly, in the ensuing dynamics $\Gamma(t)$ is *perturbed* by the strain, in contrast to the linear theory where $\Gamma(t) = \Gamma_0(t)$.

In Fig. 3.7 we show the non-linear response function for a range of strains $\gamma_0 \in (5 \times 10^{-4}, 5 \times 10^{-2})$, for two waiting times $t_w = 100$ and $t_w = 300$. On the same plot, we display also the prediction from the linear theory for each t_w, evaluated by solving Eq. (3.7) using as input the unperturbed $\Gamma_0(t)$. One notices first that for both waiting times, the smallest step strain amplitudes do indeed give a response function that matches the prediction of the linear theory. However, we see clearly that for the later waiting time more of the strain step values deviate from linear response. In other words, the extent of the linear regime shrinks considerably at later waiting times. To study this more in detail, we take the measured asymptotic relaxations for each t_w and interpolate them to obtain $1 - G_\infty(t_w; \gamma_0)$ as a function of γ_0 (see Fig. 3.21 in Appendix 3.F). From here we identify the linear regime as extending up to $\gamma_{\max}(t_w)$, which we define by setting a threshold (10 %) on the relative deviation of the amount of stress relaxation with respect to the linear value;

fixing a threshold for the relative deviations of the plateaus $G_\infty(t_w, \gamma_0)$ themselves leads to similar results. A naive expectation for the scaling of $\gamma_{max}(t_w)$ would be to consider the initial perturbation to the yield rate caused by the step strain, which (see below) is of order $\sim \gamma_0^{1+\mu/2} = \gamma_0^{3/2}$. For the linear regime one then expects the condition $\gamma_0^{3/2} \ll \Gamma(t_w)$ and hence the scaling $\gamma_{max}(t_w) \sim (\Gamma(t_w))^{2/3}$. In Fig. 3.22 in Appendix 3.F we show that the measured $\gamma_{max}(t_w)$ agrees well with this prediction.

We now proceed to study the non-linear effects on the total amount of relaxation at long times, and on the temporal evolution of the rescaled relaxation function, which we recall saturates at this final value. In Sec. 3.4 we derived analytical expressions for the linear response limit of both of these quantities, given in (3.23) and (3.22), respectively.

Starting with the plateau at which the relaxation saturates, we first need to point out a qualitative difference in the non-linear case. For finite γ_0, there is now a non-zero stress relaxation even for $t_w \to \infty$, where the stress distribution is frozen and all blocks are stable, so that $G_\infty(t_w \to \infty; \gamma_0) < 1$. To account for this, in Fig. 3.8 we rescale the plateau values by the $t_w \to \infty$ plateau, so that we plot $1 - G_\infty(t_w; \gamma_0)/G_\infty(t_w \to \infty; \gamma_0)$, which by construction does decay to zero with increasing t_w for all γ_0. As expected, the values from the linear regime agree well with the prediction (3.23), using for B the value B_0 extracted from the unperturbed numerics $\Gamma_0 \sim e^{-B_0\sqrt{t}}$. Surprisingly, we see that also the data for non-linear γ_0 (shown are four values up to $\gamma_0 = 5 \times 10^{-3}$) are well described by the expression (3.23), but with a higher "effective" value of B that we denote B_{eff}. B_{eff} increases with γ_0, implying that the final plateau value for $t_w \to \infty$ is approached already at shorter waiting times for larger step strains.

The final plateau value and the corresponding stress relaxation $1 - G_\infty(t_w \to \infty; \gamma_0)$ are purely non-linear features, because in the linear theory $\Gamma_0(t_w \to \infty) = 0$ and no more relaxation takes place. We can construct a lower bound on $1 - G_\infty(t_w \to \infty; \gamma_0)$ in the following way. Neglecting the effect of stress redistribution, which can trigger additional yield events, we can consider the proportion of blocks that are made unstable by the initial step strain γ_0. These lie in the stress interval $\sigma \in (1 - \gamma_0, 1)$. The distribution $P_0(\sigma, t_w)$ behaves as $P_0 \sim q_0(1 - \sigma)^{\mu/2}$ for $\sigma \lesssim 1$, giving to leading order in γ_0 a stress relaxation

$$1 - G_\infty(t_w \to \infty; \gamma_0) \gtrsim q_0 \frac{1}{1 + \mu/2} \gamma_0^{\mu/2} \tag{3.27}$$

The same argument also shows that the perturbation to the yield rate is $\sim \gamma_0^{1+\mu/2}$, as given above. Our data do indeed lie above this lower bound, and approach it as $\gamma_0 \to 0$ (see Fig. 3.23 in Appendix 3.F).

Finally, we turn to the temporal evolution of the relaxation function. We show this in Fig. 3.9 for $t_w = 300$ and the same four values of γ_0 as above, along with the linear response. In each case we rescale the stress by the final plateau value, and the time as $x = (t - t_w)/\sqrt{t_w}$. In this representation, the linear response indeed follows the expression (3.22) for $H(x, t_w)$ derived in Sec. 3.4, with the same value of B_0. Interestingly, even the non-linear relaxations can be fitted very well by the same expression (3.22), but (as for the plateau decay) with a higher B_{eff} value, which again increases for larger γ_0 so that larger step strains accelerate the dynamics. We note that, unlike in the linear theory, in the non-linear case the $B_{eff}(\gamma_0)$ values inferred from the plateau decays do not necessarily have to describe also the full dynamics. For later waiting times (as is the case shown in Fig. 3.9), however, we find that the

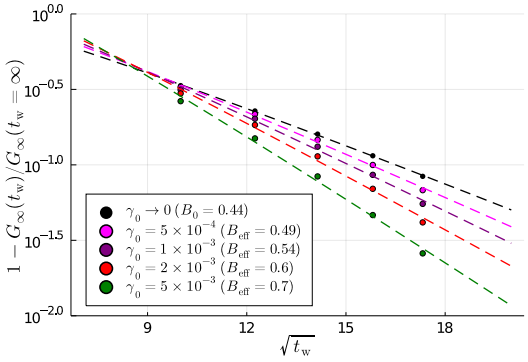

FIGURE 3.8: Plateau modulus values $G_\infty(t_w; \gamma_0)$ extracted from the non-linear step strain numerics at different waiting times, rescaled by the $t_w \to \infty$ modulus for each γ_0. Dashed lines show the analytical expression (3.23), with a fitted value $B_{eff}(\gamma_0)$ that grows for larger step strain.

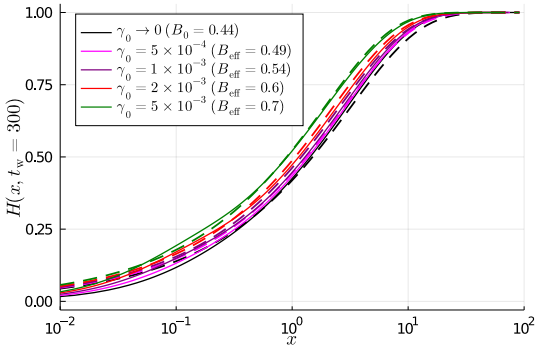

FIGURE 3.9: Stress relaxation at $t_w = 300$ for different γ_0, rescaled in each case by the final amount of relaxation. The time axis is rescaled to $x = (t - t_w)/\sqrt{t_w}$. Dashed lines show the finite-t_w expression for the stress relaxation (3.22), using the values $B_{eff}(\gamma_0)$ extracted from Fig. 3.8.

same $B_{eff}(\gamma_0)$ values fitted from the plateau decays do in fact provide a good fit for the full time evolution at each step strain γ_0.

Summarising, we have found that the extent of the linear regime shrinks considerably at later waiting times. However, we have also found that even in the (weakly) non-linear case, both the plateau decay and the stress dynamics are still well described by the linear theory through (3.23) and (3.22), but with effective constants $B_{eff}(\gamma_0) > B_0$. We therefore see that the application of non-linear step strains effectively leads to faster dynamics. The same effect will be observed in the MD simulations discussed in the following section.

3.6 Comparison with MD simulations

We now compare our mean field prediction to molecular dynamics simulations of a model athermal solid, carried out by Dr. Rituparno Mandal. For this we consider a bidisperse assembly of soft harmonic spheres at high packing fraction, immersed in an effective solvent. This model has been used widely in the literature [39], and is considered an appropriate description of, for example, dense emulsions, foams or microgels suspensions comprising droplets, bubbles or particles of typical radius

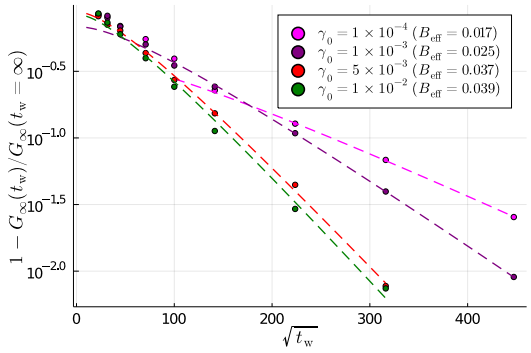

FIGURE 3.10: Plateau modulus values $G_\infty(t_{\rm w};\gamma_0)$ extracted from the MD simulation, rescaled by the $t_{\rm w} \to \infty$ modulus for each γ_0. Dashed lines show the analytical expression (3.23), with a fitted value $B_{\rm eff}(\gamma_0)$ that grows with increasing step strain.

$R \gtrsim 1\mu m$, in the athermal regime [38]. Neglecting inertia and explicit hydrodynamic interactions, the *unperturbed* dynamics of the system, starting from an initial condition with significant overlap between the spheres, is simply a gradient descent in the energy landscape. This dissipative dynamics was studied in [38] (see also [84]), where it was shown to present a slow (power–law) decay of the energy and velocity, which was referred to as *athermal aging*. Here we study the linear response of the system to a step strain at different waiting times $t_{\rm w}$ during this aging process; further simulation details may be found in Appendix 3.E.

An important difference in the particle system is that even mechanically stable (frozen) system configurations, which are reached for $t_{\rm w} \to \infty$ (in our simulations, this limit is reached at $t_{\rm w} \approx 5 \times 10^5$) show a finite stress relaxation; see Fig. 3.20 in App. 3.E. In fact, for any $t_{\rm w}$ there is always a non-affine relaxation, simply due to the particles recovering a state of force balance after the application of the step strain [21]. This does not involve any plastic yielding at small strain and so is not accounted for within our elastoplastic description (see more in the discussion). To be able to compare with our theory, we therefore need to factor out this non-affine relaxation and focus only on the relaxation due to plastic events.

In the case of the plateau values, which we consider first, this is taken care of automatically by proceeding as in the evaluation of the theory (Fig. 3.8): we rescale by the $t_{\rm w} = \infty$ relaxation, considering again $1 - G_\infty(t_{\rm w},\gamma_0)/G_\infty(t_{\rm w} = \infty,\gamma_0)$ for various values of the step strain (see Fig. 3.10). For all γ_0 we fit the analytical form (3.23), extracting an effective value of B in each case. We see that, on the one hand, the data agree well with the (modulated) stretched exponential form (3.23) in all cases; on the other hand, we find the same trend as in mean field, with the effective B increasing with the strain γ_0.

We next turn to the full temporal dynamics of the stress relaxation function. Here, we need firstly to account for the $t_{\rm w} = \infty$ relaxation, which we assume is purely due to the non-affine part. We denote this as $G^{\rm na}(\Delta t)$, formally defined as $\lim_{t_{\rm w}\to\infty} G(t_{\rm w} + \Delta t, t_{\rm w})$. We then consider the ratio between the full stress relaxation function and the contribution from the non-affinity:

$$G^{\rm pl}(t,t_{\rm w}) \equiv \frac{G(t,t_{\rm w})}{G^{\rm na}(t-t_{\rm w})} \tag{3.28}$$

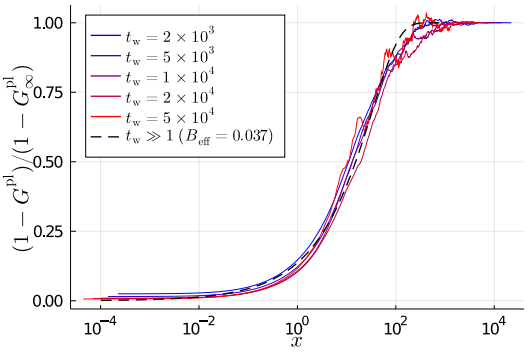

FIGURE 3.11: Plastic stress relaxation in the MD simulation with $\gamma_0 = 5 \times 10^{-3}$ for different waiting times, obtained by applying (3.28). The time axis is rescaled to $x = (t - t_{\rm w})/\sqrt{t_{\rm w}}$. Dashed line shows the $t_{\rm w} \gg 1$ expression for the stress relaxation (3.22), evaluated using $B = B_{\rm eff}(\gamma_0)$ extracted from the plateau values (Fig. 3.10).

so that for an infinitely aged system, $G^{\rm pl} = 1$ and the response is purely elastic as in our mean field model.

We show the result for $\gamma_0 = 5 \times 10^{-3}$ in Fig. 3.11. For the plot we rescale $1 - G^{\rm pl}(t, t_{\rm w})$ by the asymptotic plastic relaxation $1 - G^{\rm pl}_\infty(t_{\rm w})$ corresponding to each $t_{\rm w}$, in order to compare with the rescaled form (3.22) of the theoretical prediction, which we recall varies from 0 to 1. We find a very good collapse of the curves by rescaling the time axis as $(t - t_{\rm w})/\sqrt{t_{\rm w}}$. More importantly, the asymptotic form of (3.22) for large $t_{\rm w}$ fits excellently the data, *with* the corresponding value of B fitted from the plateau decay (Fig. 3.10).

Overall, figures 3.10 and 3.11 point to a good agreement with the theory for $\mu = 1$. We show here only the temporal data for $\gamma_0 = 5 \times 10^{-3}$, obtained by averaging over $N_{\rm rep} = 128$ repetitions. For the smaller step strains, at large waiting times, even with $N_{\rm rep} = 1024$ the numerical signal is not clear enough to study the full stress relaxation up to our largest $t_{\rm w}$. For $\gamma_0 = 10^{-3}$ we nonetheless find a similar collapse to Fig. 3.11, with the corresponding value of $B_{\rm eff}$ from Fig. 3.10, at least up to $t_{\rm w} = 2 \times 10^4$. This supports the expectation that the results in Fig. 3.11 should also be representative of the behaviour for smaller step strain values, the only difference being the slightly slower dynamics (smaller B).

3.7 Summary

In this chapter we have studied the aging linear shear response within the framework of a mean field elastoplastic model of amorphous solids, introduced in Chapter 2. The main feature of this model was the incorporation of mechanical noise due to stress propagation, which was argued to be power-law distributed with exponent μ. Here, we have obtained analytically the long-time form of the aging step response $G(t, t_{\rm w})$ for the different values of μ, along with the aging frequency response; these are summarised in Tables 3.1 and 3.2. In the aging regime we found that the stress relaxes incompletely to an age-dependent plateau, on a timescale which grows with material age. Regarding the scaling behaviours, we found, firstly, that key scaling exponents are universal and independent of the noise exponent μ. For $\mu > 1$, we then found that the stress relaxation timescale scales linearly with the age $t_{\rm w}$ of the material, corresponding to simple aging. At $\mu = 1$, which corresponds to interactions mediated by the physical elastic propagator, we found instead a $t_{\rm w}^{1/2}$ scaling

arising from the stretched exponential decay of the plastic activity. The theoretical predictions for $\mu = 1$ were then compared against data from MD simulations of a model athermal system in its aging regime, finding good correspondence with the theory. In the discussion (Chapter 5), we discuss the theoretical results in the context of other aging phenomena, and comment further on the comparison to the MD simulation and to possible experiments.

An important feature of glasses/amorphous solids, as presented in Chapter 1, is the complex disordered potential energy landscape. In particular, also on the level of mesoscopic blocks this implies a distribution of local energy minima which the local element may inhabit. This feature has not been included so far in Chapters 2 and 3, where we recall the model is characterised by a *single* value of the local yield barrier σ_c. In the next chapter, we will see that including disorder in the local yield barriers σ_c, or equivalently the landscape of local energy minima, will be crucial to understand the behaviour under oscillatory shear. This includes the athermal relaxation behaviour under cycles of shear, referred to as mechanical annealing, where we will see that local elements will be able to access deeper and deeper regions of the landscape. The separate question of whether the inclusion of disorder could be important for our results in Chapters 2 and 3 will be treated further in the final discussion (Chapter 5).

	Scaling variable	$1 - G_\infty(t_w)$	Stress response
Aging $1 < \mu \leq 2$	$x = \frac{t-t_w}{t_w}$	$ct_w^{-\frac{1}{2(\mu-1)}}$	$\frac{1-G(x)}{1-G_\infty(t_w)} = \sqrt{1-(1+x)^{-\frac{1}{\mu-1}}}$
Aging $\mu = 1$	$x = \frac{t-t_w}{\sqrt{t_w}}$	$ce^{-B\sqrt{t_w}/2} \times \sqrt{B\sqrt{t_w}+1}$	$\frac{1-G(x)}{1-G_\infty(t_w)} \sim \sqrt{1-e^{-Bx/2}}$
Fluid Near AT, $\forall\mu$	$\Delta t = t - t_w$	1	Short time: $1 - G(\Delta t) \sim \Delta t^{1/2}$ Long time: $G(\Delta t) \sim e^{-\Delta t/\tau}$
Critical aging $\forall\mu$	$x = \frac{t-t_w}{t_w}$	1	Short time: $1 - G(x) \sim \sqrt{\ln(1+x)}$ Long time: $G(x) \sim x^{-1/\mu}$

TABLE 3.1: Summary of analytical results in the time domain. The total amount of relaxation (second column) is defined by (3.16); c is an initial condition-dependent constant. The fluid state approaching the arrest transition (AT) (for $A \gtrsim A_c$), and the critical aging case (for $A = A_c$), are treated in Appendices 3.A and 3.B respectively, where the short and long time regimes are properly defined. Note that the stress response at short times follows in all cases $1 - G \sim x^{1/2}$ in the corresponding scaling variable, reflecting the universal $1/2$ exponent discussed in Sec. 3.3.

3.A Steady state linear response approaching the arrest transition

We first consider here the linear response in the steady state regime, where as explained in Sec. 3.2 we expect TTI to hold. We discuss first the HL case ($\mu = 2$), where insight may be gained through analytical arguments. Although some expressions for

	Scaling variable	Loss modulus
Aging $1 < \mu \leq 2$	$w = \omega t$	$\frac{G''(w)}{1-G_\infty(t)} \sim \left(\frac{1}{\mu-1}\right)^{1/2} \sqrt{\frac{\pi}{8}} w^{-1/2}$
Aging $\mu = 1$	$w = \omega\sqrt{t}$	$\frac{G''(w)}{1-G_\infty(t)} \sim \left(\frac{B}{2}\right)^{1/2} \sqrt{\frac{\pi}{8}} w^{-1/2}$

TABLE 3.2: Analytical results for the aging frequency response. The asymptotic expressions hold for $\omega(t - t_w) \gg 1, \omega t \gg 1$ (with $\omega \ll 1$), as detailed in the text. Although the scaling variables are different, we note the common exponent $-1/2$, which is simply a consequence of the universal behaviour in the short time regime.

the steady state linear frequency response are provided in the original paper [37], we focus here on the critical behaviour approaching the arrest transition. As α_c is approached from above, the diffusive dynamics of the local stress becomes more and more sluggish with the yield rate disappearing quadratically as $\Gamma^{ss} \sim (\alpha - \alpha_c)^2$ [66] (see also Sec. 2.5), meaning there are fewer plastic rearrangements to fluidise the system. In the limit where $\Gamma^{ss} \to 0$, one may replace the yielding term in equation (3.7) by absorbing boundary conditions at $\sigma = \pm 1$. One can then map the problem to that of a diffusing particle in a box (as discussed in Sec. 2.5), which can be solved by the technique of separation of variables. Given the antisymmetry of $\delta P(\sigma, t)$ described in Sec. 3.2, the solution is given by the asymmetric eigenmodes. Rescaling the time difference (we recall $\Delta t = t - t_w$) by the yield rate as $\Delta\tilde{t} = \Delta t\, \Gamma$, we find

$$G(\Delta\tilde{t}) = \frac{8}{\pi^2} \sum_{m,\text{odd}} \frac{1}{m^2} e^{-\alpha m^2 \pi^2 \Delta\tilde{t}} \tag{3.29}$$

This stress relaxation function separates into two different relaxation regimes. This is shown in Figs. 3.12 and 3.13 where, along with the exact limiting form (3.29), we plot the results of numerically integrating equation (3.7) for values of Γ^{ss} between 10^{-2} and 10^{-5}, starting from the steady state and using a pseudospectral method (for details see Appendix 2.E.1). At long times the relaxation is dominated by the slowest asymmetric eigenmode with absorbing boundary conditions, whose eigenvalue we write as $\lambda_1^{(2)}$ for $\mu = 2$. For $\Delta\tilde{t} \gg \tilde{\tau}$ with $\tilde{\tau} = 1/(\alpha\lambda_1^{(2)}) \approx 2/\pi^2$ one then finds an exponential relaxation (Fig. 3.12). On the other hand, in the short time regime $\Gamma \ll \Delta\tilde{t} \ll \tilde{\tau}$, we find that $1 - G(\Delta\tilde{t}) \sim (\Delta\tilde{t})^{1/2}$ (Fig. 3.13), reflecting the singular behaviour of the summation (3.29).

Looking next at the viscoelastic behaviour for $\mu = 2$ in the frequency domain, we know from Eq. (3.29) that with a rescaled frequency $\tilde{\omega} = \omega/\Gamma$, the viscoelastic moduli in the limit $\Gamma \to 0$ are given by

$$\begin{aligned} G^*(\tilde{\omega}) &= G'(\tilde{\omega}) + iG''(\tilde{\omega}) \\ &= 8 \sum_{m,\text{odd}} \frac{1}{\alpha^2 m^4 \pi^4 + \tilde{\omega}^2} \left(\frac{\tilde{\omega}^2}{\pi^2 m^2} + i\alpha\tilde{\omega} \right) \end{aligned} \tag{3.30}$$

Reflecting the behaviour in the time domain, this results in a loss modulus $G''(\tilde{\omega})$ peaked at $\tilde{\omega} \sim \tilde{\tau}^{-1}$, with a non-Maxwellian behaviour $G''(\tilde{\omega}) \sim \tilde{\omega}^{-1/2}$ (as mentioned in [37]) for $\tilde{\tau}^{-1} < \tilde{\omega} < 1/\Gamma$ (see dotted line in Fig. 3.14). The same power law in this range of frequencies also appears in the elastic modulus as $1 - G'(\tilde{\omega}) \sim$

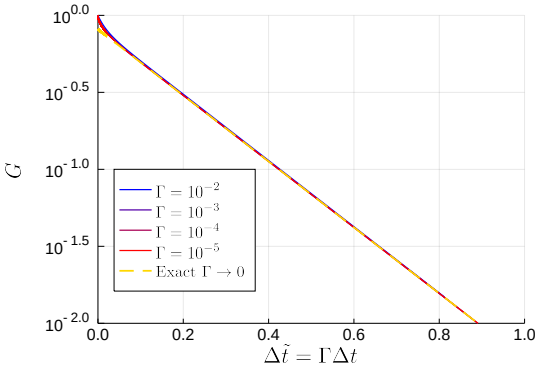

FIGURE 3.12: Stress relaxation in the long time regime in the HL model, for the steady state approaching the arrest transition ($\Gamma^{ss} \ll 1$). For $\Delta\tilde{t} \gg 2/\pi^2$, we find an exponential relaxation, purely dominated by the first term in the summation (3.29).

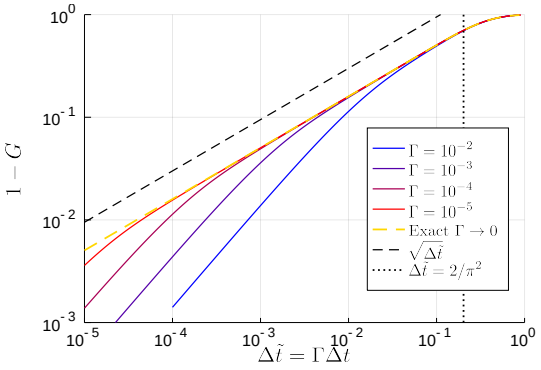

FIGURE 3.13: Same data as in Fig. 3.12, but plotted in the short time regime. For $\Gamma \ll \Delta\tilde{t} \ll \tilde{\tau}$, we see the development of a power-law regime $1 - G \sim (\Delta\tilde{t})^{1/2}$, as predicted from the analytical form (3.29) for $\Gamma \to 0$.

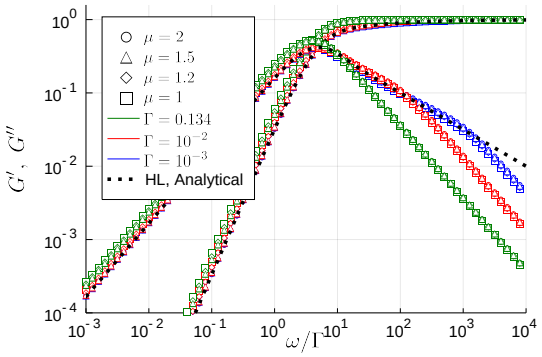

FIGURE 3.14: Viscoelastic moduli in steady state for different values of μ and Γ^{ss}, obtained via spectral decomposition of the corresponding operator. The moduli are collapsed by rescaling the frequency as $\tilde{\omega} = \omega/\Gamma$. Dotted lines show the analytical predictions for G' and G'' as $\Gamma^{ss} \to 0$ in the HL model (3.30).

$\tilde{\omega}^{-1/2}$.

We now turn to study other values of the noise exponent $0 < \mu < 2$. For convenience we do this in the frequency domain, where, instead of solving each time the PDE (3.7), we can compute the viscoelastic spectrum directly by diagonalising a discretised form [79] of the operator on the right of (3.7); for details see Appendix 2.E.2. The results are shown in Figure 3.14, where we consider values of $\Gamma^{ss} = 0.134$, 10^{-2} and 10^{-3} and consider a range of different μ.

The surprising and a priori unexpected result in Fig. 3.14 is that the moduli show the same form also for $\mu < 2$, with the same power law $G''(\tilde{\omega}) \sim \tilde{\omega}^{-1/2}$ for the loss modulus. With hindsight this simply mirrors the behaviour in the short time regime, which as argued in Sec. 3.3 turns out to have the universal form $1 - G(\Delta t) \sim \Delta t^{1/2}$ for all μ.

3.B Critical aging

We consider for completeness the special case of a relaxation at precisely the critical value of the coupling $A = A_c$ (or $\alpha = \alpha_c$ in the HL model), which we refer to as critical aging. As discussed briefly in Sec. 2.6, one finds from the analysis for $1 \leq \mu \leq 2$ that the yield rate decays as $\Gamma(t) \sim 1/t$, irrespective of the value of μ. For the short time regime (Fig. 3.15), following the same arguments as in Sec. 3.3, this implies an initial relaxation – arising from stress diffusion near the yield threshold – growing as $1 - G(t, t_w) \sim \left(\int_{t_w}^{t} \Gamma(t')dt'\right)^{1/2}$. This can be written in terms of the scaling variable $x = (t - t_w)/t_w$, so that one has simple aging and

$$1 - G \sim \sqrt{\ln(1 + x)} \quad \text{for} \quad x \ll 1 \tag{3.31}$$

For the yield rate at criticality, one expects that in fact the prefactor of the asymptotic behaviour $\Gamma(t) \sim d_1(\mu)/t$ will be initial condition independent for a given μ, given that the total number of yield events (given by the integral of $\Gamma(t)$) diverges and so all memory of the initial condition is lost. In fact, as we will show now for the HL model, this prefactor is related to the lowest asymmetric eigenvalue $\lambda_1^{(\mu)}$ of the μ-dependent propagator with absorbing boundary conditions at $|\sigma| = 1$, by the relation $d_1(\mu) = 1/(\mu\lambda_1^{(\mu)})$. The boundary conditions are non-local for $\mu < 2$, i.e.

must be imposed for all $|\sigma| > 1$ [78]; the eigenvalue $\lambda_1^{(\mu)}$ is defined in Eq. (3.38) below.

In the HL case $\mu = 2$, we can show this link on the basis of the scaling analysis in [71]. For the case of a relaxation at $\alpha = \alpha_c$, the exponent parameters in [71] take the values $l = 1$ and $s = 2$. The frozen-in distribution, on the other hand, acquires a simple form composed of two line segments, $Q_0(\sigma) = 1 - |\sigma|$. The leading order corrections in the interior ($|\sigma| < 1$) and in the exterior ($|\sigma| > 1$; where the right and left exterior tails are symmetric, we write only the right one, i.e. $\sigma > 1$) are given by

$$P(\sigma, t) = Q_0(\sigma) + t^{-\frac{1}{2}} Q_1(\sigma) \quad |\sigma| < 1 \tag{3.32}$$

$$P(\sigma, t) = t^{-\frac{1}{2}} R_1(z) \quad \sigma > 1 \tag{3.33}$$

with $z = t^{1/2}(\sigma - 1)$. Continuity of the distribution and its derivative imply the boundary conditions

$$Q_1(1) = R_1(0) \tag{3.34}$$

$$\partial_\sigma Q_0(1) = \partial_z R_1(0) = -1 \tag{3.35}$$

We consider now the master equation (2.11) in the exterior, with $\alpha = \alpha_c = 1/2$ and $\Gamma(t) = d_1/t$. Applying also the boundary condition (3.35), we have that $R_1(z) = \sqrt{d_1} e^{-z/\sqrt{d_1}}$. From the master equation in the interior, we find that

$$\partial_\sigma^2 Q_1(\sigma) + \lambda Q_1(\sigma) = 0 \tag{3.36}$$

where $\lambda \equiv 1/(2d_1)$. The boundary condition (3.34) implies that $Q_1(-1) = Q_1(1) = \sqrt{d_1}$. Furthermore, normalisation of $P(\sigma, t)$ requires that $\int Q_1 \mathrm{d}\sigma = 0$, so that integration of (3.36) yields $\partial_\sigma Q_1(-1) = \partial_\sigma Q_1(1)$. Altogether, Eq. (3.36) and the boundary conditions imply that $\lambda = m^2\pi^2$, $m \in \mathbb{N}$. Given that we are dealing with the first correction, we expect $m = 1$ so that $\lambda = \lambda_1^{(2)}$, and therefore $d_1 = 1/(2\lambda_1^{(2)})$. For $1 \leq \mu < 2$ the leading order correction scales as $P = Q_0 + t^{-1/\mu} Q_1$, so that one expects $d_1 = 1/(\mu \lambda_1^{(\mu)})$ from the same analysis. We confirm this only numerically as a full derivation would be difficult due to the presence of non-local boundary conditions.

We now show how the prefactor $d_1(\mu)$ leads to the long-time difference ($x \gg 1$) scaling of the stress relaxation function $G(x) \sim x^{-1/\mu}$. The perturbation $\delta P(\sigma, t)$ follows the dynamics (3.7), which in the interior reads

$$\partial_t \delta P(\sigma, t) = \frac{d_1(\mu)}{t} \int_{\sigma - \delta\sigma_\mathrm{u}}^{\sigma + \delta\sigma_\mathrm{u}} \frac{\delta P(\sigma', t) - \delta P(\sigma, t)}{|\sigma - \sigma'|^{1+\mu}} \mathrm{d}\sigma' \tag{3.37}$$

At long times we expect (as in the case $A > A_c$ in Appendix 3.A) the stress profile to be dominated by the slowest asymmetric eigenmode $\psi_1(\sigma)$, so that $\delta P(\sigma, t \gg 1) \approx f(t)\psi_1(\sigma)$ where $\psi_1(\sigma)$ satisfies

$$\int_{\sigma - \delta\sigma_\mathrm{u}}^{\sigma + \delta\sigma_\mathrm{u}} \frac{\psi_1(\sigma') - \psi_1(\sigma)}{|\sigma - \sigma'|^{1+\mu}} \mathrm{d}\sigma' = -\lambda_1^{(\mu)} \psi_1(\sigma) \tag{3.38}$$

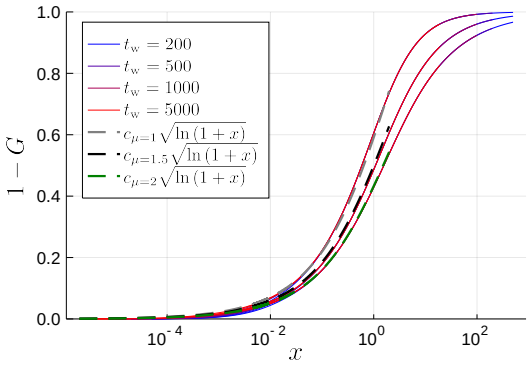

FIGURE 3.15: Stress relaxation in the short time regime for the critical aging case $A = A_c(\mu)$ (for $\mu = 2$, $\alpha = \alpha_c$), found by numerically solving (3.7), with initial conditions obtained from the unperturbed dynamics. Curves for different t_w collapse essentially on top of each other when plotted against the rescaled time difference $x = (t - t_w)/t_w$, following (3.31); c_μ is a μ-dependent prefactor.

with $\psi_1(\sigma) = 0 \; \forall \; |\sigma| > 1$, i.e. absorbing boundary conditions. Inserting the ansatz into (3.37), we find using $d_1(\mu)\lambda_1^{(\mu)} = 1/\mu$

$$\frac{\partial \ln f}{\partial \ln t} = -\frac{1}{\mu} \tag{3.39}$$

so that $\delta P(\sigma, t) \simeq \psi_1(\sigma) t^{-1/\mu}$ at long times. Considering (from the short time regime) that we have simple aging, this implies $G(x) \sim x^{-1/\mu}$ in the long time regime as claimed.

In Figs. 3.15 and 3.16 we show stress relaxation functions obtained for a range of t_w, for a system relaxing at $A_c(\mu)$ from an initial distribution with enough unstable blocks at $t = 0$. We then evolve Eq. (3.7) to find the aging stress relaxation function. For $x \gg 1$, we see from Fig. 3.16 that indeed $G(x) \sim x^{-1/\mu}$. Interestingly, a power-law stress relaxation was also found at the jamming transition point in the particle simulations of [93], with a critical behaviour $G(t) \sim t^{-1/2}$ (which would be recovered for $\mu = 2$). It is important, however, to note that in [93] the step response is studied starting from initial conditions that have already fully relaxed to mechanical equilibrium (via an energy minimization algorithm), whereas here we are considering the stress response during the physical relaxation process towards this inherent state.

3.C Scaling of $\delta P(\sigma, t)$

We give more details here regarding the scaling of the stress distribution perturbation $\delta P(\sigma, t)$ that leads to the result (3.19) for the stress relaxation function. First of all, as in Sec. 3.3 we may write Eq. (3.9) as

$$1 - G(t, t_w) = \int_{-\infty}^{\infty} \sigma \left(\delta P(\sigma, t_w) - \delta P(\sigma, t) \right) \mathrm{d}\sigma \tag{3.40}$$

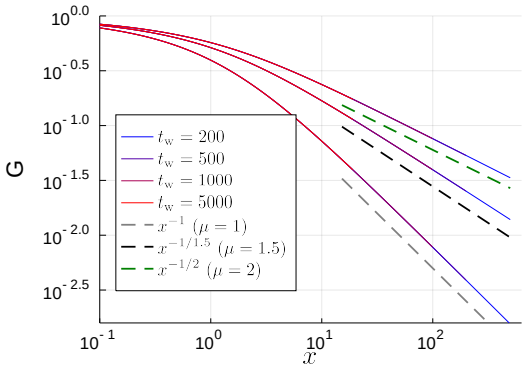

FIGURE 3.16: Same as Fig. 3.15, but in the long time regime. For $x \gg 1$, the curves follow the predicted power-law relaxation with μ-dependent exponent $G(x) \sim x^{-1/\mu}$.

In the aging regime, $\delta P(\sigma, t)$ is practically frozen in the interior[5] $|\sigma| < 1$ away from $\sigma = 1$, while the relaxation in the exterior tails $|\sigma| > 1$ will be shown below to be sub-leading. The leading contribution to the integral (3.40) will come from two symmetric interior boundary layers, on the left and the right. Focusing on the positive one at $\sigma = 1$, we introduce as a division between interior and boundary layer a fixed stress interval ϵ such that $\Delta\sigma(t_w, x) \ll \epsilon \ll 1$, $\forall t_w, x$, where $\Delta\sigma(t_w, x)$ is the width of the interior boundary layer at time $t = t_w(1 + x)$ for a perturbation applied at t_w. The leading contribution to (3.40) will then be given by

$$1 - G \simeq 2 \int_{1-\epsilon}^{1} \sigma \left(\delta P(\sigma, t_w) - \delta P(\sigma, t) \right) \mathrm{d}\sigma \tag{3.41}$$

One expects the difference $\delta P(\sigma, t_w) - \delta P(\sigma, t)$ to become a scaling function of the width $\Delta\sigma$ within the interior boundary layer. In addition, given that $\delta P(\sigma, t)$ drops significantly within this layer, one expects the height of the function itself to scale as $\Delta\sigma^{\mu/2-1}$, which is inherited from the height of the initial distribution at $\sigma \sim 1 - \Delta\sigma$; recall that the initial condition of the perturbation scales as $\delta P(\sigma, t_w) \sim (1 - \sigma)^{\mu/2-1}$ near the boundary. We then have that

$$\begin{aligned} 1 - G &\simeq 2(\Delta\sigma)^{\mu/2-1} \int_{1-\epsilon}^{1} \sigma f\left(\frac{1-\sigma}{\Delta\sigma} \right) \mathrm{d}\sigma \\ &= (\Delta\sigma)^{\mu/2} 2 \int_0^{\frac{\epsilon}{\Delta\sigma}} f(z) \mathrm{d}z - (\Delta\sigma)^{\mu/2+1} 2 \int_0^{\frac{\epsilon}{\Delta\sigma}} z f(z) \mathrm{d}z \end{aligned} \tag{3.42}$$

where we performed the change of variable $z = (1 - \sigma)/\Delta\sigma)$. As $\Delta\sigma \ll \epsilon$, the ϵ-dependence in the integrals disappears and we are left with $1 - G \simeq (\Delta\sigma)^{\mu/2}$ to leading order, confirming the result (3.19) given above. In Fig. 3.17, we check for various values of t_w and x (with $\mu = 1.7$, $A = 0.15$ as in Fig. 3.3) the above scaling of $\delta P(\sigma, t)$ in the interior boundary layer, finding a very good collapse.

Finally, we show that the exterior tail contribution to the integral (3.40) is indeed sub-leading. We find that, as in the HL model [71], at a fixed value of x the exterior tails of $\delta P(\sigma, t)$ may be collapsed by rescaling their width and the height by appropriate powers of t_w. For the σ-axis, we know already that the distribution $\delta P(\sigma, t_w)$ inherits the scaling of the boundary layer in the unperturbed dynamics. There it

[5] There is, potentially, a contribution from relaxation around the origin $\sigma = 0$, but we have checked numerically that this gives a sub-leading contribution.

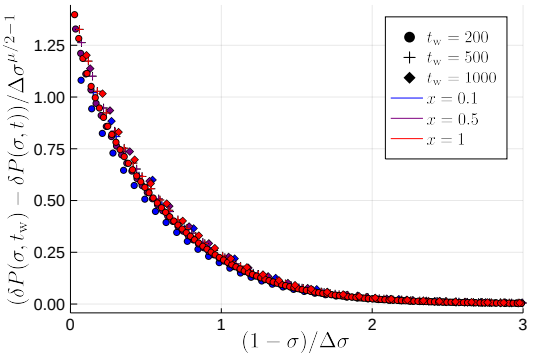

FIGURE 3.17: Decay of the linear perturbation $\delta P(\sigma, t)$ in the interior boundary layer. Data is for the same case ($\mu = 1.7$, $A = 0.15$) as shown in Sec. 3.4. Symbols show different t_w (shapes) at different $x = (t - t_w)/t_w$ (colors), which all collapse as detailed in the text.

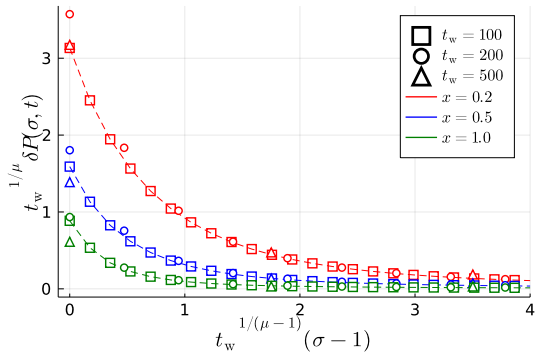

FIGURE 3.18: Decay of the external tail of $\delta P(\sigma, t)$, again for $\mu = 1.7$, $A = 0.15$. Symbols show different t_w (shapes) at different $x = (t - t_w)/t_w$ (colors), which all collapse as detailed in the text.

was shown (Sec. 2.6) that $\Gamma \sim t^{-\mu/(\mu-1)}$, while the boundary layer width scaled as $\Gamma^{1/\mu}$, so that we expect the exterior tail to have a width that evolves with x on a scale $\mathcal{O}(t_w^{-1/(\mu-1)})$. Turning now to the scaling of the height of the tail $\delta P(\sigma, t)$, we find numerically that the boundary value $\delta P(1, t)$, decays as a power law $(t - t_w)^{-1/\mu}$ beyond time differences of order unity $t - t_w > \mathcal{O}(1)$, i.e. $x > \mathcal{O}(t_w^{-1})$, leading to a height evolving with x on a scale $t_w^{-1/\mu}$. This is confirmed numerically in Fig. 3.18 for various values of t_w and x, again running the dynamics with $\mu = 1.7$, $A = 0.15$. Overall, these scalings imply that the contribution from the exterior tail is indeed sub-leading, given that it is of order $t_w^{-1/(\mu-1)-1/\mu}$, which is small compared to $\Delta\sigma^{\mu/2} = \mathcal{O}(t_w^{-1/(2(\mu-1))})$. This holds also as we approach the marginal case $\mu \to 1$, as the (negative) exponent of the leading contribution is smaller by a factor of 2.

3.D Forward spectrum

In this appendix we provide details on the derivation of the asymptotic forms (3.21) and (3.25) of the forward spectrum defined in Eq. (3.11), and discuss how the full t_w-dependent aging spectrum (3.10) approaches this limit.

We consider first the case $1 < \mu < 2$, and assume t_w is large enough for expression (3.19) to hold, that is we take

$$G(t, t_w) = 1 - c t_w^{-\frac{1}{2(\mu-1)}} \sqrt{1 - (1+x)^{-\frac{1}{\mu-1}}} \tag{3.43}$$

with $x = (t - t_w)/t_w$. We now insert this expression into (3.10). Following [71], we introduce the new variables $w \equiv \omega t$ and $w' \equiv \omega(t - t_w)$. After some algebra, (3.10) can be rewritten as

$$G^*(\omega, t, t_w) = 1 - \frac{c}{t^{\frac{1}{2(\mu-1)}}} \left(\sqrt{(1+x)^{\frac{1}{\mu-1}} - 1}\, e^{-iw\frac{x}{1+x}} + i \int_0^{w\frac{x}{1+x}} \mathrm{d}w' \sqrt{\left(1 - \frac{w'}{w}\right)^{-\frac{1}{\mu-1}} - 1}\, e^{-iw'} \right) \tag{3.44}$$

The forward spectrum (3.11), on the other hand, can be written with the change of variable $w' = \omega(t - t')$ as

$$G_f^*(\omega, t) = 1 - \frac{c}{t^{\frac{1}{2(\mu-1)}}} i \int_0^\infty \mathrm{d}w' \sqrt{1 - \left(1 + \frac{w'}{w}\right)^{-\frac{1}{\mu-1}}}\, e^{-iw'} \tag{3.45}$$

We now take the limits $w \equiv \omega t \gg 1$ and $w\frac{x}{1+x} = \omega(t - t_w) \gg 1$ in (3.44), following [71]. As shown there, the first term in brackets of (3.44) can be included into the integral over w', with a constant integrand for $w' > wx/(1+x)$. As we take the limit $wx/(1+x) \gg 1$ we are left only with the integral up to infinity of the second term in brackets, which in addition for $w \gg 1$ converges to the forward spectrum (3.45).

To find the asymptotic form (3.21) given in the main text one can exploit the large w-limit imposed above to simplify further. In (3.45), one can then expand the argument in the square root as

$$f\left(\frac{w'}{w}\right) = \sqrt{1 - \left(1 + \frac{w'}{w}\right)^{-\frac{1}{\mu-1}}} = \sqrt{\frac{1}{\mu - 1}} \sqrt{\frac{w'}{w}} + \mathcal{O}\left(\frac{w'}{w}\right) \tag{3.46}$$

which leads to the form (3.21) in the main text.

One can proceed similarly for the case $\mu = 1$, and show that the aging moduli (3.10) approach the forward spectrum (3.11), where now the required limits are $\omega(t - t_w) \gg 1$ and $w \equiv \omega\sqrt{t} \gg 1$. To compute this forward spectrum, we consider t_w large enough for (3.24) to hold, that is

$$G(t, t_w) = (1 - G_\infty(t_w))\sqrt{1 - e^{-B\frac{x}{2}}} \tag{3.47}$$

with $x = (t - t_w)/\sqrt{t_w}$. We insert this into (3.11) and obtain

$$G_f(\omega, t) = 1 - (1 - G_\infty(t)) i \int_0^\infty \mathrm{d}w' \sqrt{1 - e^{-\frac{Bw'}{2w}}}\, e^{-iw'} \tag{3.48}$$

where we performed the change of variables $w' = \omega(t - t')$, and the rescaled frequency is $w \equiv \omega\sqrt{t}$. As was done for $1 < \mu < 2$ above, we now expand the square root as

$$f\left(\frac{w'}{w}\right) = \sqrt{1 - e^{-\frac{Bw'}{2w}}} = \sqrt{\frac{B}{2}} \sqrt{\frac{w'}{w}} + \mathcal{O}\left(\frac{w'}{w}\right) \tag{3.49}$$

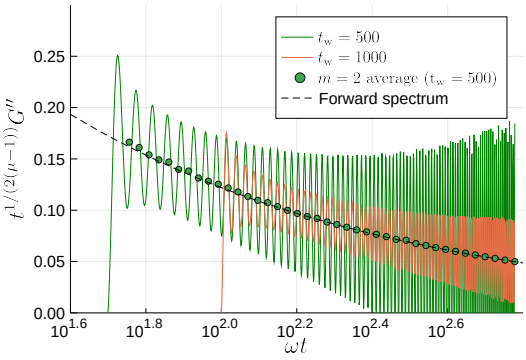

FIGURE 3.19: Comparison of the aging frequency response G^* computed directly from (3.10), with the averaged form $\bar{G}^*$ (3.14) (here averaged over $m = 2$ periods), which cancels the oscillations (circles). Dashed line shows the forward spectrum (3.21). The growth of the oscillations for large w is due to numerical instabilities in the oscillatory integral. Model parameter values as in Figs. 3.3 and 3.4.

where we have considered again $w \gg 1$. From here it is straightforward to derive expression (3.25) in the main text.

Finally, in Fig. 3.19 (for the case $\mu = 1.7$ and $A = 0.15$ considered in the main text) we compare the averaged form $\bar{G}^*(\omega, t, t_w)$ computed from (3.14) with $G^*(\omega, t, t_w)$ calculated directly from (3.10). Without the averaging, one sees that $G^*(\omega, t, t_w)$ does still approach the forward spectrum at long times, but presents oscillations around the asymptote with frequency ω. As discussed in the main text and visible in the figure, the averaging cancels these oscillations and the asymptotic form is approached sooner. We note that the growing oscillations for small t_w are a numerical artifact due to the highly oscillating integrals.

3.E Details of MD simulations

For comparison with the predictions derived from the mean field theory, we consider MD simulations (carried out by Dr. Rituparno Mandal) using a model dense athermal solid (Sec. 3.6). Here we summarize the model system and the simulation protocol.

We consider particles interacting via a pairwise repulsive harmonic potential $V_{ij}(r) = \frac{1}{2}kR^3\left(1 - r/D_{ij}\right)^2\theta\left(D_{ij} - r\right)$, where r is the distance between particle i and j. The system is bidisperse, with particles of radii R and $1.4R$ in equal number, and $D_{ij} = R_i + R_j$. Such a bidisperse mixture helps to avoid crystallisation at high area fractions. Neglecting explicit hydrodynamic interactions, and in the absence of inertia, the *unperturbed* dynamics of this system is simply a gradient descent in the energy landscape

$$\frac{\mathrm{d}\mathbf{r}_i}{\mathrm{d}t} = -\frac{1}{\zeta}\sum_{j\neq i}\frac{\partial V\left(|\mathbf{r}_i - \mathbf{r}_j|\right)}{\partial \mathbf{r}_i} \tag{3.50}$$

where $\mathbf{r}_i$ is the position vector of the i th particle and ζ is the drag coefficient. By setting $k = R = \zeta = 1$ we set the timescale $\zeta/(kR) = 1$ in all the simulation results presented here. We implement the simulation in 2d, using $N = 40000$ particles compressed to area fraction $\phi = 1$.

In the simulation we first quench the system from $T = \infty$ to $T = 0$ and then allow it to relax athermally towards a force balanced inherent state. During this

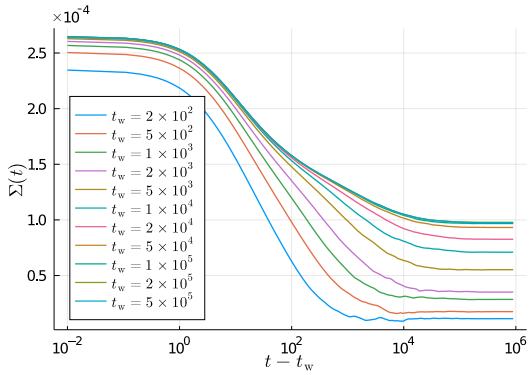

FIGURE 3.20: Full stress relaxation measured in the MD simulations for step strain $\gamma_0 = 5 \times 10^{-3}$, at different waiting times t_w during the unperturbed relaxation.

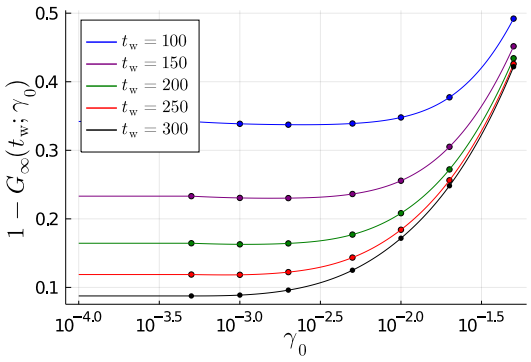

FIGURE 3.21: Total amount of stress relaxation for different step strain amplitudes and waiting times. The deviation from the linear response plateau values on the left occurs at smaller step strains as t_w increases. Lines show cubic spline interpolations as guides to the eye.

athermal aging process we collect samples that are aged up to time t_w. We then implement a single step strain of amplitude γ_0 and measure the relaxation of the shear stress $\Sigma(t)$ for a time $\sim 10^6$. This time evolution happens in the presence of Lees-Edwards periodic boundary conditions [94] implementing the fixed strain, and using an adaptive Euler algorithm as deployed in [38].

Simulation results for $\gamma_0 = 5 \times 10^{-3}$ are shown in Fig. 3.20. These are obtained by averaging over an ensemble of $N_{rep} = 128$ realizations of the random ($T = \infty$) initial condition; data for the smaller step strains shown in the paper are obtained with $N_{rep} = 1280$. For each realization we subtract the stress fluctuations of the unstrained $\gamma_0 = 0$ dynamics, which are due to the finite size. Note the non-affine stress relaxation present even for $t_w \to \infty$, as detailed in the main text.

3.F Non-linear effects

We show here three supplementary figures accompanying Sec. 3.5. In Fig. 3.21, we exemplify how we interpolate the measured plateau values to obtain the full $1 - G_\infty(t_w; \gamma_0)$ curve for each t_w. This is then used to determine $\gamma_{max}(t_w)$, which we recall was defined by setting a 10% threshold on the relative deviation of this curve with respect to the linear plateau for $\gamma_0 \to 0$.

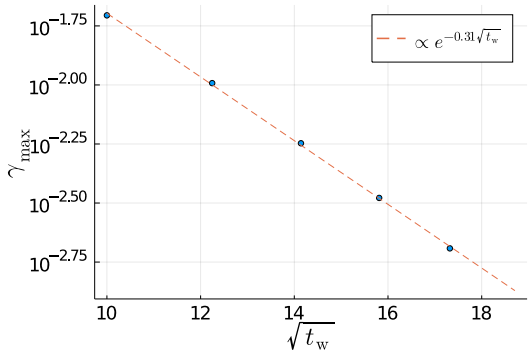

FIGURE 3.22: $\gamma_{\max}(t_w)$, obtained by fixing a 10 % threshold on the relative deviation of the amount of stress relaxed from the corresponding linear response value for each t_w. The data agree well with a stretched exponential fit, where the fitted value of the decay constant ~ 0.31 is close to the theoretical prediction $(2/3)B_0$, which for $B_0 = 0.44$ would be 0.293.

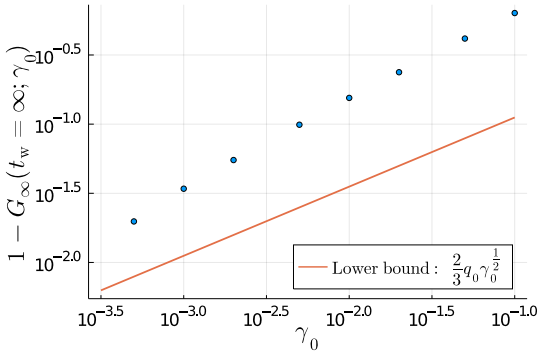

FIGURE 3.23: Amount of stress relaxation in the frozen $t_w \to \infty$ state, for the step strain values considered in Fig. 3.7. Solid line shows the lower bound (3.27) derived in the main text.

Fig. 3.22 shows the $\gamma_{\max}(t_w)$ values determined in the aforementioned fashion. The decay for increasing t_w, which leads to a narrowing of the linear response regime, roughly follows the prediction $\gamma_{\max}(t_w) \sim (\Gamma(t_w))^{2/3}$.

Finally, Fig. 3.23 concerns the relaxation for $t_w \to \infty$, which we recall is a purely non-linear feature of the theory that disappears for $\gamma_0 \to 0$. In Fig. 3.23 we check that the amount of relaxation in the frozen state, $1 - G_\infty(t_w \to \infty; \gamma_0)$, indeed lies above the lower bound derived in the paper, and approaches it for decreasing γ_0.

Chapter 4

Mean field theory of yielding under oscillatory shear

Most of the following chapter, except for the whole of App. 4.G and parts of Sections 4.1, 4.3, 4.6 and 4.7, has been reproduced from the published paper [3] and its associated supplemental material.

4.1 Introduction

As introduced in Chapter 1, amorphous solids typically show yielding behaviour: although they behave elastically at small deformation, plastic deformation eventually sets in, leading to a flowing state. Given the large variety of amorphous solids, ranging from hard metallic glasses to soft colloidal gels or emulsions, a unified description is desirable from a statistical physics point of view. Elastoplastic models have here led to important advances [13], as they keep only key ingredients of the deformation dynamics common to all these systems.

A key aspect of yielding under uniform shear, which has received much attention recently [34, 58–63], concerns the dependence on the initial degree of annealing – quantified by potential energy – of the amorphous solid (or "glass" for short) before deformation starts. Typically, it is found that poorly annealed glasses yield in a smooth, ductile manner, with plastic deformation appearing gradually, while well annealed glasses may yield in a brittle manner, accompanied by a macroscopic stress drop. Under startup of steady shear, there is strong evidence that, at least in the brittle case, and under quasistatic loading, yielding corresponds to a discontinuous non-equilibrium transition, which in finite-dimensional systems is accompanied by the sudden appearance of a unique system-spanning shear band [59–62, 95]. Some features are however still debated, in particular regarding the existence or not of a well-defined ductile to brittle transition as the initial degree of annealing is varied [34]. A clear answer to this is difficulted by very strong finite-size effects [96].

Yielding under oscillatory shear has until recently received less attention, although it may in some respects be a more informative protocol than the uniform case. One advantage is that one may probe directly the steady state after many cycles both below and above the yield point, whereas in the uniform case the states up to yielding are inherently transient. Furthermore, oscillatory strain allows one to relate macroscopic yielding directly to a sharp absorbing-to-diffusive transition in the nature of the microscopic trajectories [97–101].

Behaviour under oscillatory shear also shows intriguing dependencies on the initial degree of annealing. Atomistic simulations of model glasses [49–51] reveal the appearance of a threshold initial energy. Samples prepared above this threshold show mechanical annealing up to a common strain amplitude, the yield point,

where the energy achieves the threshold value irrespectively of the initial condition. On approaching the yield point in strain, the timescale to anneal to the threshold energy appears to diverge [97, 99–101]. On the other hand, samples prepared below the threshold are insensitive to shear up to an initial condition-dependent critical strain amplitude *above the common yield point*, where they then yield abruptly. Below, we will mostly compare our predictions with the simulations of [49]. These present the advantage that not only quasistatic shear, but also finite shear rates are considered, which as discussed below will be useful to elucidate the role of shear banding. The finite shear-rate protocol is simply implemented by overdamped Langevin dynamics [49]. As for the MD simulations in Chapter 3, the time unit (defining the shear rate) in the particle model is simply set by the dissipation timescale $\xi a^2/\epsilon$, with ξ the damping coefficient against the solvent, ϵ the energy scale of the interaction and a the typical particle size.[1] In the athermal regime, the Péclet number is infinite, and the assumption is that other relaxation processes are negligibly slow compared to the times/strains studied.

Recent attempts to tackle this problem include include energy landscape based [102, 103] and 2D lattice elastoplastic models [104, 105]. The model studied in [103] can in some sense be thought of as the initial motivation for our approach. We present briefly the main features of this model.[2] As we will see below, it can be partly recovered as a special limit ($\alpha \to 0$, i.e. no interactions) of our mean field model. The starting point is to consider the dynamics of a single "mesostate", corresponding to a mesoscopic block of material which can undergo a plastic rearrangement, see Chapter 1. Athermal dynamics under shear is considered, such that the block first loads elastically in a parabolic energy minimum of depth E. Once the local strain reaches the limit of stability $\sqrt{2E}$ (we fix the elastic modulus to $k = 1$, setting energy units), the block jumps to a new minimum whose depth is extracted from a Gaussian $\rho(E) \sim e^{-E^2/(2\sigma^2)}$ [103]. Clearly, under this athermal dynamics, if a minimum with depth $E > 2\gamma_0^2$ is reached then the block remains trapped forever.

If one nonetheless looks at the dynamics at a finite number of cycles N_{cycl}, behaviour reminiscent of the yielding transition is observed. Moreover, the dependence on the initial energy of the blocks shows similar features to the MD simulations, with the appearance of a threshold [103]. However, these are just transient effects, and indeed there is no genuine yielding transition. The behaviour at finite cycles can be understood from the scaling of the Gaussian $\rho(E)$ [103]. After one cycle, assuming the dynamics isn't trapped, the energy distribution is well approximated by $\sim \sqrt{E}e^{-E^2/(2\sigma^2)}$, referred to as the "invariant" distribution. From here, the probability of getting trapped after one cycle is given by $\sim e^{-\gamma_0^4/(2\sigma^2)}/\gamma_0$. "Yielding" at fixed N_{cycl} can then be defined by setting some threshold on the probability to not be trapped after N_{cycl}, giving the scaling $\gamma_0^* \sim \left(\ln N_{\text{cycl}}\right)^{1/4}$ for the yield point, which grows only very weakly with N_{cycl}. It was already suggested in the same work [103] that interactions between many mesoscopic blocks in a macroscopic sample could lead to a sharp transition. This is indeed what we will show in Sec. 4.3 below.

In the later work of [106], an Ehrenfest-type model was also introduced along these lines. The dynamics of a mesoscopic block is modeled there as a nearest-neighbour Markov chain, with $2N + 1$ states of energy $\epsilon_k = k/2N$, $k = 0, 1, \ldots N$. The transition rules from ϵ_k to ϵ_{k+1} are chosen as in an Ehrenfest urn model, with

[1] The model glass former of [49] is polydisperse, so the typical particle size is taken as the average over the polydispersity.

[2] We will use for this the notation adopted for our mean field model. In particular, in [103] there is a factor of $1/2$ in front of the elastic modulus which needs to be accounted for.

k the number of balls (out of $2N$) in one of two urns. At each step, one of the $2N$ balls is chosen uniformly at random and is transferred to the other urn. The reason for this choice of stochastic dynamics is that the Ehrenfest model has a well-known invariant measure, namely the binomial, which was argued to be representative of the invariant distribution found in [103]. However, this dynamics is clearly far from capturing the intricacies of oscillatory shear. Also, although a "yielding" transition is found, this relies on introducing (by hand) a simplified form of mechanical noise which does not stem from the interactions. Finally, one may argue that the Ehrenfest-model description in this case is somewhat pathological: indeed, when the continuum limit of the discretely spaced energy levels is taken ($N \to \infty$), the invariant measure (whose width $\sim 1/\sqrt{N}$) collapses, which is not what one would expect to happen in a system with disorder.

Turning to the lattice elastoplastic models [104, 105], these defy analytical progress as they implement the full spatial interaction kernel. We discuss briefly the differences between [104] and [105].

Ref. [104] may in some sense be considered as a 2D lattice version of the mean field model with local disorder which we study below.[3] Given that it incorporates the spatial propagator, it can additionally shed light on the formation/propagation of shear bands (also referred to as strain localisation). In [105], on the other hand, no local disorder is included, but a different approach to conventional EP models is adopted which sheds light on other interesting phenomena. After each event the plastic strain is incremented by an integer value [4] $\Delta\epsilon_p = 2$, and the strain field dynamics is purely deterministic given an initial condition. This set-up allows to study "reversible" plasticity. In AQS MD simulations [99], it was found that below the yield point the dynamics settles into so-called n-cycles, where the material returns to its initial configurations after n cycles of shear. The number of cycles needed to reach this limiting periodic orbit diverges as the yield point is approached, and the period of these cycles grows. The model of [105] sheds light on these non-trivial limit cycles with reversible plasticity, and reproduces some of the features above. In our mean-field model, this is something we will not have access to, given that after a transition the new energy minimum will be extracted independently from a distribution $\rho(E)$, and will thus be uncorrelated to the previous one. Both shear banding and the issue of limit cycles will be treated further in the discussion (Chapter 5).

In this chapter, we will consider a model with a similar single element description to [103, 104] that accounts for the disordered energy landscape, while including the elastic interactions in a mean field manner that allows for analytical progress. Importantly, we find a steady state yielding transition and are able to reproduce qualitatively all the main features of yielding under oscillatory shear described above.

The chapter is structured as follows. In Sec.4.2 we introduce the disordered HL model, highlighting the difference to the original version, which (like the model considered in Chapters 2 and 3) considers a single uniform local yield barrier throughout the material. In Sec. 4.3, we work out the transition line under oscillatory shear, which involves two steps: finding the limiting yield rate and then determining the limiting distribution. In Sec. 4.4 we numerically investigate the dependence on the initial degree of annealing, and the behaviour below, close to, and above the yield point. In Sec. 4.5 we specialise to well-annealed samples, which show fatigue-like

[3] The local disorder is however implemented rather differently: in [104] the new energy minimum is extracted from a triangular distribution.

[4] This value is fixed by the geometry of concatenated parabolas, if the yield strain/stress is set to unity.

behaviour. In Sec. 4.6, we discuss the relation to brittle yielding under uniform shear. Finally, in Sec. 4.7 we provide a summary of the chapter.

4.2 Disordered HL model

The Hébraud-Lequeux (HL) model for the rheology of amorphous solids [37] is a mean field mesoscopic elastoplastic model, which despite its many idealisations has had remarkable successes and been widely studied [64–69]. The material is conceptually divided into mesoscopic elements, large enough to carry a local elastic strain l and stress $\sigma = k\, l$; these are related by an elastic modulus k that is considered to be uniform throughout the system for simplicity. In the elastoplastic approach, the dynamics of the elements is described as consisting of periods of elastic loading interrupted by plastic events that are accompanied by a local stress drop. In a mean field fashion, the effect of stress propagation from other yield events is considered as a mechanical noise [13, 66], leading to a diffusive dynamics in the local strain l (or equivalently the stress).

In the original HL model [37], all elements have a common strain threshold related to the common yield energy E as $l_c = \sqrt{2E/k}$. However, due to the oversimplification of considering one single energy barrier throughout the system, this model is unable to capture the rich phenomenology under oscillatory shear found in particle simulations, for which it is essential to take into account the full energy landscape each mesoscopic element has access to.

An extension of the HL model to include this energy landscape, following previous approaches such as the SGR model [36], was introduced in [66]. The essential ingredient is the disorder in the depth E of the energy minima relative to a common reference energy, characterised by a distribution $\rho(E)$. Each time an element yields, it occupies a new local minimum with a depth extracted from this distribution. The depth E of the current local energy minimum is thus promoted to a stochastic variable, and the system is described by a joint distribution $P(E, l)$ evolving as

$$\partial_t P(E,l,t) = -\dot\gamma \partial_l P + D(t) k^{-2} \partial_l^2 P + Y(t)\rho(E)\delta(l) - \tau_{\rm pl}^{-1}\theta(|l| - \sqrt{2E/k})P \tag{4.1}$$

with

$$Y(t) = \frac{1}{\tau_{\rm pl}} \int_0^\infty {\rm d}E \int_{-\infty}^{\infty} {\rm d}l\; P(E,l,t)\; \theta\left(|l| - \sqrt{\frac{2E}{k}}\right) \tag{4.2}$$

Here $\tau_{\rm pl}^{-1}$, the plastic rate, is the rate at which a plastic event occurs once an element is strained beyond its yield threshold. We fix energy and time units by setting $k = 1$ and $\tau_{\rm pl} = 1$. The quantity $Y(t)$ in (4.2) is the *yield rate*, i.e. the fraction of elements that yield per unit time.[5] The key feature of the model is the *closure relation* relating the yield rate to the diffusion constant $D(t)$. We adopt the simple proportionality $D(t) = \alpha Y(t)$ [37]. In App. 4.F we check that a more general form, which reflects the fact that yield events contribute differently to the noise depending on their local barrier, leaves the theory essentially unchanged, with only slight quantitative changes in the transient behaviour.

After its introduction in [66], the approach described by Eqs. (4.1, 4.2) has not been developed further as it is somewhat unwieldy to tackle analytically; in particular it has not been used to study oscillatory shear. Our first contribution will be to

[5] We note that in this chapter we will use the notation $Y(t)$ for the yield rate, instead of the convention $\Gamma(t)$ used in Chapters 2 and 3.

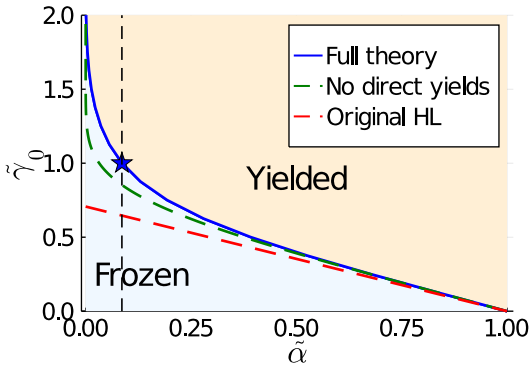

FIGURE 4.1: Phase diagram of the model in the $\tilde{\alpha} - \tilde{\gamma}_0$ plane for a Gaussian $\rho(E)$. Vertical dashed lines indicate the fixed coupling value $\tilde{\alpha} = 0.086$, where $\tilde{\gamma}_0^* = 1$ (see star), chosen for studying the initial annealing dependence.

determine a dynamical transition in Eq. (4.1) under oscillatory shear, separating a frozen elastically-deforming solid state from a yielded state.

4.3 Transition line

We consider applying oscillatory shear $\gamma(t) = \gamma_0 \sin(\omega t)$ in (4.1), with a fixed low frequency $\omega \ll 1$ so that we are in the quasistatic regime. The two control parameters are thus the strain amplitude γ_0 and the coupling constant α. For convenience, we introduce the rescaled versions $\tilde{\gamma}_0 = \gamma_0/\sqrt{\langle E \rangle}$ and $\tilde{\alpha} = \alpha/\langle E \rangle$, $\langle E \rangle$ being the average over the disorder distribution $\rho(E)$. From [66], the physically relevant parameter regime of the disordered HL model is known to be $\tilde{\alpha} < 1$, where the system is jammed in the absence of shear. Within this jammed regime, we now calculate the transition line $\tilde{\gamma}_0^*(\tilde{\alpha})$ above which there exists a yielded steady state.

We proceed as follows. At a fixed $\tilde{\alpha}$, suppose $\tilde{\gamma}_0$ is large enough so that (4.1) has a yielded steady state. Rescaling time by the period T so that $\tau = t/T = \omega t/(2\pi)$, $\tau \in [0, 1]$, this steady state is characterised by a non-zero period-averaged yield rate $\overline{Y} = \int_0^1 Y(\tau) \mathrm{d}\tau$. As $\tilde{\gamma}_0$ is decreased towards $\tilde{\gamma}_0^*$, we take $\overline{Y}$ to vanish smoothly – an assumption we show to be self-consistent in the end – with the rescaled yield rate $Y(\tau)/\overline{Y} = y(\tau)$ approaching a limiting form. In this limit, the key observation from the dynamical equations (4.1, 4.2) is that the local yielding events can be classified into two distinct groups.

Suppose an element yields at a time $\tau' \in [0, 1]$ within the period, and is assigned a new energy depth E. Neglecting strain diffusion, its local strain will subsequently evolve as $l(\tau) = \gamma(\tau) - \gamma(\tau')$. If $\gamma_0 + |\gamma(\tau')| < \sqrt{2E}$, this element will therefore not be able to yield again in the next cycle; its strain will have to change diffusively (due to mechanical noise) during a large number of ensuing cycles until it comes close enough to the threshold $\sqrt{2E}$ to be swept across it by the external shear. In the limit of vanishing strain diffusion, this will occur precisely at either the strain maximum or minimum within the cycle ($\tau = 1/4$ or $3/4$).

The second group of events are the *direct yields*. If $\gamma_0 + |\gamma(\tau')| \geq \sqrt{2E}$, the element will yield within the ensuing cycle. It will do so at a time τ_y during the cycle that will depend on the previous yield time τ' and the corresponding shear strain $\gamma(\tau') = \gamma_0 \sin(2\pi\tau')$, as well as on E and γ_0.

Overall, one can therefore separate the limiting yield rate into two contributions as $y(\tau) = y^{(1)}(\tau) + y^{(2)}(\tau)$, corresponding to indirect and direct yields respectively. Conservation of probability then implies the following pair of self-consistent equations:

$$\begin{aligned} y^{(1)}(\tau) &= \frac{1}{2}\left[\delta\left(\tau - 1/4\right) + \delta\left(\tau - 3/4\right)\right] \\ &\quad \times \int_{\gamma_0^2/2}^{\infty} \mathrm{d}E\, \rho(E) \int_0^1 \mathrm{d}\tau'\, y(\tau')\, \theta\left(\sqrt{2E} - \gamma_0 - |\gamma_0 \sin(2\pi\tau')|\right) \\ y^{(2)}(\tau) &= \int_0^{\infty} \mathrm{d}E\, \rho(E) \int_0^1 \mathrm{d}\tau'\, y(\tau')\, \delta\left(\tau - \tau_y(\tau', \gamma_0 \sin(2\pi\tau'), \gamma_0, E)\right) \end{aligned} \tag{4.3}$$

which can be solved numerically in an iterative way, see App. 4.A for details.

Once the limiting yield rate is known we can work out the limiting distribution $P(E, l)$ at the transition, the normalisation of which determines the transition line $\gamma_0^*(\alpha)$. The calculation is in fact done the other way around, by fixing a strain amplitude γ_0 and working out the α^* where the yielded state ceases to exist.

For the calculation it is useful to switch to a "co-moving" frame, defined by $u(\tau) = l - \gamma(\tau)$. In this frame of reference, yielded elements are reinserted at $u = -\gamma(\tau)$, corresponding to $l = 0$. We furthermore rescale the time-independent pdf at the transition by the prior distribution of energies, so that we work with

$$\tilde{P}(E, u) = \frac{P(E, u)}{\rho(E)} \tag{4.4}$$

At the transition, where the timescale of diffusion diverges, only elements undergoing indirect yields have nonzero steady state probability. The direct yields can effectively be considered as occurring instantaneously (on a timescale $\sim 1/\omega \ll 1/\overline{Y}$) so are negligible in the steady state distribution, but they do affect the behaviour via their contribution to $y(\tau)$. More precisely, their steady state probability vanishes as $\overline{Y}/\omega$ at the transition, but their contribution to the yield rate is of the order $\omega \times \overline{Y}/\omega \sim \overline{Y}$. The indirect yielding processes, on the other hand, amount in the same limit to absorbing boundary conditions at $\pm u_c(E) = \sqrt{2E} - \gamma_0$. With these boundary conditions, the steady state master equation (4.1) reduces to

$$0 = \alpha Y(t) \partial_u^2 \tilde{P}(E, u) + Y(t) \delta\left(u + \gamma(t)\right) \tag{4.5}$$

Averaging this over a period, and defining the rate of yield events producing yielded elements with some given u as

$$R(u) = \int_0^1 \mathrm{d}\tau\, y(\tau) \delta\left(u + \gamma(\tau)\right) \tag{4.6}$$

we obtain a simple equation for $\tilde{P}(E, u)$

$$0 = \alpha \partial_u^2 \tilde{P}(E, u) + R(u) \tag{4.7}$$

with the boundary conditions $\tilde{P}(E, u) = 0$, $|u| > u_c(E)$.

Eq. (4.7) can be solved analytically, as the diffusive propagator with absorbing boundary conditions is well known. The solution, which depends on E only via

$u_c(E)$, is

$$\tilde{P}(E,u) = \frac{1}{2\alpha u_c}\int_{-u_c}^{u_c} R(u_0) \times \Big((u_c+u_0)(u_c-u)\theta(u-u_0) + (u_c+u)(u_c-u_0)\theta(u_0-u)\Big)\theta(u_c-|u|)\mathrm{d}u_0 \quad (4.8)$$

Reverting to $P(E,u)$ and performing the integral over u yields

$$P(E) = \int \mathrm{d}u\, P(E,u) = \rho(E)\frac{1}{2\alpha}\int_{-u_c}^{u_c}\mathrm{d}u_0\, R(u_0)(u_c^2-u_0^2) = \frac{1}{2\alpha}\,\rho(E)\int_0^1 \mathrm{d}\tau\, y(\tau)\Big((\sqrt{2E}-\gamma_0)^2 - \gamma_0^2\sin(2\pi\tau)^2\Big)_+ \quad (4.9)$$

where $f_+ = f\theta(f)$. The term on the right hand side may be interpreted as the product of $\rho(E)$ and the mean first escape time, with diffusive noise of strength $\alpha\overline{Y}$, of a fictitious "particle" from a box of half-width $\sqrt{2E}-\gamma_0$, having started at $-\gamma(\tau) = -\gamma_0\sin(2\pi\tau)$. This is averaged over the possible previous yield times. Physically, it is the interplay between these two objects (the energy disorder and the timescale set by the mechanical noise) which sets the location of the transition. A further integration of (4.9) over E fixes the critical coupling α^*. For this we separate again the two contributions to the yield rate, finding

$$\alpha^*[\gamma_0, c, y^{(2)}(\tau)] = c\alpha^*_{nd}(\gamma_0) + \int_0^1 \mathrm{d}\tau\, y^{(2)}(\tau)\left(F_\rho^1(E^*(\tau)) - \sqrt{2}\gamma_0 F_\rho^{1/2}(E^*(\tau)) + \frac{\gamma_0^2}{2}(\cos(2\pi\tau))^2 F_\rho^0(E^*(\tau))\right) \quad (4.10)$$

where

$$E^*(\tau) = \frac{\gamma_0^2}{2}\left(1+|\sin(2\pi\tau)|\right)^2 \quad (4.11)$$

and

$$\alpha^*_{nd}(\gamma_0) = F_\rho^1(2\gamma_0^2) - \sqrt{2}\gamma_0 F_\rho^{1/2}(2\gamma_0^2) \quad (4.12)$$

is the critical coupling if one neglects direct yields (i.e. setting $c=1$). Returning to Eq. (4.10), we now have all the ingredients necessary to compute the transition line for any given distribution $\rho(E)$. For a fixed γ_0, one must first compute the limiting yield rate, which is then inserted into (4.10) to obtain the critical coupling. Note that as can easily be checked from Eqs. (4.10) and (4.12), the transition line can be expressed in the rescaled form $\tilde{\alpha}^*(\tilde{\gamma}_0)$, with $\tilde{\alpha} = \alpha/\langle E\rangle$ and $\tilde{\gamma}_0 = \gamma_0/\sqrt{\langle E\rangle}$.

The "no direct yields" approximation for α^* (Eq. 4.12) becomes exact for $\gamma_0 \to 0$. From this approximation, one may derive an exact bound proving in general that in the presence of disorder the phase boundary lies above the original HL model. Indeed, from (4.12) one may find analytically that the initial tangent is given by

$$\frac{\mathrm{d}\tilde{\gamma}_0}{\mathrm{d}\tilde{\alpha}} = \frac{1}{\sqrt{2}}\frac{(\langle E\rangle)^{1/2}}{\langle\sqrt{E}\rangle} \geq \frac{1}{\sqrt{2}} \quad (4.13)$$

In the original HL model, the slope is $1/\sqrt{2}$ (and in fact stays constant at this value),

while the inclusion of disorder always tends to extend the size of the frozen region[6]: this is due to the inclusion of deeper traps where the dynamics can get stuck.

Fig. 4.1 shows the transition line for the specific case of a Gaussian yield energy distribution $\rho(E) \sim e^{-E^2/(2\sigma^2)}$. This is the form for $\rho(E)$ we will adopt in the rest of the work, to match the results of earlier numerical studies [52]. In Fig. 4.1 we also show the "no direct yields" approximation (which we recall is exact for $\tilde{\alpha} \to 1$), and the transition line for the original HL model (i.e. the case $\rho(E) = \delta(E - \langle E \rangle)$).

We may comment finally on the asymptotic behaviours of (4.12) and (4.10) as $\tilde{\gamma}_0 \to \infty$ (for a Gaussian $\rho(E)$). From (4.12), i.e. for the "no direct yields" approximation, it is simple to derive (again, for a Gaussian $\rho(E)$) that

$$\alpha^*_{nd} \approx \frac{\pi}{16} \frac{1}{\tilde{\gamma}_0^4} e^{-\frac{4}{\pi}\tilde{\gamma}_0^4} \tag{4.14}$$

For the full theory (4.10), to take the limit one has to consider a saddle point expansion of the integral on the right hand side around $\tau = 1/4, 3/4$, to show that

$$\tilde{\alpha}^* \sim \frac{1}{\tilde{\gamma}_0^8} e^{-\frac{\tilde{\gamma}_0^4}{4\pi}} \tag{4.15}$$

We see that, with respect to the "no direct yields" approximation (4.14), the full theory shows a slower divergence (see Fig. 4.2), due to the prefactor in the exponent being reduced by a factor of 16, and a power-law correction is found.

In either case, one may discuss the connection to the model of [103], introduced in Sec. 4.1, which one expects to recover from the mean field model in the absence of interactions (i.e. $\tilde{\alpha} \to 0$). Interestingly, we see from either (4.15) or (4.14) that we can to leading order write

$$\tilde{\gamma}_0^* \sim \left(\ln \left(\frac{1}{\tilde{\alpha}} \right) \right)^{1/4} \quad \text{for} \quad \tilde{\alpha} \ll 1 \tag{4.16}$$

This was the same scaling for the yield point found in [103] (see Sec. 4.1), with $1/\tilde{\alpha}$ replaced by N_{cycl}. Mirroring the very slow growth of $\tilde{\gamma}_0^*$ with N_{cycl}, this scaling implies that even a very small level of interaction $\tilde{\alpha}$ can lead to moderate values of $\tilde{\gamma}_0^*$. In fact, given that $1/\tilde{\alpha}$ and N_{cycl} play an equivalent role, one may conjecture that in the $\tilde{\alpha} \ll 1$ regime of the model their ratio $N_{\text{cycl}}\tilde{\alpha}$ determines the qualitative behaviour: for $N_{\text{cycl}}\tilde{\alpha} \ll 1$, not enough cycles are performed to begin to observe indirect yields from deep traps due to the mechanical noise, and the blocks which fall in these traps would appear frozen. One would in this case recover (transiently) the behaviour described in [103].

Finally, in Fig. 4.3 we show (together with the Gaussian case already displayed in Fig. 4.1) the transition line for an exponential $\rho(E)$ expressed again in rescaled variables $\tilde{\alpha}$ and $\tilde{\gamma}_0$. The exponential case is qualitatively very similar to the Gaussian. These differ mainly in the asymptotic behaviour for $\tilde{\alpha} \to 0$, which is controlled by the tail of the $\rho(E)$ distribution, but this is in any case not the interesting parameter regime of the model. For any unbounded $\rho(E)$, $\tilde{\gamma}_0$ must diverge in this limit. This divergence is most easily found from the no direct yield form (4.12), from which one may derive that $\alpha^*_{nd}(\gamma_0) \sim e^{-2\tilde{\gamma}_0^2}$ for the exponential, while we recall $\alpha^*_{nd}(\gamma_0) \sim$

[6] Strictly speaking (4.13) only proves that the transition line for the model with disorder starts above the original model as $\tilde{\alpha}$ is decreased from 1, but our numerics (for both exponential and Gaussian $\rho(E)$) confirm that this holds down to $\tilde{\alpha} = 0$.

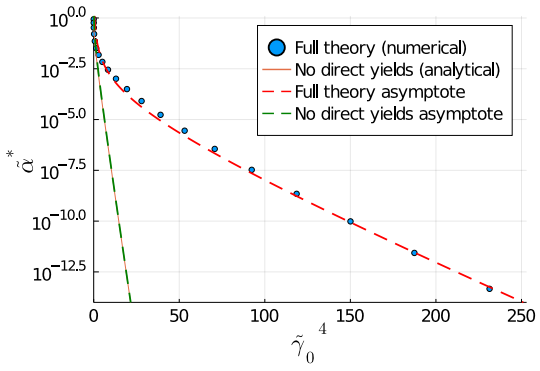

FIGURE 4.2: Critical coupling within the full theory (blue points) from (4.10) (using the numerically calculated $y(\tau)$ at each $\tilde{\gamma}_0$), and within the "no direct yields" approximation, from (4.12) (orange line), in the regime $\tilde{\gamma}_0 \gg 1$. These are compared against the respective asymptotic predictions (4.15) and (4.14) (dashed lines), finding good agreement.

$e^{-4\tilde{\gamma}_0^4/\pi}/\tilde{\gamma}_0^4$ for the Gaussian (see (4.14) above). In both cases one can obtain the same asymptotic behaviours, up to power-law corrections, from an expansion of the full theory (4.10).

We argue in general that, besides the transition line, we expect also the other main results of this chapter, including the initial annealing dependence and the fatigue behaviour (Figs. 4.4 and 4.8 below), to be qualitatively robust to the choice of $\rho(E)$, as long as it fulfils some basic properties. Indeed, there presumably needs to be an "entropic" drive towards shallow energy levels, while rare deeper local minima also need to be present, in order to be able to model the initial annealing. The Gaussian distribution is a simple ansatz fulfilling these properties, besides having been measured in numerical studies of glasses [52], as argued in [103].

4.4 Dependence on initial degree of annealing

Although we have proven that in the yielded region of Fig. 4.1 a fluid steady state *exists*, whether this ergodic state is reached depends crucially on the initial condition. We now study the master equation (4.1) numerically, while fixing $\tilde{\alpha} = 0.086$ (where $\tilde{\gamma}_0^* \approx 1$, see star in Fig. 4.1), and setting the variance of the Gaussian to[7] $\sigma = 0.05$ as in [103]. Numerical solutions entail choosing a discrete set of energy levels $\{E_i\}$, and solving a PDE in the strain variable for each (see App. 4.C for details). As a proxy for different degrees of *thermal annealing* of the initial glass, we generate initial conditions of the form $P(E, t = 0) \sim \rho(E)e^{\beta E}$, introducing an inverse temperature β. Physically, increasing β can be interpreted as decreasing the density of weak zones in the system, here represented by the shallow energy levels. As regards the initial local strains, we consider them to be well-relaxed (narrowly-distributed) within each energy level, with standard deviation in strain $l_c(E)/6$.

[7] We reproduce briefly the rough arguments behind this value, given in [103]. From the numerical measurements of [52], one expects the total number of states for a sub-volume of N particles to scale as $\Omega(N) \sim e^{\alpha N}$ with $\alpha \approx 1$. If one considers sub-volumes of $N = 50$, this implies $\Omega \sim 10^{21}$. The variance σ^2 can then be set by imposing that the DOS $\sim \Omega\rho(E)$ become $O(1)$ (or equivalently its entropy to go to zero) at the deepest accessible minimum E_c at which we cut off the distribution. This gives $\sigma^2 \sim E_c^2/(2N)$, which for the choices $E_c = 1/2$ (in units of the elastic modulus) and $N = 50$ considered in [103] yields $\sigma = 0.05$.

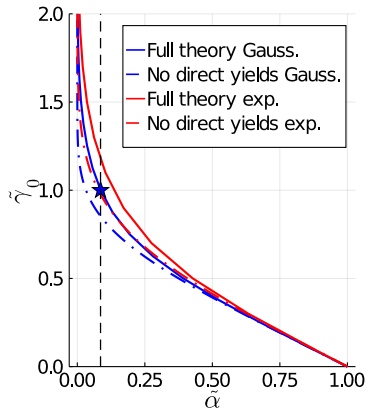

FIGURE 4.3: Transition line in the $\tilde{\alpha} - \tilde{\gamma}_0$ plane, for Gaussian (blue) and exponential (red) $\rho(E)$. We show in each case both the numerically computed result from the full theory (4.10), full lines, and the approximate no-direct-yields analytical form (4.12), dash-dotted lines. As in Fig. 4.1, vertical dashed lines indicate the fixed coupling value $\tilde{\alpha} = 0.086$, where in the Gaussian case $\tilde{\gamma}_0^* = 1$ (see star), chosen for studying the initial annealing dependence.

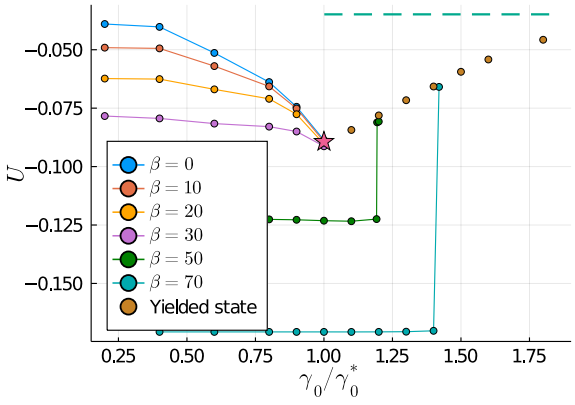

FIGURE 4.4: Stroboscopic energy in the steady state after application of many cycles of shear with amplitude γ_0. Star indicates analytically calculated threshold energy U^*; dashed line corresponds to the steady shear limit reached as $\gamma_0 \to \infty$. Steady state energy values for $\gamma_0 = \gamma_0^*$ and $0.9\gamma_0^*$ are obtained from a power-law extrapolation of the slow relaxation (see App. 3.B).

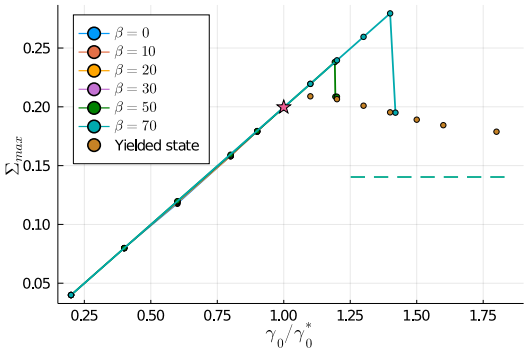

FIGURE 4.5: Stress amplitude in steady state after many cycles of shear. Star indicates analytical value at threshold, which is simply $\Sigma = \gamma_0^*$ given that the system in steady state is elastic up to that strain. Dashed lines indicate the exact macroscopic yield stress Σ_y (4.43).

In Fig. 4.4 we show the stroboscopic ($\gamma = 0$) energy in the steady state after application of many cycles of shear at a given amplitude γ_0. On the solid side, this corresponds to a frozen state with $\overline{Y} = 0$; on the yielded side, this is the ergodic state with $\overline{Y} > 0$. The total energy is measured within the model as $U = \int \mathrm{d}E \int \mathrm{d}l \ \left(-E + l^2/2\right) P(E,l)$, i.e. energy at the bottom of each minimum plus elastic energy. The main features found in MD simulations [49–51] are reproduced in Fig. 4.4. Within the precision and range of our numerics, yielding for poorly annealed samples appears as a cusp in U at the common yield point γ_0^*, while well-annealed samples are insensitive to shear up to a critical strain $\gamma_c(\beta) > \gamma_0^*$. The threshold energy (and corresponding β^*) separating the two types of yielding simply arise as the lower limit of the ergodic state.

We show in Fig. 4.5 the corresponding data for the stress amplitude, i.e. maximum stress over the cycle, once the system has reached its steady state (whether frozen elastic or yielded). This also qualitatively reproduces the behaviour in [49, 50, 101], with a finite drop in steady state stress appearing for samples prepared below the threshold. Within the precision and range of our numerics, the data are consistent with poorly annealed samples (up to $\beta = 30$) showing a slight stress increase at or just above [8] the common yield point γ_0^*. Highly annealed samples (up to $\beta = 50$, 70) behave elastically beyond this point, until at $\gamma_c(\beta)$ the stress amplitude drops to that of the ergodic steady state. We point out that in MD studies (see e.g. [50]) the initial increase is not completely elastic; in our model it is, due to the simplification of considering the same uniform elastic modulus $k = 1$ for all elements, irrespective of their energy level E. One could obtain non-elastic behaviour by considering a distribution of k-values, which should presumably be correlated with E.

The MD studies of [50, 101] report a small (essentially invisible on the scale of Figs. 4.4 and 4.5) jump in energy and stress amplitude at γ_0^*. The origin of this effect, which appears to survive for large system size, is unclear. We expect that in our mean field model both energy and stress remain continuous on approaching from the solid side, and our numerics are consistent with this. From the fluid side, our theory predicts that $\overline{Y}$ vanishes continuously, reminiscent of e.g. the second order

[8] As commented on in App. 4.E, we expect the actual yield point for this frequency to be slightly above γ_0^*, although we are not able to determine this precisely within our numerics. It is possible therefore that the stress amplitude in the yielded state monotonically decreases above the yield point. Another possibility is that the non-monotonicity disappears for $\omega \to 0$, but we have not studied this in detail.

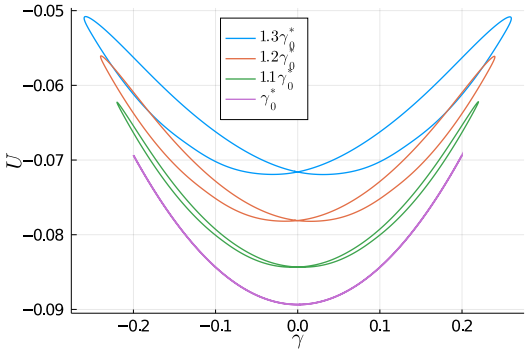

FIGURE 4.6: Energy within one cycle in the yielded steady state, plotted parametrically against the current strain $\gamma(t) = \gamma_0 \sin(\omega t)$.

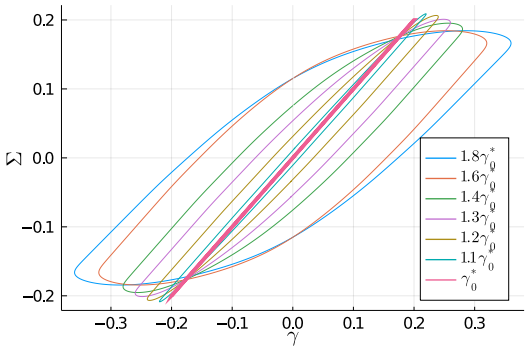

FIGURE 4.7: Macroscopic stress within one cycle in the yielded steady state, plotted parametrically against the current strain $\gamma(t) = \gamma_0 \sin(\omega t)$.

transition scenario of [107]. Closer inspection reveals that samples initialized above the threshold energy display critical behaviour at γ_0^*, where the yield rate decays as $\overline{Y}(t) \sim t^{-b}$, with an $\tilde{\alpha}$-dependent exponent $b \leq 1$. This implies a diverging number of events for long time, allowing the system to lose memory of its initial condition. The critical power law decay of $\overline{Y}(t)$ also means that relaxation timescales must diverge on the approach from either side of the transition.

On the yielded side, the energy gradually increases with strain amplitude (as found in MD [49, 50, 97, 101, 108]) towards an asymptotic value for $\gamma_0 \to \infty$, which corresponds to the known [66] energy of the system under steady quasistatic shear. This energy increase is due to a progressive shift of the element population towards shallow energy levels. We show in Fig. 4.6 and Fig. 4.7 the energy and the stress (respectively) within one cycle of shear in the yielded state. In both cases we include additionally the theoretical prediction at $\gamma_0 = \gamma_0^*$: we recall that as $\overline{Y}$ vanishes continuously at the transition, this is simply purely elastic behaviour. As γ_0 is increased, we see that (Fig. 4.6) the energy describes a "butterfly" shape, while the stress (Fig. 4.7) acquires an ever wider hysteresis loop. These are both qualitatively consistent with the behaviour in particle simulations [49, 50, 101].

4.5 Fatigue

Turning to samples with initial energy below the threshold energy, which yield at $\gamma_c(\beta) > \gamma_0^*$, we find very interesting transient behaviour. As shown in Fig. 4.8 for

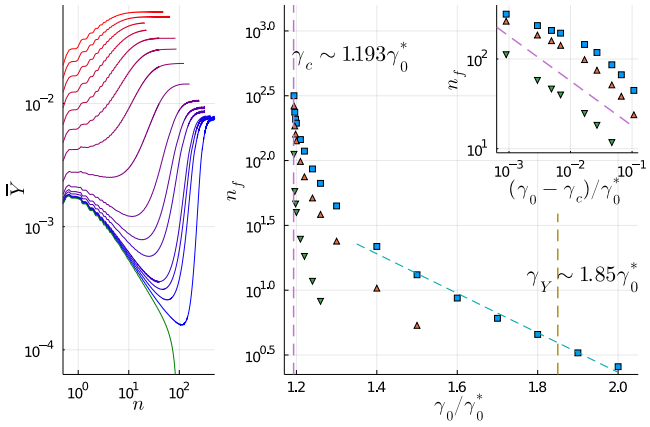

FIGURE 4.8: *Fatigue* behaviour for well-annealed sample ($\beta = 50$). Left: non-monotonic behaviour of period-averaged yield rate $\overline{Y}$ against number of cycles. Strain amplitudes γ_0 range from $1.194\gamma_0^*$ (blue) to $2\gamma_0^*$ (red) (see text for precise values); also shown is $1.192\gamma_0^*$ (green), below the fatigue limit. Right: for the same strain amplitudes, three measures of the fluidisation time as described in the text, 75% of final yield rate (squares), inflection point (up-triangles) and cycles to reach the minimum (down-triangles). Inset: divergence of timescales above $\gamma_c(\beta)$, consistent with an inverse square root (dashed line) for the minimum.

$\beta = 50$, close to $\gamma_c(\beta)$ the yield rate $\overline{Y}$ displays strongly non-monotonic behaviour. The 16 strain amplitudes shown above yield are, from blue to red: 1.194, 1.196, 1.198, 1.2, 1.21, 1.22, 1.24, 1.26, 1.3, 1.4, 1.5, 1.6, 1.7, 1.8, 1.9 and 2 γ_0^*. We show in addition a run below yield, for 1.192 γ_0^* (green). As a proxy for the time to failure (expressed in number of cycles, n_f [9]), we take the inflection point of $\overline{Y}(t)$ as done in [65] for creep (where it is associated to banding [109]), as well as the point at which $\overline{Y}$ reaches 75% of its steady state value, which allows us to analyse larger γ_0 where an inflection is not present. We additionally consider the number of cycles at which the minimum of $\overline{Y}$ is reached. We find (Fig. 4.8) that the number of cycles n_f decreases rapidly (consistent with an exponential) towards unity as γ_0 is increased towards γ_Y, the yield point determined for $\beta = 50$ under startup of steady shear (see Sec. 4.6). This is very reminiscent of *fatigue failure* [110–114] found e.g. in metallic glasses. Close to $\gamma_c(\beta)$, the timescale associated to the minimum shows a clear power-law divergence, consistent with an inverse square root. The similarity of this mean field fatigue behaviour with creep flow suggests the intriguing possibility that this divergence may be understood from a Landau-type scaling argument, as recently proposed in [115] for creep. We will discuss this connection further in Sec. 5.3. It is interesting to note that an inverse square root divergence of the failure time is also found in the extensively studied fiber bundle model [111], although in that case failure is studied under a constant load.

In Fig. 4.9, we show the same runs as in Fig. 4.8, but this time plotting the energy U. The near-constancy of the run below the fatigue limit, with $\gamma_0 = 1.19\tilde{\gamma}_0^*$, shows clearly that, approaching γ_c from below, the energy remains very largely insensitive to the shear, due to the very low yield rates involved.

A closer look at the dynamics of the mean field model near γ_c reveals that, during the initial cycles, the plastic activity is dominated by direct yielding of rare shallow

[9] For the number of cycles we simply take the time divided by the period, so that it takes continuous values in Fig. 4.8.

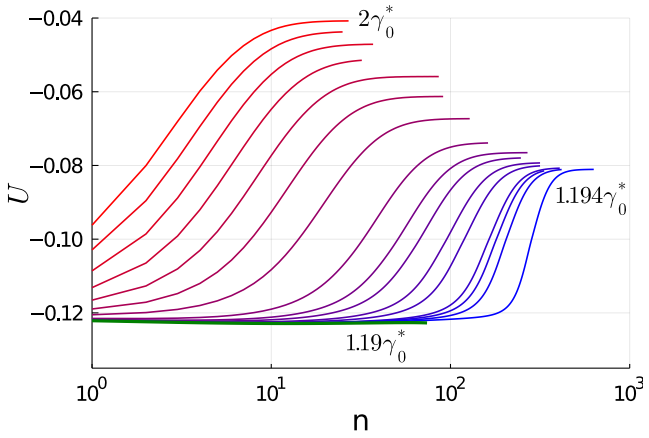

FIGURE 4.9: Energy U against number of cycles, for $\beta = 50$ and a range of strain amplitudes around the fatigue limit γ_c as given in the text.

elements, which we recall may be thought of as weak zones in the material. This is substantiated in Fig. 4.10, where we show the yield rate of each energy level during the first five cycles. Significant direct yields only occur for $E < 2\gamma_0^2$; for the strain amplitude $\gamma_0 = 1.194\gamma_0^*$, and our discrete set of levels, this condition is fulfilled by the first eight energy levels.

At intermediate times, the energy distribution $P(E)$ then almost settles down to a frozen fixed point. However, eventually the accumulated strain diffusion is enough to trigger yield events across the entire energy spectrum (including deep levels where the bulk of the population lies), driving the system away towards the yielded steady state. In Fig. 4.11 we show the evolution of the energy distribution $P(E)$ for the run closest to γ_c (from above), $\gamma_0 = 1.194\gamma_0^*$. We see indeed that the initial energy distribution (red dashed line) initially approaches a fixed frozen state (orange dashed line), which it comes closest to at $n_{\min}$ (defined as the point where $\overline{Y}$ reaches its minimum value). Beyond $n_{\min}$, yield events across the system drive the distribution towards the yielded state. The intriguing approach to and escape from a frozen stationary state leads to the interesting non-monotonic behaviour we observe, and associate with fatigue behaviour.

4.6 Uniform shear and the role of shear banding

We discuss here the connection to yielding under uniform shear, and the relative role of shear banding, the absence of which is arguably the main limitation of our mean field model. Both MD studies [49, 50] and an elastoplastic model [104] have suggested that the transition to brittle yielding under uniform shear as the initial energy is varied occurs at, or at least very close to, the threshold energy of oscillatory shear. Significant differences between the two types of shear remain, however. Firstly, under oscillatory shear, in particle simulations [49] the existence of a sharp yielding transition and its dependence on degree of annealing (Fig. 4.4) are only quantitatively affected by shear rate $\dot{\gamma}_0$ (equivalent to frequency via $\dot{\gamma}_0 = \gamma_0\omega$), with just a shift in γ_0^*. This remains true even for larger $\dot{\gamma}_0$, where *no* banding is present [49]. Also in our mean field model, we have seen above that data for finite frequency ($\omega = 0.1$) largely agrees with the $\omega \to 0$ theory. Under uniform shear, on the other hand, a sharp transition between ductile and brittle yielding can only strictly be defined in the $\dot{\gamma} \to 0$ limit, where a macroscopic stress drop is caused by the formation

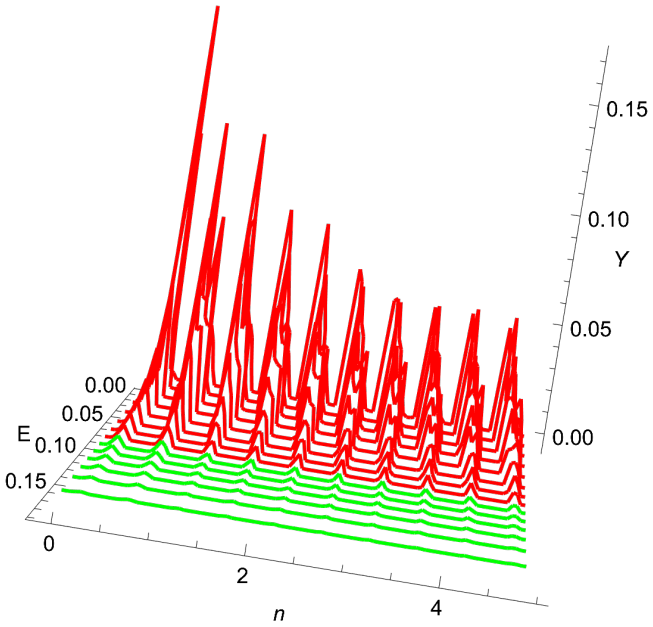

FIGURE 4.10: Yield rate $Y(E)$ of energy level E in the first 5 cycles, for $\gamma_0 = 1.194\gamma_0^*$. Shown in red are the first eight energy levels $\{E_i\}$ within our discrete set, which satisfy $E < 2\gamma_0^2$, while levels with $E > 2\gamma_0^2$ are shown in green. These are levels where no direct yields are possible, so that their contribution to the plastic activity during the initial cycles is vanishingly small.

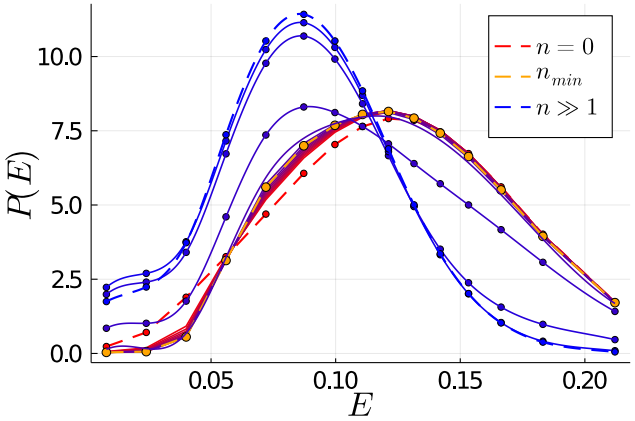

FIGURE 4.11: Evolution of $P(E)$ for $\gamma_0 = 1.194\gamma_0^*$. Log-times are uniformly spaced, from red to blue. Shown explicitly are the initial distribution (red dashed line), the almost frozen distribution at $n_{\min}$ (orange dashed line), and the distribution in the yielded steady state (blue dashed line). The last curves are smooth fits as a guide to the eye. Note that in general we expect $P(E)$ in the yielded state to vanish as $\sim \sqrt{E}$ as $E \to 0$ (see Fig. 4.14). We cannot resolve this within our energy discretisation, but the region of very small E in any case does not contribute significantly to macroscopic quantities.

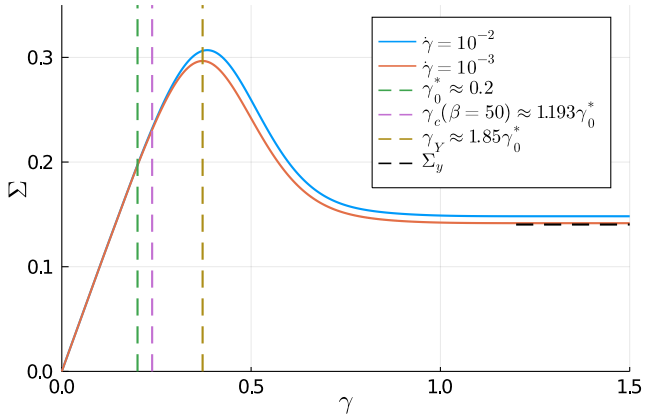

FIGURE 4.12: Stress-strain curves for $\beta = 50$, obtained with two different shear rates. Also shown is the exact macroscopic yield stress (4.43).

of a system-spanning shear band [62]. In essence, the distinction between the two types of shear reflects the difference between the two protocols pointed out in the introduction: the ductile/brittle distinction in uniform shear applies inevitably to transients, while in the oscillatory case one is referring to continuous or discontinuous changes in energy (or stress amplitude) in the steady state after many cycles.

The disordered HL model that we have explored captures this qualitative difference between oscillatory and uniform shear: in the latter case we find no sign of brittle yielding even in the $\dot{\gamma} \to 0$ limit, at least for the β-dependent initial conditions studied here, reflecting the absence of banding in the mean field model. This is shown in the following figures.

In Fig. 4.12, we show the stress-strain curve under uniform shear for the intial condition $\beta = 50$, from which we extract the yield point $\gamma_Y \approx 1.85\gamma_0^*$ (reported in Fig. 3 of the main text) as the strain at which the overshoot is reached.

In Fig. 4.13, we show stress-strain curves under uniform shear with the small shear rate $\dot{\gamma} = 10^{-3}$, for a range of β values up to $\beta = 70$. We see that the stress overshoot grows with β, but remains smooth and shows no sign of developing a discontinuity.

In Fig. 4.14 we check that in the steady state limit under slow shear ($\dot{\gamma} = 10^{-3}$) our numerics reproduces very well the exact form (4.41) of $P(E)$ derived by Agoritsas et al. [66] in the limit $\dot{\gamma} \to 0$.

We contrast our results in Fig. 4.12 and 4.13 with two claims in the literature, in [59] and [116], where spinodal-type discontinuous yielding under uniform shear was claimed to be found in mean field. We note, firstly, that [59] neglects the alternating signs of the elastic kernel, in stark contrast to the fully symmetric mechanical noise considered here. Indeed, the mean field approach of [59] is essentially a depinning model, where, given that the interaction kernel is strictly positive, any plastic event destabilises all other regions of the system. This is true for the elastic Eshelby kernel along a given axis (and indeed in the 2D stetting may be relevant for studying how a shear band nucleates along a line [117]), but is certainly far from capturing the full form of the interactions. The importance of the alternating sign of the propagator and the implications for studying brittle yielding in mean field will be discussed further in Chapter 5.

The authors of [59] attempt to justify their approach by pointing to "similar behaviour found in more involved mean-field models" [59]. This refers to the work of

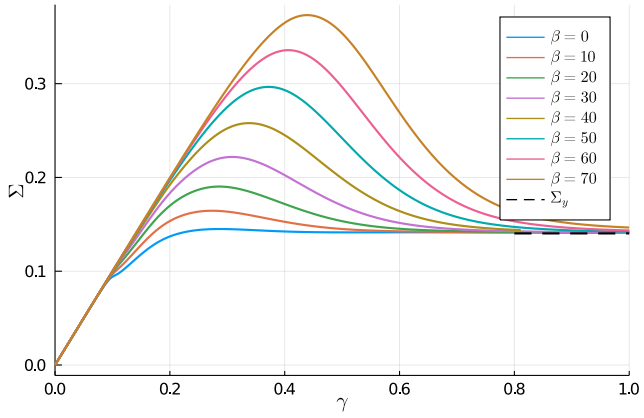

FIGURE 4.13: Stress-strain curves under uniform shear obtained with $\dot{\gamma} = 10^{-3}$ for a range of β. Also shown is the exact macroscopic yield stress (4.43).

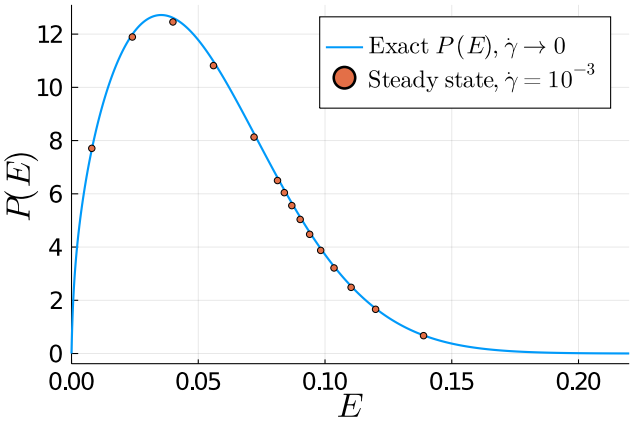

FIGURE 4.14: Comparison of numerically measured $P(E)$ in the steady state with the exact form (4.41). Energy discretisation shown corresponds to $\hat{\beta} = 0$ (higher values of $\hat{\beta}$ show similar agreement).

[116], where the original HL model is considered under quasistatic shear ($\dot{\gamma} \to 0$). The results reported there imply that there is a transition from continuous (ductile) to discontinuous (brittle) yielding as the initial local strain distribution is made narrower. One may consider for definiteness a family of Gaussian distributions $P_0(l) \sim e^{-l^2/(2\sigma_l^2)}$; as σ_l is reduced, one expects from [116] a critical value σ_l^c below which the stress drop becomes discontinuous. In App 4.G we show numerics which support this scenario, by using an improved numerical method with respect to the approximate one employed in the original work [116].

To investigate the possibility of brittle yielding in the disordered HL model, we now rewrite the model in the same way as considered in [116] for the original HL model, in terms of a quasistatic evolution in plastic strain. Starting with the original master equation

$$\partial_t P(E,l,t) = -\dot{\gamma}\partial_l P(E,l,t) + \alpha Y(t)\partial_l^2 P(E,l,t) + Y(t)\rho(E)\delta(l) - \theta\left(|l| - l_c(E)\right) P(E,l,t) \quad (4.17)$$

we divide this by the yield rate $Y(t)$. Noting that $1/Y\partial_t = \partial_{\epsilon_p}$, with ϵ_p the plastic strain, we have that

$$\partial_{\epsilon_p} P(E,l,\epsilon_p) = -\frac{\dot{\gamma}}{Y}\partial_{\epsilon_p} P + \alpha\partial_l^2 P + \rho(E)\delta(l) \quad (4.18)$$

where in the $Y \ll 1$ limit one can replace the yielding term by absorbing boundary conditions at $l_c(E)$ [10]. On the other hand, from (4.17) the evolution of the macroscopic stress is

$$\partial_t \Sigma = \dot{\gamma} - \langle l_u \rangle Y \quad (4.19)$$

where $\langle l_u \rangle$ is the average unstable strain, which in the quasistatic limit *may* under certain conditions be well approximated by $\int \mathrm{d}E\, P(E,t) l_c(E)$ (see App. 4.G for a discussion of this in the original model), neglecting yield events at the negative thresholds. This implies that the advective term in (4.18), denoted by v in [116], is given by

$$v = \frac{\dot{\gamma}}{Y} = \langle l_u \rangle + \frac{\dot{\Sigma}}{Y} = \langle l_u \rangle + \frac{\partial \Sigma}{\partial \epsilon_p} \quad (4.20)$$

Now, as argued in [116], "failure" would occur if $\dot{\Sigma}/Y \to$ approaches $-\langle l_u \rangle$ (from above), where v would vanish. Once this bound is surpassed, one sees that $\dot{\gamma}$ effectively has to become negative to be able to continue the dynamics, leading to an overhang in a plot of Σ vs γ.

In the original time-dependent formulation (4.17), this implies that at some γ during startup Y has to diverge, given that one cannot relax more than $\langle l_u \rangle$ per plastic yield event. Although we do not have an exact argument, we find it implausible on physical grounds that in the disordered case Y could grow without bound at some point, given that it is now coupled to the dynamics of a whole range of energy levels: due to the spectrum of different yield barriers present, the strain distributions in different energy levels will inevitably begin to approach their respective yield threshold at continuously distributed time (or strain) points.

Returning to the brittle yielding of the original HL model reported in [116], following the above discussion we are inclined to think of this rather as an artefact of

[10] Note that Eq. (4.18) with absorbing boundary conditions only strictly conserves normalisation if the derivatives at the boundaries satisfy $\partial_l P(E,l_c) - \partial_l P(E,-l_c) = -\rho(E)/\alpha$ (valid in steady state). This severely restricts the class of initial conditions that can be studied.

the model without disorder. Modelling the initial degree of thermal annealing of the glass as an increasingly narrow local strain distribution is also physically questionable. A first argument in this regard are the results presented in this chapter: it is clear that without including the additional "dimension" of energy levels E and modelling thermal annealing through the occupancy of these energy levels, the different regimes of yielding under oscillatory shear cannot be studied. A further argument comes from the direct empirical study of local yield stress distributions [74] or energy barriers [118] in computer models of well-annealed glasses. We will discuss these arguments (and the general question of modelling initial annealing in elastoplastic models) further in Chapter 5 (see also Fig. 5.2 there).

The importance of heterogeneity is in fact already pointed to in the same work [116]. The brittle yielding scenario described by the original HL model implies system-spanning avalanches and crackling noise all the way up to failure; this in particular would allow one to predict failure from the avalanche statistics. As argued by the authors in the subsequent section of [116], however, the way brittle yielding actually occurs in well-annealed amorphous solids is through the sudden nucleation of a shear band. The authors model this in a lattice elastoplastic model by including by hand a "weak" region of linear size a in the lattice. These are sites with a lower yield barrier; this means that in fact a disordered distribution of yield barriers (albeit with only two possible discrete values of the yield barrier, low ("weak") in the soft region and large elsewhere) is already being considered as essential to understand brittle yielding.

4.7 Summary

In this chapter we have studied a mean field elastoplastic model with local disorder to understand yielding behaviour under oscillatory shear. We first demonstrated the existence of a dynamical yielding transition, and analytically determined the threshold energy, which we identified with the energy of the yielded state approaching the arrest transition. We then showed that the inclusion of disorder allows to study different levels of initial thermal annealing, and we reproduced in mean field the key features found in MD simulations. Samples prepared with an initial energy above the threshold show mechanical annealing towards this threshold, and display critical behaviour at the yielding point with divergent timescales at either side of this point. Samples with initial energy below the threshold, in contrast, are insensitive to shear up to a critical strain amplitude above the yield point, at which point their steady state energy/stress changes discontinuously, with the discontinuity growing for increasingly well-annealed samples. We further studied the transient behaviour of well-annealed samples in the model. This showed strong non-monotonic behaviour reminiscent of an important phenomenon known as fatigue failure. Approaching the fatigue limit from above, we found that the "failure" time diverges. The measured divergence is consistent with an inverse square root in the deviation of the amplitude from the critical strain amplitude. We provided already some insights into how the fatigue behaviour comes about in the mean field model, but will point to further work in this direction in Chapter 5.

Finally, we discussed the behaviour of the model under uniform shear, which shed light on the differences in the notions of ductile/brittle yielding between the two protocols. Under uniform shear, we have discussed that brittle yielding refers to a discontinuity of stress/energy during the transient startup of shear due to the appearance of a sudden shear band. Shear banding is however absent in the mean

field model, and there is no discontinuous behaviour under uniform shear even for well-annealed samples, as we have confirmed for the disordered HL model. We also questioned previous claims of brittle yielding under uniform shear in mean field, casting doubt on how the interaction kernel was treated in mean field, and on how the initial annealing of the glass was modelled. We will discuss these points further in Chapter 5.

Another obvious question which arises concerns the form of the mechanical noise. In this chapter we have considered a diffusive noise for the sake of analytical progress, while our main motivation for the model introduced in Chapter 2 was that the "correct" form of mechanical noise as arising from Eshelby events is in fact power-law distributed. We will also discuss the possible implications of this in Chapter 5.

4.A Limiting yield rate

We give here details regarding the pair of self-consistent equations determining the limiting form of the yield rate as the transition is approached. We focus firstly on the contribution from the indirect yields $y^{(1)}(\tau)$, which we recall is determined by

$$y^{(1)}(\tau) = c[y]\frac{1}{2}\left(\delta\left(\tau - \frac{1}{4}\right) + \delta\left(\tau - \frac{3}{4}\right)\right) \tag{4.21}$$

As explained in the main text, the prefactor (given explicitly in the main text and below) is simply set by the fraction of elements which (after the previous yield event at τ') now satisfy the condition $\gamma_0 + |\gamma(\tau')| < \sqrt{2E}$, so that they cannot yield again in the next cycle. This gives

$$\begin{aligned} c[y] &= \int_{\gamma_0^2/2}^{\infty} \mathrm{d}E\, \rho(E) \int_0^1 \mathrm{d}\tau'\, y(\tau')\, \theta\left(\sqrt{2E} - \gamma_0 - |\gamma_0 \sin(2\pi\tau')|\right) \\ &= \int_0^1 \mathrm{d}\tau'\, y(\tau')\, F_\rho^0\left(\frac{\gamma_0^2}{2}\left(1 + |\sin(2\pi\tau')|\right)^2\right) \end{aligned} \tag{4.22}$$

where in the second line we have performed the integral over E, and introduced the following notation for the cumulative integrals over $\rho(E)$:

$$F_\rho^n(E) = \int_E^\infty (E')^n \rho(E') \mathrm{d}E' \tag{4.23}$$

For the numerics it is inconvenient to work with the delta peaks in (4.21), and we instead write the self-consistency equation directly in terms of the scalar quantity $c[y]$. Performing the integral over $y^{(1)}$, this becomes a functional of $y^{(2)}$ only, which obeys

$$c = cF_\rho^0(2\gamma_0^2) + \int_0^1 \mathrm{d}\tau'\, y^{(2)}(\tau')\, F_\rho^0\left(\frac{\gamma_0^2}{2}\left(1 + |\sin(2\pi\tau')|\right)^2\right) \tag{4.24}$$

We now consider the contribution from the direct yields, denoted by $y^{(2)}(\tau)$. In the main text we wrote this as

$$y^{(2)}(\tau) = \int_0^\infty \mathrm{d}E\, \rho(E) \int_0^1 \mathrm{d}\tau'\, y(\tau')\, \delta\left(\tau - \tau_y(\tau', \gamma_0 \sin(2\pi\tau'), \gamma_0, E)\right) \tag{4.25}$$

Here the function $\tau_y(\tau', \gamma_0 \sin(2\pi\tau'), \gamma_0, E)$ gives, for each combination of previous yield time τ' and energy level E, the time $\tau_y \in (0, 1)$ of the next direct yield event.

In practice, it is not necessary to know this function, and we instead change variables in the delta function, writing the condition now in terms of energy so that $\delta(\tau - \tau_y(\tau', E)) \to \delta(E - E^*(\tau, \tau'))$ (along with the Jacobian associated with the transformation, see below). In other words, a combination of previous yield time τ' and a subsequent direct yield event at τ fixes the value of the depth $E^*(\tau, \tau')$ of the energy minimum that the element must be in. Explicitly, one has simply

$$E^*(\tau, \tau') = \frac{1}{2}\left\{\gamma_0^2[\sin(2\pi\tau) - \sin(2\pi\tau')]\right\}^2 \tag{4.26}$$

because the expression in square brackets on the right (times γ_0) is the strain the element has acquired between times τ' and τ. Expressing the delta function in terms of $E - E^*$ now gives explicitly

$$\int_0^\infty \mathrm{d}E\, \rho(E)\, \delta\left(\tau - \tau_y(\tau', \gamma_0 \sin(2\pi\tau'), \gamma_0, E)\right) = \rho(E^*(\tau, \tau'))\left|\frac{\mathrm{d}E}{\mathrm{d}\tau}\right| \chi(\tau, \tau') \tag{4.27}$$

where

$$\left|\frac{\mathrm{d}E}{\mathrm{d}\tau}\right| = 2\pi\gamma_0^2 \left|\sin(2\pi\tau) - \sin(2\pi\tau')\right| \left|\cos(2\pi\tau)\right| \tag{4.28}$$

and we have carried out the integration over E. The final factor $\chi(\tau, \tau')$ in (4.27) is an indicator function ($\chi = 1$ or 0) enforcing the condition that τ corresponds to the *first* direct yield event in the cycle after a previous yield event at τ'. From trigonometric arguments, this condition is satisfied, and hence $\chi = 1$, in the following four cases:

1. Case $(0 < \tau' < 1/4)$:
   $(\tau' < \tau < 1/4) \cup (\tau_1^* < \tau < 3/4)$,
   with $\tau_1^* = 1/(2\pi)\,(\pi + \arcsin(1 - 2\sin(2\pi\tau')))$.

2. Case $(1/4 < \tau' < 1/2)$:
   $(\tau' < \tau < 3/4)$.

3. Case $(1/2 < \tau' < 3/4)$:
   Define $\tau_2^* = 1/(2\pi)\,(\arcsin(1 + 2\sin(2\pi\tau')) + 2\pi)$.
   If $\tau_2^* < 1$, $(\tau' < \tau < 3/4) \cup (\tau_2^* < \tau < 1) \cup (0 < \tau < 1/4)$.
   If $\tau_2^* > 1$, $(\tau' < \tau < 3/4) \cup (\tau_2^* - 1 < \tau < 1/4)$.

4. Case $(3/4 < \tau' < 1)$:
   $(\tau' < \tau < 1) \cup (0 < \tau < 1/4)$.

Otherwise, $\chi = 0$. A plot of $\chi(\tau, \tau')$ is shown in Fig. 4.15. Note that values of τ that would be in the next period ($\tau > 1$) are mapped back to $\tau \in [0, 1]$ in determining χ.

For clarity we illustrate two example cases in Fig. 4.16, $\tau' = 1/8$ and $\tau' = 7/8$, which belong respectively to case 1 and case 4 above. Plotted is the strain variable l, starting from $l = 0$ at the previous yield time τ'. Dashed lines indicate where $\chi(\tau, \tau') = 0$: intuitively, these are simply segments of the period where a yield event would have already happened, given that $|l|$ has previously reached a higher or equal value. Note that for $\tau' = 1/8$, yields can occur both at positive and at negative l, while for $\tau' = 7/8$ yields always happen first for positive l.

Putting all this together, the second self-consistency equation becomes

$$y^{(2)}(\tau) = \int_0^1 \mathrm{d}\tau'\, y(\tau')\rho(E^*(\tau, \tau'))\left|\frac{\mathrm{d}E}{\mathrm{d}\tau}\right| \chi(\tau, \tau') \tag{4.29}$$

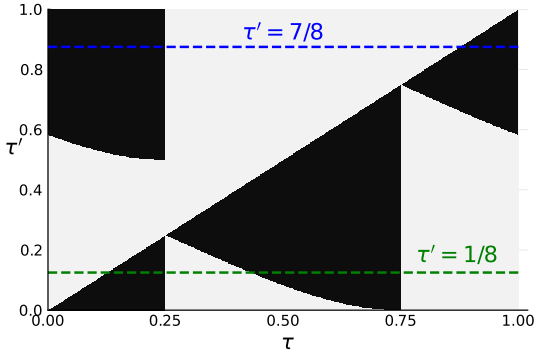

FIGURE 4.15: The function χ in the τ, τ' plane, where it takes the values 1 (black) or 0 (white). Note that the condition for the first next yield is not simply $\tau > \tau'$, and also that the next event may occur in the following period (upper left section). Horizontal dashed lines mark the two horizontal slices of χ exemplified in Fig. 4.16.

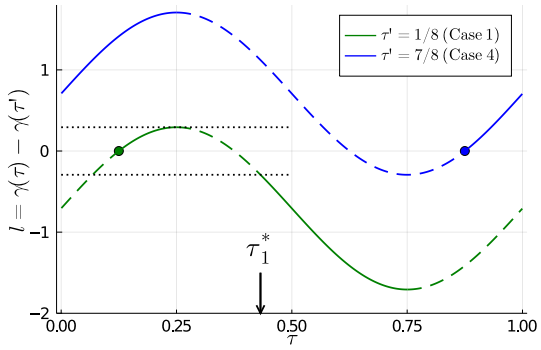

FIGURE 4.16: Plot of the local strain l against τ, with $\gamma_0 = 1$, illustrating two examples of how the χ function is obtained. The initial strains at $\tau' = 1/8$ and $\tau' = 7/8$ are marked with circles. Full lines indicate where $\chi(\tau, \tau') = 1$, dashed lines where $\chi(\tau, \tau') = 0$. Dotted lines mark $l = \pm(\gamma_0 - \gamma(\tau' = 1/8))$, which is the maximum absolute value of strain attained in the initial sweep for $\tau' = 1/8$, and determines the point $\tau_1^*(\tau' = 1/8)$ (see text for definition) beyond which the first yields with negative l can occur. Note that γ_0 just sets the vertical scale and does not feature in the χ function.

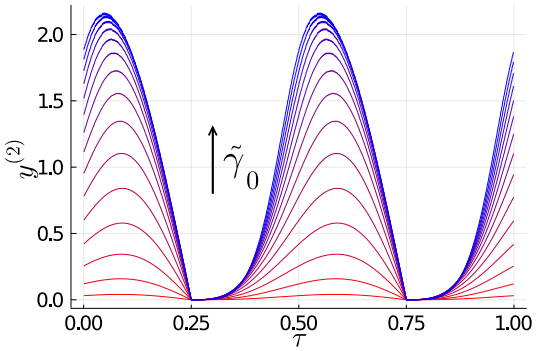

FIGURE 4.17: $y^{(2)}$ obtained from iteratively solving (4.24) and (4.29), for a Gaussian $\rho(E)$. Results are shown for 15 values of $\tilde{\gamma}_0 = \gamma_0/\sqrt{\langle E \rangle}$ that are linearly spaced between 0.125 (red) and 1.875 (blue). The $\tau-$axis has been discretised into $N = 1000$ points.

Eqs (4.24) and (4.29) constitute a pair of self-consistent equations which completely determine the yield rate through c and $y^{(2)}(\tau)$. To solve for $y^{(2)}(\tau)$ and c, one can start from a normalised arbitrary initial condition $y_0(\tau)$ and apply them iteratively until convergence. The iterative scheme indeed conserves the norm $\int_0^1 \mathrm{d}\tau\, y(\tau) = c + \int_0^1 \mathrm{d}\tau\, y^{(2)}(\tau) = 1$. This condition reads explicitly

$$\int_0^1 \mathrm{d}\tau'\, \rho(E^*(\tau,\tau')) \left|\frac{\mathrm{d}E}{\mathrm{d}\tau}\right| \chi(\tau,\tau') + F_\rho^0 \left(\frac{\gamma_0^2}{2}\left(1+|\sin(2\pi\tau')|\right)^2\right) = 1 \tag{4.30}$$

and can be verified to hold for $\forall \tau' \in [0,1]$ as it must. Intuitively, the normalization condition simply expresses the fact that an element with previous yield time τ' must either subsequently yield directly (first term) or fall into a deep energy level where it then yields diffusively (second term).

We show the converged $y^{(2)}(\tau)$ in Fig. 4.17, for a Gaussian $\rho(E)$ and a range of shear amplitudes. As initial condition of the iteration we simply use in each case $c = 1$, $y^{(2)} = 0$. We note that as expected the rate of direct yields rate is periodic with double the frequency of the oscillatory shear, and increases slowly from zero at $\tau = 1/4$ and $3/4$, where the modulus of the strain reaches a maximum given that $\gamma(t) = \gamma_0 \sin(2\pi\tau)$. Notice also that as γ_0 is increased the peaks in the direct yield rate move towards $\tau = 0$ and $1/2$, where the shear *rate* is maximal.

4.B Threshold energy

We here address the calculation of the energy at the transition point, as denoted by the star in Fig. 4.4 of the main text. We recall that the energy is defined within the model as

$$U = \int \mathrm{d}E \int \mathrm{d}l\ \left(l^2/2 - E\right) P(E,l) \tag{4.31}$$

so that one may consider separately the elastic energy (first term) and the potential energy (relative to our chosen reference energy of 0, second term).

Starting with the potential energy E_{pot}, this is simply (minus) the average over the marginal distribution $P(E)$, given by (4.9) with α replaced by the corresponding $\alpha^*(\gamma_0)$. As one may easily check, $P(E)$ vanishes for energy levels with $E < \gamma_0^2/2$,

where all yields are direct. An example of the distribution $P(E)$ at the threshold is shown in Fig. 4.19 below.

To calculate the elastic energy, it is convenient to work again with $\tilde{P}(E,u)$ ((4.8), with α replaced by α^*), giving

$$E_{\rm el} = \int \mathrm{d}E\, \rho(E) \int \mathrm{d}u\, \frac{l^2}{2} \tilde{P}(E,u) \tag{4.32}$$

Using then that $l = u + \gamma(t)$, and the symmetry $\tilde{P}(E,u) = \tilde{P}(E,-u)$, we have that

$$E_{\rm el} = \int \mathrm{d}E\, \rho(E) \int \mathrm{d}u\, \frac{u^2}{2} \tilde{P}(E,u) + \frac{\gamma(t)^2}{2} \tag{4.33}$$

which shows that the system behaves purely elastically at the transition. If we look at the energy stroboscopically, at $\gamma = 0$, then we are left only with the first integral. We introduce

$$\tilde{E}_{\rm el}(E) = \int \mathrm{d}u\, \frac{u^2}{2} \tilde{P}(E,u) \tag{4.34}$$

which using the expression (4.8) for $\tilde{P}(E,u)$ simplifies to

$$\tilde{E}_{\rm el}(E) = \frac{1}{4\alpha} \int_{-u_c(E)}^{u_c(E)} \mathrm{d}u_0\, R(u_0)\, \frac{u_c^4 - u_0^4}{6} \tag{4.35}$$

We can then finally integrate over the energy spectrum to obtain the total elastic energy:

$$E_{\rm el} = \int \mathrm{d}E\, \rho(E) \tilde{E}_{\rm el}(E) \tag{4.36}$$

4.C Numerical methods

As noted in the main text, the numerical solution of the model entails choosing a discrete set of energy levels $\{E_i\}$ and solving a PDE in the strain variable for each. We recall that we consider throughout the Gaussian distribution of energy levels

$$\rho(E) = \sqrt{\frac{2}{\pi\sigma^2}} e^{-\frac{E^2}{2\sigma^2}} \tag{4.37}$$

with $\sigma = 0.05$, and we fix the coupling to $\alpha = 0.086\,\langle E\rangle$ with $\langle E\rangle = \sqrt{2/\pi}\,\sigma \approx 0.03989$. We recall from the main text that this value of the coupling corresponds to $\gamma_0^* \approx \sqrt{\langle E\rangle} \approx 0.1997$, and that we use the fixed finite frequency $\omega = 0.1$ throughout. We describe here firstly how the energy levels are chosen, before we turn to the numerical solution of the PDE, and finally to the question of how the levels are coupled to each other through the yield rate.

For the numerical results shown in the paper, we consider 15 $\{E_i\}$ points. The spacings between those are chosen to ensure that we obtain a reasonable sampling of the Gaussian $\rho(E)$, including both the range of shallow minima with $E < 2\gamma_0^{*2}$ and the tail of deep minima. Explicitly, the first five E_i are chosen uniformly spaced within $(0, 2\gamma_0^{*2} \approx 0.08)$, in order to always keep the same fixed resolution for the shallow elements. Beyond this value, we consider another 10 points, the spacing of which can be tuned in order to better resolve the well-annealed initial conditions. We introduce a "Boltzmann" factor $\hat{\beta}$ (note that this is independent of and not in

general equal to the β that sets the initial condition), which defines a distribution

$$\hat{\rho}(E) = N(\hat{\beta})^{-1}\sqrt{\frac{2}{\pi\sigma^2}}e^{-\frac{E^2}{2\sigma^2}}e^{\hat{\beta}E} \tag{4.38}$$

with the normalization factor

$$N(\hat{\beta}) = e^{\hat{\beta}^2\sigma^2/2}\left(1+\mathrm{erf}(\hat{\beta}\sigma/\sqrt{2})\right) \tag{4.39}$$

We then set the 10 remaining energy levels by requiring them to capture the same amounts of (weighted) probability $\hat{\rho}(E)$. Explicitly this means we choose them as on a uniform grid in q within $(q(2\gamma_0^{*2}), 1)$, where $q(E)$ is defined as the cumulative distribution

$$\frac{\mathrm{d}q}{\mathrm{d}E} = \hat{\rho}(E) \tag{4.40}$$

The above method therefore gives us a parameter $\hat{\beta}$ that we can tune in order to resolve better the tail of the distribution in the well-annealed cases. For the poorly annealed samples, $\beta = 0$ to 30, we use the intermediate value $\hat{\beta} = 20$. For $\beta = 50$ and 70, we use $\hat{\beta} = 50$. For the yielded state, we use $\hat{\beta} = 0$. The different values of $\hat{\beta}$ lead to slight differences in macroscopic stress and energy values measured in the yielded state, as may be noticed in Fig. 2 of the paper.

Once the $\{E_i\}$ are chosen, one needs to solve the PDE in strain to evolve $P(E, l, t)$. We work with a rescaled strain $\tilde{l} = l/l_c(E)$, so that the strain thresholds are always at $\tilde{l} = \pm 1$. We discretize the $\tilde{l}$-axis by considering $N = 4096$ points in the interval $[-4, 4)$. We then update the distribution in time using a pseudospectral method as described in [1], implementing the diffusive term in Fourier space. As stated in the main text, we initialise the strains in a narrow distribution, with standard deviation $l_c(E)/6$. In particular we use the power law form $\sim (1-|\tilde{l}|)^\delta$ with $\delta = 6$ and $|\tilde{l}| < 1$. As long as this distribution is sufficiently narrow, we do not expect its precise form to make any qualitative difference to the results.

We do the updates of $P(E, l, t)$ in parallel for each energy level, but of course the different levels are coupled by the yield rate $Y(t)$, which must be computed from the whole system. For this we exploit the natural separation of timescales within the model. On the one hand, we notice that $Y(t)$ varies smoothly within the period on timescales of the order of $1/\omega$. We therefore introduce a fixed "macroscopic" timestep $\mathrm{d}t_{\mathrm{macro}} = 10^{-2}$. After each step of $\mathrm{d}t_{\mathrm{macro}}$, $Y(t)$ is calculated by performing the discretised integral of $Y(E, t)$ over the $\{E_i\}$. Within each $\mathrm{d}t_{\mathrm{macro}}$, we update each level in parallel, with an energy dependent $\mathrm{d}t_{\mathrm{micro}}(E) = CE \ll \mathrm{d}t_{\mathrm{macro}}$. The reason for the linear energy dependence is that, within rescaled units $\tilde{l} = l/l_c$, one sees that the diffusive term (which is the hardest to resolve) scales as $1/E$, so that the timestep has to be scaled down accordingly. Finally, we update the prefactor C adaptively during the dynamics depending on the period-average $\overline{Y}$ after each cycle, which is especially important to efficiently simulate the long transient behaviour of the well-annealed samples.

4.D Limit of steady shear

In Fig. 4.5 we have included the dynamical yield stress of the model, which should be attained as $\gamma_0 \to \infty$. The expression for this was derived by Agoritsas et al. [66]. We reproduce it here for completeness; we also give the derivation of the limiting $\gamma_0 \to \infty$ value of the energy, shown in Fig. 4.4 of the main text. We note that the

total energy in our numerical evaluations has been measured stroboscopically at $\gamma = 0$ (where the shear rate is far from being reversed), so that for large γ_0 one indeed expects it to coincide (for small ω) with the steady state energy attained under uniform shear as $\dot{\gamma} \to 0$.

In the $\dot{\gamma} \to 0$ limit of steady shear, it was found that [66]

$$P(E) = \frac{\sqrt{E_0}}{\alpha} \sqrt{E} \tanh\left(\sqrt{\frac{E}{E_0}}\right) \rho(E) \tag{4.41}$$

where the characteristic energy scale E_0 is determined by the normalization condition:

$$1 = \frac{\sqrt{E_0}}{\alpha} \left\langle \sqrt{E} \tanh\left(\sqrt{\frac{E}{E_0}}\right) \right\rangle \tag{4.42}$$

where the average is over $\rho(E)$. An example of the distribution (4.41) is shown in Fig. 4.14 later in Sec. VI where we discuss results for uniform shear. The corresponding macroscopic yield stress was found to be [66]

$$\Sigma_y = \frac{1}{\sqrt{2}} \left(\frac{\langle E \rangle}{\left\langle \sqrt{E} \tanh\left(\sqrt{\frac{E}{E_0}}\right) \right\rangle} - \sqrt{E_0} \right) \tag{4.43}$$

To find the limiting value of the total energy, we proceed again by separating the potential and elastic contributions. For the potential energy, one simply needs to take the average over (4.41). To compute the elastic contribution, we proceed in the following way, which is exact for $\tilde{\alpha} = 0$, and should be a good approximation for $\tilde{\alpha} \ll 1$. In particular we expect this to be fairly accurate for the particular case $\tilde{\alpha} = 0.086$ studied in the paper, given that the macroscopic yield stress is already quite close to the limiting value at $\tilde{\alpha} = 0$ (for the Gaussian considered in the paper $\Sigma_y(\tilde{\alpha} = 0.086) = 0.140328$, to be compared with $\Sigma_y(\tilde{\alpha} = 0) = 0.15345$).

The approximation consists in assuming that the distribution in strain is flat across positive strains in all energy wells, with an energy-dependent height fixed by the distribution $P(E)$, that is

$$P(E, l) = A(E) \quad \text{for} \quad l \in (0, l_c(E)) \tag{4.44}$$

with the height $A(E)$ fixed by

$$\int_0^{l_c(E)} \mathrm{d}l \, P(E, l) = P(E) \tag{4.45}$$

which yields

$$A(E) = \sqrt{\frac{E_0}{2}} \frac{1}{\alpha} \tanh\left(\sqrt{\frac{E}{E_0}}\right) \rho(E) \tag{4.46}$$

Now the elastic energy is simply

$$\int_0^{\infty} \mathrm{d}E \int_0^{l_c(E)} \mathrm{d}l \, \frac{l^2}{2} P(E, l) \tag{4.47}$$

Carrying out the l-integral explicitly one finds

$$E_{\rm el} = \frac{\sqrt{E_0}}{3\alpha} \int_0^\infty \mathrm{d}E\, \rho(E) \tanh\left(\sqrt{\frac{E}{E_0}}\right) E^{3/2} \tag{4.48}$$

In the limit $\alpha \to 0$, where from (4.42) $\sqrt{E_0} \sim \alpha / \langle \sqrt{E} \rangle$, one has the limiting (exact) value

$$E_{\rm el}(\alpha = 0) = \frac{\langle E^{3/2} \rangle}{3\langle \sqrt{E} \rangle} \tag{4.49}$$

4.E Critical behaviour

We address here details regarding the critical behaviour on the solid (frozen) side as the common yield point γ_0^* is approached. In Fig. 4.18 we show the evolution of the total energy, measured stroboscopically ($\gamma = 0$) at each cycle, with an applied oscillatory shear amplitude $\gamma_0 = \gamma_0^*$. Due to the finite discretisation of the strain axis, our numerical setup is unable to explore the dynamics reliably once the yield rate becomes very small; with our numerical parameters this range extends roughly down to $\overline{Y} \approx 10^{-3.5}$). This can be seen from the full lines in Fig. 4.18, which stop after around a hundred cycles. It is clear from the figure, however, that the energy is still decaying. Therefore, as noted in the main text, to obtain the steady state values of the energy for $\gamma_0 = \gamma_0^*$ (and $0.9\gamma_0^*$) in Fig. 2 of the paper we extrapolate the $U(n)$ curve, using a power-law fit

$$U(n) = U_\infty + An^{-\delta} \tag{4.50}$$

where we fit the three parameters U_∞, A and δ. These fits are shown in Fig. 4.18 for $\beta = 0, 10, 20, 30$, where we fit $\delta = 0.423, 0.384, 0.319, 0.304$ respectively.

Also shown in Fig. 4.18 is the "discretised" value of U^*, which is simply the total energy (both potential and elastic) calculated at the transition using the same discrete energy points as in the numerical solutions. We note that it is slightly lower than the true U^* calculated for a continuous spectrum of energy levels. Fig. 4.18 therefore suggests that the U^* corresponding to the energy discretisation used has still not quite been reached at γ_0^*, so that the real yield point is in fact slightly higher than the one calculated analytically in the $\omega \to 0$ limit. This is consistent with MD studies [49], where the yield point was found to increase slightly with the shear rate (related to the frequency as $\dot{\gamma}_0 = \gamma_0 \omega$). We do not characterise this here in detail, as determining the precise yield point is made difficult by the fact that we are unable to numerically resolve steady states with very low $\overline{Y}$ just above yielding.

In Fig. 4.19, we show the last (stroboscopic) energy distribution $P(E)$ measured from our numerical solutions at a given shear amplitude γ_0, for the initial condition $\beta = 20$. We see that as γ_0 increases towards γ_0^*, the system mechanically anneals towards the analytically calculated distribution. At $\gamma_0 = \gamma_0^*$, the last $P(E)$ we measure has not quite reached this theoretical prediction for $\omega \to 0$, mirroring the incomplete decay of the energy in Fig. 4.18. Here it is difficult to perform an extrapolation; instead we look at a slightly larger $\gamma_0 = 1.07\gamma_0^*$, where the system is expected from theory to fluidize but is still in the regime where we cannot resolve numerically the steady state. We can then extract the last $P(E)$ before our discretization limit is reached, and we find almost perfect agreement with the theory.

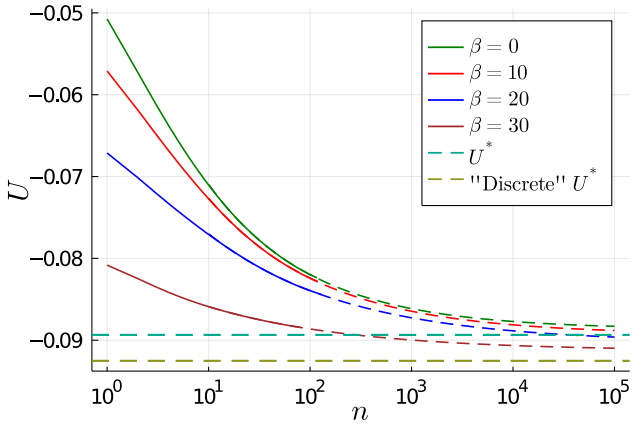

FIGURE 4.18: Decay of the stroboscopic total energy U against number of cycles n at strain amplitude $\gamma_0 = \gamma_0^*$. Dashed lines show the fitted power-law extrapolation.

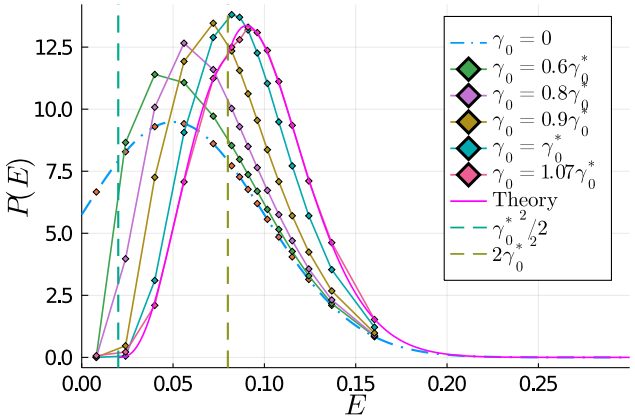

FIGURE 4.19: Final stroboscopic $P(E)$ distribution measured from the numerical solution at different strain amplitudes, for the initial condition $\beta = 20$. We also show by vertical dashed lines the two special values $\gamma_0^{*2}/2$ and $2\gamma_0^{*2}$. The theoretical distribution is zero below the first value, whereas it shows a small kink at the second one, where direct yields cease to be present.

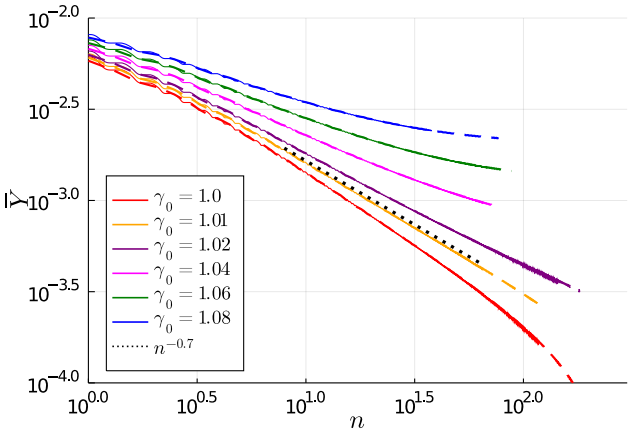

FIGURE 4.20: Critical behaviour at $\tilde{\alpha} = 0.086$, where we measure $b \approx 0.7$. Dashed lines show runs with a coarser discretisation in stress ($N = 2048$), which agree within the time window shown. γ_0 values in legend are in units of γ_0^*.

We next study the critical behaviour of the (period-averaged) yield rate $\overline{Y}$. In order to find clearly the power-law regime and minimise transient effects [11], we use here an initial distribution already "close" to the limiting distribution at the transition, at least in the energy variable. The ensuing relaxation dynamics therefore involves primarily the strain variable, presumably controlled by boundary layers as studied in Chapter 2 (and in [71]) for the aging dynamics. In particular, we consider

$$P(l, E, t = 0) = P^*(E) \frac{1}{\sqrt{2\pi} l_c \sigma_l} e^{-\frac{l^2}{2 l_c^2 \sigma_l^2}} \tag{4.51}$$

with $\sigma_l = 0.4$. The Gaussian strain distribution ensures a small but finite fraction of unstable elements in each energy level, so that the initial condition is not "frozen".

We show results for $\tilde{\alpha} = 0.086$ (the value considered throughout the paper) in Fig. 4.20, for a range of γ_0 near γ_0^*. We measure a power law n^{-b} with exponent $b \approx 0.7$, clearly below 1. This fact is important, as it implies a diverging number of events in the long time limit, allowing the system to lose memory of the initial condition.

Although we do not have an analytical understanding of the exponent b, we conjecture that is non-universal and dependent on $\tilde{\alpha}$. In the limiting case of $\tilde{\alpha} = 1$ (where $\tilde{\gamma}_0^* = 0$), we have checked that $b = 1$ for the critical dynamics in the absence of shear. This is the value found for the original HL model (see Chapter 2), and can be understood from a boundary layer analysis.

4.F Effect of closure relation

We consider here the effect of a general closure relation

$$D(t) = \int \mathrm{d}E \, \alpha(E) Y(E, t) \tag{4.52}$$

[11] We note that these transient effects due to the energy redistribution could slightly modify the numerically measured value of the exponent b.

where

$$Y(E,t) = \int \mathrm{d}l\, \theta\left(|l| - l_c(E)\right) P(E,l,t) \tag{4.53}$$

The case considered in the main paper is the one of constant $\alpha(E)$, which leads back to the simple proportionality $D(t) \propto Y(t)$. Once an E-dependence is allowed for, a natural choice is $\alpha(E) = \hat{\alpha}E$, with $\hat{\alpha}$ a now dimensionless coupling parameter. We will refer to this as linear closure, and consider it for the numerics below. Physically, the linear closure corresponds to yield events at different energy levels contributing to the mechanical noise proportionally to E, which in turn is proportional to σ_c^2 (σ_c being the local yield stress). This is the form one would expect if the model is derived e.g. from the KEP perspective [66, 76]. We firstly show that the general form (4.52) does not change qualitatively the phase diagram of the model, i.e. the transition line. This is due to the following result. Starting from the master equation

$$\begin{aligned}\partial_t P(E,l,t) = -\dot{\gamma}(t)\partial_l P(E,l,t) + D(t)\partial_l^2 P(E,l,t) \\ - \theta\left(|l| - l_c(E)\right) P(E,l,t) + Y(t)\rho(E)\delta(\sigma)\end{aligned} \tag{4.54}$$

and integrating over strain, one has

$$\partial_t P(E,t) = -Y(E,t) + Y(t)\rho(E) \tag{4.55}$$

If we then average (4.55) over a period in steady state it follows that

$$\overline{Y}(E) = \overline{Y}\rho(E) \tag{4.56}$$

Eqs. (4.52) and (4.56) imply that the following holds in any periodic steady state:

$$\overline{D} = \int \mathrm{d}E\, \overline{Y}(E)\alpha(E) = \overline{Y}\int \mathrm{d}E\, \rho(E)\alpha(E) \equiv \alpha_{\mathrm{eff}}\overline{Y} \tag{4.57}$$

where we have defined

$$\alpha_{\mathrm{eff}} = \int \mathrm{d}E\, \rho(E)\alpha(E) \tag{4.58}$$

so that in the linear closure case $\alpha_{\mathrm{eff}} = \hat{\alpha}\langle E\rangle$.

We now recall that the equations for the limiting yield rate depend *only* on γ_0. The closure relation comes in at the next step, where the normalization condition is enforced; however, one is there dealing with period-averaged quantities, so that one can simply replace α by α_{eff}. In the linear closure case, we then have precisely the same transition line as in the main text, provided we consider the rescaled quantity, i.e. $\tilde{\gamma}_0^*(\hat{\alpha}) = \tilde{\gamma}_0^*(\tilde{\alpha})$.

Although the transition line remains unchanged, one expects differences both in the transient and in the steady state above yield. Note that even *at* the transition the actual form of $D(t)$ (4.52) within the period will in general change, even though $y(t)$ is independent of the closure relation.

In Figures 4.21 and 4.22 we show numerical solutions with the linear closure relation with $\hat{\alpha} = 0.086$, alongside the simple version with $\alpha/\langle E\rangle = 0.086$. Firstly, in Fig. 4.21 we show runs for the initial condition $\beta = 0$: we confirm that the transition is indeed located roughly at the same strain amplitude, and overall the dynamics is largely unaffected.

In Fig. 4.22, on the other hand, where we show instead runs for $\beta = 50$ around the fatigue limit, we do see appreciable differences. With the E-dependent closure

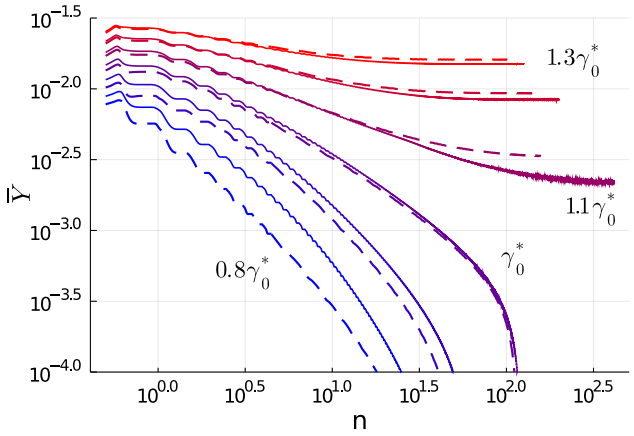

FIGURE 4.21: Dynamics at a range of strain amplitudes around the transition for $\beta = 0$. These are (from blue to red): 0.8, 0.9, 1.0, 1.1, 1.2 and 1.3 γ_0^*. Full lines correspond to simple closure, dashed to E-dependent.

relation the system "freezes" faster, but also re-fluidizes at a faster rate. Also, although in this case we have not performed a thorough analysis of the yield times, the fatigue limit γ_c appears to be slightly larger than in the simple closure relation.

4.G Brittle yielding in original HL

4.G.1 Total and plastic strain methods

We consider in this appendix the behaviour of the original HL model under quasistatic shear ($\dot{\gamma} \to 0$). To study the model directly in this limit, we firstly propose a novel method which to our knowledge has not been employed in the literature [13]. We first write the original HL equation [37] in terms of the evolution of the total strain (i.e. changing variable $t \to \gamma = \dot{\gamma} t$)

$$\partial_\gamma P = -\partial_l P + \frac{Y}{\dot{\gamma}} \partial_l^2 P + \frac{Y}{\dot{\gamma}} \delta(l) - \frac{1}{\dot{\gamma}} \theta\left(|l| - 1\right) P \tag{4.59}$$

We see that in the quasistatic limit the last term becomes an absorbing boundary condition. We then study (4.59) numerically by setting up a strain grid of size M between -1 and 1 (in practice, we use $M = 4096$), and evolve the system by discrete strain steps $\mathrm{d}\gamma$ (generally $\mathrm{d}\gamma = 10^{-7}$). After each strain step, we simply measure the probability loss, i.e. $1 - \int_{-1}^{1} P \mathrm{d}l$, which divided by the strain step $\mathrm{d}\gamma$ gives the term $Y/\dot{\gamma}$. This quantity is then used in the next step to implement the diffusive term.

Given that the original HL model [37] can be solved exactly in steady state, one can take the $\dot{\gamma} \to 0$ limit analytically and compare with the numerics. In particular one finds analytically that the limit $\lim_{\dot{\gamma}\to 0} Y/\dot{\gamma}$ is given by c/α, where c is defined by [66]

$$c \tanh\left(\frac{1}{2c}\right) = \alpha \tag{4.60}$$

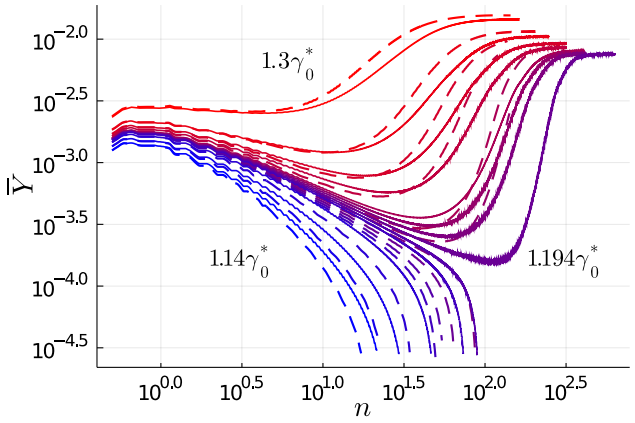

FIGURE 4.22: Dynamics at a range of strain amplitudes around the fatigue limit for $\beta = 50$. These are (from blue to red): 1.14, 1.16, 1.18, 1.19, 1.192, 1.194, 1.196, 1.198, 1.2, 1.21, 1.22, 1.24 and 1.3 γ_0^*. Full lines correspond to the simple closure, dashed to the linear $\dot{E}$-dependent one. Note that with the linear closure relation, the runs with 1.196 and 1.194 γ_0^* end up freezing, while in the simple case these re-fluidise. This suggests that the fatigue limit is slightly higher in the linear closure case.

The steady state stress in the quasistatic limit (referred to as the dynamical yield stress Σ_y) is also set by c:

$$\Sigma_y = \frac{1}{2}\left(-2c + \coth\left(\frac{1}{2c}\right)\right) \tag{4.61}$$

An interesting insight from the exact solution is that in the quasistatic limit the elements become unstable solely due to the diffusive term in (4.59), whose contribution scales as $\dot{\gamma}$, while the drift term contributes only as $\dot{\gamma}^{3/2} \ll \dot{\gamma}$. With the numerical method described above, we have checked that in steady state the exact values are very well reproduced.

In [116], on the other hand, the quasistatic limit is studied differently, namely as an evolution in plastic strain. The evolution equation is obtained as described in Sec. 4.6 for the disordered model, and is given by

$$\partial_{\epsilon_p} P = -\frac{\dot{\gamma}}{Y}\partial_l P + \alpha\partial_l^2 P + \delta(l) \tag{4.62}$$

with absorbing boundary conditions at $l = \pm 1$. Note that now the diffusive and "re-injection" terms have fixed prefactors. As described in Sec. 4.6, the term $\dot{\gamma}/Y$ is related to the stress change as

$$\frac{\dot{\gamma}}{Y} = \langle l_u \rangle + \frac{\partial \Sigma}{\partial \epsilon_p} \tag{4.63}$$

To numerically implement the plastic strain method, then, one can measure the stress change after each plastic strain step, and obtain the driving term from (4.63). In the steady state, where the stress change term in (4.63) vanishes, $\langle l_u \rangle$ therefore must converge to α/c (see above).

There are some problematic issues with the original numerical implementation in [116], however. The first concerns the approximation made there regarding $\langle l_u \rangle$. The

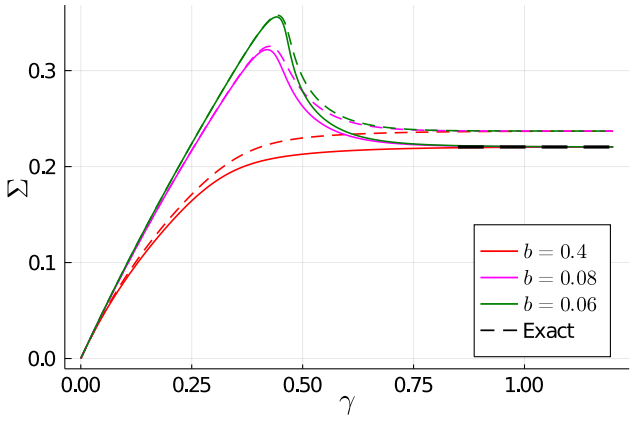

FIGURE 4.23: Startup of quasistatic shear, using the total strain (full lines) and plastic strain (dashed lines) methods. We fix $\alpha = 0.3$. Initial conditions are a very narrow Gaussian ($\sigma_l = 0.05$) with a parabolic term of amplitude b (see footnote). Shown is the exact value of the steady state macroscopic stress for $\alpha = 0.3$, which is very well recovered by the total strain method. We use the same discretisation ($M = 4096$) in both cases, and $\mathrm{d}\gamma = \mathrm{d}\epsilon_p = 10^{-7}$. We have checked that for $M = 8192$ the error of the plastic strain method is unchanged.

authors simply set $\langle l_u \rangle = 1$. Although this is a good approximation during purely elastic loading, this leads to a consistent error in the steady state, and in particular a large accumulated error in the steady state stress. Secondly, unless the condition $\partial_l P|_1 - \partial_l P|_{-1} = -1/\alpha$ is precisely met, Eq. (4.62) does not conserve normalisation. To circumvent this, one can add (by hand) a additional term to the re-injection, to ensure that probability is conserved. This was how the numerics were carried out in [116], as confirmed by a private communication.

The error in steady state is visible in Fig. 4.23, where we study quasistatic shear start-up using the total strain method (4.59) and the plastic strain method (4.62) in its original implementation. We choose for this the same initial conditions $P(l, 0)$ (referred to below as $P_0(l)$) as shown in [116], namely a very narrow Gaussian with a small parabolic term of amplitude b.[12]

We also show both approaches in the graphs below, where we numerically investigate the possibility of brittle yielding. For the initial conditions we now choose a family of Gaussian $P_0(l)$ (with a very small parabolic term of fixed amplitude $b = 0.01$) parametrised by the standard deviation σ_l. Using our method for the evolution of the total strain, we are unable to follow the dynamics below $\sigma_l = 0.18$ due to the sharply rising yield rate (Fig. 4.24). Presumably this should be possible with more computational time by increasing M and decreasing $\mathrm{d}\gamma$, but we have not explored this further here. With the plastic strain method, on the other hand, $Y/\dot{\gamma}$ (measured by inverting $1 + (\partial\Sigma)/(\partial\epsilon_p)$ (4.63)) diverges as σ_l is decreased to 0.16, indicating brittle yielding. The two approaches are roughly consistent regarding the transient $Y/\dot{\gamma}$ down to $\sigma_l = 0.18$. We note that although the error of the plastic strain method regarding the steady state value of $Y/\dot{\gamma}$ is not visible (given that the exact

[12] For the numerics we add a parabolic term to the Gaussian as in [116], so that $P_0(l) = \mathcal{N}^{-1}\left(b(1-l)(1+l) + (1-b)e^{-l^2/(2\sigma_l^2)}\right)$, and $\mathcal{N}$ a normalisation. Without this additional term, which ensures a non-vanishing probability weight near the boundaries, one cannot evolve numerically the plastic strain method due to the very large initial $(\partial\Sigma)/(\partial\epsilon_p)$. The total strain method (4.59) does not have this limitation.

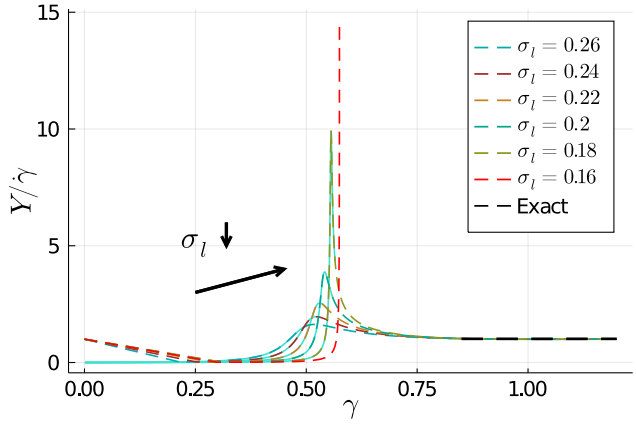

FIGURE 4.24: $Y/\dot{\gamma}$ measured for the total strain (full lines) and plastic strain (dashed lines) methods, for decreasing σ_l. $M = 4096$, $\mathrm{d}\gamma = \mathrm{d}\epsilon_p = 10^{-7}$. We fix $\alpha = 0.2$, so that in steady state $Y/\dot{\gamma} \to 1.014585$ from (4.60) (black dashed line). We see that the plastic strain method predicts a diverging Y at $\sigma_l = 0.16$ (red dashed line).

value is close to one for small α) there is a significant accumulated error in the steady state stress (not shown).

4.G.2 Improved plastic strain method

For the previous Figures 4.23 and 4.24, we have used the plastic strain method in its original implementation as in [116]. We now present two improvements of the plastic strain method. The improvements dispel some doubts that may arise regarding the reliability of the method, due to the above-mentioned numerical inaccuracies.

The first (minor) improvement concerns the choice of initial condition. We noted already above that unless the boundary condition

$$\partial_l P|_1 - \partial_l P|_{-1} = -1/\alpha \tag{4.64}$$

is met at all times, normalisation is not conserved. The choice of initial conditions in [116], which added a parabolic term to the Gaussian, does not respect (4.64). We propose instead the form

$$P_0(l) = ba\left(\sqrt{c - l^2} - \sqrt{c-1}\right) + (1-b)\frac{1}{\sqrt{2\pi\sigma_l^2}} e^{-\frac{l^2}{2\sigma_l^2}} \tag{4.65}$$

where the tunable parameter $b \in (0,1)$ will control the yielding behaviour. Given that the Gaussian is narrow, it does not contribute to the derivatives at the boundaries, and the boundary condition can be satisfied by setting $c = 1 + 4a^2\alpha^2$. a, on the other hand, is fixed by normalisation.

The second (and more important) improvement regards the approximation employed in (4.63), where the authors of [116] set $\langle l_u \rangle = 1$. This approximation becomes increasingly inaccurate for larger α, where one certainly cannot neglect yield events occurring at the negative boundary. We recall that in steady state, the second term of (4.63) vanishes, so that we have $\langle l_u \rangle = c/\alpha$. For $\alpha = 0.45$, for example, the ratio $c/\alpha = 0.525 < 1$. This issue can be dealt with fairly simply by estimating $\langle l_u \rangle$ from

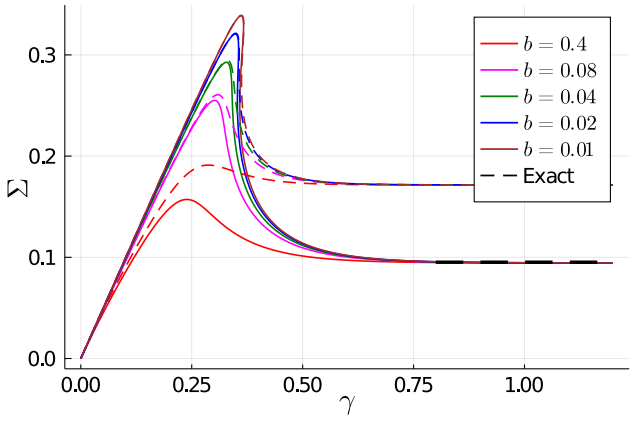

FIGURE 4.25: Stress versus strain under quasistatic loading, for fixed $\sigma_l = 0.24$ and different values of b, following the initial condition (4.65), with coupling $\alpha = 0.45$. Full lines show the result of applying the improved method accounting for the average unstable strain at each step using (4.66), dashed lines are with the approximation $\langle l_u \rangle = 1$. We see the improved method correctly reaches the exact steady state.

the derivatives at the boundaries at each step. Because the flux across each boundary is (in the quasistatic limit) proportional to the absolute value of the derivative, we have

$$\lim_{\dot{\gamma}\to 0} \langle l_u \rangle = \frac{|P'(1)| - |P'(-1)|}{|P'(1)| + |P'(-1)|} \tag{4.66}$$

We show numerics using this improved method in Figs. 4.25 and 4.26. We now set $\alpha = 0.45$, a larger coupling, where brittle yielding is already predicted for a Gaussian of width around $\sigma_l \approx 0.24$. Using the initial condition (4.65), by tuning the parameter b one can therefore go from smooth ductile yielding to discontinuous yielding as b is decreased towards 0. We firstly show stress-strain curves for this in Fig. 4.25, where we see that brittle yielding is predicted for the two smallest values of b, $b = 0.02$ and 0.01. We compare the stress-strain curves obtained from the corrected method (4.66) to those obtained with the approximation of setting $\langle l_u \rangle = 1$, finding that the corrected method converges to the exact steady state. This strengthens support for the existence of brittle yielding in the original HL model.[13]

In Fig. 4.26 we show the same runs, but plotting now the plastic strain ϵ_p against the total strain γ. This makes clearer the implications for the yield rate at the transition. We recall that the derivative of the plastic versus total strain curve is $Y/\dot{\gamma}$. Assuming smoothness, one expects a square-root singularity as the stress drop at γ^* is approached, which would entail a diverging yield rate $Y \sim (\gamma^* - \gamma)^{-1/2}$. ϵ_p then has a finite jump, corresponding to a delta function in the yield rate, whereby a finite fraction of elements yield at once in a mean field avalanche.

The above analysis sheds more light on this intriguing feature of the original HL model. An interesting open question concerns the dependence on shear rate $\dot{\gamma}$: is the catastrophic stress drop unique to the quasistatic limit, or does it survive for finite $\dot{\gamma}$? Exploring this numerically is challenging, given the difficulty of distinguishing a "true" divergence of the model against "numerical" divergences due to the sharply rising yield rate.

[13] We have also checked that the results for the diverging yield rate shown in Fig. 4.24 are essentially unaffected by the correction, because $\langle l_u \rangle$ is practically 1 during the initial loading.

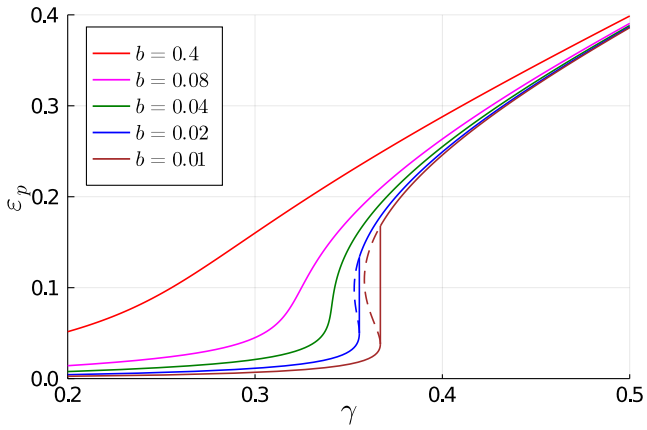

FIGURE 4.26: For the same runs as shown in Fig. 4.25, plastic strain ϵ_p against total strain γ. Dashed lines indicate the "unphysical" portion where the strain recoils. The derivative of this curve is $Y/\dot{\gamma}$, so that the finite jump for $b = 0.02$ and 0.01 corresponds to a delta function in the yield rate.

Chapter 5

Summary and outlook

In this final chapter, we first provide a general summary, bringing together the results already summarised at the end of each chapter. We then discuss the results within a broader context, and point to several open questions and directions for future research. This will be done separately for the athermal aging problem (concerning Chapters 2 and 3), creep flow, and the problem of yielding (concerning Chapter 4). Parts of Sections 5.1, 5.2 and 5.4 have been reproduced from the publications [1, 3] and the pre-print [2].

5.1 General summary

In this thesis we have studied mean field elastoplastic models of athermal amorphous solids. These consider the dynamics of mesoscopic blocks of material, which alternate between elastic and plastic deformation. In mean field, the interactions mediated by the elastic stress propagator are treated as a mechanical noise. Our main contribution has been to extend these models in two important directions, concerning the nature of the mechanical noise (Chapters 2 and 3) and the disordered local energy landscape (Chapter 4). Although the groundwork for such extensions was already laid out in the literature [28, 66], these previous studies were limited to the case of steady shear. Here we have developed these ideas further to study two important phenomena: the aging of athermal systems, and their yielding behaviour, particularly (but not only) under oscillatory shear.

In the first chapter, we constructed a novel time-dependent mean field elastoplastic model, incorporating the power-law mechanical noise spectrum arising from localized plastic events [28, 70, 75]. This model allows the exploration of general time-dependences, including aging and arbitrary rheological protocols. We showed firstly the phase diagram of the model (in the absence of external shear), which separates the arrested (i.e. glassy) from the flowing (liquid) states. We then developed a boundary layer scaling approach, with the aim of studying the behaviour of the model at very low yield rates, as they appear e.g. during aging. As a first application, this allowed us to find the various scalings of the plastic rate in the (stationary) liquid regime just above the dynamical arrest transition.

The main findings of Chapter 1 concern the long time aging regime, the mean-field predictions for which we summarize here. We obtained three different regimes as the exponent $\mu = d/\beta$ (with d the spatial dimension) characterizing the noise spectrum was varied. We recall that β is a general decay exponent of the propagator $r^{-\beta}$, so that varying μ can be thought of as tuning the interaction range. We found that for $1 < \mu < 2$ the plastic activity $\Gamma(t)$ decays in a power-law fashion as $\sim t^{-\mu/(\mu-1)}$, reflecting the dominance of far-field events in determining the long-time dynamics. For $\mu < 1$, on the other hand, near field events are dominant, and

the relaxation becomes exponential. This is encoded in the boundary layer equation, where the crossing of the boundary is dominated by “small" jumps in the first case and “large" jumps in the second, giving rise to the *homogeneous* and *inhomogeneous* solutions respectively. In the marginal case $\mu = 1$, where both near and far-field events are relevant, we found a stretched exponential decay of $\Gamma(t)$ that arises mathematically from the superposition of the two types of boundary layer solution. We compared this last case to simulations (performed by Prof. Suzanne Fielding) on a lattice elastoplastic model, and measured a decay consistent with the predicted stretched exponential. In fact even the pre-asymptotic decay of the plastic activity is extremely well captured by the mean field predictions, up to a modest rescaling of time. This lent a first strong support to our mean field approach to the dynamics of amorphous solids.

In Chapter 3, we went further and studied the predictions of the model for the aging linear response to strain, which unlike the yield rate can be compared directly to stress measurements in particle-based simulations or experiments. We obtained analytically the long-time form of the aging step response $G(t, t_w)$ for the different values of μ, along with the aging frequency response; these are summarised in Tables 3.1 and 3.2. In the aging regime we found that the stress relaxes incompletely to an age-dependent plateau, on a timescale which grows with material age. Regarding the scaling behaviours, we found, firstly, that key scaling exponents are universal and independent of the noise exponent μ. For $\mu > 1$, we then found that the stress relaxation timescale scales linearly with the age t_w of the material, corresponding to simple aging. At $\mu = 1$, which corresponds to interactions mediated by the physical elastic propagator, we found instead a $t_w^{1/2}$ scaling arising from the stretched exponential decay of the plastic activity. The theoretical predictions for $\mu = 1$ were then compared against data from MD simulations (performed by Dr. Rituparno Mandal) of a model athermal system in its aging regime, finding good correspondence with the theory.

In Chapter 4 we included the local disordered energy landscape into the mean field elastoplastic model, while reverting to the diffusive approximation of mechanical noise ($\mu \to 2$), to study yielding under oscillatory shear. We first demonstrated the existence of a dynamical yielding transition, and analytically determined the threshold energy, which we identified with the energy of the yielded state approaching the arrest transition. We then showed that the inclusion of disorder allows to study different levels of initial thermal annealing, and we reproduced in mean field the key features found in MD simulations. Samples prepared with an initial energy above the threshold show mechanical annealing towards this threshold, and display critical behaviour at the yielding point with divergent timescales at either side of this point. Samples with initial energy below the threshold, in contrast, are insensitive to shear up to a critical strain amplitude above the yield point, at which point their steady state energy and stress change discontinuously, with the discontinuity growing for increasingly well-annealed samples. We further studied the transient behaviour of well-annealed samples in the model. This showed strong non-monotonic behaviour reminiscent of an important phenomenon known as fatigue failure. Approaching the fatigue limit from above, we found that the “failure” time diverges. The measured divergence is consistent with an inverse square root in the deviation of the amplitude from the critical strain amplitude. Although a theoretical understanding for this exponent is lacking, we provided some insights into how the fatigue behaviour comes about in the mean field model.

Finally, we discussed the behaviour of the disordered model under uniform

shear, which shed light on the differences in the notions of ductile/brittle yielding between the two protocols. Under uniform shear, we have discussed that brittle yielding refers to a discontinuity of stress and energy during the transient startup of shear due to the appearance of a sudden shear band. Shear banding is however absent in the mean field model, and there is no discontinuous behaviour under uniform shear even for well-annealed samples, as we have confirmed for the disordered HL model. We also questioned previous claims of brittle yielding under uniform shear in mean field, casting doubt on how the interaction kernel was treated in mean field, and on how the initial annealing of the glass was modelled. This led to the conclusion that, while mean field elastoplastic models can capture the steady state discontinuities under oscillatory shear, the insight they can provide into the occurrence of brittle yielding under uniform shear is intrinsically limited by their mean field nature.

5.2 Athermal aging

We will first discuss from a theoretical point of view the results for the aging response found in Chapter 3. It is interesting to compare the athermal aging response found here with "classical" aging phenomena, studied particularly in spin glasses [41]. As in [44], we refer to the step strain response in our model as *aging* due to the fact that the stress relaxation takes place on timescales that grow with the age t_w of the system. An important difference, however, is that our results cannot be fitted to the general form advocated by Cugliandolo and Kurchan [119], where $G(t, t_w) = G[h(t)/h(t_w)]$, $h(t)$ being an effective clock. This is due to several key assumptions in [119] that are violated here. For starters, our model *does not* have weak long-term memory, nor is the response function related to any correlation function. Weak long-term memory refers to the property that if a perturbation (in this case, a step strain) is applied for a short time and then turned off, the system is able to forget this perturbation asymptotically. This is not the case here, due to the incomplete relaxation which leads to frozen-in stress. This is all in contrast with the soft glassy rheology model [36, 44, 120], where the yielding through effective activation always leads to full relaxation at long times (thus ensuring weak long-term memory), and the aging response can be cast into the Cugliandolo-Kurchan form [119].

It is interesting also to contrast our results with "memory" effects studied in a range of athermal systems, including crumpled metallic sheets [121]. These are systems which typically show logarithmic relaxation of the pressure (i.e. normal stress) when compressed, which can in turn be understood as arising from the collective effect of a broad distribution of relaxation rates [122]. In experiments these systems show a non-monotonic pressure response under a two-step protocol, whereby the system is decompressed somewhat after an initial compression. In particular, the response after the decompression shows a local maximum, which occurs at a time which scales linearly with "age". Here the "age" is measured as the time since the application of the initial compression; importantly, this initial compression is applied on an already *arrested* state, i.e. infinitely aged in our context. In [123] such a scenario was reproduced using computer simulations of jammed harmonic spheres (the same particle model we considered in Chapter 3), by applying a two-step protocol on arrested configurations. Importantly, the authors showed that the linear scaling with "age" of the timescale for the maximum of the response is in fact accounted for purely by *time translation-invariant* response functions, so that the memory is in fact not caused by an underlying aging dynamics [123]. This should be

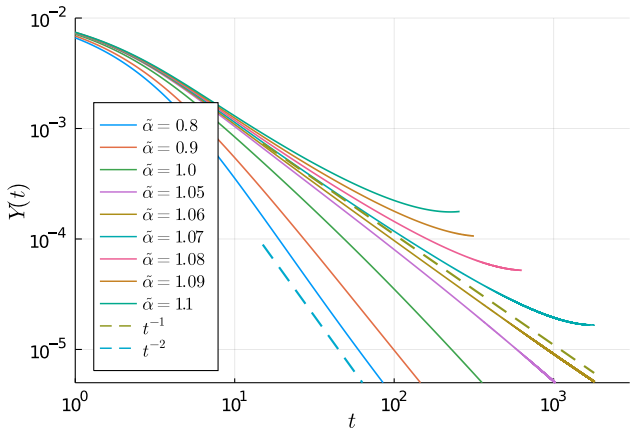

FIGURE 5.1: Aging of the yield rate $Y(t)$ in the disordered HL model, for a range of coupling values around the critical coupling $\tilde{\alpha} = 1$. As initial condition we use (4.51) but with $P^*(E) \sim E\rho(E)$, which is the threshold distribution at $\tilde{\alpha} = 1$ [66]. We find behaviour consistent with the exponents of the original HL model ($\mu = 2$), with $Y(t) \sim t^{-1}$ at criticality and $\sim t^{-2}$ below. Note that criticality occurs slightly above $\tilde{\alpha}$=1, presumably due to the discrete set of energy levels used for the numerics.

contrasted with the "genuine" athermal aging dynamics described here, where we have modelled the response of the system during its slow relaxation towards the arrested state.

We now turn to an issue which was already raised at the end of Chapter 3, namely whether the inclusion of local disorder could be important for the aging results. We recall that in Chapters 2 and 3, the model was characterised by a *single* value of the local yield barrier σ_c. We saw in Chapter 4, on the other hand, that including the disordered energy landscape was crucial to understanding oscillatory shear, including the athermal relaxation under repeated cycles of shear (referred to as mechanical annealing). In Fig. 5.1 we firstly show preliminary numerics for the aging behaviour of the disordered HL model ($\mu = 2$). We recall that in the absence of disorder, the asymptotic behaviour for the yield rate is $\Gamma(t) \sim t^{-2}$ for $\alpha < \alpha_c$, and $\Gamma(t) \sim t^{-1}$ at criticality $\alpha = \alpha_c$. We see from Fig. 5.1 that indeed the same exponents fit well the behaviour of the yield rate in the disordered model: this suggests that the long-time asymptotics we have derived for the aging hold also in the presence of disorder. Physically, one may also argue that an athermally relaxing particle system quenched from a $T = \infty$ configuration (as considered in Chapter 3) presumably is predominantly characterised by low yield barriers and cannot access very deep local energy minima. One may compare the local yield stress maps obtained for glass-forming liquids which are quenched from different "parent temperatures", see e.g. the HTL sample in Fig. 5.4 below (reproduced from [74]), which is obtained by quenching instantaneously from a high temperature liquid: this shows a predominantly homogeneous profile of low energy barriers. This suggests that the role of disorder is not so crucial in this context.

Another simplification of the model considered for aging concerns the nature of the local stress variable. We have considered scalar stresses (shear component only), while of course in reality stresses are tensorial. The inclusion of normal stresses may affect the aging dynamics, although the good agreement we found in Sec. 2.7 with the lattice simulations – which do account for these normal stresses – suggests that such effects would only change the qualitative behaviour. We will return to the

tensorial nature of stress in Sec. 5.4, where we will discuss the relevance of so-called softness [124].

Regarding a comparison of our aging results to experiments, we note again that to test directly the predictions of the yield rate is somewhat challenging. To compare results quantitatively to ours would require a method for extracting the rate of plastic rearrangements $\Gamma(t)$; such a method would, in particular, have to be able to separate events that occur together in an avalanche, which is a significant challenge (see e.g. the methods employed in [82] for a granular system). For the predictions of the stress response in Chapter 3, on the other hand, one could compare directly with measurements on aging suspensions. Carbopol microgels [81, 125], for instance, which are considered to be prototypical of athermal dynamics, could be a good candidate. Linear viscoelastic moduli in these systems would be interesting to measure, as was done in [46–48] for a class of thermosensitive suspensions, whose behaviour could be captured by the predictions of the soft glassy rheology model [120].

We now discuss further the comparison with the model athermal suspension considered in Sec. 3.6. It would firstly be interesting to extend our elastoplastic description in order to account for the non-affine relaxation, which we recall we removed from the data for our comparison. Presumably, what would need to be added to our current picture is the heterogeneity of elastic moduli in the material, which would imply the system falls out of force balance after application of a step strain.

In order to connect further the mesoscopic model to the model particle system, an obvious route would be to study in detail the statistics of plastic events within the MD simulations. An important detail we left aside in Sec. 3.6 concerns the evolution of the system properties during the aging process: as studied in [38], for later times the root mean square velocity decreases, and the active "hotspots" where non-affine relaxation occurs grow in size. One may then also expect the parameters of the corresponding elastoplastic model not to be constant. In fact, by considering the squared ratio of the constants B measured in MD and mean field, it is in principle possible to infer the value of τ_{pl} in MD time units. Given that the coupling A is also unknown, we may take a range of B values measured in the mean field model ($B = 0.4$ to 1.7, as A is decreased), which along with the simulation value $B \approx 0.037$ in Fig. 3.11 would yield $\tau_{\mathrm{pl}} \in (123,\ 2000)$ in MD time units. It would be interesting to measure the plastic timescale in the MD simulation and check whether it lies in the above-mentioned range, and stays roughly constant at least for the range of waiting times in Fig. 3.11.

Another avenue for exploring the mesoscopic assumptions of the elastoplastic model would be to employ a frozen-matrix method [126] (discussed further in the next section) as in [67, 74, 127–129], to obtain direct information on the full local stress distributions. One could then compare the distributions in the final arrested state with and without the previous application of a step strain during the aging, and test the theory against this. Although the results in Sec. 3.6, in particular the good fits of the plateau and stress dynamics with the same value of B shown in Figs. 3.10 and 3.11, already provide good support for the boundary layer dynamics described here, probing the distributions themselves would of course provide stronger evidence, and would shed more light on further questions such as the value of the coupling A.

Finally, it would be interesting to see if/how the elastoplastic description in terms of local stress would connect to an (as of yet unknown) effective microscopic description of the particle dynamics during the athermal aging process. A fascinating finding of [84], where the overdamped gradient descent dynamics (as in Sec. 3.6)

is studied in three different model glass formers via computer simulations, is that for a relaxation from a $T = \infty$ configuration the root mean square velocity decays as a power-law $v_{\mathrm{rms}}(t) \sim t^{-\beta}$, with an exponent β which appears to be roughly universal across the different glass formers and depends only on the spatial dimension (e.g. $\beta \approx 0.92$ in 2D). There is at present no theoretical understanding of this exponent.

It is important to point out that although in Chapter 3 we measure the aging linear response of the model suspension, the underlying dynamics of the system (described within our model through the unperturbed yield rate $\Gamma_0(t)$) is profoundly *non-linear*. This reflects the gradient descent dynamics through a complex energy landscape, where the system crosses saddles (corresponding in our model to plastic events) which become increasingly rare as the arrested state is approached. The landscape is chaotic as well as being rugged, with slight perturbations typically leading to different arrested states [84]. Even starting from the same initial condition, different minimization schemes lead also to different arrested states. This is illustrated in [84] by plotting the displacement field between two such final states, which elucidates the presence of localised "defects" surrounded by an Eshelby quadrupolar field as for the plastic events described here. In this work we are indeed describing the athermal aging as a cascade of such localised defects/excitations, which are here (importantly) triggered by mechanical noise arising from other localised events, and not by shear as in a driven amorphous solid [13] or temperature as in unsheared colloids [130].

5.3 Creep flow

Besides the oscillatory shear studied in Chapter 4, it would also be interesting to study creep behaviour under a constant applied stress in the disordered HL model. Creep has already been studied in [65] using the original HL model. However, different levels of annealing were modelled there as increasingly narrow Gaussian distributions in local elastic strain (or equivalently local stress). As discussed in Sec. 4.6, and argued by pointing to the measurement of local yield stresses [74, 128] or energy barriers [118], we expect the modelling of thermal annealing in terms of occupation of energy levels[1] to be a more realistic approach, e.g. via the β-parametrised distributions in Sec. 4.4 (see Fig. 5.2). For the well-annealed cases (large β) one expects long transient dynamics under creep, where the system almost "runs out" of plastic events until it can eventually re-fluidise. The characteristic s-shaped behaviour of the shear rate under creep has been found in a range of different experimental systems [125, 131].

We show preliminary numerical results confirming this scenario in Fig. 5.3. For the well-annealed initial condition $\beta = 50$, and the same parameter values for $\tilde{\alpha}$ and $\rho(E)$ as considered in the oscillatory shear numerics of Chapter 4, we apply a constant stress to the system by adjusting the shear rate at each step according to the plastic strain relaxation, see relation (4.19). We express the applied stress in terms of the *dynamical* yield stress $\Sigma_y \approx 0.14$, known analytically from (4.43) [66]. We observe that the minimum applied stress to yield (*static* yield stress) is close to the stress overshoot Σ_M under shear startup: for $\beta = 50$, we can indeed extract Σ_M from Fig. 4.12, for the small but finite shear rate $\dot{\gamma} = 10^{-3}$. This gives a value

[1] In the disordered model there is additionally a choice of initialisation in the local strain variable; we have however argued in Chapter 4 that as long as the initial residual strains are relatively small in each energy level with respect to $l_c(E)$ (i.e. $P(l|E)$ sufficiently narrow), the precise form of the local strain distribution does not have a qualitative impact on the behaviour.

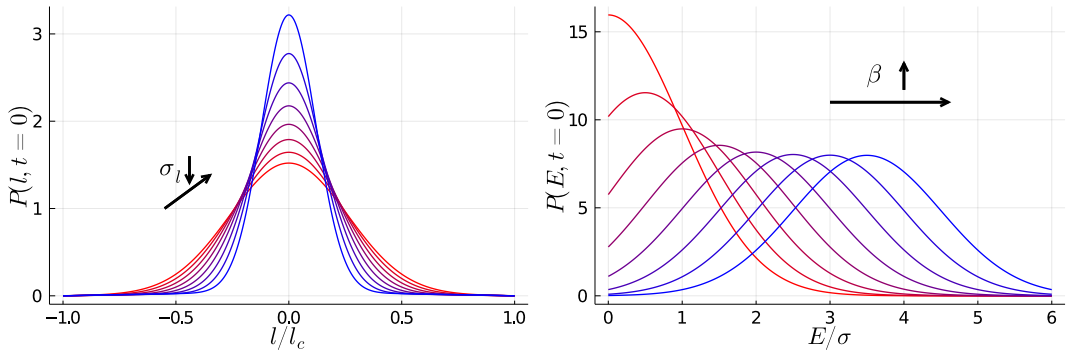

FIGURE 5.2: Two different notions of "annealing" in elastoplastic models. (A): In models without local disorder, defined by a unique threshold $l_c = \sqrt{2E/k}$ with a fixed single value of E, the approach has been to consider increasingly narrow Gaussian distributions in the local elastic strain. This was done to study creep [65, 115] and brittle yielding [116] (see also App. 4.G) using the original HL model. (B) In the model with disorder, one can tune the initial annealing through the occupation of the energy levels, larger β leading to the depletion of "weak" regions. Shown are the distributions defined in Sec. 4.4, with Gaussian local density of states $\rho(E)$ characterised by a fixed variance σ^2.

$\Sigma_M(\dot{\gamma} = 10^{-3}) \approx 2.11\,\Sigma_y$, which is close to (within 2% relative deviation) but slightly larger than the value $\approx 2.07\,\Sigma_y$ estimated for the static yield stress from Fig. 5.3.

In the recent pre-print of [115], a scaling description of creep flow has been proposed. This is based around the flow curve exponent β for stationary flows, defined by $\dot{\gamma} \sim (\Sigma - \Sigma_y)^\beta$. For the HL model, in both its original [37] and disordered [66] versions, $\beta = 2$. The assumption of [115] is that the shear rate under creep is also controlled in this way, and the authors introduce a transient stress $\Sigma_t(\gamma; \Sigma)$ that represents the stress that a configuration can sustain after an accumulation of plastic strain γ under creep at imposed stress Σ. One then assumes that, during creep, $\dot{\gamma} \sim (\Sigma - \Sigma_t(\gamma; \Sigma))^\beta$, and further that $\Sigma_t(\gamma; \Sigma)$ displays a smooth overshoot of magnitude Σ_M for well-annealed samples. This simple Landau-like argument is enough to predict the subcritical creep exponent of the shear rate as $\dot{\gamma}(t) \sim t^{-\beta/(\beta-1)}$, while at criticality $\dot{\gamma}(t) \sim t^{-2\beta/(2\beta-1)}$. The typical timescale (taken in [115] as the time to reach the minimum of the shear rate) diverges as the imposed Σ is reduced towards Σ_M with $\tau_m \sim (\Sigma - \Sigma_M)^{1/2-\beta}$. We show the two power law decays of $\dot{\gamma}(t)$ in Fig. 5.3, with $\beta = 2$ for the disordered HL model, and find that these are fairly consistent with the data (more runs would be needed to confirm the critical power law).

This raises two interesting questions. Firstly, it was found in [83] that the mean field elastoplastic model with power law noise μ has a flow curve exponent $\beta = \mu$ for $1 < \mu \leq 2$, with a logarithmic correction at $\mu = 1$. This implies that within this family of mean field models the subcritical creep exponent is equal to the aging exponent in the absence of shear (where we recall we derived $\Gamma(t) \sim t^{-\mu/(\mu-1)}$ from a boundary layer analysis in Chapter 2). This reflects an interesting symmetry of the mean field model. Indeed, one may notice that the scalings we derived in Sec. 2.5, Eqs. (2.30), for the plastic activity just above the arrest transition ($A \gtrsim A_c$), are the same as those found in [83] for the shear rate under an applied stress just above

the yield stress ($\Sigma \gtrsim \Sigma_y$). This implies that in some sense the activity in the system increases in the same way for an increase in coupling (leading to more noise) as for a small "push" (i.e. increasing stress above yield). The equivalence of the two aging behaviours is an intriguing feature, and it would be interesting to see if it is relevant also in particle simulations or experiments. An advantage of the creep setup is that one may measure directly the shear rate, not the plastic activity as in the absence of shear (see discussion on the challenges of this in Sec. 5.2).

This however may indeed be a purely mean field feature, given that in particle models and in experiments one generally finds flow curve exponents $\beta \approx 2$ [132] (HB law [72]), higher than the $\mu = 1$ prediction.[2] This was argued in [83] to be due to strong finite-dimensional effects, possibly related to the fractal dimension of avalanches. Also in a 2D lattice elastoplastic model, although we found in Chapter 2 that the aging in the absence of shear was well captured by $\mu = 1$, for the flow curve exponent $\beta \approx 1.5$ is measured [31]. This was in turn argued to arise from the cumulative effect of avalanches, leading to a higher effective mechanical noise $\mu \approx 3/2$ [30, 31, 33]. One may argue that indeed such discrepancies in finite dimensions are to be expected, given that the application of a shear stress/strain selects an orientation along which Eshelby events will tend to align, whereas in the absence of shear all orientations are equivalent and it may make more sense to talk of "isolated" plastic events.

The second interesting question concerns a possible connection to the fatigue failure studied in Sec. 4.5. Indeed, although the deformation mechanism is very different, the behaviour of the shear rate under creep is very reminiscent of that of the period-averaged yield rate $\overline{Y}$ shown in Fig. 4.8. This raises the question of whether also for fatigue failure one can find a Landau-like description, which would in particular give a theoretical prediction for the divergence of the failure time (or the time to reach the minimum). However, in the fatigue case it is unclear what physical quantities would play the role of the transient stress Σ_t. Furthermore, under oscillatory shear it is likely that the critical exponents (e.g. the exponent for the critical power-law decay of $\overline{Y}(t)$ precisely at the fatigue limit) are not universal. We recall the discussion in App. 4.E, where we argued that presumably the exponent $b \leq 1$ characterising the critical behaviour $\overline{Y}(t) \sim t^{-b}$ of poorly annealed samples at the common yield point γ_0^* is non-universal and dependent on $\tilde{\alpha}$.

5.4 Yielding beyond mean field

Before we turn to a further discussion beyond mean field, we consider firstly additional features which could already be included in the mean field disordered HL model we have studied to understand yielding behaviour.

A first issue already raised at the end of Chapter 4 concerns the form of the mechanical noise considered. We recall that the main novel feature of the model in Chapters 2 and 3 was the power-law mechanical noise, which was shown to arise from the form of the elastic propagator. For the sake of analytical progress we have nonetheless considered in Chapter 4 a diffusive mechanical noise, i.e. the HL form. Although we do not expect this to change quantitatively the frozen-yielded phase diagram under oscillatory shear (Fig. 4.1), it would certainly affect power-law exponents, e.g. for the critical behaviour, as we saw for the unsheared non-disordered case in Chapter 2.

[2] e.g. for the harmonic sphere system considered in Chapter 3, $\beta \approx 2.0$ [132]

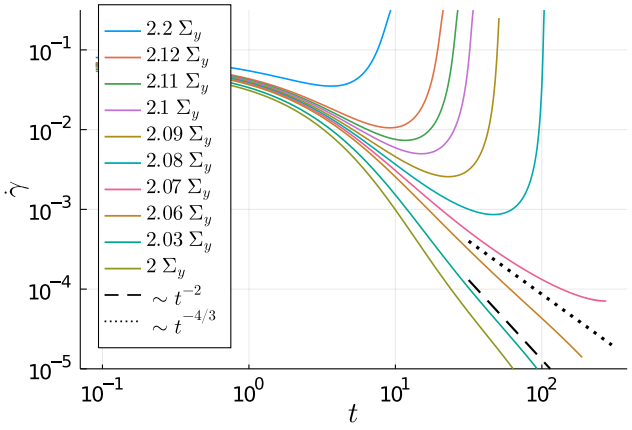

FIGURE 5.3: The disordered HL model under creep (imposed stress), for the well-annealed initial condition $\beta = 50$, and same parameters for $\tilde{\alpha}$ and $\rho(E)$ considered for the numerics in Chapter 4. Stresses are expressed in terms of $\Sigma_y \approx 0.14$ (from (4.43)). Also shown are the power law predictions of [115] in terms of the flow exponent $\beta = 2$; $t^{-\beta/(\beta-1)}$ below yield and $t^{-2\beta/(2\beta-1)}$ at criticality.

The approximation of Gaussian mechanical noise should in any case improve for larger driving, as found in lattice elastoplastic models [29]. In the regime of large shear rate, MD studies have also shown that neither transient nor persistent shear banding occurs [49]. This leads us to expect that the transient dynamics described by the disordered HL model also becomes more accurate away from the quasistatic limit. Preliminary support for this is obtained by comparing the evolution of the energy in the well-annealed sample ($\beta = 50$) above the fatigue limit in our mean field model (Fig. 4.9) with the results shown in the SM of [49] (Fig. S4a). There, a well-annealed sample is considered at a higher shear rate, where both initial and persistent shear banding are absent. The behaviour of the energy is qualitatively very similar to our numerical results, lending credence to the expectation that the transient behaviour described in mean field should become more accurate in this regime.

One could also study the inclusion of temperature within the mean field model. For the conceptual distinction between mechanical noise and thermal noise in the context of amorphous solids, we refer to the thorough discussion in [66] (in particular see Fig. 1 there). Briefly, while the mechanical noise concerns the local stress and hence the forces exerted on a mesoscopic block, tilting the local potential energy landscape towards or away from the next saddle point, the thermal noise can be thought of as acting directly on the local degrees of freedom. A direct way of incorporating this into an elastoplastic picture is by including an Arrhenius-like activation term, so that even when the local strain or stress has not reached its threshold it can "jump" over the barrier due to thermal activation. This was studied in [133] for the original HL model, showing that it leads to a thermal rounding of the yielding transition. A more detailed study of the role of temperature can be found in [33], where also a Prandtl-Tomlison [134] one-particle description, under the simultaneous influence of thermal (Gaussian) and mechanical (power-law distributed, through a stochastic term in the external driving) noise, was shown to reproduce the key scaling laws. It would be interesting to extend the Prandtl-Tomlinson-like description to study the effect of disorder and/or oscillatory shear.

Coming back to the disordered HL model under oscillatory shear, interesting

questions arise regarding the effect of adding thermal activation. In particular, it would be interesting to see the relative roles played by mechanical and thermal noise on the fatigue behaviour studied in Sec. 4.5. Although it is possible that with a finite temperature a yielded state would always be reached, this would presumably involve very long transients at low temperature.

In the introduction of Chapter 4 (Sec. 4.1), we mentioned two aspects of oscillatory shear which could be studied in lattice elastoplastic models [104, 105], but not in our mean field model. The first of these concerned so-called *reversible plasticity*. We recall that his has been studied in MD simulations [99], where it was found that below the yield point the system can settle into non-trivial limit cycles, returning to its initial configuration only after n cycles. We have already argued that reversibility cannot be studied in the current version of the model, given that successive energy minima are extracted independently from $\rho(E)$, and in any case carry no "label". Reversibility could presumably be studied by explicitly including the connectivity of local minima which can be visited by a mesoscopic block. This has been measured in computer simulations [135], where a (sparse) "network" of local minima separated by plastic rearrangements was mapped out. Potentially one could continue to treat the interactions in a mean field manner also in this context.

The other aspect discussed in relation to lattice elastoplastic models was shear banding. We argued in Sec. 4.6 that shear banding, and by extension brittle yielding under uniform shear, presumably cannot be described within a mean field elastoplastic model. The community is now in an ideal position to bridge this gap, however. The increase in computational power has led to a breakthrough in the ability to predict local plasticity from local properties of the material after preparation; we refer to [136], involving the collaboration of several groups around the world, as the state of the art in this direction. There, different local measures are compared with respect to their ability to predict the occurrence of plastic events under shear. The local stress increment to yield turns out to be consistently the best measure. This is obtained via the frozen matrix method [126], whereby a small region is strained up to its closest instability while enforcing affine deformation in the rest of the material. Maps of the local stress increment to yield, obtained with this method, are shown in Fig. 5.4 (reprinted from [74]), for three different preparation protocols ranging from poorly to well-annealed samples.

Within the elastoplastic description, the local stress increment to yield for a block labelled by i corresponds to $\sigma_c - \sigma_i$. Assuming a homogeneous elastic modulus as in Chapter 4, this is also equivalent to the local strain increment $l_c - l_i$. Obtaining the statistics of σ_c or l_c after sample preparation is important for comparing with our modelling approach, as it is equivalent to finding the distribution $P(E, t = 0)$ up to a change of variable. Shown in [74] are only the distributions of the local stress increments to yield, so that one would need to add to these the so-called "residual" stresses after preparation (i.e. the σ_i) to obtain the statistics of the yield stresses or energy barriers. This should however not affect qualitatively the following discussion on the effect of annealing.

From Fig. 5.4, one sees that indeed the "weak" regions (low local stress increment to yield) correlate well with the occurrence of plastic events, as indicated by the numbers. A further observation is that the hallmark of a well-annealed sample is the depletion of such weak zones; the overall distribution of local stress increments (and thus local yield stresses, up to the residual contribution) as a whole does not become narrower, however, as argued in Sec. 4.6 (see also Fig. 4 in [74] for the actual distributions). This is all consistent with how we have modelled different levels of initial annealing (i.e. the choice of $P(E, t = 0)$) in the present work. "Weak"

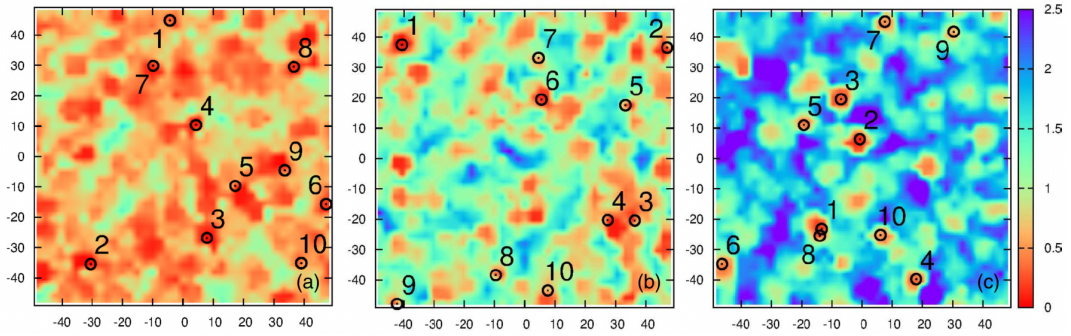

FIGURE 5.4: Maps of local stress increment to yield obtained via the frozen matrix method, for 3 different levels of sample annealing. Quench protocol from left (poorly annealed) to right (well-annealed): HTL (instantaneous quench from a high-temperature liquid), ESL (instantaneous quench from an equilibrium supercooled liquid just above the glass transition) and GQ (gradual quench in which temperature is continuously decreased from a liquid state across the glass transition). Numbers indicate the order of appearance of plastic event locations during loading; these clearly correlate with regions of low local stress increment to yield. Note the depletion of "weak" regions in the well-annealed samples, as discussed in the text. Reprinted with permission from [Barbot et al., Phys. Rev. E, 97, 033001 (2018)]. Copyright (2018) by the American Physical Society.

regions have also been found to correlate well with so-called quasi-localised excitations (QLEs), anomalous vibrational modes of structural glasses which are currently under intense study [137, 138].

An additional local measure found to correlate well with plasticity (and hence by extension to the local stress increment to yield) is so-called "softness". This is a machine-learned quantity: from a set of different structure functions describing the local structural environment, a linear combination is learned which correlates well with rearrangements [124]. The authors of [124] showed that a local rearrangement induces a volumetric strain field, which can affect the softness of far-away particles and lower their local yield stress. This is an effect which has not been included in elastoplastic models so far, which only account for the shear strain field caused by a rearrangement. It would be interesting to try and account for this along the lines already suggested in [124]. One could potentially extend the disordered mean field description, including additionally a "softness" dynamics which would effectively reduce local yield barriers.[3]

We return now to the issue of shear banding, which we recall is especially relevant for well-annealed samples. For example in creep flow (Fig. 5.3), one often finds banding beyond the inflection point of the shear rate $\dot{\gamma}(t)$ [109] (corresponding to the maximum of $\partial_t \dot{\gamma}$); likewise, in the fatigue failure scenario under oscillatory shear, one may also expect banding to occur around the inflection point of the period-averaged yield rate $\overline{Y}(t)$. Although the simpler case of uniform shear is treated, we discuss briefly the findings of [129], where local yield stress distributions were measured and analysed in well-annealed samples which undergo banding. What is measured in this work is the *actual* yield stress, corresponding to our distribution of local yield barriers $P(E)$ (up to a change of variables), not the distribution of local

[3] One could imagine this would entail an additional "drift" term in the E variable, proportional to the yield rate.

stress increments to yield discussed above. The key finding of [129] concerns the nucleation of the shear band, which is found to occur very abruptly, with a sharp contrast in local yield stress appearing already beyond a strain scale corresponding to essentially one plastic event. In the framework of Chapter 4, this means that the distribution of barriers $P(E)$ quickly becomes bimodal. Beyond this point, one may envisage a two-population description, where the sub-population in the shear band would feel a "noisier" environment, with a higher corresponding yield rate. Understanding how such an instability arises, on the other hand, is presumably beyond a mean field description, and would require quantifying in detail how nearby excitations interact and self-organise [136].

We recall finally that interactions stemming from the Eshelby propagator lead in mean field to a *symmetric* mechanical noise, so that the stress increment elsewhere can play either a stabilising or a de-stabilising role. This is arguably the main reason why we do not observe brittle failure in the mean field elastoplastic model with local disorder, the inclusion of which we argued is necessary to properly model different levels of annealing. When the Eshelby propagator is projected onto a 1D line, however, it has a purely positive sign (with a decaying power-law). This is absolutely key for the nucleation of a shear band, see e.g. the discussion in [60]. How this process of nucleation should be described is still debated. [116] proposed a description in terms of fracture mechanics, but it was argued in [60] that this is based on a flawed assumption of pure elasticity. Another approach was followed in [117], considering an elastoplastic setup to study the nucleation of a crack along a line: it would be interesting to extend this analysis to the case with disorder in the local yield barriers.

To sum up, we have proposed in this final chapter some further theoretical developments beyond the main novel[4] elements considered in this thesis: we recall these were the power-law distributed mechanical noise and the inclusion of local disorder. Such refinements on the modelling side should be accompanied by extensive numerical measurements of the relevant quantities in model amorphous solids, as briefly discussed above, in the aim of "calibrating" the mean field models against particle-based simulations. We hope this thesis will inspire future work in this direction.

[4] For scenarios beyond steady shear.

Bibliography

[1] J. T. Parley, S. M. Fielding, and P. Sollich, "Aging in a mean field elastoplastic model of amorphous solids", Physics of Fluids **32**, 127104 (2020).

[2] J. T. Parley, R. Mandal, and P. Sollich, "Mean field description of aging linear response in athermal amorphous solids", arXiv:2202.04387 [cond-mat] (2022).

[3] J. T. Parley, S. Sastry, and P. Sollich, "Mean-Field Theory of Yielding under Oscillatory Shear", Phys. Rev. Lett. **128**, 198001 (2022).

[4] P. W. Anderson, "Through the Glass Lightly", Science **267**, Publisher: American Association for the Advancement of Science, 1610–1610 (1995).

[5] L. Berthier, G. Biroli, J.-P. Bouchaud, L. Cipelletti, and W. van Saarloos, eds., *Dynamical Heterogeneities in Glasses, Colloids, and Granular Media*, International Series of Monographs on Physics (Oxford University Press, Oxford, 2011).

[6] A. J. Liu and S. R. Nagel, "The Jamming Transition and the Marginally Jammed Solid", Annual Review of Condensed Matter Physics **1**, 347–369 (2010).

[7] L. Berthier and G. Biroli, "Theoretical perspective on the glass transition and amorphous materials", Rev. Mod. Phys. **83**, 587–645 (2011).

[8] G. Parisi, P. Urbani, and F. Zamponi, *Theory of Simple Glasses: Exact Solutions in Infinite Dimensions* (Cambridge University Press, Cambridge, 2020).

[9] F. Ritort and P. Sollich, "Glassy dynamics of kinetically constrained models", Advances in Physics **52**, 219–342 (2003).

[10] L. M. C. Janssen, "Mode-Coupling Theory of the Glass Transition: A Primer", Frontiers in Physics **6** (2018).

[11] W. Kob, "The Mode-Coupling Theory of the Glass Transition", in *Supercooled Liquids*, Vol. 676, ACS Symposium Series 676, Section: 3 (American Chemical Society, Sept. 1997), pp. 28–44.

[12] D. Bonn, M. M. Denn, L. Berthier, T. Divoux, and S. Manneville, "Yield stress materials in soft condensed matter", Rev. Mod. Phys. **89**, 035005 (2017).

[13] A. Nicolas, E. E. Ferrero, K. Martens, and J.-L. Barrat, "Deformation and flow of amorphous solids: Insights from elastoplastic models", Rev. Mod. Phys. **90**, 045006 (2018).

[14] E. M. Lifshitz, A. M. Kosevich, and L. P. Pitaevskii, "CHAPTER I - FUNDAMENTAL EQUATIONS", in *Theory of Elasticity (Third Edition)*, edited by E. M. Lifshitz, A. M. Kosevich, and L. P. Pitaevskii (Butterworth-Heinemann, Oxford, Jan. 1986), pp. 1–37.

[15] E. M. Lifshitz, A. M. Kosevich, and L. P. Pitaevskii, "CHAPTER IV - DISLOCATIONS††This chapter was written jointly with A. M. Kosevich.", in *Theory of Elasticity (Third Edition)*, edited by E. M. Lifshitz, A. M. Kosevich, and L. P. Pitaevskii (Butterworth-Heinemann, Oxford, Jan. 1986), pp. 108–132.

[16] A. S. Argon and H. Y. Kuo, "Plastic flow in a disordered bubble raft (an analog of a metallic glass)", Materials Science and Engineering **39**, 101–109 (1979).

[17]A. S. Argon and L. T. Shi, "Development of visco-plastic deformation in metallic glasses", Acta Metallurgica **31**, 499–507 (1983).

[18]P. Schall, D. A. Weitz, and F. Spaepen, "Structural Rearrangements That Govern Flow in Colloidal Glasses", Science **318**, Publisher: American Association for the Advancement of Science, 1895–1899 (2007).

[19]K. W. Desmond and E. R. Weeks, "Measurement of Stress Redistribution in Flowing Emulsions", Phys. Rev. Lett. **115**, Publisher: American Physical Society, 098302 (2015).

[20]A. S. Argon, "Plastic deformation in metallic glasses", Acta Metallurgica **27**, 47–58 (1979).

[21]C. E. Maloney and A. Lemaître, "Amorphous systems in athermal, quasistatic shear", Phys. Rev. E **74**, 016118 (2006).

[22]A. Tanguy, F. Leonforte, and J. .-L. Barrat, "Plastic response of a 2D Lennard-Jones amorphous solid: Detailed analysis of the local rearrangements at very slow strain rate", Eur. Phys. J. E **20**, 355–364 (2006).

[23]F. Puosi, J. Rottler, and J.-L. Barrat, "Time-dependent elastic response to a local shear transformation in amorphous solids", Phys. Rev. E **89**, 042302 (2014).

[24]J.-L. Barrat and A. LemaÎtre, "Heterogeneities in amorphous systems under shear", in *Dynamical Heterogeneities in Glasses, Colloids, and Granular Media* (Oxford University Press, Oxford, 2011).

[25]G. Picard, A. Ajdari, F. Lequeux, and L. Bocquet, "Elastic consequences of a single plastic event: A step towards the microscopic modeling of the flow of yield stress fluids", The European Physical Journal E **15**, 371–381 (2004).

[26]J. D. Eshelby, "The Determination of the Elastic Field of an Ellipsoidal Inclusion, and Related Problems", Proceedings of the Royal Society A: Mathematical, Physical and Engineering Sciences **241**, 376–396 (1957).

[27]J. Lin, E. Lerner, A. Rosso, and M. Wyart, "Scaling description of the yielding transition in soft amorphous solids at zero temperature", Proceedings of the National Academy of Sciences **111**, 14382–14387 (2014).

[28]J. Lin and M. Wyart, "Mean-Field Description of Plastic Flow in Amorphous Solids", Phys. Rev. X **6**, 011005 (2016).

[29]C. Liu, E. E. Ferrero, F. Puosi, J.-L. Barrat, and K. Martens, "Driving Rate Dependence of Avalanche Statistics and Shapes at the Yielding Transition", Phys. Rev. Lett. **116**, 065501 (2016).

[30]I. Fernández Aguirre and E. A. Jagla, "Critical exponents of the yielding transition of amorphous solids", Phys. Rev. E **98**, 013002 (2018).

[31]E. E. Ferrero and E. A. Jagla, "Criticality in elastoplastic models of amorphous solids with stress-dependent yielding rates", Soft Matter **15**, 9041–9055 (2019).

[32]E. E. Ferrero and E. A. Jagla, "Properties of the density of shear transformations in driven amorphous solids", J. Phys.: Condens. Matter **33**, 124001 (2021).

[33]E. E. Ferrero, A. B. Kolton, and E. A. Jagla, "Yielding of amorphous solids at finite temperatures", Phys. Rev. Materials **5**, 115602 (2021).

[34]H. J. Barlow, J. O. Cochran, and S. M. Fielding, "Ductile and brittle yielding in thermal and athermal amorphous materials", Phys. Rev. Lett. **125**, 168003 (2020).

[35]M. L. Falk and J. S. Langer, "Dynamics of viscoplastic deformation in amorphous solids", Phys. Rev. E **57**, 7192–7205 (1998).

[36]P. Sollich, F. Lequeux, P. Hébraud, and M. E. Cates, "Rheology of Soft Glassy Materials", Phys. Rev. Lett. **78**, 2020–2023 (1997).

[37]P. Hébraud and F. Lequeux, "Mode-Coupling Theory for the Pasty Rheology of Soft Glassy Materials", Physical Review Letters **81**, 2934–2937 (1998).

[38]R. N. Chacko, P. Sollich, and S. M. Fielding, "Slow Coarsening in Jammed Athermal Soft Particle Suspensions", Phys. Rev. Lett. **123**, 108001 (2019).

[39]D. J. Durian, "Bubble-scale model of foam mechanics:mMelting, nonlinear behavior, and avalanches", Phys. Rev. E **55**, 1739–1751 (1997).

[40]A. Ikeda, L. Berthier, and P. Sollich, "Unified study of glass and jamming rheology in soft particle systems", Phys. Rev. Lett. **109**, Publisher: American Physical Society, 018301 (2012).

[41]L. F. Cugliandolo, J. Kurchan, and F. Ritort, "Evidence of aging in spin-glass mean-field models", Phys. Rev. B **49**, 6331–6334 (1994).

[42]G. L. Hunter and E. R. Weeks, "The physics of the colloidal glass transition", Rep. Prog. Phys. **75**, 066501 (2012).

[43]J. M. Brader, T. Voigtmann, M. Fuchs, R. G. Larson, and M. E. Cates, "Glass rheology: From mode-coupling theory to a dynamical yield criterion", Proceedings of the National Academy of Sciences **106**, Publisher: Proceedings of the National Academy of Sciences, 15186–15191 (2009).

[44]S. M. Fielding, P. Sollich, and M. E. Cates, "Ageing and Rheology in Soft Materials", Journal of Rheology **44**, 323–369 (2000).

[45]M. Cloitre, R. Borrega, and L. Leibler, "Rheological Aging and Rejuvenation in Microgel Pastes", Physical Review Letters **85**, 4819–4822 (2000).

[46]E. H. Purnomo, D. v. d. Ende, J. Mellema, and F. Mugele, "Linear viscoelastic properties of aging suspensions", Europhys. Lett. **76**, 74–80 (2006).

[47]E. H. Purnomo, D. van den Ende, J. Mellema, and F. Mugele, "Rheological properties of aging thermosensitive suspensions", Phys. Rev. E **76**, 021404 (2007).

[48]E. H. Purnomo, D. van den Ende, S. A. Vanapalli, and F. Mugele, "Glass Transition and Aging in Dense Suspensions of Thermosensitive Microgel Particles", Phys. Rev. Lett. **101**, 238301 (2008).

[49]W.-T. Yeh, M. Ozawa, K. Miyazaki, T. Kawasaki, and L. Berthier, "Glass Stability Changes the Nature of Yielding under Oscillatory Shear", Phys. Rev. Lett. **124**, 225502 (2020).

[50]H. Bhaumik, G. Foffi, and S. Sastry, "The role of annealing in determining the yielding behavior of glasses under cyclic shear deformation", PNAS **118**, e2100227118 (2021).

[51]H. Bhaumik, G. Foffi, and S. Sastry, "Yielding transition of a two dimensional glass former under athermal cyclic shear deformation", arXiv:2108.07497 [cond-mat] (2021).

[52]S. Sastry, "The relationship between fragility, configurational entropy and the potential energy landscape of glass-forming liquids", Nature **409**, 164–167 (2001).

[53]P. Charbonneau, J. Kurchan, G. Parisi, P. Urbani, and F. Zamponi, "Fractal free energy landscapes in structural glasses", Nat Commun **5**, Number: 1 Publisher: Nature Publishing Group, 3725 (2014).

[54]J. Lauridsen, M. Twardos, and M. Dennin, "Shear-Induced Stress Relaxation in a Two-Dimensional Wet Foam", Phys. Rev. Lett. **89**, Publisher: American Physical Society, 098303 (2002).

[55]T. G. Mason, J. Bibette, and D. A. Weitz, "Yielding and Flow of Monodisperse Emulsions", Journal of Colloid and Interface Science **179**, 439–448 (1996).

[56]T. C. Hufnagel, C. A. Schuh, and M. L. Falk, "Deformation of metallic glasses: Recent developments in theory, simulations, and experiments", Acta Materialia **109**, 375–393 (2016).

[57]A. L. Greer, Y. Q. Cheng, and E. Ma, "Shear bands in metallic glasses", Materials Science and Engineering: R: Reports **74**, 71–132 (2013).

[58]Y. Shi and M. L. Falk, "Strain Localization and Percolation of Stable Structure in Amorphous Solids", Phys. Rev. Lett. **95**, 095502 (2005).

[59]M. Ozawa, L. Berthier, G. Biroli, A. Rosso, and G. Tarjus, "A random critical point separates brittle and ductile yielding transitions in amorphous materials", Proceedings of the National Academy of Sciences **115**, 6656–6661 (2018).

[60]M. Ozawa, L. Berthier, G. Biroli, and G. Tarjus, "Rare events and disorder control the brittle yielding of amorphous solids", arXiv:2102.05846 [cond-mat] (2021).

[61]M. Ozawa, L. Berthier, G. Biroli, and G. Tarjus, "Role of fluctuations in the yielding transition of two-dimensional glasses", Phys. Rev. Research **2**, 023203 (2020).

[62]M. Singh, M. Ozawa, and L. Berthier, "Brittle yielding of amorphous solids at finite shear rates", Phys. Rev. Materials **4**, 025603 (2020).

[63]H. Borja da Rocha and L. Truskinovsky, "Rigidity-Controlled Crossover: From Spinodal to Critical Failure", Phys. Rev. Lett. **124**, 015501 (2020).

[64]E. Agoritsas and K. Martens, "Non-trivial rheological exponents in sheared yield stress fluids", Soft Matter **13**, 4653–4660 (2017).

[65]C. Liu, K. Martens, and J.-L. Barrat, "Mean-Field Scenario for the Athermal Creep Dynamics of Yield-Stress Fluids", Phys. Rev. Lett. **120**, 028004 (2018).

[66]E. Agoritsas, E. Bertin, K. Martens, and J.-L. Barrat, "On the relevance of disorder in athermal amorphous materials under shear", Eur. Phys. J. E **38**, 71 (2015).

[67]F. Puosi, J. Olivier, and K. Martens, "Probing relevant ingredients in mean-field approaches for the athermal rheology of yield stress materials", Soft Matter **11**, 7639–7647 (2015).

[68]J.-P. Bouchaud, S. Gualdi, M. Tarzia, and F. Zamponi, "Spontaneous instabilities and stick-slip motion in a generalized Hébraud–Lequeux model", Soft Matter **12**, 1230–1237 (2016).

[69]T. Ekeh, E. Fodor, S. M. Fielding, and M. E. Cates, "Power fluctuations in sheared amorphous materials: A minimal model", arXiv:2106.12962 [cond-mat] (2021).

[70]A. Lemaître and C. Caroli, "Plastic Response of a 2D Amorphous Solid to Quasi-Static Shear : II - Dynamical Noise and Avalanches in a Mean Field Model", arXiv:0705.3122 [cond-mat], arXiv: 0705.3122 (2007).

[71]P. Sollich, J. Olivier, and D. Bresch, "Aging and linear response in the Hébraud–Lequeux model for amorphous rheology", J. Phys. A: Math. Theor. **50**, 165002 (2017).

[72]W. H. Herschel and R. Bulkley, "Konsistenzmessungen von Gummi-Benzollösungen", Kolloid-Zeitschrift **39**, 291–300 (1926).

[73]B. Shang, P. Guan, and J.-L. Barrat, "Elastic avalanches reveal marginal behavior in amorphous solids", PNAS **117**, 86–92 (2020).

[74]A. Barbot, M. Lerbinger, A. Hernandez-Garcia, R. García-García, M. L. Falk, D. Vandembroucq, and S. Patinet, "Local yield stress statistics in model amorphous solids", Phys. Rev. E **97**, Publisher: American Physical Society, 033001 (2018).

[75]A. Lemaître and C. Caroli, "Plastic response of a two-dimensional amorphous solid to quasistatic shear: Transverse particle diffusion and phenomenology of dissipative events", Physical Review E **76**, 10.1103/PhysRevE.76.036104 (2007).

[76]L. Bocquet, A. Colin, and A. Ajdari, "Kinetic Theory of Plastic Flow in Soft Glassy Materials", Phys. Rev. Lett. **103**, 036001 (2009).

[77]A. A. Dubkov, B. Spagnolo, and V. V. Uchaikin, "Lévy flight superdiffusion: an introduction", Int. J. Bifurcation Chaos **18**, Publisher: World Scientific Publishing Co., 2649–2672 (2008).

[78]A. Zoia, A. Rosso, and M. Kardar, "Fractional Laplacian in bounded domains", Phys. Rev. E **76**, 021116 (2007).

[79]S. V. Buldyrev, S. Havlin, A. Y. Kazakov, M. G. E. da Luz, E. P. Raposo, H. E. Stanley, and G. M. Viswanathan, "Average time spent by L\'evy flights and walks on an interval with absorbing boundaries", Phys. Rev. E **64**, 041108 (2001).

[80]A. Giménez, F. Morillas, J. Valero, and J. M. Amigó, "Stability and Numerical Analysis of the Hébraud-Lequeux Model for Suspensions", Discrete Dynamics in Nature and Society **2011**, edited by M. Pituk, 415921 (2011).

[81]M. Agarwal and Y. M. Joshi, "Signatures of physical aging and thixotropy in aqueous dispersion of Carbopol", Physics of Fluids **31**, 063107 (2019).

[82]R. Candelier, O. Dauchot, and G. Biroli, "Dynamical facilitation decreases when approaching the granular glass transition", EPL (Europhysics Letters) **92**, 24003 (2010).

[83]J. Lin and M. Wyart, "Microscopic processes controlling the Herschel-Bulkley exponent", Phys. Rev. E **97**, Publisher: American Physical Society, 012603 (2018).

[84]Y. Nishikawa, M. Ozawa, A. Ikeda, P. Chaudhuri, and L. Berthier, "Relaxation dynamics in the energy landscape of glass-forming liquids", arXiv:2106.01755 [cond-mat] (2021).

[85]R. Mandal and P. Sollich, "Multiple Types of Aging in Active Glasses", Phys. Rev. Lett. **125**, 218001 (2020).

[86]J. P. Bouchaud, "Weak ergodicity breaking and aging in disordered systems", J. Phys. I France **2**, 1705–1713 (1992).

[87]S. Boettcher, D. M. Robe, and P. Sibani, "Aging is a log-Poisson process, not a renewal process", Phys. Rev. E **98**, 020602 (2018).

[88]M. Maier, A. Zippelius, and M. Fuchs, "Emergence of Long-Ranged Stress Correlations at the Liquid to Glass Transition", Phys. Rev. Lett. **119**, 265701 (2017).

[89]R. N. Chacko, F. P. Landes, G. Biroli, O. Dauchot, A. J. Liu, and D. R. Reichman, "Elastoplasticity Mediates Dynamical Heterogeneity Below the Mode Coupling Temperature", Phys. Rev. Lett. **127**, 048002 (2021).

[90]A. Zoia, A. Rosso, and S. N. Majumdar, "Asymptotic Behavior of Self-Affine Processes in Semi-Infinite Domains", Phys. Rev. Lett. **102**, 120602 (2009).

[91]E. S. Andersen, "On the fluctuations of sums of random variables II", MATHEMATICA SCANDINAVICA **2**, 194–222 (1954).

[92] A. J. Bray, S. N. Majumdar, and G. Schehr, "Persistence and first-passage properties in nonequilibrium systems", Advances in Physics **62**, 225–361 (2013).

[93] K. Saitoh, T. Hatano, A. Ikeda, and B. P. Tighe, "Stress Relaxation above and below the Jamming Transition", Phys. Rev. Lett. **124**, 118001 (2020).

[94] A. W. Lees and S. F. Edwards, "The computer study of transport processes under extreme conditions", J. Phys. C: Solid State Phys. **5**, 1921–1928 (1972).

[95] G. Parisi, I. Procaccia, C. Rainone, and M. Singh, "Shear bands as manifestation of a criticality in yielding amorphous solids", Proceedings of the National Academy of Sciences **114**, Publisher: Proceedings of the National Academy of Sciences, 5577–5582 (2017).

[96] D. Richard, C. Rainone, and E. Lerner, "Finite-size study of the athermal quasistatic yielding transition in structural glasses", J. Chem. Phys. **155**, Publisher: American Institute of Physics, 056101 (2021).

[97] D. Fiocco, G. Foffi, and S. Sastry, "Oscillatory athermal quasistatic deformation of a model glass", Phys. Rev. E **88**, 020301 (2013).

[98] N. V. Priezjev, "Heterogeneous relaxation dynamics in amorphous materials under cyclic loading", Phys. Rev. E **87**, 052302 (2013).

[99] I. Regev, T. Lookman, and C. Reichhardt, "Onset of irreversibility and chaos in amorphous solids under periodic shear", Phys. Rev. E **88**, 062401 (2013).

[100] T. Kawasaki and L. Berthier, "Macroscopic yielding in jammed solids is accompanied by a nonequilibrium first-order transition in particle trajectories", Phys. Rev. E **94**, 022615 (2016).

[101] P. Leishangthem, A. D. S. Parmar, and S. Sastry, "The yielding transition in amorphous solids under oscillatory shear deformation", Nat Commun **8**, 14653 (2017).

[102] A. Szulc, O. Gat, and I. Regev, "Forced deterministic dynamics on a random energy landscape: Implications for the physics of amorphous solids", Phys. Rev. E **101**, 052616 (2020).

[103] S. Sastry, "Models for the Yielding Behavior of Amorphous Solids", Phys. Rev. Lett. **126**, 255501 (2021).

[104] C. Liu, E. E. Ferrero, E. A. Jagla, K. Martens, A. Rosso, and L. Talon, "The Fate of Shear-Oscillated Amorphous Solids", arXiv:2012.15310 [cond-mat] (2021).

[105] K. Khirallah, B. Tyukodi, D. Vandembroucq, and C. E. Maloney, "Yielding in an Integer Automaton Model for Amorphous Solids under Cyclic Shear", Phys. Rev. Lett. **126**, 218005 (2021).

[106] M. Mungan and S. Sastry, "Metastability as a Mechanism for Yielding in Amorphous Solids under Cyclic Shear", Phys. Rev. Lett. **127**, 248002 (2021).

[107] C. Ness and M. E. Cates, "Absorbing-State Transitions in Granular Materials Close to Jamming", Phys. Rev. Lett. **124**, 088004 (2020).

[108] A. D. S. Parmar, S. Kumar, and S. Sastry, "Strain Localization Above the Yielding Point in Cyclically Deformed Glasses", Phys. Rev. X **9**, 021018 (2019).

[109] T. Divoux, C. Barentin, and S. Manneville, "From stress-induced fluidization processes to Herschel-Bulkley behaviour in simple yield stress fluids", Soft Matter **7**, 8409 (2011).

[110] H. A. Carmona, F. Kun, J. S. Andrade, and H. J. Herrmann, "Computer simulation of fatigue under diametrical compression", Phys. Rev. E **75**, 046115 (2007).

[111]S. Pradhan, A. Hansen, and B. K. Chakrabarti, "Failure processes in elastic fiber bundles", Rev. Mod. Phys. **82**, 499–555 (2010).

[112]B. P. Bhowmik, H. G. E. Hentschel, and I. Procaccia, "Fatigue and Collapse of Cyclically Bent Strip of Amorphous Solid", arXiv:2103.03040 [cond-mat] (2021).

[113]F. Kun, M. H. Costa, R. N. C. Filho, J. S. Andrade, J. B. Soares, S. Zapperi, and H. J. Herrmann, "Fatigue failure of disordered materials", J. Stat. Mech. **2007**, P02003–P02003 (2007).

[114]Z. D. Sha, S. X. Qu, Z. S. Liu, T. J. Wang, and H. Gao, "Cyclic Deformation in Metallic Glasses", Nano Lett. **15**, 7010–7015 (2015).

[115]M. Popović, T. W. J. de Geus, W. Ji, A. Rosso, and M. Wyart, "Scaling description of creep flow in amorphous solids", arXiv:2111.04061 [cond-mat] (2021).

[116]M. Popović, T. W. J. de Geus, and M. Wyart, "Elastoplastic description of sudden failure in athermal amorphous materials during quasistatic loading", Phys. Rev. E **98**, 040901 (2018).

[117]S. M. Fielding, "Yielding, shear banding and brittle failure of amorphous materials", arXiv:2103.06782 [cond-mat] (2021).

[118]L. Tang, H. Liu, G. Ma, T. Du, N. Mousseau, W. Zhou, and M. Bauchy, "The energy landscape governs ductility in disordered materials", Mater. Horiz. **8**, Publisher: The Royal Society of Chemistry, 1242–1252 (2021).

[119]L. F. Cugliandolo and J. Kurchan, "On the out-of-equilibrium relaxation of the Sherrington-Kirkpatrick model", J. Phys. A: Math. Gen. **27**, 5749–5772 (1994).

[120]P. Sollich, "Rheological constitutive equation for a model of soft glassy materials", Phys. Rev. E **58**, 738–759 (1998).

[121]Y. Lahini, O. Gottesman, A. Amir, and S. M. Rubinstein, "Nonmonotonic Aging and Memory Retention in Disordered Mechanical Systems", Phys. Rev. Lett. **118**, Publisher: American Physical Society, 085501 (2017).

[122]A. Amir, Y. Oreg, and Y. Imry, "On relaxations and aging of various glasses", PNAS **109**, Publisher: National Academy of Sciences Section: Physical Sciences, 1850–1855 (2012).

[123]R. Mandal, D. Tapias, and P. Sollich, "Memory in non-monotonic stress response of an athermal disordered solid", Phys. Rev. Research **3**, Publisher: American Physical Society, 043153 (2021).

[124]G. Zhang, S. A. Ridout, and A. J. Liu, "Interplay of Rearrangements, Strain, and Local Structure during Avalanche Propagation", Phys. Rev. X **11**, Publisher: American Physical Society, 041019 (2021).

[125]P. Lidon, L. Villa, and S. Manneville, "Power-law creep and residual stresses in a carbopol microgel", Rheol Acta **56**, 307–323 (2017).

[126]P. Sollich, in CECAM Workshop (ACAM, Dublin, Ireland, 2011).

[127]C. Ruscher and J. Rottler, "Residual stress distributions in amorphous solids from atomistic simulations", Soft Matter **16**, 8940–8949 (2020).

[128]S. Patinet, D. Vandembroucq, and M. L. Falk, "Connecting Local Yield Stresses with Plastic Activity in Amorphous Solids", Phys. Rev. Lett. **117**, Publisher: American Physical Society, 045501 (2016).

[129]A. Barbot, M. Lerbinger, A. Lemaître, D. Vandembroucq, and S. Patinet, "Rejuvenation and shear banding in model amorphous solids", Phys. Rev. E **101**, Publisher: American Physical Society, 033001 (2020).

[130] A. Lemaître, "Structural Relaxation is a Scale-Free Process", Phys. Rev. Lett. **113**, Publisher: American Physical Society, 245702 (2014).

[131] M. Siebenbürger, M. Ballauff, and T. Voigtmann, "Creep in Colloidal Glasses", Phys. Rev. Lett. **108**, Publisher: American Physical Society, 255701 (2012).

[132] A. Ikeda, L. Berthier, and P. Sollich, "Disentangling glass and jamming physics in the rheology of soft materials", Soft Matter **9**, Publisher: The Royal Society of Chemistry, 7669–7683 (2013).

[133] M. Popović, T. W. J. de Geus, W. Ji, and M. Wyart, "Thermally activated flow in models of amorphous solids", Phys. Rev. E **104**, 025010 (2021).

[134] L. Prandtl, "Ein Gedankenmodell zur kinetischen Theorie der festen Körper", ZAMM - Journal of Applied Mathematics and Mechanics / Zeitschrift für Angewandte Mathematik und Mechanik **8**, 85–106 (1928).

[135] M. Mungan, S. Sastry, K. Dahmen, and I. Regev, "Networks and Hierarchies: How Amorphous Materials Learn to Remember", Phys. Rev. Lett. **123**, 178002 (2019).

[136] D. Richard, M. Ozawa, S. Patinet, E. Stanifer, B. Shang, S. A. Ridout, B. Xu, G. Zhang, P. K. Morse, J.-L. Barrat, L. Berthier, M. L. Falk, P. Guan, A. J. Liu, K. Martens, S. Sastry, D. Vandembroucq, E. Lerner, and M. L. Manning, "Predicting plasticity in disordered solids from structural indicators", Phys. Rev. Materials **4**, Publisher: American Physical Society, 113609 (2020).

[137] E. Lerner and E. Bouchbinder, "Low-energy quasilocalized excitations in structural glasses", J. Chem. Phys. **155**, Publisher: American Institute of Physics, 200901 (2021).

[138] W. Ji, M. Popović, T. W. J. de Geus, E. Lerner, and M. Wyart, "Theory for the density of interacting quasilocalized modes in amorphous solids", Phys. Rev. E **99**, 023003 (2019).